

PERFORMANCE EVALUATION OF THE MODIFIED MOISTURE BARRIER IN
STABILIZING SHALLOW SLOPE FAILURES

by

MUHASINA MANJUR DOLA

Presented to the Faculty of the Graduate School of
The University of Texas at Arlington in Partial Fulfilment
of the Requirements
for the Degree of

DOCTOR OF PHILOSOPHY IN CIVIL ENGINEERING

THE UNIVERSITY OF TEXAS AT ARLINGTON

DECEMBER 2022

Copyright © by Muhasina Manjur Dola 2022

All Rights Reserved



ACKNOWLEDGEMENT

I would like to express my sincere gratitude to my supervising professor, Dr. Sahadat Hossain, for his motivation, encouragement, and guidance throughout my graduate study. His knowledge, experience and mentorship paved the way for the successful completion of my dissertation. I am grateful for the opportunity to have worked under him as a part of his research group.

I would like to acknowledge Dr. Xinbao Yu, Dr. Laureano Hoyos and Dr. Muhammad N. Huda for serving on my dissertation committee and for their valuable insights. I also wish to acknowledge the Texas Department of Transportation for providing the funding for this research study.

I would like to thank all the SWIS members for their support and assistance. The fieldwork would not have been possible without Sachini Madanayake and Alinda Gupta Abhro and I greatly appreciate their invaluable help. I am very thankful for the unwavering support of Dr. Aminul Islam, Dr. Prabesh Bhandari and Dr. Pratibha Pandey.

Finally, I would like to express deep gratitude to my parents for their unconditional love and encouragement. I would not have been able to achieve this milestone without them. Last but not least, I would like to thank my husband Mahbub for his patience and his belief in me throughout my academic journey.

October 15, 2022

ABSTRACT

PERFORMANCE EVALUTATION OF THE MODIFIED MOISTURE BARRIER IN STABILIZATION SHALLOW SLOPE FAILURES

Muhasina Manjur Dola, PhD

The University of Texas at Arlington, 2022

Supervising Professor: MD Sahadat Hossain

Each year significant number of highway slope failures are reported in the United States, especially in states like Texas where expansive clayey soil is prevalent. Slopes constructed over expansive clay often experience recurring shallow failures following their construction which poses maintenance problems to the Texas Department of Transportation (TxDOT). These shallow slope failures can be primarily attributed to the considerable volume change that expansive clay soil undergoes from seasonal climatic variation. Furthermore, under unsaturated conditions during dry periods, high matric suction (i.e., negative porewater pressure) exists in soil slopes. The existence of matric suction contributes to the shear strength of the soil. Contrastingly, during prolonged wet periods, sufficient infiltration occurs into the slope and decreases the matric suction of the soil. The loss of matric suction in turn results in an increase in soil water content and subsequent reduction of the additional shear strength provided by the matric suction eventually leading to shallow slope failures. Since rainfall infiltration is a major cause of shallow failures of highway slopes, it is worthwhile to study preventive measures that can minimize rainfall infiltration into soil slopes which will in turn maintain the long-term stability of the slope.

Conventional slope stabilization methods include earthwork, moisture control and mechanical reinforcement methods. To this end, a slope stabilization method was developed utilizing the

modified moisture barrier to minimize rainfall intrusion into a soil slope. A portion of a failed section of a highway slope located along interstate highway 20 in Arlington, Texas was designed to be stabilized with a modified moisture barrier. The failed section was divided into two test sections modified moisture barrier and recycled plastic pins sections, while a portion of the original slope was established as the control section. The test sections were instrumented with integrated temperature-moisture sensors, soil water potential sensors, and vertical inclinometer casings. Additionally, a topographic survey of the slope was conducted using a total station and field hydraulic conductivity testing was carried out in the test sections.

Measurement of volumetric water content and matric suction revealed that the control section experienced instantaneous fluctuations with respect to rainfall events while that of the MMB section was considered insignificant. The maximum variation of moisture content in the control section ranged from approximately 14.7 to 32.6 % while that of the MMB section was almost constant. The insignificant change in moisture content of the MMB section soil was reflected in the field measurements of soil permeability. The hydraulic conductivity of the soil under the MMB section remained almost constant while that of the other sections showed considerable variation with time and rainfall, as exposed to climatic conditions. The insignificant fluctuation of the moisture content in the MMB section also influenced the lateral and vertical movement of the slope. The MMB section experienced maximum lateral deformation of 0.29 inches over a monitoring period of 36 months which was about 40% lower than that of the control section while the RPP section showed maximum lateral movement of 0.26 inches. In comparison, the MMB and RPP section showed a very similar reduction in maximum lateral deformation of the slope compared to the control section. Similar trend was observed in the vertical settlement of the slope: the MMB section showed 65% reduction in movement compared to the control while that of the

RPP section was 37% less. Therefore, it can be concluded that use of the modified moisture barrier reduces the lateral and vertical settlement of the slope caused by the swell-shrink behavior of expansive soil by controlling rainfall infiltration.

TABLE OF CONTENT

ACKNOWLEDGEMENT	iii
ABSTRACT.....	iv
LIST OF FIGURES	xvi
LIST OF TABLES.....	xxv
CHAPTER 1 INTRODUCTION.....	1
1.1 Background.....	1
1.2 Problem Statement.....	3
1.3 Research Objectives	4
1.4 Thesis Organization.....	5
CHAPTER 2 LITERATURE REVIEW	8
2.1 Introduction	8
2.2 Expansive Soil	8
2.2.1 Cyclic Swelling and Shrinkage Mechanism.....	9
2.2.2 Softening Mechanism of Expansive Soil	10
2.3 Unsaturated Soil and Matric Suction.....	11
2.4 Factors affecting Infiltration.....	11
2.4.1 Vegetation	12
2.4.2 Surface Cover	13
2.4.3 Cracks.....	14

2.4.4	Slope Angle.....	14
2.4.5	Rainfall Intensity.....	15
2.5	Damages due to Expansive Soils.....	16
2.6	Shallow Slope Failures.....	16
2.6.1	Active Zone.....	18
2.7	Methods of Repair.....	19
2.7.1	Rebuilding of Slope.....	20
2.7.2	Geogrid Repair.....	20
2.7.3	Soil Cement Repair.....	21
2.7.4	Pipe Piles and Wood Lagging.....	22
2.7.5	Soil Nails.....	23
2.7.6	Plate Piles.....	24
2.7.7	Micro piles.....	25
2.7.8	Recycled Plastic Pins.....	25
2.7.8.1	Stability of Reinforced Slopes.....	26
2.7.8.2	Design Method.....	27
2.7.8.3	Field Performance of RPP Stabilized Slopes.....	29
2.8	Moisture Control Methods for Slope Stabilization.....	37
2.8.1	Horizontal Drains.....	37
2.8.2	Capillary Barrier System (CBS).....	38

2.8.3	CBS using Fine Sand and Granite Chips	38
2.8.4	CBS using Fine Sand and Recycled Crushed Concrete Aggregate	39
2.8.5	CBS using Fine Sand and Geosynthetics (Secudrain)	41
2.8.6	Geosynthetic Capillary Break	43
2.8.7	Modified Moisture Barrier	44
2.8.7.1	Mechanism	44
2.8.7.2	Field Performance of Modified Moisture Barrier	46
CHAPTER 3 SITE INVESTGATION AND SLOPE STABILIZATION PLAN.....		51
3.1	Introduction	51
3.2	Project Background	51
3.3	Site Investigation	52
3.3.1	Geotechnical Drilling	53
3.3.1.1	Gravimetric Moisture Content	55
3.3.1.2	Grain Size Distribution.....	56
3.3.1.3	Atterberg Limit.....	58
3.3.1.4	Hydraulic Conductivity	59
3.3.1.5	Shear Strength	61
3.3.2	Geophysical Testing.....	62
3.4	Assessment of Site Investigation Results	63
3.5	Controlling Rainwater Intrusion in Slopes	64

3.5.1	Design of Test Sections.....	66
3.5.1.1	MMB Section.....	66
3.5.1.2	RPP Section.....	69
3.5.1.3	Control Section.....	71
CHAPTER 4 FIELD INSTALLATION AND INSTRUMENTATION.....		72
4.1	Introduction	72
4.2	Field Installation.....	72
4.2.1	Installation of Modified Moisture Barrier.....	72
4.2.2	Installation of Recycled Plastic Pins	74
4.3	Field Instrumentation.....	77
4.3.1	Monitoring Instruments.....	78
4.3.2	Calibration of Sensors	79
4.3.3	Installation of Sensors	80
4.3.4	Installation of Inclinometer Casings	82
4.3.5	Data Collection and Field Monitoring	83
4.4	Field Testing.....	84
4.4.1	Hydraulic Conductivity.....	84
CHAPTER 5 FIELD RESULTS AND DISCUSSION		87
5.1	Introduction	87
5.2	Variation of Volumetric Moisture Content and Matric Suction.....	87

5.2.1	Variation of Volumetric Moisture Content	87
5.2.1.1	MMB Section	87
5.2.1.2	Control Section.....	89
5.2.1.3	Comparison of Test Sections.....	91
5.2.1.4	Comparison with previous literature	92
5.2.2	Variation of Matric Suction.....	92
5.2.2.1	Comparison with previous literature	94
5.2.3	Variation of Temperature	95
5.3	Lateral Deformation of the Slope	96
5.3.1	Control Section.....	96
5.3.2	MMB Section	98
5.3.3	RPP Section.....	99
5.3.4	Comparison of Lateral Deformation of Test Sections	99
5.3.5	Comparison with previous literature	102
5.4	Vertical Settlement of Slope.....	102
5.4.1	Crest of the Slope	103
5.4.1.1	Comparison of Test Sections.....	104
5.4.2	Middle of the Slope	105
5.4.2.1	Comparison of Test Sections.....	106
5.4.3	Comparison with Previous Literature	107

5.5	Variation of Field Hydraulic Conductivity.....	108
5.5.1	Crest of the Slope	109
5.5.2	Middle of the Slope.....	111
5.5.3	Effectiveness of the MMB	112
5.5.4	Comparison with Previous Literature	114
CHAPTER 6 NUMERICAL STUDY.....		115
6.1	Background.....	115
6.2	Finite Element Based Numerical Model	116
6.3	Development of Model.....	116
6.3.1	Model Geometry and Boundary Conditions	117
6.3.2	Material Properties	119
6.3.2.1	Soil Water Characteristic Curve (SWCC).....	119
6.3.2.2	Hydraulic Conductivity Function (HCF)	120
6.3.2.3	Shear Strength Parameter	122
6.3.3	Climatic Flux Boundary	123
6.4	Addition of Modified Moisture Barrier	128
6.5	Flow Analysis of Modified Moisture Barrier System	131
6.5.1	Variation of Porewater Pressure within MMB.....	132
6.5.2	Variation of Volumetric Water Content within MMB.....	135
6.5.3	Flow Diversion Capacity of the MMB.....	136

6.5.4	Diversion Length of the MMB.....	138
6.5.4.1	Comparison with Analytical Solutions	140
6.6	Effect of Length of MMB on Slope Stability	144
6.7	Effect of Rainfall on Slope Stability.....	146
6.8	Parametric Study.....	150
6.8.1	Effect of Slope Geometry.....	153
6.8.2	Effect of Soil Shear Strength Properties	160
6.8.3	Effect of Soil Hydraulic Properties	166
6.8.4	Effect of Rainfall Intensity	169
6.8.5	Sensitivity Assessment.....	172
CHAPTER 7 PREDICTION MODEL		174
7.1	Background.....	174
7.2	Statistical Analysis	175
7.3	Correlation Analysis	177
7.3.1	Predictor vs Predictor	177
7.3.2	Response vs Predictor Plots	179
7.4	Preliminary Model Development	181
7.5	Verification of Preliminary Model	183
7.5.1	Constant Error Variance.....	183
7.5.2	Normality	185

7.5.3	Outlier.....	187
7.5.4	Multicollinearity.....	187
7.6	Transformation of Variables and MLR Assumptions Check.....	188
7.7	Verification of Final Model.....	189
7.7.1	Constant Error Variance.....	189
7.7.2	Normality Test.....	190
7.7.3	Outlier Test.....	192
7.7.4	Multicollinearity.....	192
7.8	Final Model Selection.....	192
7.8.1	Best Subset Selection.....	192
7.8.2	Backward Elimination.....	193
7.8.3	Stepwise Regression.....	194
7.9	Final Model Validation.....	195
7.10	Design Methodology.....	196
7.10.1	Design Charts.....	198
7.10.2	Design Example.....	200
7.10.2.1	Ordinary Method of Slices.....	201
7.10.2.2	Infinite Slope.....	204
7.10.2.3	Prediction Equation.....	206
7.11	Limitations of the Prediction Model.....	208

CHAPTER 8	SUMMARY AND CONCLUSIONS	210
8.1	Background.....	210
8.1.1	Site Investigation.....	211
8.1.2	Variation of Moisture Content and Matric Suction.....	211
8.1.3	Lateral Deformation	212
8.1.4	Vertical Settlement.....	213
8.1.5	Hydraulic Conductivity	213
8.1.6	Numerical Study.....	214
8.1.7	Prediction Model and Design Methodology	215
8.2	Recommendation for Future Studies	215
REFERENCES.....		217
APPENDIX A.....		226
APPENDIX B.....		229
BIOGRAPHY.....		231

LIST OF FIGURES

Figure 1-1 Schematic illustration of rainfall induced shallow slope failure.	4
Figure 2-1 Soil map of Texas (Adopted from Olive et al. (1989)).	9
Figure 2-2 Expansion of clay due to water infiltration (Amakye et al., 2021).	10
Figure 2-3 Comparisons of peak, fully softened, and residual shear strength (Skempton, 1970).	10
Figure 2-4 Matric suction profiles under various flux boundary conditions (Adapted from (Fredlund et al., 1996))	11
Figure 2-5 Variation of matric suction with rainfall (a) vegetated area (b) non vegetated area (Kim and Lee, 2010)	12
Figure 2-6 Variation of volumetric water content with rainfall (a) vegetated area (b) non vegetated area (Kim and Lee, 2010).	13
Figure 2-7 Decrease in matric suction with time at different depths during rainfall events of February 1994 (Lim et al., 1996).	13
Figure 2-8 Infiltration rates for cracked and intact soils (Zhan et al., 2007).	14
Figure 2-9 Effect of rainfall intensity on factory of safety of a slope (Huat et al., 2006).	16
Figure 2-10 Typical surficial slope failure (redrawn after Day and Axten, 1989).	17
Figure 2-11 Shallow slope failure near eastbound IH20 in Dallas, Texas (Rauss,2019).	18
Figure 2-12 Classification of slope repair methods (Shahandashti et al., 2019).	20
Figure 2-13 Geogrid repair of surficial slope failure (Day, 1996).	21
Figure 2-14 Schematic of soil cement repair method (Day, 1996).	22
Figure 2-15 Graphical representation of pipe piles and wood lagging system (Day, 1996).	23
Figure 2-16 Schematic of slope repair using launched soil nails (redrawn from Titi and Helwany, 2007).	24

Figure 2-17 Schematic of plate pile stabilization (Collins and Short, 2006).....	25
Figure 2-18 Equilibrium of an individual slice in the method of slices (Khan, 2014).	27
Figure 2-19 Combined limit resistance curve (Loehr and Bowders, 2007).....	29
Figure 2-20 Layout of RPP at the slide areas (a) S1 and S2 (b) S3 (Loehr and Bowders, 2007 and Parra et al., 2003).....	31
Figure 2-21 Result of inclinometer I2 at S2 (Parra et al., 2003).....	31
Figure 2-22 Displacement profile at slide section S3 from inclinometers (a)I-6 (b) I-7 (c) I-8 (d) I-9 (Loehr and Bowders, 2007).	32
Figure 2-23 Layout of RPP (a) Cross sectional view (b) Plan view (Loehr and Bowders, 2007).	33
Figure 2-24 Cumulative lateral displacement with time for I-2 (Parra et al., 2003).....	34
Figure 2-25 Layout of RPP at US 287 slope section (Khan, 2014).....	35
Figure 2-26 Cumulative lateral deformation of slope at from inclinometer (a) I-1 and (b) I-3 (Rauss, 2019).	36
Figure 2-27 Vertical settlement of the slope at the crest (Rauss, 2019).	37
Figure 2-28 (a) Schematic of stabilized slope (b) Cross section of CBS (Rahardjo et al., 2012).	39
Figure 2-29 Variation of porewater pressure with rainfall and time near the creast of the slope (a) with CBS (b) without CBS (Rahardjo, et al., 2012).	39
Figure 2-30 (a) Schematic of stabilized slope (b) Cross section of CBS (Rahardjo et al., 2013).	40
Figure 2-31 Variation of porewater pressure with time at the middle of the slope (a) Slope with CBS (b) Original slope (c) Rainfall intensity with respect to time.	41
Figure 2-32 (a) Schematic of stabilized slope (b) Cross section of CBS.....	42
Figure 2-33 Variation of porewater pressure with time at the middle of the slope (a) Slope with CBS (b) Original Slope (c) Rainfall intensity with respect to time.	43

Figure 2-34 Schematic of GCB (Park and Fleming, 2006).	44
Figure 2-35 Lateral drainage in unsaturated soil with (a) capillary barrier (b) transport layer above a capillary barrier (c) GCBD with overlying soil (Redrawn from Henry et al., 2002).....	45
Figure 2-36 Modified moisture barrier used in pavement subgrade (Ahmed, 2017).	46
Figure 2-37 Comparison of moisture content for barrier section and control section at 3 feet depth (Ahmed et al.,2017).	47
Figure 2-38 Schematic diagram of slope stabilized with recycled plastic pins and modified moisture barrier (Sapkota et al., 2019).....	48
Figure 2-39 Change in volumetric moisture content with time and rainfall (a) control section (b) barrier section (Sapkota et al., 2019).	49
Figure 2-40 Depth wise comparison of lateral deformation at (a) control section (b) barrier section (Sapkota et al., 2019).	50
Figure 3-1 (a) Site Location (b) and (c) Shallow Slope Failure.	52
Figure 3-2 Locations of geotechnical borings (BH) and electrical resistivity imagine (ERI line).	53
Figure 3-3 (a) Drilling using hollow stem auger. (b) Undisturbed Shelby tube sample.....	54
Figure 3-4 Moisture content profile with respect to depth.	56
Figure 3-5 Hydrometer test samples.	57
Figure 3-6 Grain size distribution curves.....	58
Figure 3-7 Plasticity chart.	59
Figure 3-8 Permeability test set up.	61
Figure 3-9 (a) Location of ERI line (b) 8 Channel SuperSting Equipment.	63
Figure 3-10 Result of ERI.	63

Figure 3-11 (a) Detailed mechanism of the modified moisture barrier (b) Capillary barrier effect in the MMB.....	65
Figure 3-12 Schematic of test sections.	66
Figure 3-13 Materials used in the MMB (a) HDPE Geocomposite (https://skaps.com/) (b) LLDPE Geomembrane (https://www.americover.com/).....	67
Figure 3-14 Layout of MMB section.	68
Figure 3-15 Layout of RPP section.....	70
Figure 4-1 Modified Moisture Barrier Installation Process (a) Excavation of trench at crest of the slope (b) Cleaning of trench (c) Placement of geomembrane (d) Placement of geocomposite (e) Backfilling of trench with excavated soil.	74
Figure 4-2 Recycled Plastic Pins Installation Process (a) Placement of the RPPs in the marked locations (b) Driving of the RPPs into the ground (c) Backfilling of the slope.....	76
Figure 4-3 As built layout of RPP installation.....	76
Figure 4-4 Instrumentation Layout.	77
Figure 4-5 (a) Integrated Moisture-Temperature Sensor (b) Soil Water Potential Sensor (c) Datalogger.....	78
Figure 4-6 (a)Vertical Slope Indicator (b) Total Station.	79
Figure 4-7 Calibration of Sensors.	79
Figure 4-8 Location of sensors and data logger for MMB Section.	81
Figure 4-9 Installation of Sensors (a) Installation of the sensor at the desired depth (b) Moisture sensor inserted into the soil (c) Compaction of backfilled soil into the borehole.....	82
Figure 4-10 Installation of Inclinator Casing (a) Drilling of borehole (b) Placement of inclinometer casing into borehole (c) Completele inserted casing.	83

Figure 4-11 Instrumental Setup of Guelph Permeameter.	85
Figure 4-12 Field Testing Location.	85
Figure 4-13 Hydraulic Conductivity Testing Procedure for (a) MMB Section (b) 2 ft. Deep Test Boreholes (c) Test Performed using Guelph Permeameter (d) Backfilling of Test Boreholes. ...	86
Figure 5-1 Variation of volumetric moisture content with time and rainfall events at the MMB Section.....	88
Figure 5-2 Variation of volumetric moisture content with time and rainfall events at the control section (a) Crest of the slope (b) Middle of the slope.....	90
Figure 5-3 Comparison of moisture content variation at 3 ft depth at the crest of the slope.....	91
Figure 5-4 Variation of matric suction with time and rainfall events (a) Control Section (b) MMB Section.....	94
Figure 5-5 Variation of soil temperature with time.	96
Figure 5-6 Lateral deformation with time and rainfall for control section.	97
Figure 5-7 Lateral deformation with time and rainfall for MMB section.....	98
Figure 5-8 Lateral deformation with time and rainfall for RPP section.	99
Figure 5-9 Comparison of test sections (a) Depth wise lateral deformation (b) Maximum lateral deformation.	101
Figure 5-10 Location of survey lines.	103
Figure 5-11 Vertical settlement at the crest of the slope.	104
Figure 5-12 Comparison of average settlement of test sections at crest of the slope.	105
Figure 5-13 Vertical settlement at the middle of the slope.....	106
Figure 5-14 Comparison of average settlement of test sections at middle of the slope.....	107
Figure 5-15 Seasonal slope movement patterns (Less et al., 2013).....	108

Figure 5-16 Variation of field hydraulic conductivity at the crest of the slope.	111
Figure 5-17 Variation of field hydraulic conductivity at the middle of the slope.	112
Figure 5-18 Comparison of hydraulic conductivity of the MMB section (s) crest of the slope (b) middle of the slope.	113
Figure 5-19 Average hydraulic conductivity in each season (Gupta et al., 1994).	114
Figure 6-1 Schematic of Slope Section.	118
Figure 6-2 Slope geometry and boundary conditions used for analyses.	118
Figure 6-3 SWCC (a) Layer 1 (b) Layer 2 (c) Layer 3.	120
Figure 6-4 HCF (a) Layer 1 (b) Layer 2 (c) Layer 3.	122
Figure 6-5 (a) Estimated PET (b) AET/PET as a function of suction.	124
Figure 6-6 Initial porewater pressure distribution profile.	126
Figure 6-7 Measured and Modeled Volumetric Water Content.	126
Figure 6-8 Variation of Porewater Pressure with Time.	127
Figure 6-9 Result of slope stability analysis (initial).	128
Figure 6-10 Model geometry with MMB.	129
Figure 6-11 Measured and Modeled Volumetric Moisture Content for Slope with MMB.	130
Figure 6-12 Measured and Modeled Porewater Pressure for Slope with MMB.	130
Figure 6-13 Results of Slope Stability Analysis after 90 days of Natural Rainfall for the slope with MMB.	131
Figure 6-14 Points along the geocomposite.	132
Figure 6-15 Change in Porewater Pressure within the MMB (a) at the interface of Geotextile 1 and the Geonet (b) at the interface of the Geonet and Geotextile 2.	134

Figure 6-16 Change in Volumetric Water Content within the MMB (a) at the interface of Geotextile 1 and the Geonet (b) at the interface of the Geonet and Geotextile 2.	136
Figure 6-17 Development of infiltration into MMB (a) Flow in geotextile (b) Flow in geonet.	138
Figure 6-18 Schematic of flow diversion for MMB in slope.....	139
Figure 6-19 Flow in geonet with various rainfall intensity.....	139
Figure 6-20 Flow in geonet with various slope angles.	140
Figure 6-21 Diversion length against slope inclination.	140
Figure 6-22 Comparison of flow diversion length obtained from numerical study and analytical solutions.	143
Figure 6-23 Porewater pressure profiles for different lengths of MMB along slope (a) 10 ft. (b) 15 ft. (c) 20 ft. (d) 25 ft. (e) 30 ft. (f) 35 ft.	145
Figure 6-24 Effect of length of MMB on slope stability.	146
Figure 6-25 Slope at failure	147
Figure 6-26 Factor of safety of recompacted slope (a) Initial (b) After Rainfall.	147
Figure 6-27 Factor of safety of slope stabilized with RPP (a) Initial (b) After Rainfall.	148
Figure 6-28 Factor of safety of slope stabilized with MMB (a) Initial (b) After Rainfall.....	149
Figure 6-29 FS reduction due to rainfall for different stabilization methods.	150
Figure 6-30 Schematic of slope angles used for parametric study.	154
Figure 6-31 Effect of slope angle on factor of safety.	154
Figure 6-32 Variation of FS with respect to increase in MMB length for different slope inclination.	155
Figure 6-33 Combined effect of MMB and slope angle on FS of the slope (a) 4 (H): 1 (V) (b) 3.5 (H): 1 (V) (c) 3 (H): 1 (V) (d) 2.5 (H): 1(V) (e) 2 (H): 1(V).....	156

Figure 6-34 Schematic of slope height range used in parametric study.	157
Figure 6-35 Effect of slope height on factor of safety.	158
Figure 6-36 Effect of MMB on FOS for different slope heights.	159
Figure 6-37 Combined effect of MMB and slope height on FS of slope (a) H=10 ft. (b) H=15 ft. (c) H=20 ft. (d) H=25 ft. (e) H=30 ft.	160
Figure 6-38 Effect of cohesion of factor of safety.	161
Figure 6-39 Effect of MMB on FOS for various cohesion.	162
Figure 6-40 Combined effect of variation of MMB length and cohesion on FS of slope (a) c=100 psf (b) c=150 psf (c) c=200 psf (d) c=250 psf (e) c=300 psf.	163
Figure 6-41 Effect of soil friction angle on slope stability at constant MMB length.	164
Figure 6-42 Effect of MMB on FOS for various angle of friction.	165
Figure 6-43 Combined effect of variation of MMB length and soil friction angle on FS of slope (a) $\phi=5^\circ$ (b) $\phi=10^\circ$ (c) $\phi=15^\circ$ (d) $\phi=20^\circ$ (e) $\phi=25^\circ$	166
Figure 6-44 Effect of soil hydraulic conductivity on slope stability.	168
Figure 6-45 Combined effect of variation of MMB length and soil hydraulic conductivity on slope FS (a) $k=1.5 \times 10^{-5}$ ft/s (b) $k=1.5 \times 10^{-6}$ ft/s (c) $k=3 \times 10^{-6}$ ft/s (d) $k=1.5 \times 10^{-7}$ ft/s (e) $k=3 \times 10^{-7}$ ft/s.	169
Figure 6-46 Effect of rainfall intensity on slope stability.	171
Figure 6-47 Combined effect of length of MMB and rainfall intensity on slope stability (a) $q=0.15$ in/h (b) $q=0.20$ in/h (c) $q=0.25$ in/h.	172
Figure 6-48 Sensitivity assessment: percentage change in factor of safety versus percent of change in input parameters.	173
Figure 7-1 Flow of statistical analysis for model development.	176

Figure 7-2 Correlation among predictor variables.....	178
Figure 7-3 Correlation of FS with predictor variables (a) cohesion (b) angle of friction (c) height of slope (d) slope angle (e) hydraulic conductivity (f) rainfall (g) length of MMB.	180
Figure 7-4 Pareto chart showing standardized effects for the preliminary model.....	183
Figure 7-5 Plot of residual vs. fitted value for the preliminary model.	184
Figure 7-6 Plot of standardized residuals versus fitted values for preliminary model.	185
Figure 7-7 Normal probability plot for the preliminary model.....	186
Figure 7-8 Histogram of residuals for preliminary model.	186
Figure 7-9 Plot of residual vs. fitted value for the final model.....	190
Figure 7-10 Plot of standardized residuals versus fitted values for the final model.....	190
Figure 7-11 Normal probability plot for the final model.....	191
Figure 7-12 Frequency distribution of residuals for final model.....	191
Figure 7-13 Validation of final prediction model.	196
Figure 7-14 Flowchart for designing MMB stabilized slope.....	198
Figure 7-15 Design charts for slope height of 15 feet and 3 (H): 1 (V) geometry (a) $L_B=10$ ft. (b) $L_B=15$ ft. (c) $L_B=20$ ft. (d) $L_B=25$ ft. (e) $L_B=30$ ft. (f) $L_B=35$ ft.	200
Figure 7-16 Schematic of slope for example calculation.....	201
Figure 7-17 Schematic for Ordinary Method of Slices.....	203
Figure 7-18 Schematic of infinite slope approach.	205
Figure 7-19 Obtaining FS using design chart.	208

LIST OF TABLES

Table 2-1 Effect of slope angle on infiltration rate.....	15
Table 2-2 Depth of active zones in selected cities (O'Neil and Poormoayed, 1980).....	19
Table 2-3 Failures modes considered for limit resistance curves (Loehr and Bowders, 2007)....	28
Table 3-1 Geotechnical drilling details.....	54
Table 3-2 Results from TCP test.....	55
Table 3-3 Particle size distribution.	58
Table 3-4 Results of permeability test.	60
Table 3-5 Shear strength properties.	62
Table 3-6 Properties of geocomposite*.....	68
Table 3-7 Properties of geomembrane.....	69
Table 3-8 Properties of RPP (Khan, 2014).....	71
Table 4-1 Driving time for RPP.....	77
Table 4-2 Monitoring Schedule.....	84
Table 5-1 Summary of test sections (Sapkota et al.,2019)	102
Table 6-1 Saturated hydraulic conductivity determined from field and laboratory testing.....	121
Table 6-2 Soil shear strength properties used for slope stability analysis.....	122
Table 6-3 Hydraulic Properties for MMB.	129
Table 6-4 Parametric Study Matrix.....	152
Table 7-1 Correlation between predictor variables.....	178
Table 7-2 Correlation between factor of safety and predictor variables.....	181
Table 7-3 Parameter estimates of the preliminary model.....	182
Table 7-4 ANOVA Summary of preliminary model.....	183

Table 7-5 Parameter estimates of the final model.	188
Table 7-6 ANOVA summary of final model.	189
Table 7-7 Summary of best subset selection method.....	193
Table 7-8 Parameter estimates of the final model with 6 predictors.	194
Table 7-9 ANOVA summary of final model with 6 predictors.	195
Table 7-10 Summary table for calculating factor of safety using ordinary method of slices.	203

CHAPTER 1 INTRODUCTION

1.1 Background

Expansive soils are characterized by the presence of clay minerals that swell and shrink upon changes in soil moisture content. During seasonal wet and dry periods, a cyclic change in moisture content causes expansive soils to undergo significant volume change. Expansive soil exists in 40 out of 50 states of the United States (Steinberg, 2000). Certain geographical locations of the United States like the north Texas, with large surficial deposits of clayey soil and climate characterized by alternating periods of rainfall and drought, are more susceptible to damage from expansive clay. As a result, damage to highway slopes constructed over expansive soil is a matter of great concern in Texas. The recurrent wetting and drying of the soil cause a reduction in shear strength over time through the softening effect, ultimately leading to failure (Rogers and Wright, 1986; Skempton, 1997). Additionally, the cyclic swelling and shrinkage leads to the formation of desiccation cracks in highway slopes which creates pathways for rainwater intrusion which is detrimental to their long-term stability. With no mitigation measures, such distresses can potentially lead to shallow slope failures (Hossain et al., 2017).

There are various methods in practice to repair and stabilize surficial failures of embankment slopes. Some commonly used methods are installation of drilled shafts, reinforcement of the slope with geogrids, installation of soil nails and replacement of the slope using a retaining wall. Among other mechanical methods, a sustainable and economic solution to shallow slope failures is the reinforcement of a slope with recycled plastic pins (Hossain et al., 2017). Recycled plastic pins are predominantly a polymeric material, fabricated from recycled plastic waste and other waste materials (Bowders et al., 2003; Chen et al., 2007;). In the last two decades, the use of recycled plastic pins to stabilize rainfall induced shallow slope failures has been proven to be successful in

the states of Missouri, Iowa, and Texas. Although recycled plastic pins act as slope reinforcement, they do not prevent the infiltration of rainwater. Therefore, it is important to identify moisture control methods to prevent rainfall induced shallow failures of highway slopes.

Various moisture control barriers can be used to control the intrusion of moisture into soil. Typically, moisture control barriers such as a vertical barrier, horizontal barrier, capillary barrier, and modified moisture barrier have been used in roadways to control moisture fluctuation in the subgrade soil by enhancing drainage and preventing moisture intrusion (Christopher et al., 2000; Elseifi et al., 2001a; Henry et al., 2002; Ahmed et al., 2018). Among these, the capillary barrier system and the modified moisture barrier have also been implemented as slope stabilization techniques by limiting intrusion of rainwater into the slope (Rahardjo et al., 2012, 2013; Sapkota et al., 2019). Capillary barriers consist of fine-grained soil with an underlying layer of coarse-grained soil or a geocomposite layer and the downward movement of water is reduced by the difference in permeability of the two layers (Rahardjo et al., 2012; 2013). A capillary barrier system does not entirely prevent the intrusion of water into the underlying soil as it may allow some percolation (break-through) (Rahardjo et al., 2013). On the other hand, the modified moisture barrier reduces such chances of percolation by including a geomembrane as the bottom layer (Ahmed et al., 2018).

The modified moisture barrier is a layer of geocomposite which is an interconnected layer of two geotextiles and a geonet in the geotextile-geonet-geotextile configuration, underlain by a geomembrane layer (Ahmed et al., 2018). The purpose of the geocomposite layer is to promote drainage of infiltrated rainwater while the geomembrane layer prevents any further infiltration of rainwater into the subgrade. Sapkota (2019) has used the modified moisture barrier in combination with recycled plastic pins in a two-step mechanism to stabilize a shallow slope failure. However,

the effectiveness of the modified moisture barrier alone to combat rainfall induced shallow slope failures is yet to be explored. Therefore, the current study implements a modified moisture barrier at the crest of a highway slope to prevent shallow slope failures.

1.2 Problem Statement

Moisture control techniques, including a modified moisture barrier, have been implemented in the past in roadways to improve their serviceability. A modified moisture barrier has been proved to be an effective way of preventing moisture intrusion into the pavement subgrade (Ahmed et al., 2018). Following the successful use of modified moisture barrier in pavement subgrades, a combination of modified moisture barrier and recycled plastic pins have been used in a two-step mechanism to stabilize a shallow slope failure along Texas Highway US 287 (Sapkota, 2019). In the two-step mechanism, recycled plastic pins helped to prevent formation of the slip surface at shallower depth while the modified moisture barrier helped to prevent intrusion of moisture through cracks in the pavement shoulder. However, past research has not studied the effectiveness of using a modified moisture barrier alone in preventing shallow slope failure by controlling moisture fluctuation in highway embankment slopes. Hence, this study proposes to evaluate the performance of a modified moisture barrier (a moisture control method) to stabilize rainfall induced shallow slope failures and further compares its performance to that of recycled plastic pins (a mechanical method) in stabilizing shallow slope failures. The detailed mechanism of the modified moisture barrier is shown in Figure 3-11. When rainwater infiltrates a slope, the geocomposite (interconnected geotextile-geonet-geotextile layer) provides adequate drainage while the underlying geomembrane layer prevents any further infiltration of rainwater into the slope.

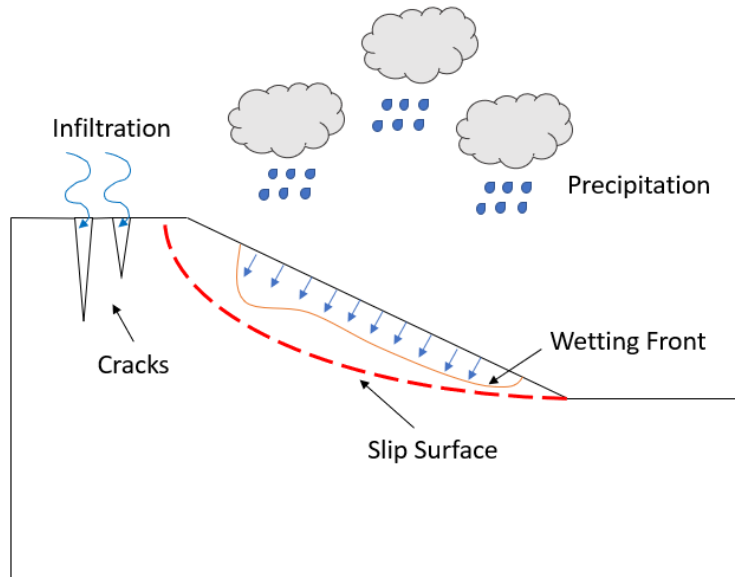


Figure 1-1 Schematic illustration of rainfall induced shallow slope failure.

1.3 Research Objectives

The objective of the current study is to evaluate the performance of the modified moisture barrier in stabilizing rainfall induced shallow slope failures. The specific tasks performed fulfil the objective of the study were as follows:

- Site reconnaissance and selection of field study area.
- Development of preliminary slope stabilization scheme, using a modified moisture barrier and recycled plastic pins in two separate test sections, based on literature and numerical modeling.
- Field installation of modified moisture barrier and recycled plastic pins in their designated sections.
- Instrumentation of the test sections.
- Performance monitoring of the study area.

- Analysis of field results to determine effectiveness of a modified moisture barrier in preventing shallow slope failures.
- Development of a numerical model and verification of numerical results with field performance monitoring results.
- Parametric study to develop a prediction model for slope stabilization using a modified moisture barrier.

1.4 Thesis Organization

The dissertation is organized into eight chapters as listed below. The content of each chapter is also summarized as follows:

Chapter 1 provides the background, problem statement and research objective of the current study.

Chapter 2 presents a comprehensive literature review on the subject including the volume change behavior of expansive clay in response to climatic variation, its impact on the stability of highway slopes along with remedial measures for shallow slope failures. Moreover, various methods of slope stabilization used in previous studies are discussed. Finally, the limitations of previous studies were highlighted and the need for the current study was established.

Chapter 3 focuses on the detailed site investigation conducted for this study including details of the selected highway test section, geotechnical drilling, geophysical testing, and laboratory testing. Site investigation results were evaluated and incorporated to design the stabilization schemes using the modified moisture barrier and recycled plastic pins in the respective test sections. Additionally, to design the test section using recycled plastic pins, soil shear strength parameters were used to run numerical analysis.

Chapter 4 consists of the field installation, field instrumentation, field performance monitoring, field testing and data acquisition procedures. Field installation plan includes selection procedures for materials: modified moisture barrier and recycled plastic pins. Field instrumentation plan includes selection of the instruments and procedures utilized for performance monitoring.

Chapter 5 focuses on the field performance monitoring results. Performance of the current stabilization method was monitored using integrated temperature moisture sensors, soil water potential sensors, vertical inclinometers, topographic survey, and hydraulic conductivity testing. Results obtained are compared to that of the recycled plastic pins and control section, along with its comparison to existing literature.

Chapter 6 presents results and analyses of the numerical study conducted using 2D finite element software SEEP/W and SLOPE/W from the GeoStudio package. SEEP/W and SLOPE/W were used to conduct a coupled transient seepage and slope stability analysis for a slope with and without the modified moisture barrier. A calibrated numerical model was developed by comparing the results of the numerical model to that from field instrumentation. Flow analysis of the modified moisture barrier was conducted using the calibrated numerical model. Finally, a parametric study was conducted to study the effect of various parameters (soil shear strength properties, slope geometry, soil hydraulic properties, rainfall, and length of barrier along the slope) on the slope's factor of safety.

Chapter 7 includes the statistical analysis conducted using the comprehensive dataset obtained from the parametric study. Multiple linear regression analysis was performed to develop a prediction model for the factory of safety of a slope stabilized with the modified moisture barrier. Simple design charts were developed using the predictive equation. Finally, the steps for designing a slope with the modified moisture barrier are outlined with an example calculation.

Chapter 8 summarizes the findings of the current study and provides recommendations for future research.

CHAPTER 2 LITERATURE REVIEW

2.1 Introduction

The \$20 trillion dollar US economy depends on a vast network of infrastructure ranging from roads and bridges to freight rail and ports to electrical grids and internet provision, which supports almost every aspect of human life (McBride and Siripurapu. 2021). However, in spite of its dire importance, the current condition of US infrastructure is unsatisfactory which is represented by a C- grade assigned by the American Society of Civil Engineers (ASCE, 2021). Poor infrastructure imposes large costs on the economy and threatens the safety of human lives with disastrous failures such as collapse of bridges, breach of dams, and inadequately maintained roads. Hence, the dire need for research on infrastructure maintenance, rehabilitation and resilience enhancement is evident. Research on rehabilitation of highway systems occupies a major chunk due to their cruciality. However, because of the implication of several vulnerabilities, a set of challenges remain unaddressed. The negative impact caused by the volume change behavior of expansive soils is one such vulnerability.

2.2 Expansive Soil

Expansive soils exist in 40 out of 50 states of the United States and cover about one-fifth of the total land area (Petry and Armstrong, 1989; Steinberg, 2000). In a typical year, expansive soils cause a greater loss to property owners than earthquakes, floods, hurricanes, and tornadoes, combined (Nelson and Miller, 1992). Certain geographical locations of the United States like North Texas, with large surficial deposits of clayey soil and climates characterized by alternating periods of rainfall and drought, are more susceptible to damage from expansive clay. The frequency of occurrence of expansive soil in Texas is depicted in Figure 2-1. One of the primary reasons why expansive clay can cause such significant damage is its swell-shrink behavior.

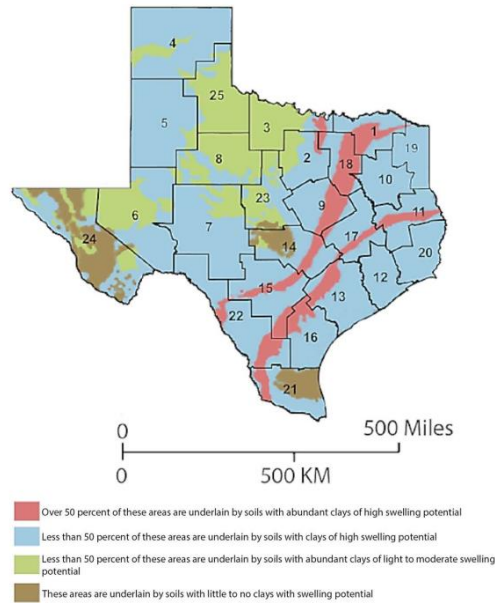


Figure 2-1 Soil map of Texas (Adopted from Olive et al. (1989)).

2.2.1 Cyclic Swelling and Shrinkage Mechanism

Expansive soils are characterized by the presence of clay minerals that swell (increase in volume) and shrink (decrease in volume) upon changes in soil moisture content. During seasonal wet and dry periods, a cyclic change in moisture content causes expansive soils to undergo significant volume change. Factors including the type of clay mineral, overburden and confining pressure, soil initial moisture content and dry density, and the presence of free water govern the pattern and extent of this volumetric deformation. (Chen, 2012). Significant variation of water content in soils with high shrink-swell potential can have severe impact. This is because swelling and shrinkage are not entirely reversible processes (Holtz and Kovacs, 1981). The process of soil shrinkage causes cracks to develop on the surface which, upon rewetting, do not close entirely causing slight bulging of the soil and hence allowing enhanced access to water for the swelling process.

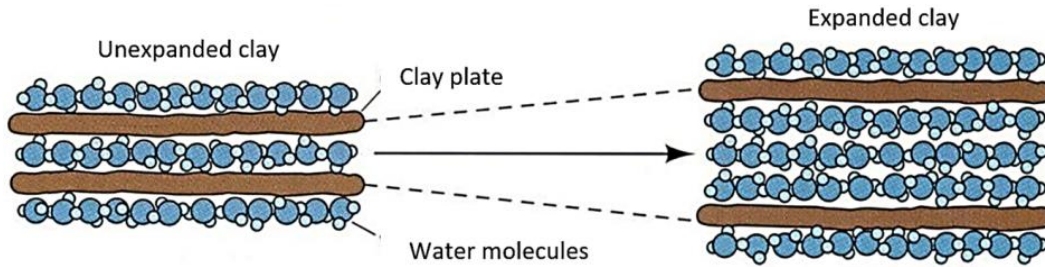


Figure 2-2 Expansion of clay due to water infiltration (Amakye et al., 2021).

2.2.2 Softening Mechanism of Expansive Soil

Cyclic wetting and drying causes expansive soil to undergo softening and experience a reduction in shear strength ultimately reaching a fully softened state (Wright, 2005). Fully softened shear strength refers to the shear strength of clay with high plasticity which develops over time, due to recurrent wetting and drying (Wright, 2005). Skempton (1977) indicated that fully softened shear strength is comparable to the shear strength of the soil in a normally consolidated state and lies between peak and residual strength as shown in Figure 2-3.

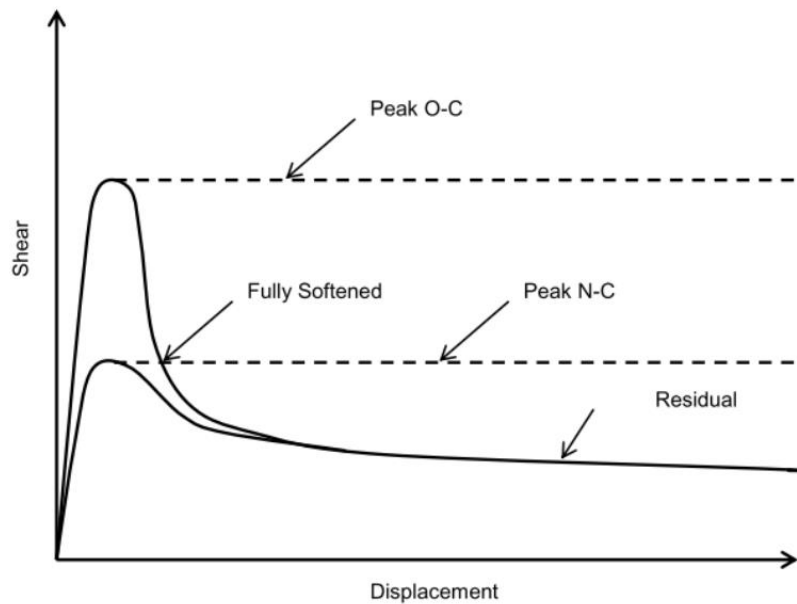


Figure 2-3 Comparisons of peak, fully softened, and residual shear strength (Skempton, 1970).

2.3 Unsaturated Soil and Matric Suction

The existence of matric suction or negative porewater pressure increases the shear strength of a soil (Abd et al.,2020). In cases where deep groundwater table exist, the role of matric suction is significant in controlling the soil shear strength and hence the stability of many slopes. Matric suction in unsaturated soil is highly influenced by many changes in flux boundary conditions, such as infiltration, evaporation, and transpiration, caused by various climatic conditions (Rahardjo et al.,2012). Matric suction profiles under different flux boundary conditions are depicted in Figure 2-4. When water starts to infiltrate into the soil, the matric suction slowly reduces and becomes zero as the soil approaches saturated conditions. Reduction in soil shear strength results from significant decrease in matric suction and can subsequently result in shallow landslides.

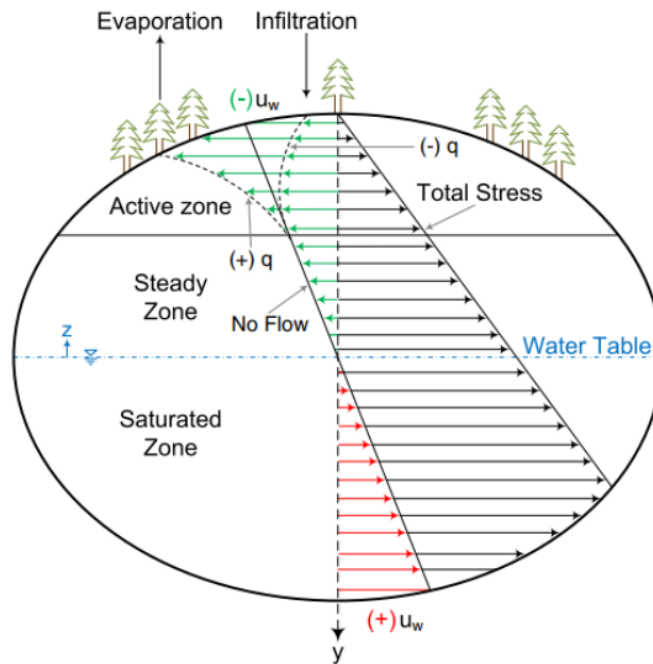


Figure 2-4 Matric suction profiles under various flux boundary conditions (Adapted from (Fredlund et al., 1996))

2.4 Factors affecting Infiltration

As wetting depth in a slope is important in evaluating the rainfall induced slope instability, field infiltration due to natural rainfall should be characterized (Kim and Lee, 2010).

2.4.1 Vegetation

In a study conducted by Kim and Lee (2010), field monitoring of soil matric suction was carried out on a highway slope in South Korea, at both vegetated and non-vegetated areas. It can be deduced from Figure 2-5 and Figure 2-6 that variation of soil volumetric water content has a direct relationship with rainfall infiltration while the change of water content follows an inverse pattern from that of matric suction. As volumetric water content of the soil increases, matric suction is observed to decrease. Furthermore, the study found that during the dry season there was a high increase in matric suction in the vegetated area due to less evaporation caused by higher humidity and lower temperature near the surface.

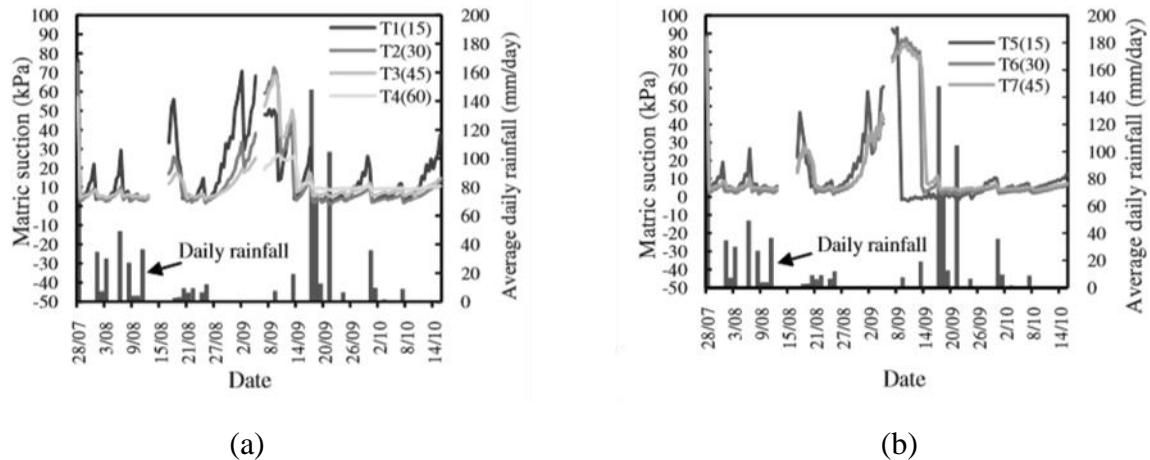


Figure 2-5 Variation of matric suction with rainfall (a) vegetated area (b) non vegetated area

(Kim and Lee, 2010)

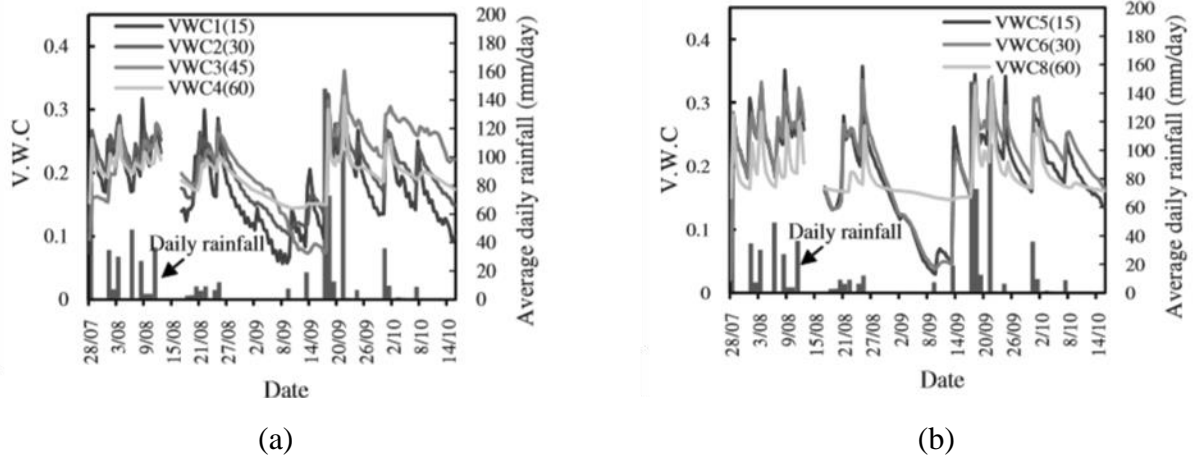


Figure 2-6 Variation of volumetric water content with rainfall (a) vegetated area (b) non vegetated area (Kim and Lee, 2010).

2.4.2 Surface Cover

Lim et al. (1996) monitored the matric suction of an instrumented residual soil slope of the sedimentary Jurong Foundation in Singapore, under different cover systems: canvas over grass, grass, and bare ground. The slope was instrumented with piezometers and tensiometers. The study found that variation of matric suction caused by rainfall events was significantly lower under the canvas covered section compared to the other sections as shown in Figure 2-7.

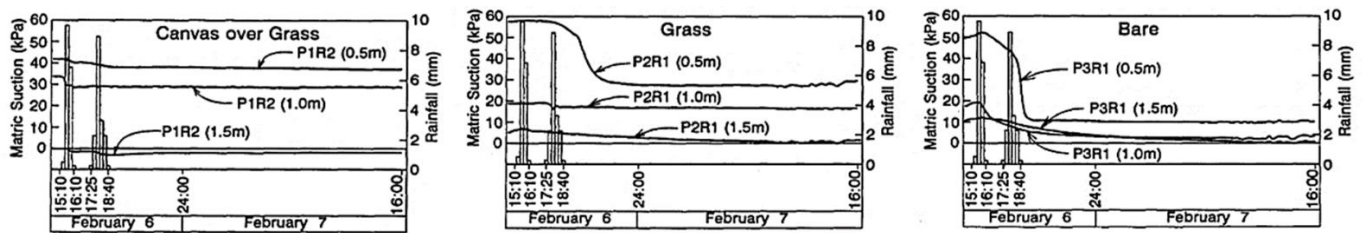


Figure 2-7 Decrease in matric suction with time at different depths during rainfall events of February 1994 (Lim et al., 1996).

2.4.3 Cracks

Cracks can frequently occur on soil slopes (Senior, 1981; Hossain, 2013; Khan et al., 2017). Slopes cracks can be categorized into tension, weathering, and desiccation cracks (Spencer, 1967; Chowdhury and Zhang, 1991). Commonly, desiccation cracks are formed on expansive soil slopes due to the impact of seasonal wet and dry cycles. As water evaporates from the surface, the soil begins to shrink leading to the formation of cracks. Desiccation cracks can significantly affect soil properties such as permeability, residual shear strength and tensile strength (Kodikara, 2018). According to Omidi et al. (1995), shrinkage cracks can increase soil hydraulic conductivity by 452 times in clayey soil. Zhan et al. (2007) measured the infiltration rates for cracked and intact soils using infiltrometer on a slope constructed over expansive clay as shown in Figure 2-8. It was found that the infiltration rate for the non-cracked soil was distinctly lower than that of cracked soil.

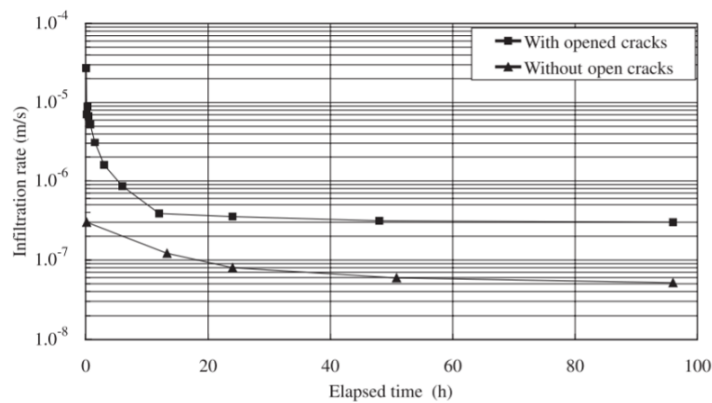


Figure 2-8 Infiltration rates for cracked and intact soils (Zhan et al., 2007).

2.4.4 Slope Angle

It is important to evaluate the effect of slope angle on infiltration to assess stability of slopes. Huat et al. (2006) conducted a laboratory model study to evaluate the effect of slope angle on water infiltration into soil and matric suction. A series of infiltration tests were conducted at slope angles

of 0°, 15°, 30° and 45°. It was found that with increase in slope steepness, infiltration reduces as shown in Table 2-1. On steep slopes, water that falls on the soil surface has little time to infiltrate and therefore runoff is higher whereas on gentle slopes, water moves slowly hence leading to greater infiltration into the soil.

Table 2-1 Effect of slope angle on infiltration rate.

Soil surface cover	Slope angle (deg)	Infiltration rate (mm/s)
No cover (bare soil)	0°	2.45×10^{-2}
Geosynthetic net	0°	2.15×10^{-2}
Geosynthetic net	15°	1.74×10^{-2}
Geosynthetic net	30°	1.64×10^{-2}
Geosynthetic net	45°	1.5×10^{-2}
Grass cover	0°	2.25×10^{-2}
Grass cover	15°	1.92×10^{-2}
Grass cover	30°	1.75×10^{-2}

2.4.5 Rainfall Intensity

Rainfall intensity affects the infiltration rate of the slope soil in turn governing the factor of safety of the slope. Huat et al. (2006) showed that during rainfall events of low intensities, the factor of safety of a slope remains almost constant while that experiences a marked drop during higher rainfall intensities. Foley and Silburn (2002) also observed higher infiltration rates with higher rainfall intensities. According to Dunne et al. (1991), infiltration increases with rainfall intensity for two reasons: (i) high rainfall intensities exceed the saturated hydraulic conductivity of larger proportions of soil surface hence raising the spatially average hydraulic conductivity and (ii) increasing rainfall intensity increases run off rate and flow depth.

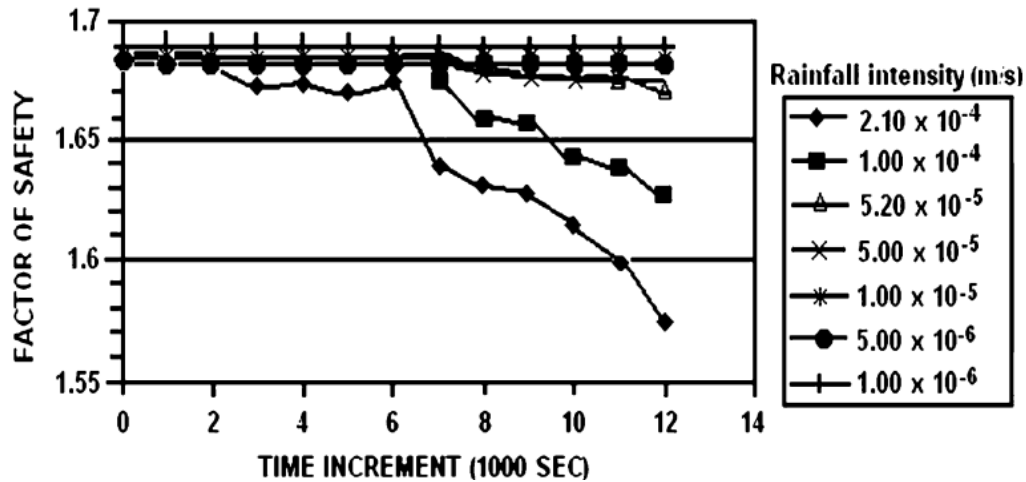


Figure 2-9 Effect of rainfall intensity on factory of safety of a slope (Huat et al., 2006).

2.5 Damages due to Expansive Soils

The swell shrink behavior of expansive soils makes them unsuitable for construction. According to Chen (2012), expansive soils can damage infrastructures constructed over them, such as foundations, pavements and pipelines, and other facilities, due to high swelling pressures. Furthermore, highway system infrastructures such as pavements (Hedayati, 2014; Ahmed, 2017), embankments (Khan, 2014; Bhandari et al., 2020), and bridge abutments are affected by the volume change behavior of expansive soils. Damages of expansive soils commonly include longitudinal edge cracks on pavements, edge drops of crests of highway slopes, and shallow slope failures.

2.6 Shallow Slope Failures

Shallow slope failures are surficial instabilities that occur along highway cut and fill slopes and embankments (Stauffer and Wright, 1984). They are common occurrences throughout the United States but are more likely in slopes constructed on expansive soil after periods of prolonged rainfall. During a period of prolonged rainfall, a shallow slope becomes saturated up to a depth

and when the intensity of rainfall exceeds the infiltration rate of the soil, failure takes place (Abramson et al., 2001). Depths and plan dimensions for such slides differ with predominant soil type, soil stratification, groundwater, slope geometry, and seepage, but are characterized by sliding depths of less than 10 feet, with depths of 3 to 6 feet being commonplace (Loehr et al, 2007; Titi and Helwany, 2007). According to Day and Axten (1989), shallow slope failures can be considered as infinite slope failure meaning the failure plane is approximately parallel to the slope face (Das, 2010). An illustration of a typical surficial slope failure is shown in Figure 2-10.

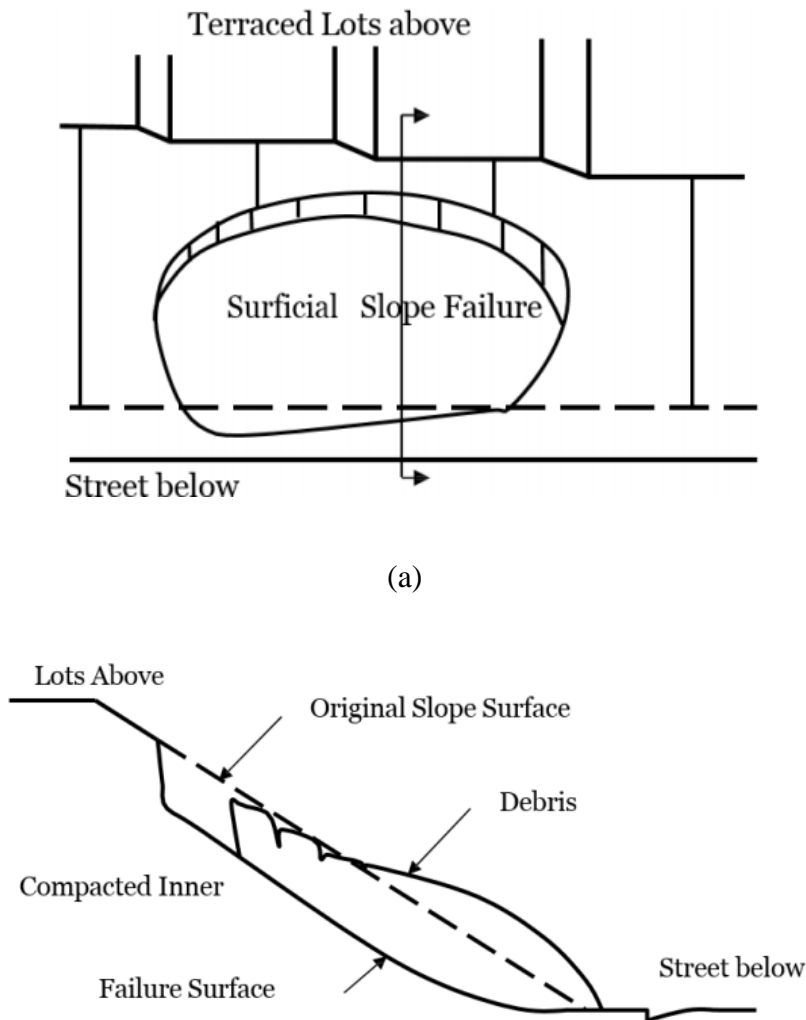


Figure 2-10 Typical surficial slope failure (redrawn after Day and Axten, 1989).



Figure 2-11 Shallow slope failure near eastbound IH20 in Dallas, Texas (Rauss,2019).

2.6.1 Active Zone

Volume change behavior of expansive soils is triggered by moisture redistribution in the soil which may occur when the equilibrium condition in the soil mass is disturbed due to infiltration or exfiltration of water through various means. Climatic conditions affect the soil water content more significantly up to a certain depth below the surface-this zone is referred to as the zone of seasonal fluctuations or the active zone. Nelson (2001) defined active zone as the zone where changes in moisture content are currently taking place and the maximum depth of the active zone is defined as the point where overburden pressure equals zero swell pressure.

It is important to determine the depth of the active zone since weather conditions can affect the shear strength of the soil at the active zone. Soil moisture content profiles provide an idea of the depth of the active zone. A study conducted by O'Neil and Poormoayed (1980) determined the depth of the active zone in several Texas cities as shown in Table 2-2. The study reported that the active zone in Houston was 5-10 feet deep while that in Dallas was about 7-15 feet deep.

Table 2-2 Depth of active zones in selected cities (O'Neil and Poormoayed, 1980)

City	Depth of Active Zone (ft)
Houston	5-10
Dallas	7-15
Denver	10-15
San Antonio	10-30

2.7 Methods of Repair

Several slope stabilization techniques exist in practice. Selection of an appropriate method for implementation is governed by many factors including site accessibility, availability of equipment, experienced contractors, time constraints and project budget. Slope repair methods can be divided into several categories: mechanical methods, earthwork methods, biotechnical methods, additives, and water management as shown in Figure 2-12. Some repair methods compiled from previous literature are presented below.

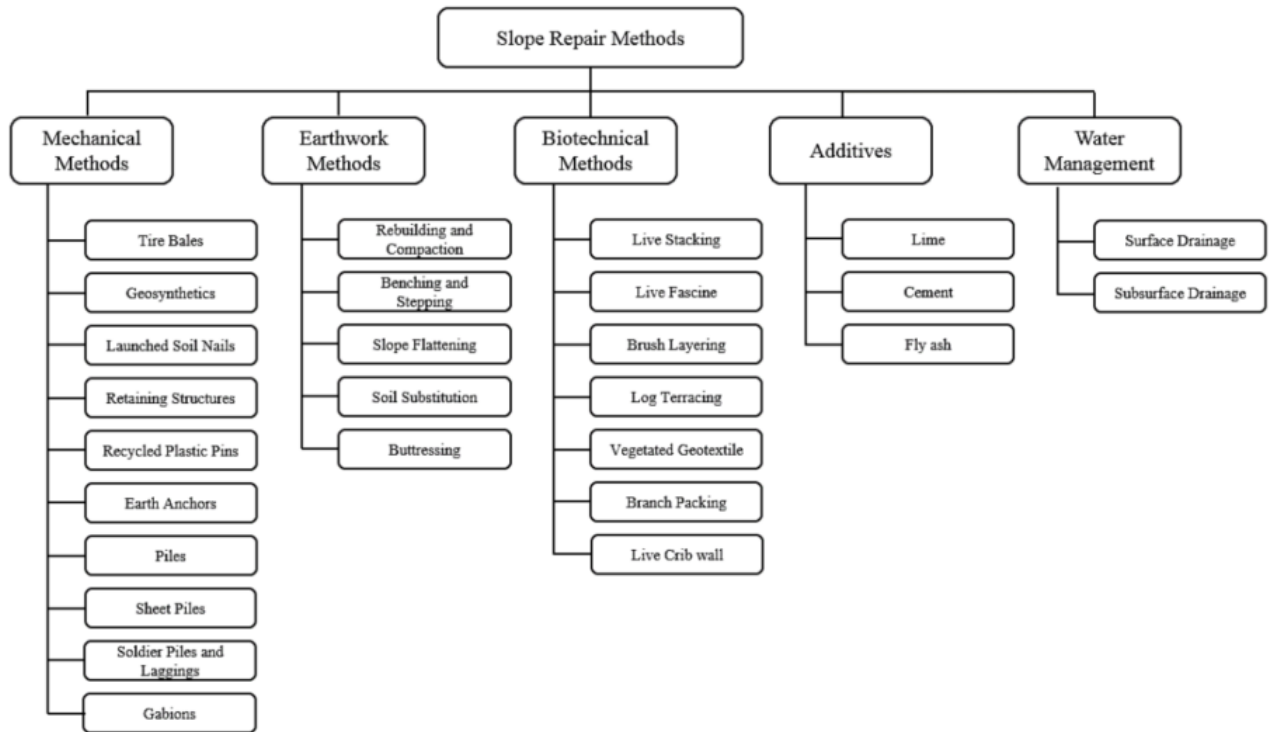


Figure 2-12 Classification of slope repair methods (Shahandashti et al., 2019).

2.7.1 Rebuilding of Slope

An easy and economical repair is to take the failed soil mass and use it to rebuild the area. Organic matter, such as trees and grass, is separated from the surficial failure mass. The soil is then air dried and recompacted in the failure area (Day, 1996). However, this method of repair may be ineffective. During the following wet period, when the clay swells again the benefit of compaction will be lost (Titi and Helwany, 2007).

2.7.2 Geogrid Repair

Geogrids, manufactured from high density polyethylene resins, are designed to increase the shear strength of the soil. They act as soil reinforcement similar to the effect of plant roots. In the repair method using geogrid, the failed soil mass is removed from site. Benches are then cut into the slope which provide frictional contact between the new fill mass and horizontal portion of the

bench (Day, 1996). After excavating the benches, horizontal back drains are installed. Vertical drains are used to intercept seepage that may migrate through the ground and horizontal back drains collect water from vertical drains. The slope is then rebuilt using layers of geogrid and compacted fill. Finally, an erosion control fabric is placed on top of the slope.

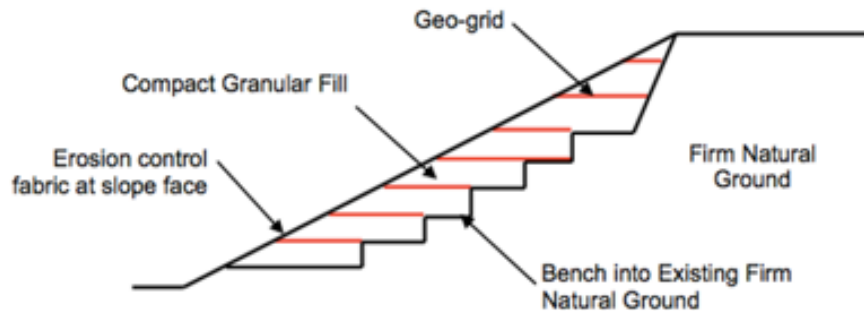


Figure 2-13 Geogrid repair of surficial slope failure (Day, 1996).

2.7.3 Soil Cement Repair

The soil cement repair method is similar to the geogrid repair method: cement mixed with granular fill is used instead of geogrid reinforcement. Cement increases the shear strength of the imported granular fill (Day, 1996). However, a major difficulty faced while implementing this method is the mixing of the cement and the soil. If the soil and the cement are not mixed thoroughly, uncemented zones may be created which are susceptible to erosion and failure.

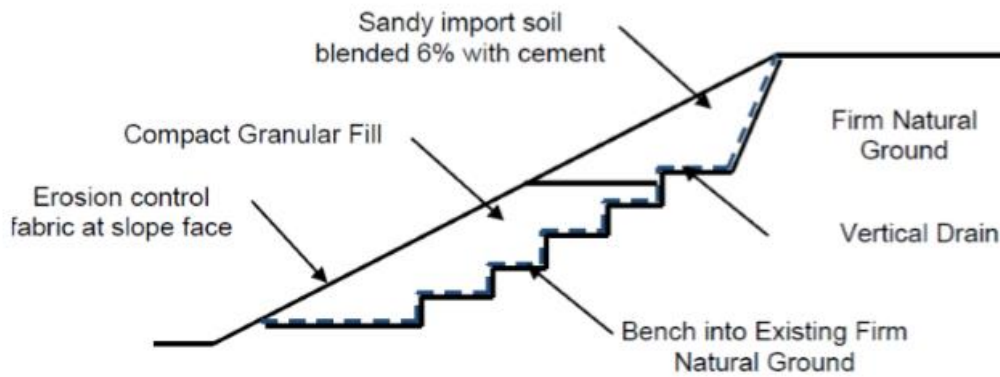


Figure 2-14 Schematic of soil cement repair method (Day, 1996).

2.7.4 Pipe Piles and Wood Lagging

Slide debris is removed, and benches are cut into the natural ground. Hollow galvanized steel pipe piles are either driven or placed into predrilled holes filled with concrete. Pressure treated wood lagging is then placed behind the pipe piles and a drainage system is installed behind the wood lagging. Finally, the slope is then rebuilt with a compacted fill and the slope face is provided with an erosion control fabric (Day, 1996). One disadvantage of this method is the low flexural strength of the steel pipe piles (Titi and Helwany, 2007). Wood lagging transfers all the load to the steel pipe piles and since large soil forces can be generated in the surficial zone, pipe piles frequently fail in bending.

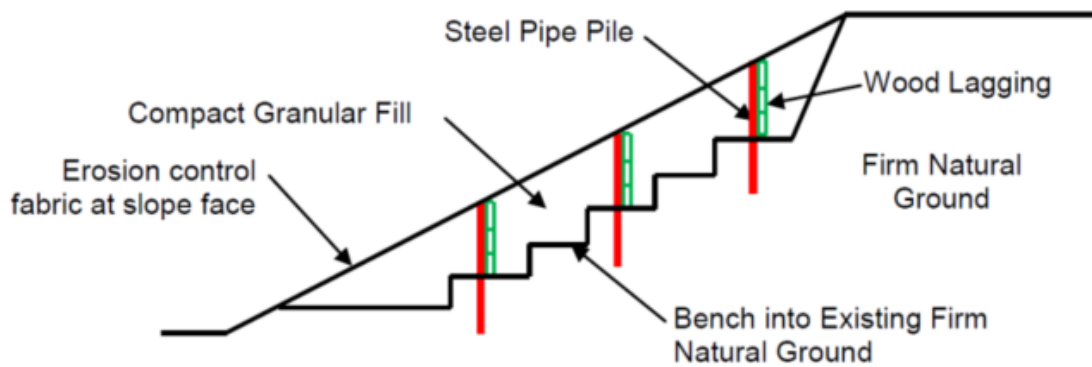


Figure 2-15 Graphical representation of pipe piles and wood lagging system (Day, 1996).

2.7.5 Soil Nails

Soil nails are solid or hollow steel bars used to stabilize shallow slope failure. Typically, a hollow on galvanized bar is 20 feet long with an outer diameter of 1.5 inches. Galvanized steel bars are used in highly abrasive environments due to their corrosion resistance. These steel bars are driven into the slope face at high speed, using high pressure compressed air. Soil nails go beyond the slip surface, providing resistance along the slipping plane eventually leading to an increase in the factor of safety of the slopes. The steel bars should have minimum yield strength of 36 ksi (Titi and Helwany, 2007). Once the installation of the nails is completed, the surface of the slope is treated with an erosion mat, steel mesh and shotcrete.

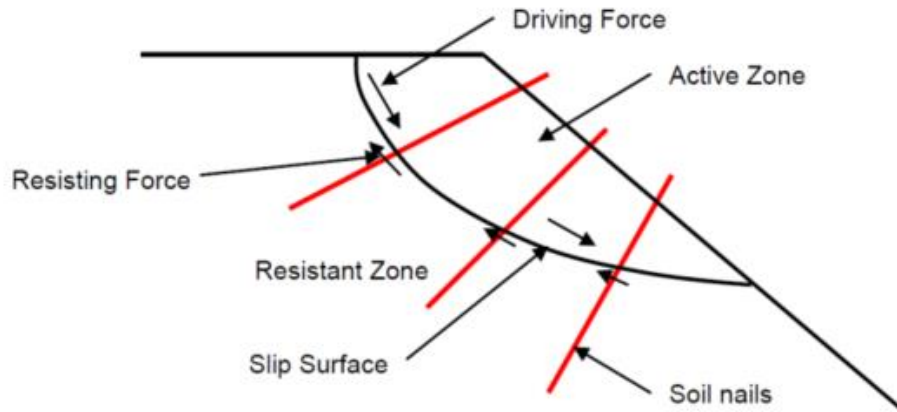


Figure 2-16 Schematic of slope repair using launched soil nails (redrawn from Titi and Helwany, 2007).

2.7.6 Plate Piles

Collins and Short (2006) investigated the use of plate piles as a slope stabilization measure. The use of plate piles increases the resistance of the slope to sliding through the application of the vertical members in resisting shear stresses. Generally, plate piles are about 6-6.5 feet long with a 2.5-inch x 2.5-inch galvanized steel angle section with a 2 feet x 1 feet rectangular steep plate welded to one end (Collins and Short, 2006). Plate piles are driven into the potential slide area to a depth of 2 to 3 feet of the residual soil over stiffer soil or bedrock. This is done so that the plate then transfers the load to the stiffer soil hence causing a reduction in the driving forces on the upper soil mass.

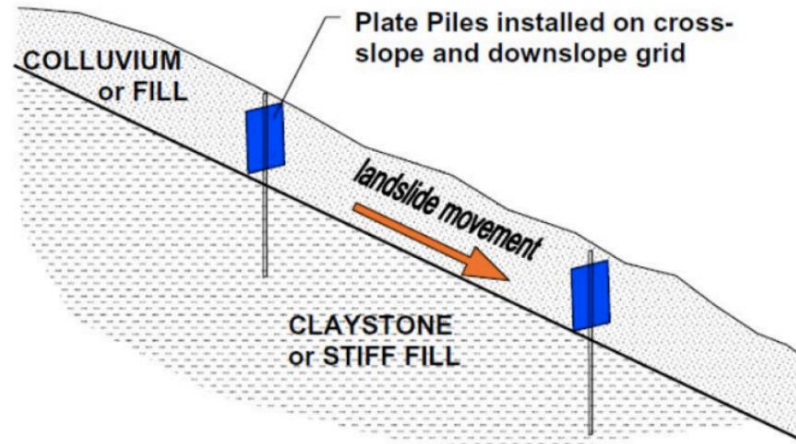


Figure 2-17 Schematic of plate pile stabilization (Collins and Short, 2006).

2.7.7 Micro piles

Micro piles (also known as pin piles or mini piles) are small diameter (less than 300 mm) drilled and grouted piles (Bruce and Juran, 1997). They are constructed by drilling a borehole, placing reinforcement, and using a grout to backfill the hole (Sun et al., 2013). The benefits of using micro piles for slope stabilization are in areas with constraints of equipment access. Landslides on hilly, steep, or mountainous areas are suitable for micro pile application.

2.7.8 Recycled Plastic Pins

In recent years, several engineering applications of recycled plastic waste have been explored. For instance, according to a study conducted by Shruti Singh (2022), inclusion of plastic will extend the service life of pavements. Recycled plastic pins (RPP) are manufactured using recycled plastic waste and other waste materials such as sawdust, polymers, and fly ash (Chen et al., 2007). They are resistant to biological and chemical degradation compared to traditional structural materials. The main principle of using RPP in slope stabilizations is that once driven into the slope, it

intercepts the potential failure plane and provides resistance against the lateral driving force, thereby increasing the stability of the slope.

2.7.8.1 Stability of Reinforced Slopes

In the limit equilibrium method of evaluating the stability of a reinforced slope, a potential sliding surface is considered. The factor of safety of the slope is then determined using the following equation

$$F = \frac{\int s}{\int \tau}$$

Where F is the factor of safety against sliding along the considered sliding surface, s is the maximum shear strength of the soil and reinforcement along the considered sliding surface, and τ is mobilized shear stress. Method of slice can be utilized to carry out the integration. The method of slices concept involves dividing the slope continuum into several vertical slices, as shown in Figure 2-18. Each slice is then analyzed by applying the equations of equilibrium. Strength parameters of the soil and reinforcement are calculated using Mohr Coulomb failure criterion and limiting strength of reinforcement, respectively and the mobilized shear stress is calculated by applying the principle of equilibrium to each slice. Similar calculations are carried out for all the slices to obtain the factor of safety of the slope against sliding. The process is then repeated for many potential and unique failure surfaces to identify the failure surface which generates the minimum factor of safety. Finally, the minimum factor of safety is considered to be the factor of safety of the slope against sliding.

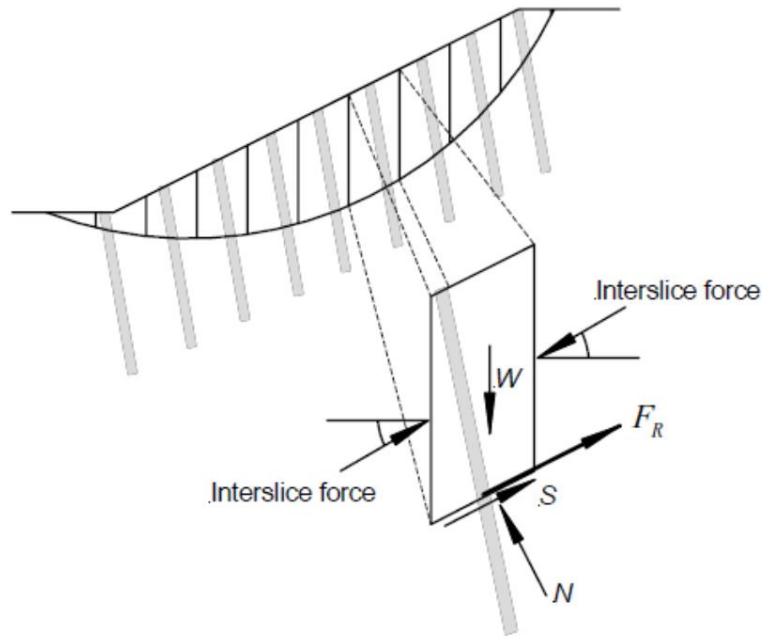


Figure 2-18 Equilibrium of an individual slice in the method of slices (Khan, 2014).

2.7.8.2 Design Method

Loehr and Bowders (2007) generated limit resistance curves of RPP and demonstrated that the resistance offered by reinforcement against sliding is a function of the depth of the failure surface. In order to generate these curves, two modes of failure of the surrounding soil and two modes of failure of the RPP itself were considered, as shown in Table 2-3.

Failure mode 1 is with regards to the failure of soil mass above the sliding surface by flowing between or around reinforcing members while in failure mode 2, the soil below the sliding surface adjacent to the reinforcing member was assumed to fail with the member sufficiently anchored into the moving soil above the sliding surface. In failure mode 3, two subcategories are considered: failure due to excessive moments from the applied soil pressure above the sliding surface (Failure Mode 3a) and failure due to excessive moments from the soil pressure below the sliding surface

(Failure Mode 3b). Similarly, failure mode 4 corresponds to a phenomenon similar to failure mode 3 except the failure causing stresses are induced by shear.

Based on all failure modes and considering a moment reduction factors to resist structural failure, Loehr and Bowders (2007) proposed a combined limit resistance curve as shown in Figure 2-19. The combined limit resistance curve provides an envelope of limiting resistance provided by the reinforcing members which can be used for further analysis.

Table 2-3 Failures modes considered for limit resistance curves (Loehr and Bowders, 2007).

Failure Mode	Description
Mode 1	Failure of soil mass above the sliding surface
Mode 2	Failure of soil mass below the sliding surface due to insufficient anchorage
Mode 3	Bending failure of member
Mode 4	Shear failure of member

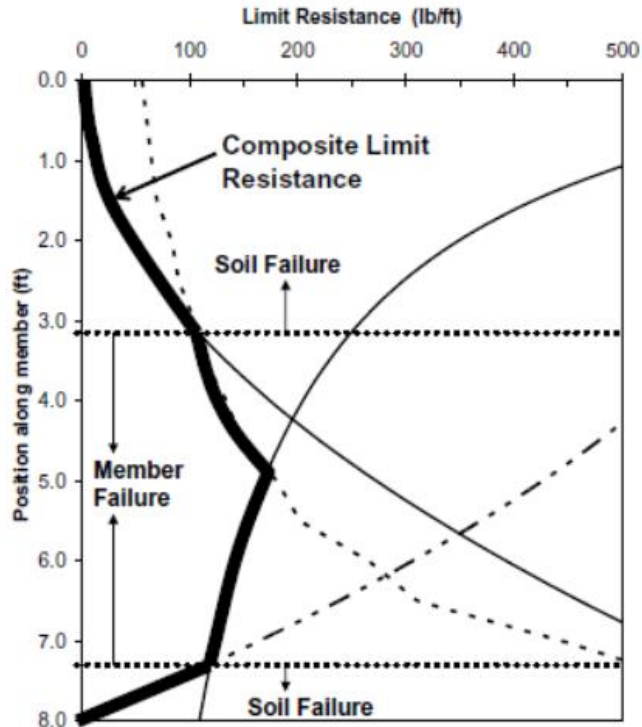


Figure 2-19 Combined limit resistance curve (Loehr and Bowders, 2007).

2.7.8.3 Field Performance of RPP Stabilized Slopes

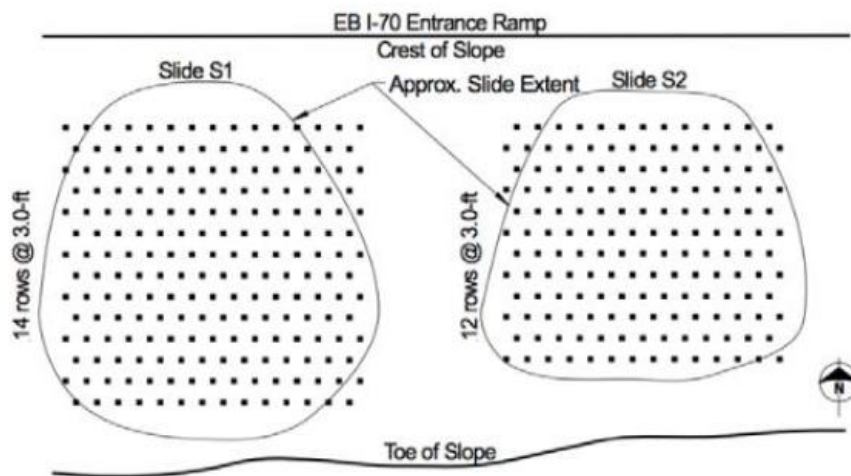
RPPs have been utilized in the states of Missouri, Iowa, Kansas, and Texas to stabilize shallow slope failures as they are cost effective compared to traditional methods (Loehr and Bowders, 2007; Hossain et al., 2017). A few case studies that used RPPs as a slope stabilization method are described below.

I-70 Slope Site- Emma Field Test Site in Columbia, Missouri (Loehr and Bowders, 2007) and Parra et al., 2003)

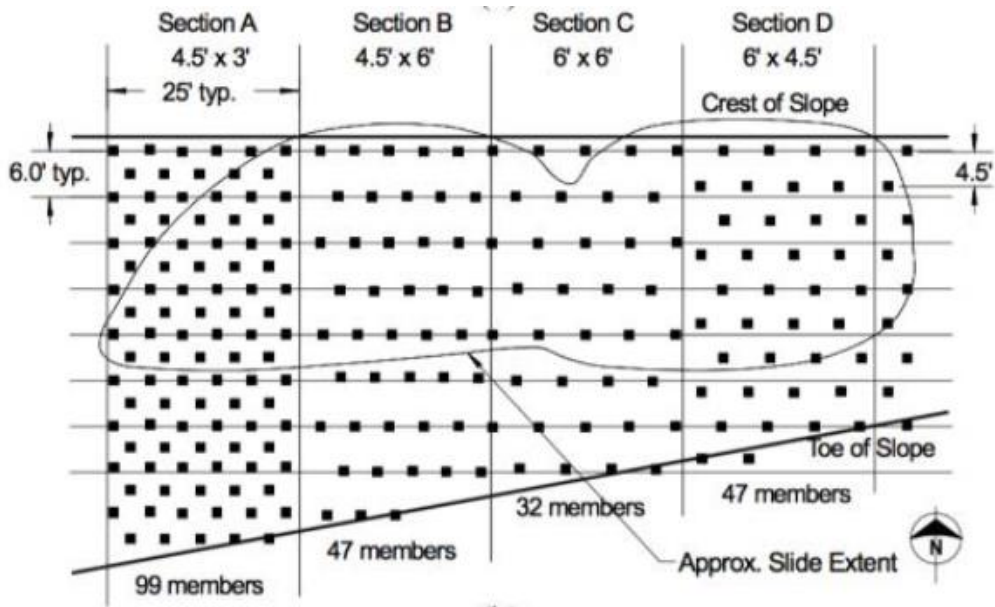
The I-70 Emma slope site was located approximately 65 miles west of Columbia, Missouri. The slope was 22 feet in height with a geometry of 2.5 H: 1 V. Results from site investigation results revealed the presence of both lean clay (CL) and fat clay (CH). Four different sections of the slope

(S1, S2, S3 and S4) experienced recurring failures. Slide areas (S1 and S2) were stabilized using RPP while the remaining sections (S1 and S2) were established as control sections for monitoring the effectiveness of RPP for slope stabilization. However, S3 was later stabilized with RPP after several slides occurred in the section. The plan and layout of RPPs used to stabilize the slide areas are shown in Figure 2-20.

The stabilized sections were monitored using slope inclinometers for lateral deformation, strain gauges for load on reinforcing members, jet-filled tensiometers for soil suction, and piezometer for groundwater table. The lateral displacement results obtained from inclinometer I-2 at S2 is shown in Figure 2-21. A maximum lateral deformation of 0.8 inches was observed at a depth of 2 feet. Lateral deformation was also observed to decrease as depth increased. Results from inclinometers I-6, I-7, I-8, and I-9 installed in S3 are shown in Figure 2-22. The results revealed increments in the value of horizontal displacement with respect to RPP spacing. Sections with small spacing deformed less than other sections.



(a)



(b)

Figure 2-20 Layout of RPP at the slide areas (a) S1 and S2 (b) S3 (Loehr and Bowders, 2007 and Parra et al., 2003).

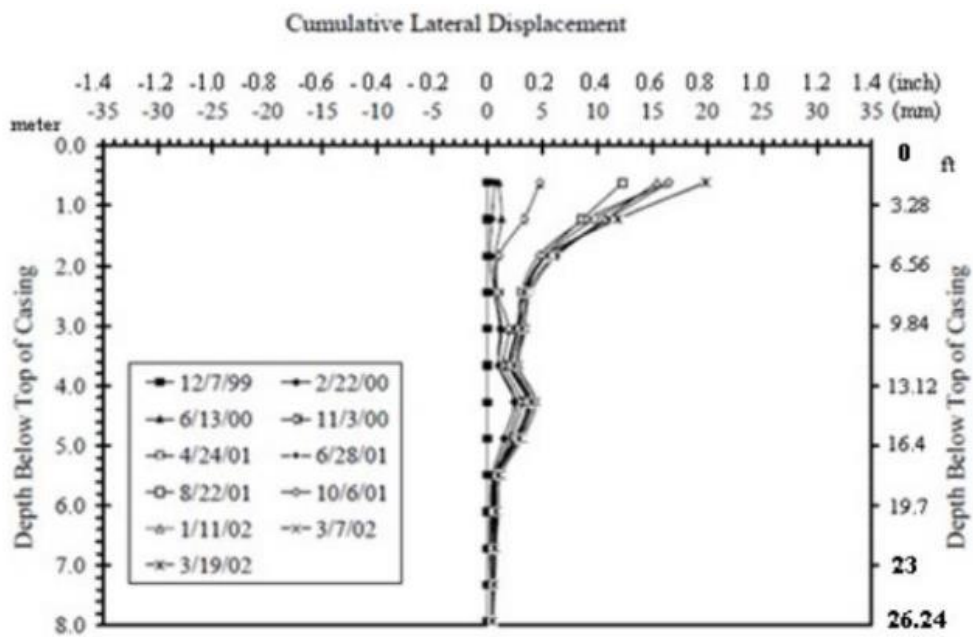


Figure 2-21 Result of inclinometer I2 at S2 (Parra et al., 2003).

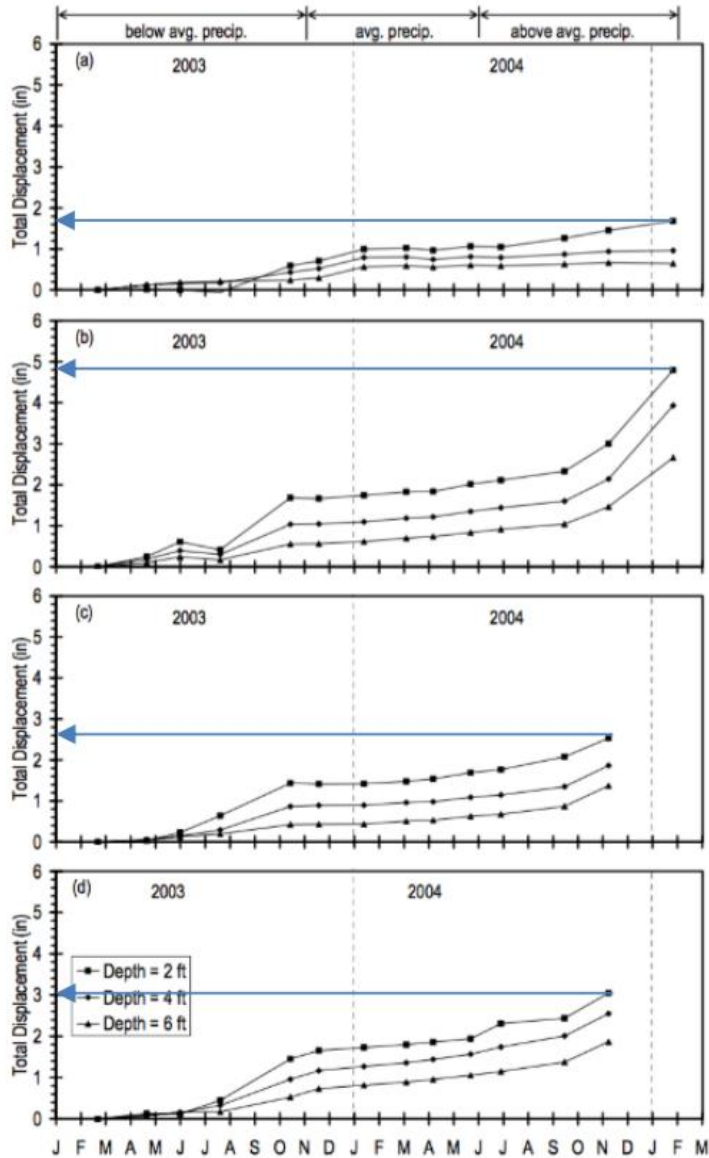


Figure 2-22 Displacement profile at slide section S3 from inclinometers (a)I-6 (b) I-7 (c) I-8 (d) I-9 (Loehr and Bowders, 2007).

I-435 Slope Site: Wornall Road Field Test Site (Loehr and Bowders, 2007)

Stabilization of the test slope site was done using four rows of RPPs with 3 ft. c/c spacing in the transverse direction, and 6 ft. c/c spacing in the longitudinal direction. Next, 15 rows of RPPs were installed with 3 ft. c/c spacing in both directions. The layout of RPP is shown in Figure 2-23. The

stabilized slope was instrumented with inclinometer casings, strain gauges, standpipe piezometers and moisture sensors. In this study, Parra et al. (2003) observed a maximum cumulative displacement of approximately 1.2 inches in inclinometer I-2 as shown in Figure 2-24.

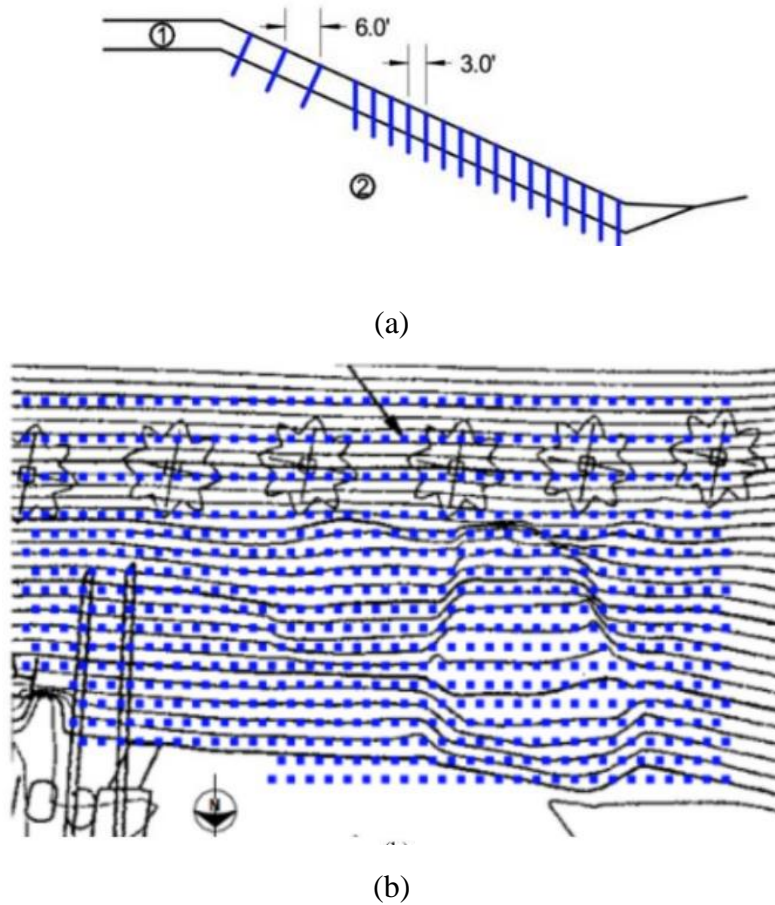


Figure 2-23 Layout of RPP (a) Cross sectional view (b) Plan view (Loehr and Bowders, 2007).

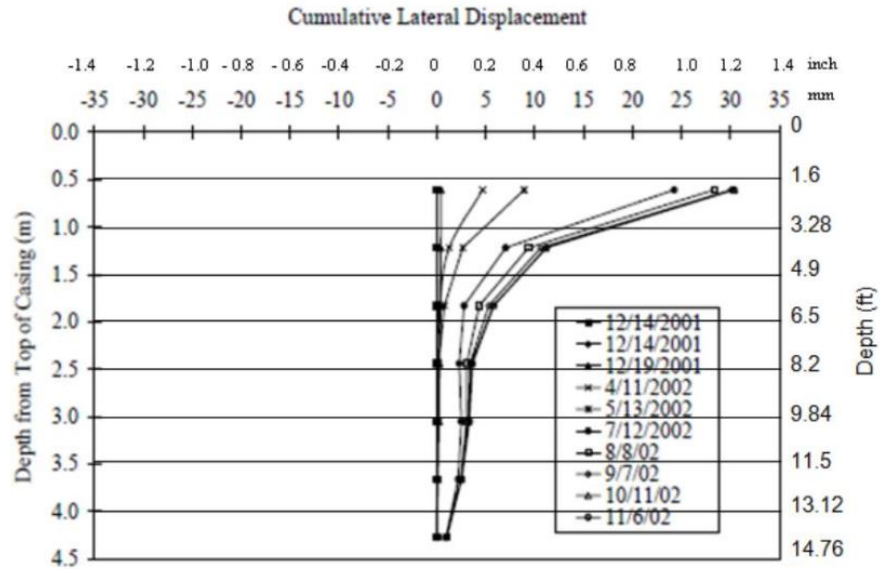


Figure 2-24 Cumulative lateral displacement with time for I-2 (Parra et al., 2003).

US Highway 287 Slope Site (Khan, 2014 and Rauss, 2019)

The failed section of the slope located at US Highway 287, near the St. Paul overpass in Midlothian, Texas was stabilized in 2007. The slope had a height of approximately 30 to 35 feet and a geometry of 3 H: 1 V. Field investigation results showed the presence of highly plastic expansive clay and a high moisture zone between depths of 5 and 14 feet. Khan (2014) designed the slope stabilization plan as shown in Figure 2-25 based on finite element modeling analysis. Khan (2014) considered 5 sections along the slope, of which 3 were stabilized with RPP using various depth and spacings, and two were left unstabilized and considered to be control sections for the study.

Field performance of the slope was evaluated by taking vertical inclinometers and conducting topographic surveys. Lateral deformation results obtained from inclinometers 1 and 3 installed in reinforced sections 1 and 3, respectively showed maximum cumulative displacements of 2.22 inches and 2.50 inches at a depth of 2.5 feet below the surface as shown in Figure 2-26.

Furthermore, the results of the topographic surveys conducted at the crest of the slope, presented in Figure 2-27, showed maximum vertical settlements of 4.99 inches, 7.02 inches, and 6.3 inches in reinforced sections 1, 2, and 3 respectively while that of control sections 1 and 2 were 15 inches and 11 inches respectively (Rauss, 2019). Field results indicated that the use of RPP effectively controlled the lateral displacement and vertical settlement of the slope.

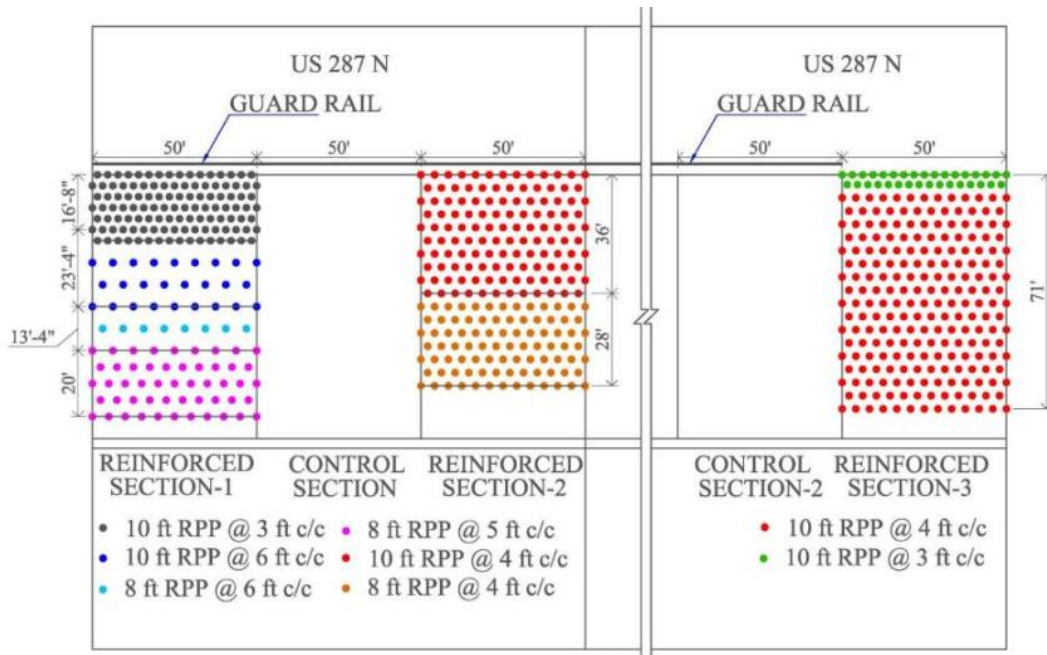
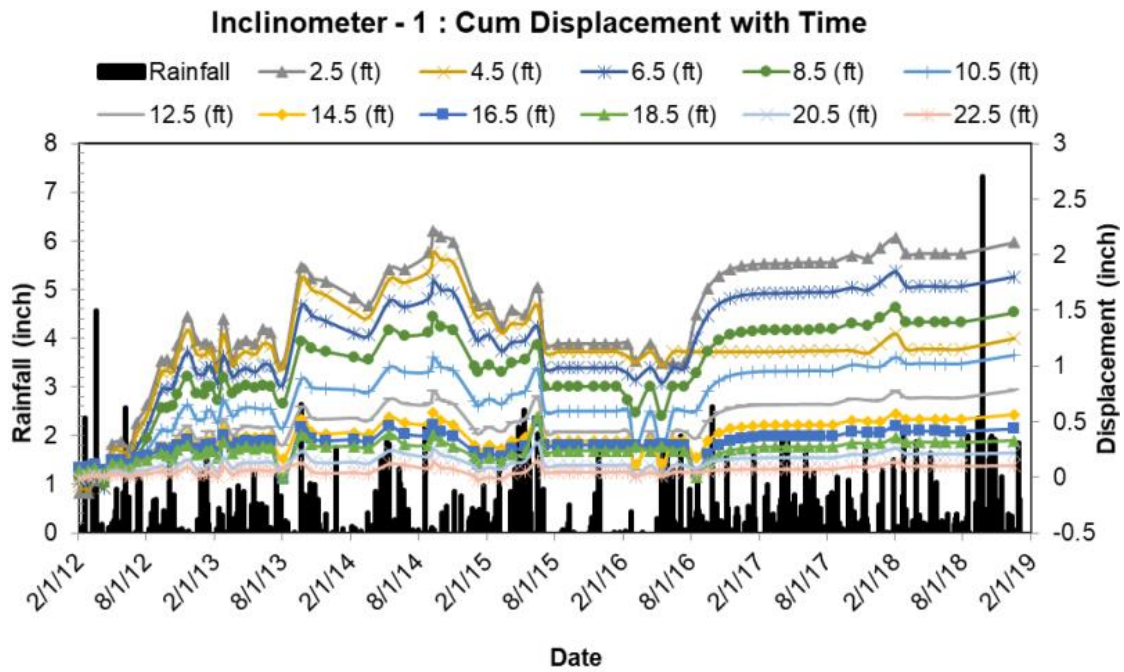
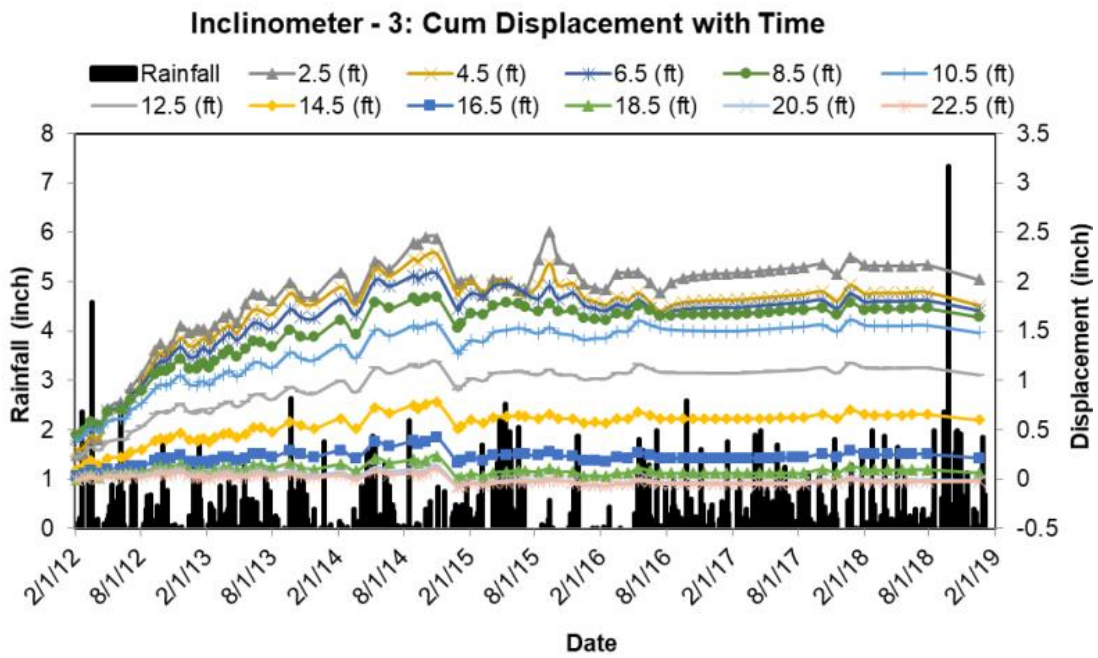


Figure 2-25 Layout of RPP at US 287 slope section (Khan, 2014).



(a)



(b)

Figure 2-26 Cumulative lateral deformation of slope at from inclinometer (a) I-1 and (b) I-3 (Rauss, 2019).

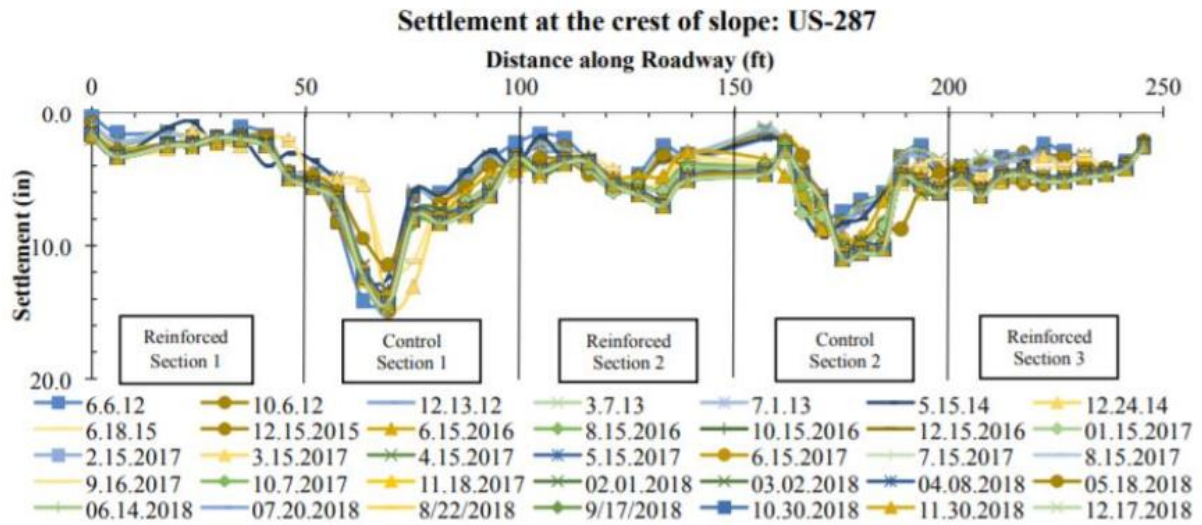


Figure 2-27 Vertical settlement of the slope at the crest (Rauss, 2019).

2.8 Moisture Control Methods for Slope Stabilization

Shear strength of soil is important in assessing the stability of a slope, especially fill embankment slopes. Such slopes have a substantial, thick, and unsaturated soil layer and the existence of matric suction in the unsaturated zone provides an apparent shear strength. Infiltration of moisture caused by rainfall events increases the porewater pressure of the soil (reduction of matric suction) consequently reducing the shear strength. Although mechanical methods of slope stabilization provide reinforcement against sliding, the intrusion of moisture into the soil is not prevented. In order to preserve matric suction of the soil, several measures have been discussed in the following sections.

2.8.1 Horizontal Drains

Horizontal drains are holes drilled in cut or fill slopes, encased with a perforated metal or slotted plastic liner (Royster,1980). The main purpose of using a horizontal drain is to drain away groundwater and maintain the dry condition of the soil in order to control landslides. In several

studies, the factor of safety of slopes with horizontal drains was found to be higher than that of a slope without a horizontal drain (Barrett, 1980; Royster, 1980).

2.8.2 Capillary Barrier System (CBS)

A capillary barrier system is used as a cover system which consists of two different layers of soil: a fine-grained layer overlying a coarse-grained layer (Rahardjo et al., 2012). These soil layers have dramatically different hydraulic properties which prevent the intrusion of rainwater into the underlying soil by utilizing the principles of unsaturated soil mechanics (Nicholson et al. 1989; Ross, 1990; Steenhuis et al, 1991; Stormont, 1996). Various materials have been used for the fine grained and coarse-grained layers to form a capillary barrier system in existing literature.

2.8.3 CBS using Fine Sand and Granite Chips

In order to stabilize a shallow slope failure, Rahardjo et al. (2012) conducted a study using a capillary barrier system which comprised of a 20 cm thick layer of fine sand for the fine-grained layer and a 20 cm thick layer of granite chips for the coarse-grained layer as shown in Figure 2-28. The construction sequence involves laying a geodrain on top of the slope after trimming it to the correct depth and then steel wires are used to secure the geodrain to prevent slippage. Next, geocells filled with granite chips are laid on top of the geodrain to form the coarse-grained layer. Lastly, a geotextile layer is placed as a separator layer, a second layer of geocell is laid and filled with fine sand to form the fine-grained layer.

Results obtained from tensiometers installed at the crest of the slope stabilized with a capillary barrier system and that without one is presented in Figure 2-29. The slope with a capillary barrier system effectively maintained negative porewater pressure (matric suction) compared to the slope without CBS. Moreover, in the slope without CBS rise in porewater pressure was observed with respect to rainfall events indicating percolation of rainwater into the slope.

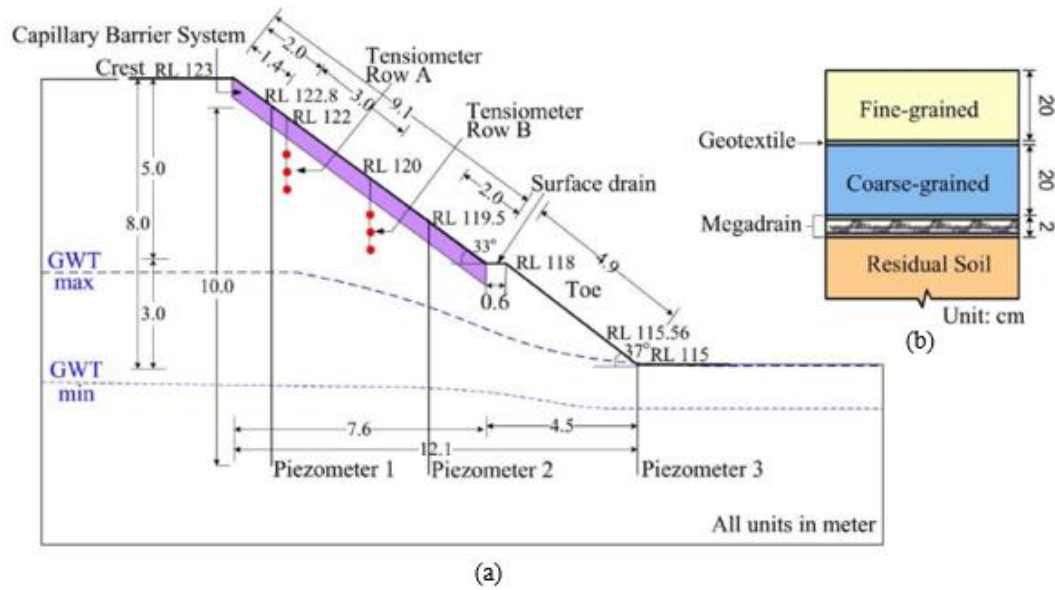


Figure 2-28 (a) Schematic of stabilized slope (b) Cross section of CBS (Rahardjo et al., 2012).

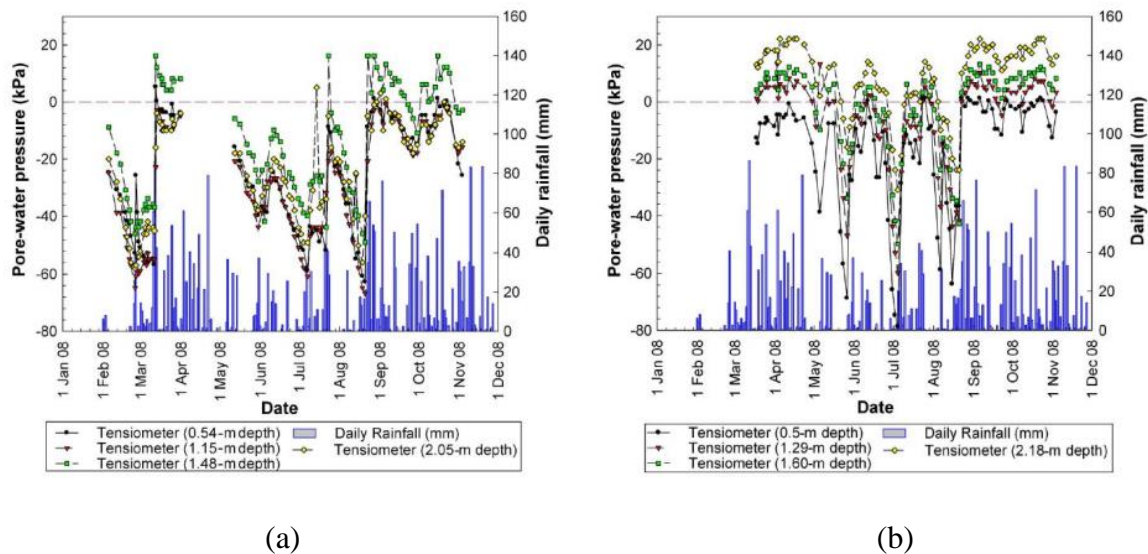


Figure 2-29 Variation of porewater pressure with rainfall and time near the crest of the slope (a) with CBS (b) without CBS (Rahardjo, et al., 2012).

2.8.4 CBS using Fine Sand and Recycled Crushed Concrete Aggregate

Rahardjo et al. (2013) utilized fine sand as the fine-grained layer and recycled crushed concrete aggregate as the coarse-grained layer in a capillary barrier system to stabilize rainfall induced slope

failure, as shown in Figure 2-30. The construction of this CBS involves laying down a 6.5 mm thick geosynthetic drainage layer as a separator layer on top of the slope, after it is trimmed to 540 mm depth. Geocells are then laid on top of the separator layer in order to place the recycled crushed concrete aggregate as a coarse-grained layer. The geocells are secured in place with the use of steel J pins of 75 cm length. Finally, following the placement of the recycled crushed concrete aggregate, a layer of geotextile is placed as a separator layer and a second layer of geocells filled with fine sand are laid to form the fine-grained layer.

Results of tensiometers installed at the middle of the slope stabilized with CBS and slope without CBS are presented in Figure 2-31. The slope with CBS effectively maintained the negative porewater pressure compared to the original slope. Additionally, the original slope experiences a rise in porewater pressure with respect to rainfall events, indicating rainwater infiltration into the slope.

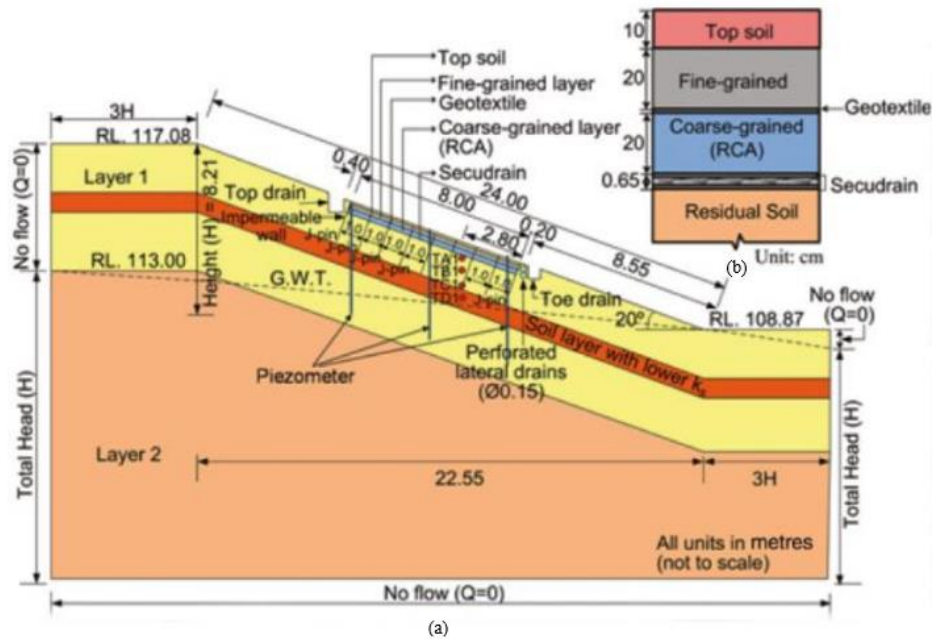
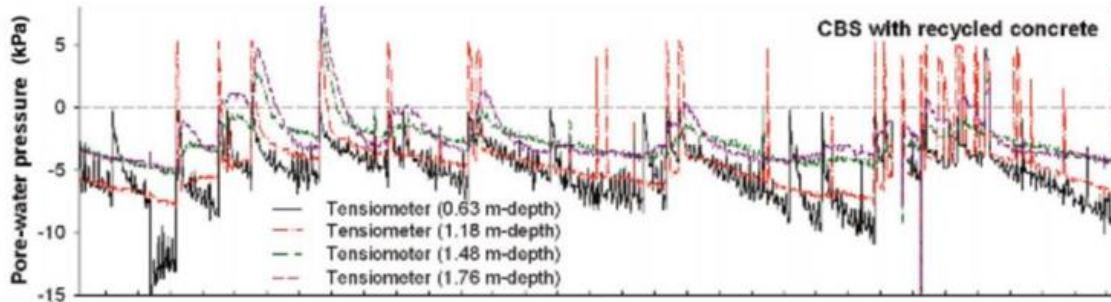
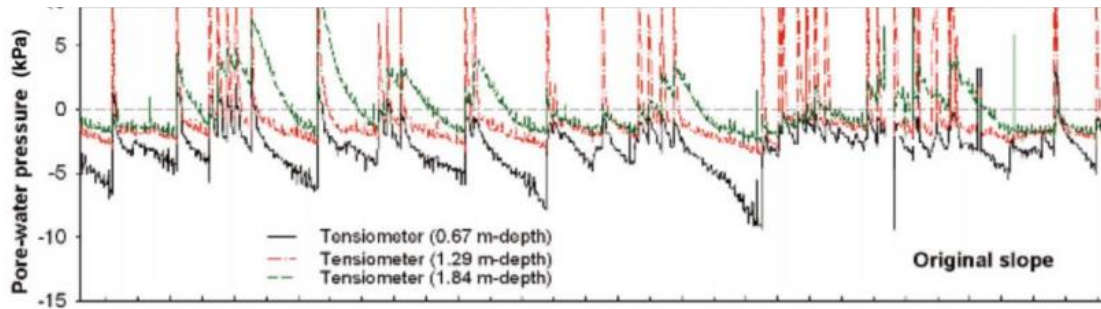


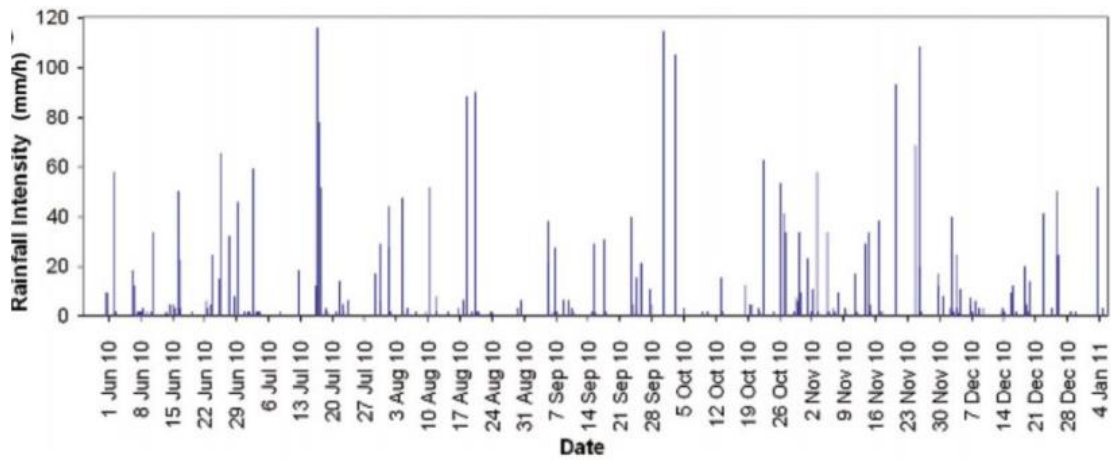
Figure 2-30 (a) Schematic of stabilized slope (b) Cross section of CBS (Rahardjo et al., 2013).



(a)



(b)



(c)

Figure 2-31 Variation of porewater pressure with time at the middle of the slope (a) Slope with CBS (b) Original slope (c) Rainfall intensity with respect to time.

2.8.5 CBS using Fine Sand and Geosynthetics (Secudrain)

Rahardjo et al. (2013) utilized fine sand as the fine-grained layer and geosynthetic (secudrain) as the coarse-grained layer to stabilize rainfall induces slope failure as shown in Figure 2-32. The

construction sequence involves first laying down geosynthetic drainage layer of 6.5 mm thickness to serve as a separator layer on top of the slope after trimming it to 360 mm depth. Another layer of geosynthetic drainage material / secudrain is placed as a coarse-grained layer. Geocells are then laid over the secudrain and secured in place through the use of steel J pins of 75 cm length, penetrating 54 cm into the ground. Finally, geocell areas are filled with fine sand to form the fine-grained layer.

Results of the tensiometers installed at the middle of the slope stabilized with CBS and the original slope is presented in Figure 2-33. The slope with CBS maintained negative porewater pressure more effectively than the original slope.

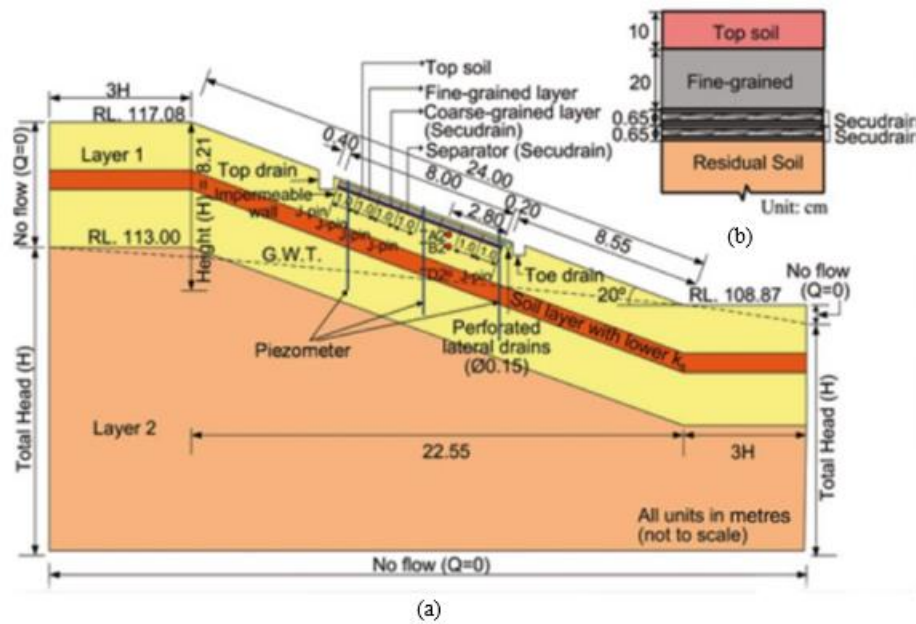


Figure 2-32 (a) Schematic of stabilized slope (b) Cross section of CBS.

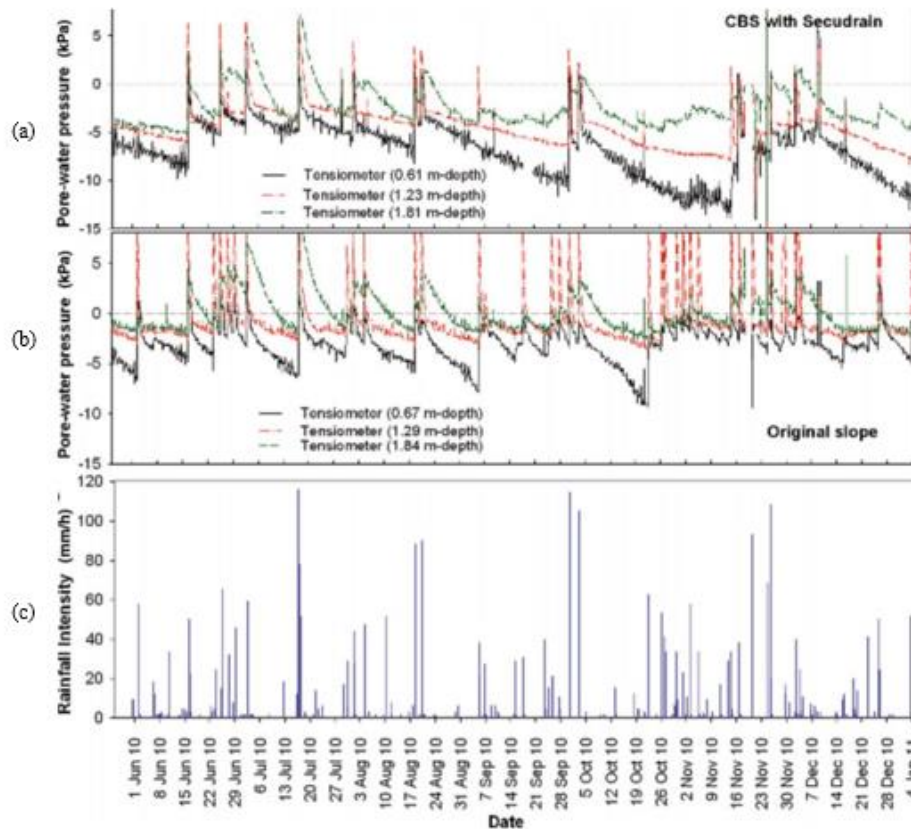


Figure 2-33 Variation of porewater pressure with time at the middle of the slope (a) Slope with CBS (b) Original Slope (c) Rainfall intensity with respect to time.

2.8.6 Geosynthetic Capillary Break

Geosynthetic capillary break (GCB) functions similarly as a traditional soil capillary barrier and can be used as part of an engineered cover system to reduce net percolation. In a study conducted by Park and Fleming (2006), the unsaturated hydraulic properties of geotextile, fine grained rock flour, as well as cover soil and mine tailings were determined in order to develop a set of inputs for numerical modelling. Preliminary results of modelling showed that including a geosynthetic capillary barrier decreased the suction developed in the overlying cover soil which will cause mitigation of downward moisture movement.

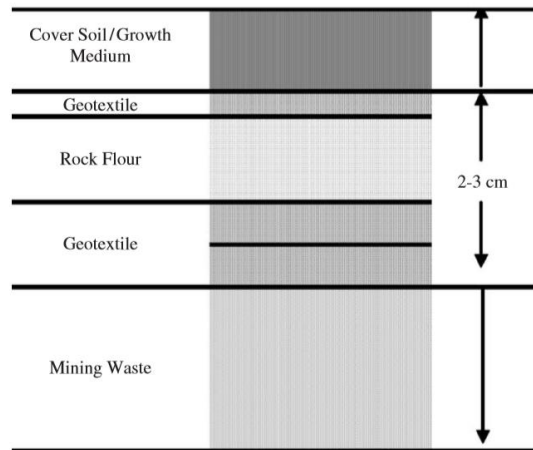


Figure 2-34 Schematic of GCB (Park and Fleming, 2006).

2.8.7 Modified Moisture Barrier

The modified moisture barrier system is a layer of geocomposite underlain by a layer of geomembrane. It is a relatively new moisture control system used in pavement subgrade to reduce moisture fluctuations of the subgrade soil and hence improve the service life of the pavement (Ahmed, 2017; Pandey et al., 2022; Sapkota, 2019).

2.8.7.1 Mechanism

Henry and Stormont (2001) developed a geosynthetic capillary drain (G CBD) to drain water from soils at negative porewater pressure. Following precipitation events, water infiltrates into fine soil and accumulates at the interface of a layer of coarse-grained soil (capillary barrier effect). Eventually the water breaks into the lower layer (Figure 2-35 a) when soil water suction reaches the entry suction of the underlying layer (Henry and Barna, 2002). Inclusion of a transport layer like fine sand between the two soil layers (Figure 2-35 b) significantly increases the amount and rate of drained water. A system of geosynthetics (Figure 2-35 c) can perform the same action of transport and capillary barrier layers due to their contrasting hydraulic properties. The upper

geotextile acts as a transport layer, while the geonet acts as a capillary barrier. A geonet is a geosynthetic with large, open pores that replace the underlying coarse soil. The third component is a separator geotextile which prevents the underlying soil from intruding into the pore spaces of the geonet (capillary barrier layer).

The modified moisture barrier utilizes the same concept as a GCBD but has an additional component. An impermeable geomembrane is included beneath the geocomposite system. Figure 2-36 shows the schematic of the modified moisture barrier installed in a pavement subgrade section.

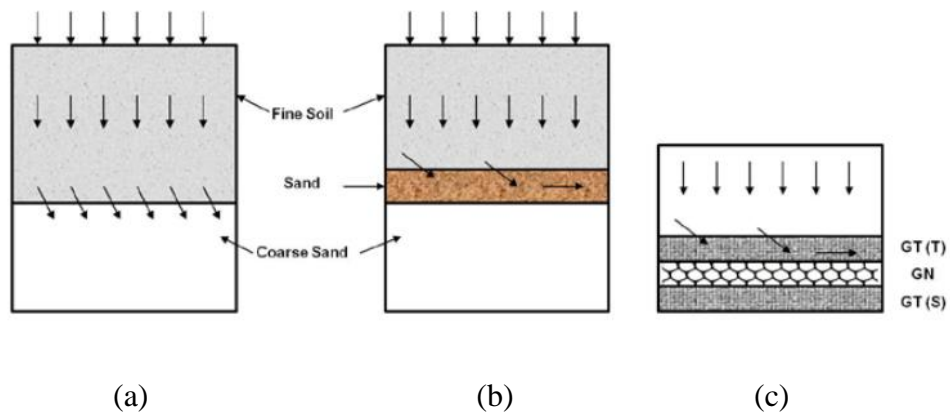


Figure 2-35 Lateral drainage in unsaturated soil with (a) capillary barrier (b) transport layer above a capillary barrier (c) GCBD with overlying soil (Redrawn from Henry et al., 2002).

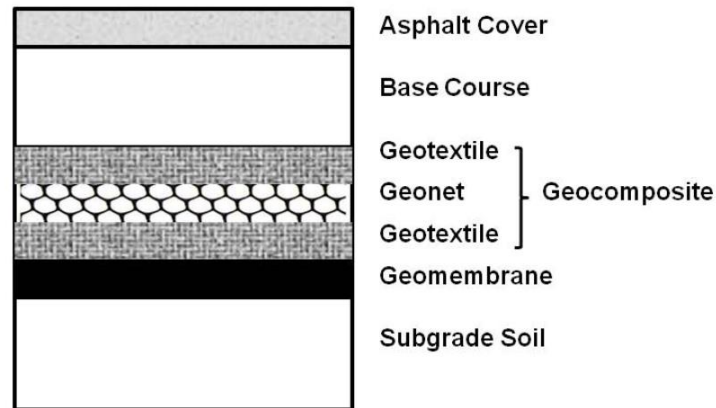


Figure 2-36 Modified moisture barrier used in pavement subgrade (Ahmed, 2017).

2.8.7.2 Field Performance of Modified Moisture Barrier

FM-987: Kaufman, Texas (Ahmed, 2017)

The modified moisture barrier was first utilized by Ahmed (2017) to prevent edge drops and cracks on farm to market road FM 987 in Post Oak, Bend County, Kaufman, Texas. A 50 feet section was stabilized with the modified moisture barrier and an adjacent 50 feet section was considered to be the control section for this study. Similar instrumentations were carried out in both sections to compare and evaluate the effectiveness of the barrier in reducing the moisture intrusion into the pavement subgrade and subsequently controlling the deformation.

Moisture variation at a depth of 3 feet obtained from field installed moisture sensors in both test section and control section is presented in Figure 2-37. From the results, it was observed that the barrier section was able to maintain almost constant moisture content in the subgrade soil while significant fluctuation due to climatic loading was observed in the control section. The results indicated the effectiveness of modified moisture barrier in preventing rainwater from reaching the subgrade soil hence preventing its detrimental effect on pavement structure.

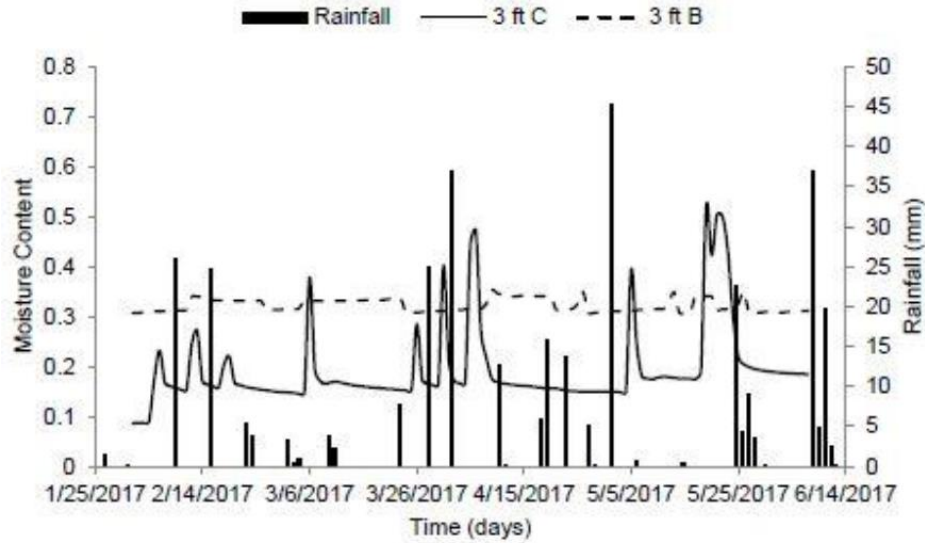


Figure 2-37 Comparison of moisture content for barrier section and control section at 3 feet depth (Ahmed et al.,2017).

Highway US 287: Midlothian, Texas (Sapkota et al.,2019)

Sapkota et al. (2019) used the modified moisture barrier in a two-step mechanism to stabilize a rainfall induced shallow slope failure. The slope had a geometry of 3.3 H: 1V and supported a two-lane roadway with 11 feet wide shoulders on each side. The mechanism involved the installation of recycled plastic pins for lateral stabilization of the slope followed by the installation of a modified moisture barrier for preventing the infiltration of rainwater through desiccation cracks. A 50 feet section of the slope was stabilized using both recycled plastic pins and the modified moisture barrier while the adjacent 50 feet of the slope was considered to be the control section for this study. The schematic diagram of the slope stabilized with both recycled plastic pins and modified moisture barrier is shown in Figure 2-38.

The slope was instrumented with moisture sensors and inclinometers to monitor the fluctuation of moisture content and lateral deformation of the slope in both the barrier section and the control

section. It can be seen that with successive rainfall events the barrier section experienced insignificant variation in volumetric moisture content compared to that of the control section. Furthermore, the maximum lateral deformation of the barrier section was approximately three times lower than that of the control section. The combined use of recycled plastic pins and modified moisture barrier can effectively stabilize shallow slope failures.

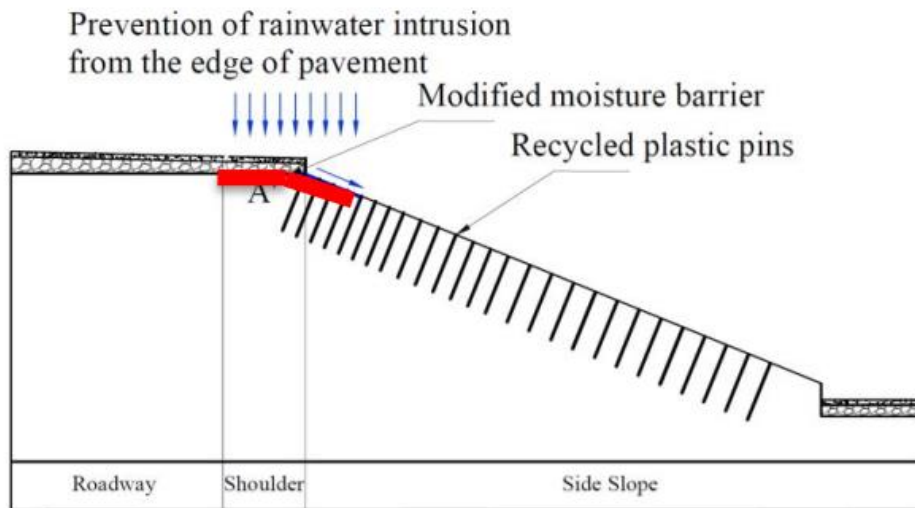
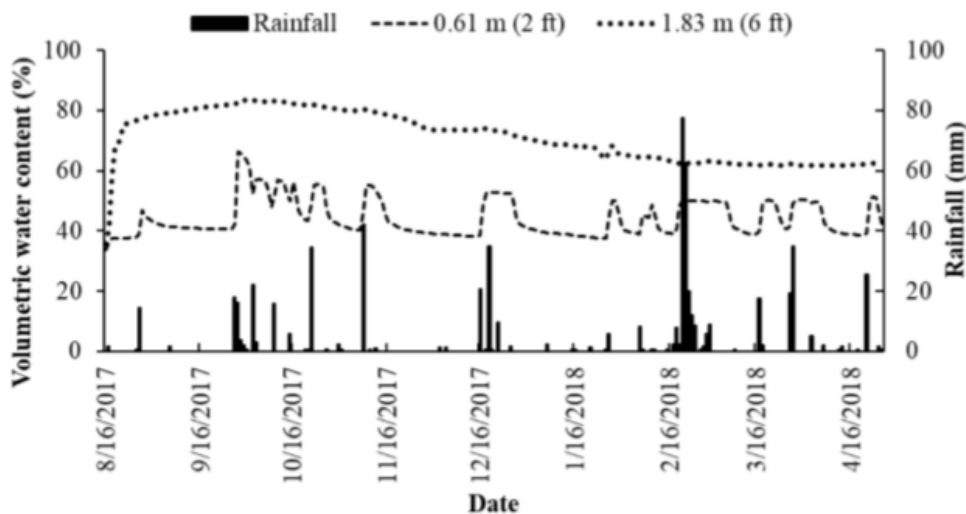
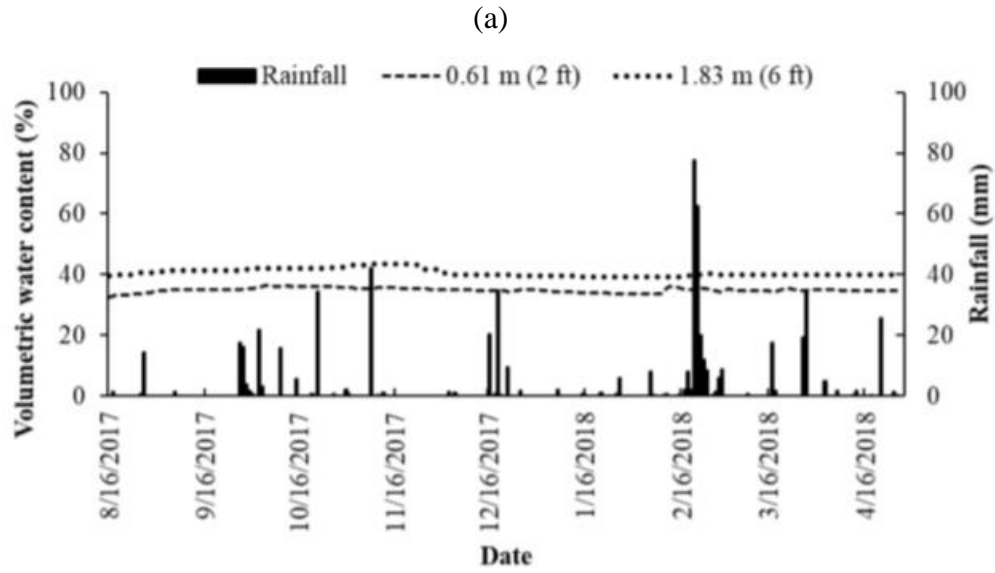


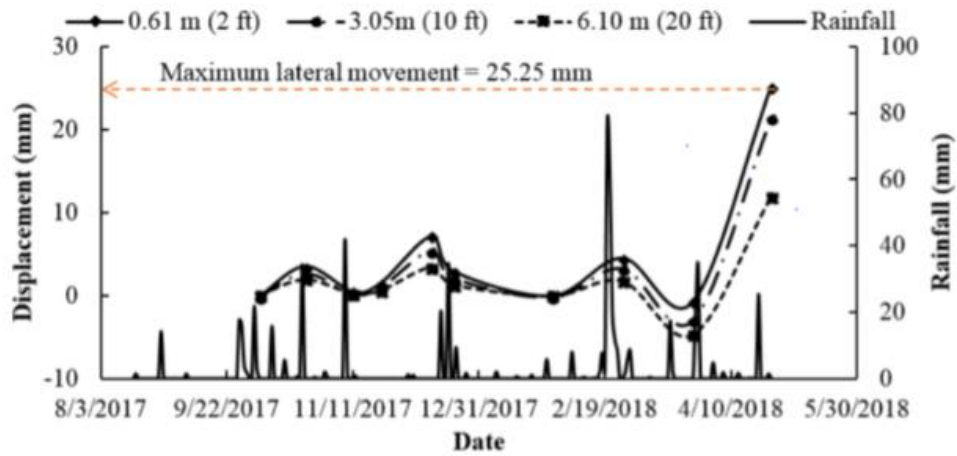
Figure 2-38 Schematic diagram of slope stabilized with recycled plastic pins and modified moisture barrier (Sapkota et al., 2019).



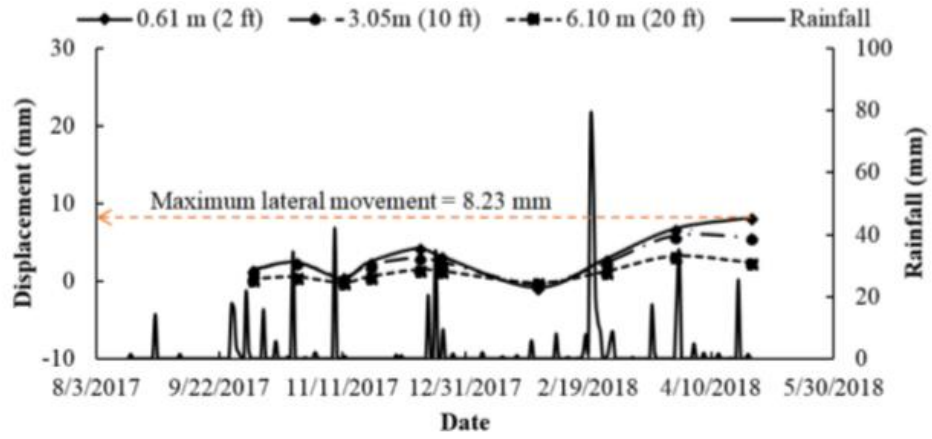


(b)

Figure 2-39 Change in volumetric moisture content with time and rainfall (a) control section (b) barrier section (Sapkota et al., 2019).



(a)



(b)

Figure 2-40 Depth wise comparison of lateral deformation at (a) control section (b) barrier section (Sapkota et al., 2019).

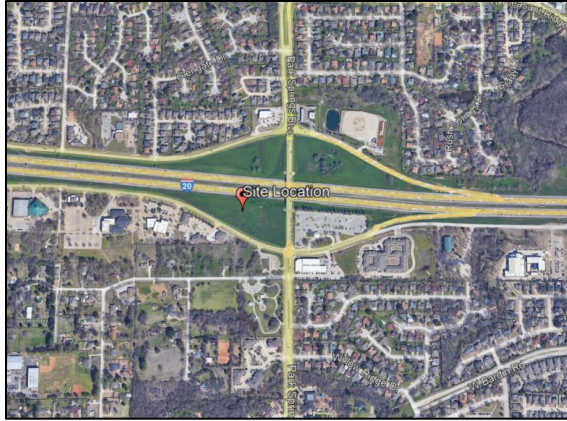
CHAPTER 3 SITE INVESTIGATION AND SLOPE STABILIZATION PLAN

3.1 Introduction

This chapter discusses the adopted methodology to fulfill the research objectives. The objective of this study is to evaluate the performance of the modified moisture barrier as a slope stabilization method, through field implementation and performance monitoring. Field performance study constitutes a major portion of this dissertation as it is a performance indicator in presence of various uncertainties existing in the field. A failed section of a slope constructed on expansive soil was selected and stabilized with the proposed moisture barrier to evaluate its effectiveness. As part of evaluating the performance of the modified moisture barrier, a section of the failed slope was stabilized with recycled plastic pins to compare the performance of a moisture control method to that of a mechanical method of slope stabilization. Lastly, an adjacent portion of the natural slope with similar dimensions was established near the test section to serve as the control section for this study. This chapter discusses the details on site selection and investigation, and design of the slope stabilization plan.

3.2 Project Background

In June 2019, a failed section of a highway slope located near the intersection of Eastbound Interstate Highway 20 (IH 20) and Parks Springs Blvd. in Arlington, Texas, was selected for the study. The location of the slope is shown in Figure 3-1 (a). The failure line was first observed in 2018 and the slope failed in the summer of 2019 as shown in Figure 3-1 (b) and (c). The slope was about 15 feet in height and had a geometry of 3 (H): 1 (V). During preliminary reconnaissance, it was observed that the slope had an edge drop of about 1.5 feet and had experienced a shallow slope failure of about 3 feet depth. The failed section was approximately 120 feet in length and 60 feet in width.



(a)



(b)



(c)

Figure 3-1 (a) Site Location (b) and (c) Shallow Slope Failure.

3.3 Site Investigation

Site investigation was carried out according to the recommendations outlined in the TxDOT Geotechnical Manual, Section 1- Soil Survey. Site investigation was conducted in June 2019 to understand subsurface soil conditions and identify the reason behind the slope failure. Preliminary site investigation program included subsurface exploration utilizing geotechnical drilling and geophysical testing, using electrical resistivity imaging (ERI). The location of geotechnical drilling and ERI line is shown in Figure 3-2.



Figure 3-2 Locations of geotechnical borings (BH) and electrical resistivity image (ERI line).

3.3.1 Geotechnical Drilling

Two soil borings (BH-01 and BH-02), each of 20 feet depth were drilled at the crest of the slope. A hollow stem auger with an outer diameter of 5 inches powered by a track mounted drill rig was used for drilling. Both disturbed and undisturbed soil samples were collected from the boreholes for laboratory testing. Details of geotechnical drilling is presented in Table 3-1. The drilling set up and collected undisturbed sample is shown in Figure 3-3. Undisturbed samples were collected from each borehole at every 5 feet interval using thin-walled Shelby tube samples with an outer diameter of 3 inches.

Texas cone penetrometer (TCP) testing was conducted in accordance with Tex-132-E, at 5 feet intervals, to measure the soil resistance in order to classify the soil compaction. The test set up consisted of a 170 lbs. hammer with a drop height of 24 ± 0.5 inches, a drill stem, an anvil threaded to fit the drill stem and slotted to accept the hammer, and a TCP Cone of 3 in. diameter with a 2.5 in. long point. The test began by dropping the hammer to drive the penetrometer cone attached to the stem. The cone was then driven into the ground up to 6 inches or 12 blows, whichever occurred

first and seated in the soil. Blow counts (N-values) were noted for the first and second 6 inches for a total of 12 inches for relatively soft materials, while the penetration depth (inches) was noted for the first and second 50 blows for a total of 100 blows for stiffer materials. The TCP blow counts are shown in Table 3-2.

Table 3-1 Geotechnical drilling details.

Location	IH 20 & Park Springs Blvd., Arlington, Texas
Date of Boring	June 20, 2019
Client	Texas Department of Transportation (TxDOT)
Number of Boreholes	2
Depth of Boring	20 feet
TCP Location	8
Undisturbed Sampling Location	8
Disturbed Sampling Location	10



(a)

(b)

Figure 3-3 (a) Drilling using hollow stem auger. (b) Undisturbed Shelby tube sample.

Table 3-2 Results from TCP test.

Depth (ft.)	N-Values		Soil Condition
	BH-1	BH-2	
5	23	52	Very Stiff
10	59	64	Hard
15	17-50(3")	50(0.5")-50(0.5")	Hard
20	50(0")-50(0")	50(0.75")-50(0.75")	Hard

Visual observations and classifications revealed the predominant soil type as lean clay with silt. Boring logs of geotechnical drilling are presented in Appendix A. Laboratory testing was performed on the collected disturbed and undisturbed soil samples to determine the index properties and strength parameters, respectively. Soil properties were determined based on the following tests.

3.3.1.1 Gravimetric Moisture Content

Moisture content tests were performed on disturbed samples to examine the variation in soil moisture content with depth following ASTM D2216 *Standard Test Methods for Laboratory Determination of Water (Moisture) Content of Soil and Rock by Mass*. Soil moisture content profiles, with respect to depth below the ground surface, for both boreholes are shown in Figure 3-4. Gravimetric moisture content varied from about 8 % to about 20 %. Additionally, higher moisture content was observed in the top 8 feet.

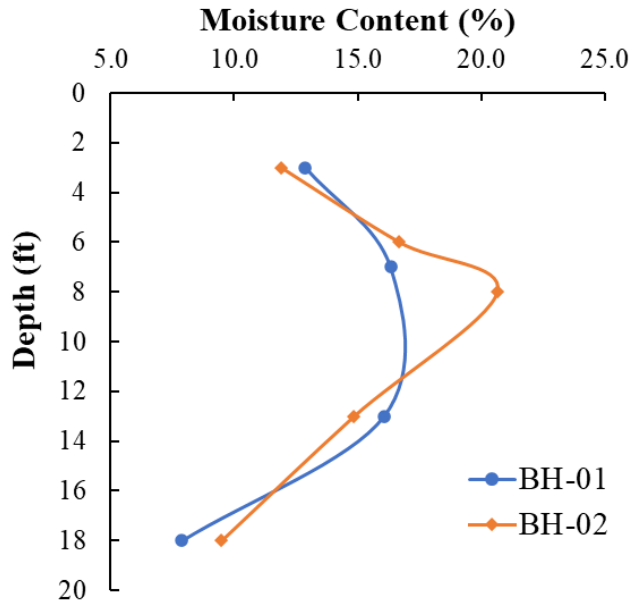


Figure 3-4 Moisture content profile with respect to depth.

3.3.1.2 Grain Size Distribution

Grain size distribution analysis was carried out as per ASTM D 422-63 *Standard Test Method for Particle Size Analysis of Soils*. Results from mechanical sieve analysis and hydrometer tests were combined to obtain the full range of particle size distribution. Three test samples were selected to represent different layers of the soil strata. The soil samples were oven dried at a temperature of 120 °F, crushed and washed with flowing water through No. 200 sieve. The mass of soil retained on No. 200 sieve was then dried in the oven and mechanical sieves analysis was performed using #4, #10, #30, #40, #60, #100 and #200 US Standard Sieves. Additionally, hydrometer tests were performed on samples passing through No. 200 sieve. Hydrometer samples prepared for the test are shown in Figure 3-5. The mass of soil retained on No. 10 sieve along with the soil from the hydrometer test was then subjected to wash sieving. Then, sieve analysis was carried out using a mechanical sieve shaker to obtain the grain size distribution of the soil. The depth wise distribution

curves for the test samples from borehole 1 are shown in Figure 3-6. Results of grain size distribution test, tabulated in

Table 3-3, were used to classify the soil according to the Unified Soil Classification System (USCS). In all layers, the fine fraction ranged from 82 to 92 %. The soil was found to be predominantly clay of low plasticity (CL), which is in accordance with the visual observation during drilling.



Figure 3-5 Hydrometer test samples.

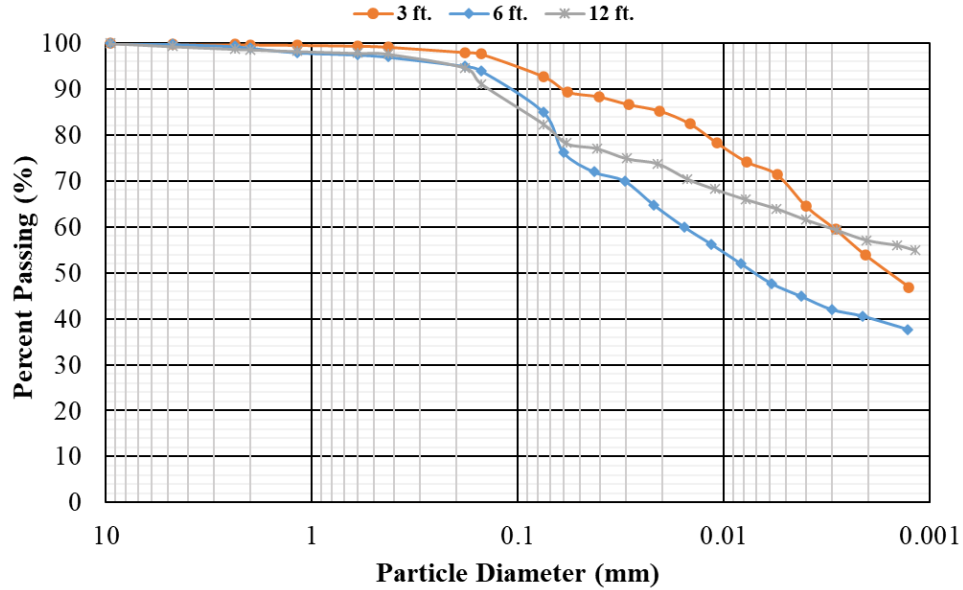


Figure 3-6 Grain size distribution curves.

Table 3-3 Particle size distribution.

Depth (ft)	% Gravel	% Sand	% Silt or Clay	USCS Classification
3	0.1	7.8	92.1	Lean Clay (CL)
6	0.2	17.6	82.2	Lean Clay with Sand (CL)
12	0.25	19.8	80	Lean Clay with Sand (CL)

3.3.1.3 Atterberg Limit

The Atterberg limits test was conducted on collected disturbed soil samples following ASTM D 4318 *Standard Test Methods for Liquid Limit, Plastic Limit, and Plasticity Index of Soils*. The liquid limit of the soil varied from 30 to 48 %. The plasticity index of the soil was calculated using the formula:

$$PI = LL - PL$$

where PI=Plasticity Index, LL=Liquid Limit and PL=Plastic Limit. The plasticity indices of the soil ranged from 20 to 22%. The plasticity chart (graphical plot of liquid limit versus plasticity index) is presented in Figure 3-7. According to United Soil Classification System (USCS), the soil was classified at low plastic clay (CL) at all depths which is in accordance with the soil classification results obtained from grain size distribution.

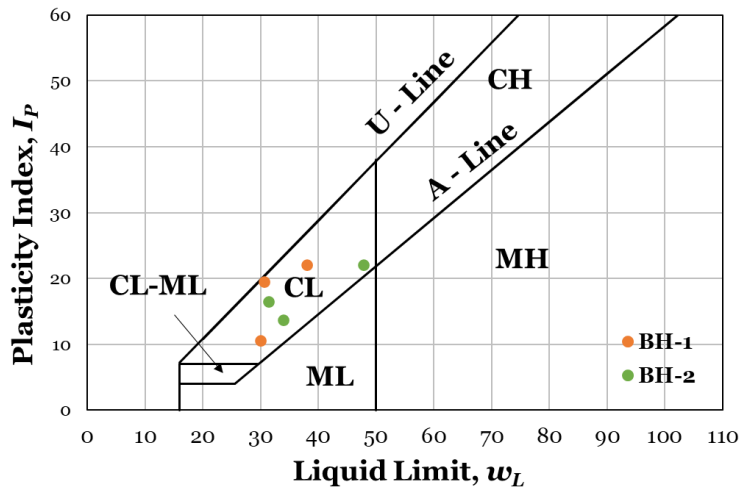


Figure 3-7 Plasticity chart.

3.3.1.4 Hydraulic Conductivity

The falling head permeability test was conducted following ASTM D5084 *Standard Test Methods for Measurement of Hydraulic Conductivity of Saturated Porous Materials Using a Flexible Wall Permeameter*, to determine the hydraulic conductivity of the soil. The test was conducted in a triaxial cell, as shown in Figure 3-8, where a flexible membrane is used to keep the sample tightly compressed during the experiment through the application of a cell pressure. The possibility of seepage between the interface of the soil and membrane is reduced through the use of a flexible membrane. Remolded soil samples were utilized for permeability testing. Disturbed soil samples were oven dried, pulverized and then passed through a No. 40 sieve. The sample was then mixed with water to obtain the desired field water content and allowed to stand for 48 hours. Following

saturation, the specimen was compacted in a standard compaction mold. The compacted specimens were then trimmed to a diameter of 2.5 in and height of 5 in, to maintain a diameter to height ratio of 2:1 as suggested by Carpenter and Stephenson, 1986. Extreme care was exercised during trimming of the soil sample to minimize the influence of smear zones on infiltration. Back pressure saturation technique was applied to saturate the sample. Once the sample was considered to be saturated (Skempton's B coefficient was greater than 0.95), the inflow stand tube pressure was increased while keeping that of the outflow line constant. This was done to establish a hydraulic gradient across the specimen. An automatic volume change apparatus measured the volume of flow continuously. The hydraulic gradient was computed in terms of water head and the hydraulic conductivity of the soil was calculated using the falling head equation.

$$K = \frac{aL}{A(t_i - t_f)} \ln \left(\frac{h_f}{h_i} \right)$$

Where k=hydraulic conductivity (cm/s), a=cross sectional area of the standpipe (cm²), A= cross sectional area of the sample (cm²), L= length of sample (cm), t_i-t_f = elapsed time (s), h_i=initial head difference between inflow and outflow stands tube (cm of water) and h_f=final head difference between inflow and outflow of water (cm of water). Results are permeability test are shown in Table 3-4. The results showed low hydraulic conductivity of the soil which may be due to conducting the tests on recompacted samples.

Table 3-4 Results of permeability test.

Depth (ft.)	Saturated Hydraulic Conductivity (ft/s)	Saturated Hydraulic Conductivity (ft/s)
7	7.1x10 ⁻⁷	2.32x10 ⁻⁸

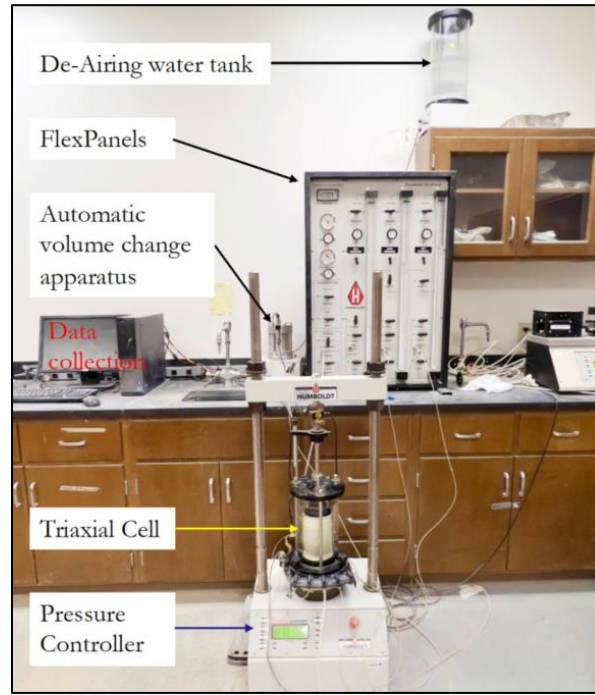


Figure 3-8 Permeability test set up.

3.3.1.5 Shear Strength

Undisturbed soil samples from different depths were further tested for shear strength properties following *ASTM D7263 Standard Test Methods for Laboratory Determination of Density and Unit Weight of Soil Specimens* and *ASTM D3080 Standard Test Method for Direct Shear Test of Soils Under Consolidated Drained Conditions*. Results of shear strength tests are shown in Table 3-5, and were utilized to conduct slope stability analysis. At shallow depths the soil had lower cohesion while at depth of 15 feet, both cohesion and angle of friction was found to be high. During field investigation, sandstone was observed at depth of 20 feet below the ground surface which explains the high shear strength parameters around 15 feet depth.

Table 3-5 Shear strength properties.

Depth (ft.)	Unit Weight (pcf)	Cohesion (psf)	Angle of Friction (°)
5	110	115	11
10	130	245	15
15	135	2450	31

3.3.2 Geophysical Testing

Geophysical methods of subsurface investigation are regarded as economic and efficient techniques. They provide a continuous image of the subsurface, qualitatively depicting changes in soil properties such as moisture content. The application of electrical resistivity imaging as a practical method to evaluate compacted soils has been assessed (Akhtar et al., 2022). It is an efficient method to visualize the stratigraphy of the subsoil at different times and locations (Kibria,2014). Resistivity imaging (RI) is one of the well-established methods of geophysical testing. RI is commonly used for investigating the vertical and horizontal variations of soil moisture content, environmental anomalies, and near surface geology.

2D electrical resistivity imaging (ERI) which provides a continuous image of the subsurface, was performed as part of geophysical testing, using a multi electrode array system and inversion modeling. The 2D ERI was conducted using an 8 channel SuperSting equipment utilizing 28 electrodes. The location and equipment of electrical resistivity imaging are shown in Figure 3-9. The result of resistivity imaging is presented in Figure 3-10. An inverse relation exists between electrical resistance and soil moisture content. Results of resistivity imaging indicated the presence of high resistivity (represented by red zones) near the surface which implied that the soil was loose with high void ratio. Furthermore, between depths of 5 and 10 feet, the resistivity values were low

(depicted by blue zones) indicating the presence of a moisture pocket. Overall, the section had high resistivity values indicated low moisture content of the soil which means that the soil was loose and not well compacted. The resistivity imaging result was as expected since the test was conducted during summer, after the slope was backfilled following the failure.



Figure 3-9 (a) Location of ERI line (b) 8 Channel SuperSting Equipment.

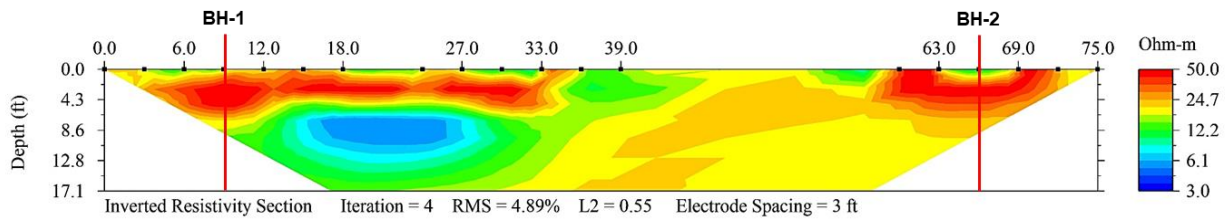


Figure 3-10 Result of ERI.

3.4 Assessment of Site Investigation Results

Results from site investigation revealed that the failed slope section was constructed over clay of low plasticity with liquid limit and plasticity indices ranging from 30 to 48% and 20 to 22%, respectively. Such soil is problematic due to its tendency to undergo swelling and shrinkage with variation in moisture content. Cyclic swelling and shrinkage of the expansive soil will cause a reduction in shear strength with time, eventually reaching a fully softened state where the value of cohesion is almost zero while the change in angle of friction is insignificant (Saleh and Wright,

1997). Highway embankment slopes constructed on expansive soil often show distresses such as desiccation cracks on their surface which later act as conduits for water infiltration. Site investigation results of the current study showed that the slope was constructed on expansive clayey soil with presence of desiccation cracks near the crest of the slope. Furthermore, the crest of the slope was identified to be the point of initiation of failure. Therefore, infiltration of rainwater was identified as the primary cause of failure in the current study.

3.5 Controlling Rainwater Intrusion in Slopes

The use of moisture control barriers can regulate the intrusion of moisture into soil through desiccation cracks. Moisture control barriers such as horizontal drains, capillary barrier systems and modified moisture barrier can be used to control moisture fluctuation in slope soil by enhancing drainage of infiltrated water and preventing further infiltration into underlying soil layers (Park and Fleming, 2006; Stormont, 1996; Rahardjo et al., 2012; Rahardjo et al., 2013; Sapkota et al., 2019).

The modified moisture barrier (MMB) is a layer of geocomposite which is an interconnected layer of two geotextiles and a geonet in the geotextile-geonet-geotextile configuration, underlain by a geomembrane layer (Ahmed, 2017). The function of the geocomposite layer is to enhance lateral drainage of infiltrated rainwater: the first geotextile layer functions as a transport layer, the geonet with relatively large open pores can function a capillary break, and the second layer of geotextile functions as a separator layer to prevent the underlying soil from intruding the pore spaces of the capillary barrier (Stormont et al., 2001; Zornberg, 2009). With this configuration, capillary break may take place and rainwater can percolate into the underlying soil layer (Stormont and Stockton, 2000; Bouazza et al., 2013). However, the impermeable geomembrane layer in the MMB will

prevent such percolation hence reduction moisture intrusion into the underlying soil. Detail mechanism of the MMB is demonstrated in Figure 3-11.

Considering the effectiveness of the modified moisture barrier in controlling moisture intrusion in previous studies (Ahmed, 2017 and Sapkota et al., 2019), the current study utilized the modified moisture barrier alone at the crest of a highway slope to prevent shallow slope failure.

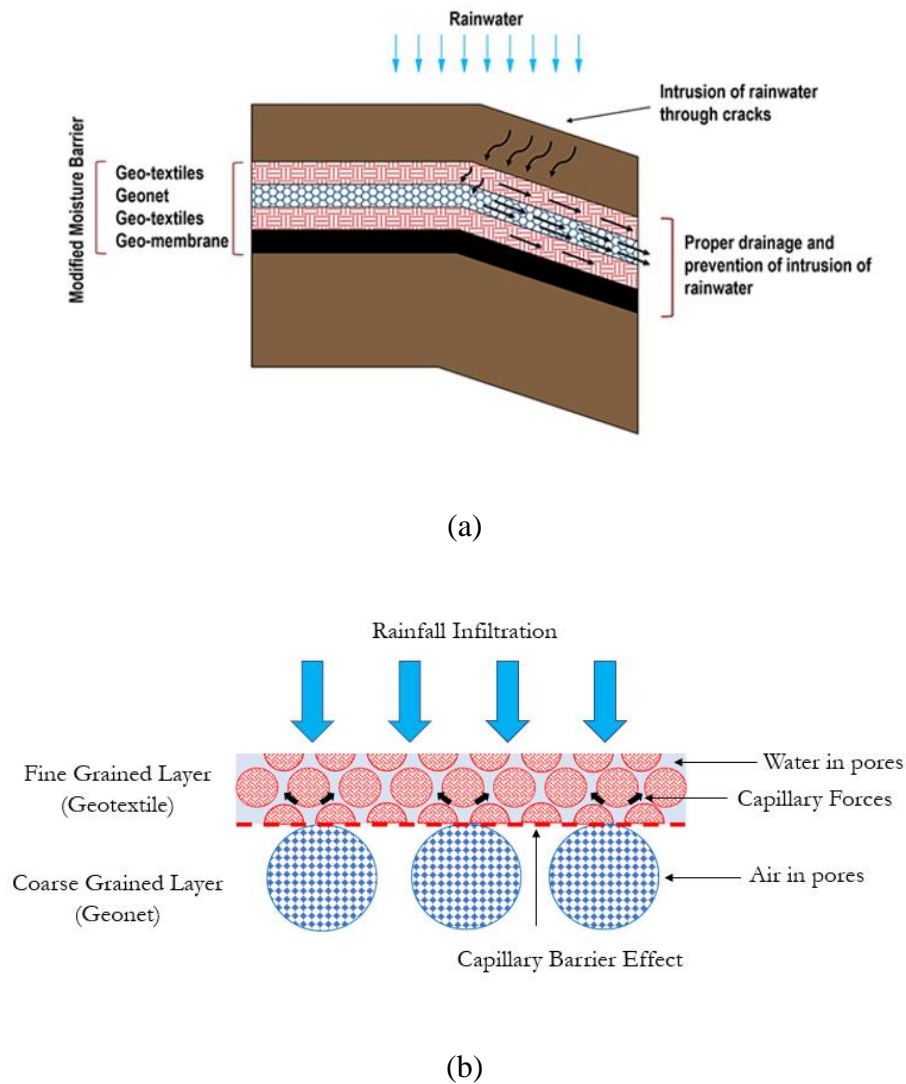


Figure 3-11 (a) Detailed mechanism of the modified moisture barrier (b) Capillary barrier effect in the MMB.

The slope stabilization plan was designed to evaluate the effectiveness of the modified moisture barrier to combat rainfall induced shallow slope failure and further compare its performance to that of recycled plastic pins (a mechanical stabilization method). To this end, a failed portion of the highway slope was stabilized using two sections: modified moisture barrier section (MMB Section) and recycled plastic pins section (RPP Section). A portion of the original slope adjacent to the test sections was selected to serve as the control section for this study. Each test section (MMB Section, RPP Section and Control Section) was 60 ft. in length and width along the slope as shown in Figure 3-12. The design of the test section and selection of materials is discussed in the following sections.

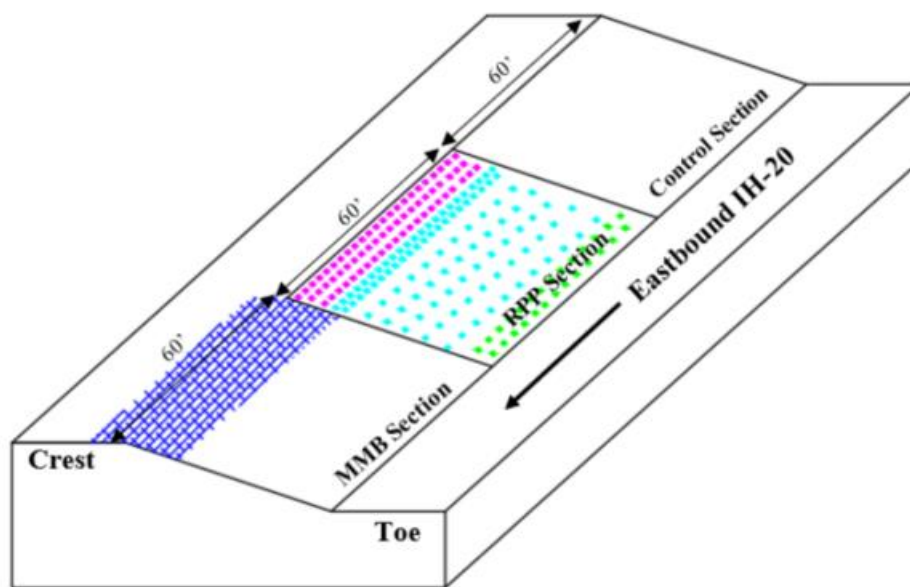


Figure 3-12 Schematic of test sections.

3.5.1 Design of Test Sections

3.5.1.1 MMB Section

The modified moisture barrier, observed to have effectively prevented moisture intrusion into underlying soil, was selected for this study (Ahmed et al., 2017; Sapkota et al., 2019; Pandey et al.,

2022). A 60 ft. section of the failed portion of the slope was stabilized using the modified moisture barrier. The modified moisture barrier used in this study was 60 ft. in length and 14 ft. in width. Of the 14ft. width of the MMB, 4ft. was designed to be towards the crest of the slope while the remaining 10 ft. was designed to be along the slope as shown in Figure 3-14. It consisted of a 40 mil Linear Low-Density Polyethylene (LLDPE) impermeable geomembrane and an 8 oz. High Density Polyethylene (HDPE) geocomposite as shown in Figure 3-13. The selection criteria of the materials are discussed below.



Figure 3-13 Materials used in the MMB (a) HDPE Geocomposite (<https://skaps.com/>) (b) LLDPE Geomembrane (<https://www.americover.com/>)

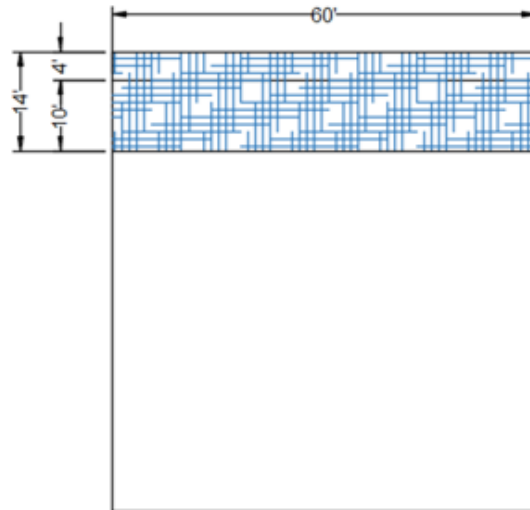


Figure 3-14 Layout of MMB section.

Selection of Geocomposite

A geocomposite is an interconnected layer of two geotextiles and a geonet. The commercially available SKAPS Transnet 300 Geocomposite was selected for this study. The SKAPS Geonet is made from HDPE resin with non-woven polypropylene geotextile fabric heat bonded on both sides of the geonet. The thermally bonded geotextile filter/separator on the geonet helps to avoid a potentially weak interface layer (Koerner, 2012). The size of the geocomposite was 60 feet in length and 14 feet in width. The primary purpose of the geocomposite was to provide adequate drainage and thus flow properties were considered during the selection process. The properties of the selected geocomposite are presented in Table 3-6.

Table 3-6 Properties of geocomposite* .

Component	Property	Value	Units	Test Method
Geotextile	AOS	0.007	in	ASTM D4751
	Permittivity	1.26	sec ⁻¹	ASTM D4491
	Permeability	0.12	in/sec	ASTM D4491

	Grab Tensile Strength	225	lb	ASTM D4632
Geonet	Transmissivity	29	gal/min/ft	ASTM D4716
	Tensile Strength	65	lb/in	ASTM D7179
Geocomposite	Transmissivity	3.38	gal/min/ft	ASTM D4716

*Provided by the manufacturer.

Selection of Geomembrane

The commercially available LLDPE smooth geomembrane of 40 mil thickness manufactured by GSE Environmental was selected for this study. LLDPE geomembranes have great flexibility, high tensile break elongation and high puncture resistance compared to other commercially available geomembranes (Stark, 2008; Divya et al., 2012). It is impermeable and its primary purpose in this study was to prevent the intrusion of rainwater into the underlying soil. The selected geomembrane was similar to that used in a landfill bottom liner system. The geomembrane was 60 feet in length and 14 feet in width. The properties of the geomembrane are summarized in Table 3-7.

Table 3-7 Properties of geomembrane.

Component	Property	Value	Units	Test Method
Geonet	Tensile Strength	1.53	lb/in	ASTM D6693
	Puncture Resistance	56	lb	ASTM D4833

*Provided by the manufacturer.

3.5.1.2 RPP Section

The remaining 60 ft. section of the failed slope was stabilized using RPPs. The layout consisted of a staggered pattern with 3 ft. c/c spacing near the crest, 5 ft. c/c spacing at the middle and 4 ft. c/c spacing near the toe of the slope as shown in Figure 3-15. Khan (2014) reported that the crest of the slope is critical due to the potential maximum lateral movement, therefore closest spacing of

RPP was provided at the crest. Several iterations of slope stability analysis were carried out utilizing different RPP layout using the Finite Element Program PLAXIS 2D and the layout that generated a factor of safety greater than 1.5 was selected for this study. Results of numerical analysis are presented in Appendix B.

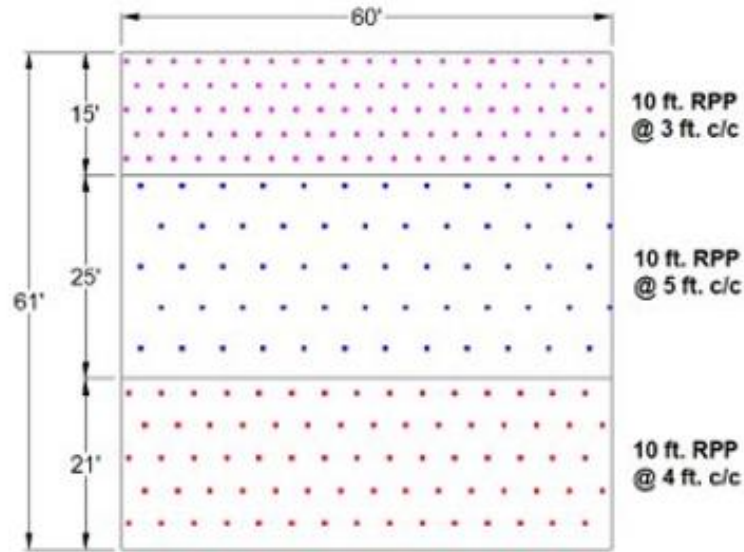


Figure 3-15 Layout of RPP section.

Selection of RPP

Commercially available 10 feet long fiber reinforced recycled plastic pins with 4 in square cross section were selected for this this study. RPPs are available in different lengths, sizes (cross sectional area) and shapes (rectangular, square, or circular). RPPs are manufactured from a combination of polymers and additives: HDPE (55-70%), low density polyethylene, LDPE (5-10%), polystyrene, PS (2-10%) and other additives like sawdust and fly ash (0-5%) (McLaren, 1995). Fiber reinforced RPPs have improved elastic modulus and creep resistant behavior (Hossain et al., 2017). The properties of the RPP used in the current study are summarized in Table 3-8.

Table 3-8 Properties of RPP (Khan, 2014).

Property	Value	Unit	Test Method
Length	10	feet	-
Width	4	inch	-
Height	4	inch	-
Flexural Strength	3.7 to 4.7	ksi	ASTM D790
Elastic Modulus	190 to 200	ksi	ASTM D790

3.5.1.3 Control Section

A 60 ft. section of the original slope was selected next to the RPP section to serve as the control section for this study.

CHAPTER 4 FIELD INSTALLATION AND INSTRUMENTATION

4.1 Introduction

This chapter presents the field installation and instrumentations processes. Field installation was based on the slope stabilization plan using the Modified Moisture Barrier (MMB) and Recycled Plastic Pins (RPPs). The MMB section of the slope was stabilized by using a modified moisture barrier to prevent rainfall intrusion into the slope soil and hence maintain the factor of safety. On the other hand, the RPP section of the slope was reinforced with recycled plastic pins to provide additional resistance to the soil against movement, hence maintaining the factor of safety of the slope. The test sections were instrumented with integrated temperature and moisture sensors, soil water potential sensors and vertical inclinometer casings to evaluate the performance of the proposed method.

4.2 Field Installation

Field installation program included the installation of the MMB in the MMB Section and the RPPs in the RPP section, respectively and was implemented based on the slope stabilization scheme discussed in Chapter 3. The installation procedures are described in the following sections.

4.2.1 Installation of Modified Moisture Barrier

A trench of 60 ft. length, 14 ft. width and 2 ft. depth, was excavated at the crest of the slope. Of the 14 ft. width of the trench, 4 ft. was towards the crest and the remaining 10 ft. was along the slope. After the excavation, the trench was swept clear of large debris, and compacted properly to make sure no rocks or gravel could puncture the geomembrane and a thin layer of sand was poured in the trench before placing the geomembrane. The trench was then laid with the geomembrane and the geocomposite was then placed on top of the geomembrane layer. Finally, the trench was

backfilled with the excavated soil. The field installation procedure for the MMB is depicted in Figure 4-1.



(a)



(b)



(c)



(d)



(e)

Figure 4-1 Modified Moisture Barrier Installation Process (a) Excavation of trench at crest of the slope (b) Cleaning of trench (c) Placement of geomembrane (d) Placement of geocomposite (e) Backfilling of trench with excavated soil.

4.2.2 Installation of Recycled Plastic Pins

According to previous studies, a crawler mounted drilling rig was the most suitable and economical equipment to drive the RPPs into the slope. Khan (2014) utilized a crawler type drilling rig with a mast mounted vibratory hammer (Klemm 802 drill rig and KD 1011 percussion head drifter) to install the RPPs on the slope at US 287. The use of crawler-type rigs has performed well during the installation process as no external anchorage is required to maintain the stability of the equipment. Tamrakar (2015) reported that a crawler mounted rig with pseudo vibratory hammer (Casagrande M9-1) was not suitable due to the steepness of the slope at the crest. Further installation was carried out with an excavator equipped with a hydraulic breaker (Deer 200D with FRD, F22 Hydraulic Hammer). Therefore, a similar excavator (Komatsu PC200 LC), equipped with a hydraulic hammer (NPK GH-15), was utilized for the installation of the RPPs in the current study.

It took two days (August 29, 2019 – August 31, 2019) to install a total of 205 RPPs as per the layout shown in Figure 3-15. At first the slope was cleared of vegetation and flags were used to mark the locations where the RPPs would be installed, based on the slope stabilization layout. A steel pin of about 8 ft. length was used to make a hole and each location. The RPPs were placed in that hole and then driven into the slope. Due to the existence of relatively stiff soil at shallow depths, it was not possible to drive the entire 10 feet length of the RPPs into the ground and the driving depth of RPP was limited to 7 to 8 feet at the middle section of the slope and 5 feet towards the toe of the slope. Furthermore, a few lines of reinforcement towards the toe of the slope were skipped due to breakage of RPP during driving as a result of stiff soil at shallow depths. The as built layout of RPP installation is shown in Figure 4-3.



(a)



(b)



(c)

Figure 4-2 Recycled Plastic Pins Installation Process (a) Placement of the RPPs in the marked locations (b) Driving of the RPPs into the ground (c) Backfilling of the slope.

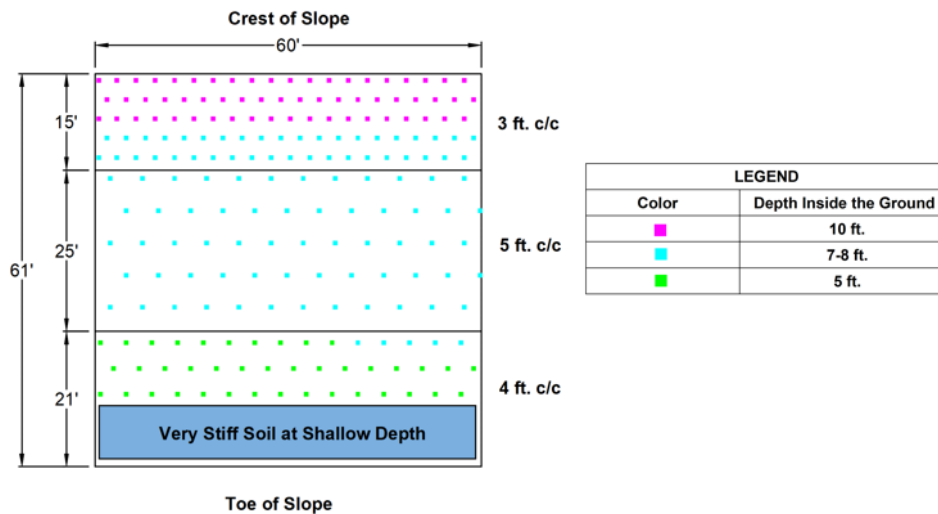


Figure 4-3 As built layout of RPP installation.

The driving time of the RPPs was measured during the installation process. The installation time for each RPP is the summation of the time required to drive the RPP into the ground and the time needed to maneuver the equipment to the next location (Khan, 2014). The driving times of the RPP at different locations along the slope are summarized in Table 4-1. The average driving rate

ranged from 0.94-2.5 ft./min. High driving time signifies stiffer soil while lower driving time indicates relatively soft soil.

Table 4-1 Driving time for RPP.

Line	Average Driving Time Per Pin (min)	Length of RPP (ft)
1	0.70	10
2	0.43	10
3	0.98	10
4	2.26	7-8
8	2.23	7-8
10	2.51	7-8

4.3 Field Instrumentation

The test slope sections were instrumented with integrated moisture temperature sensors, suction sensors, and inclinometer casings as shown in Figure 4-4.

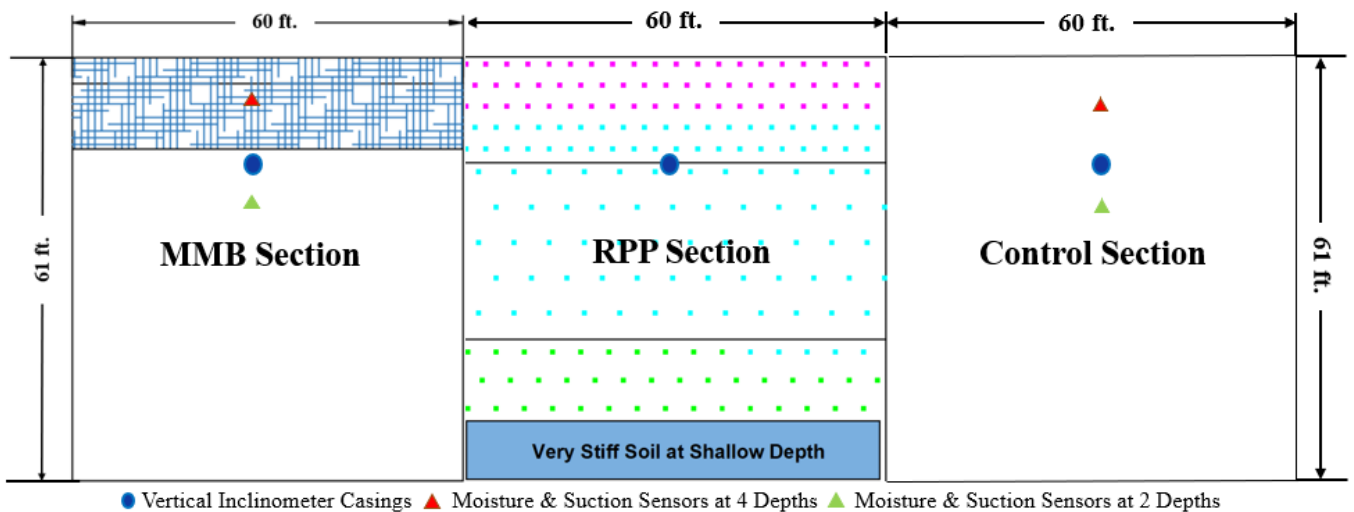


Figure 4-4 Instrumentation Layout.

4.3.1 Monitoring Instruments

Commercially available integrated moisture -temperature sensors, Teros 12 from Meter Group and soil water potential sensors, Teros 21 from Meter Group were installed to measure the volumetric water content, temperature, and matric suction of the soil respectively. The sensors were then connected to a data logger, ZL6 from Meter Group to record, collect and store data. The selected datalogger collects data continuously and can store up to 80000 scans. The sensors and datalogger are shown in Figure 4-5.

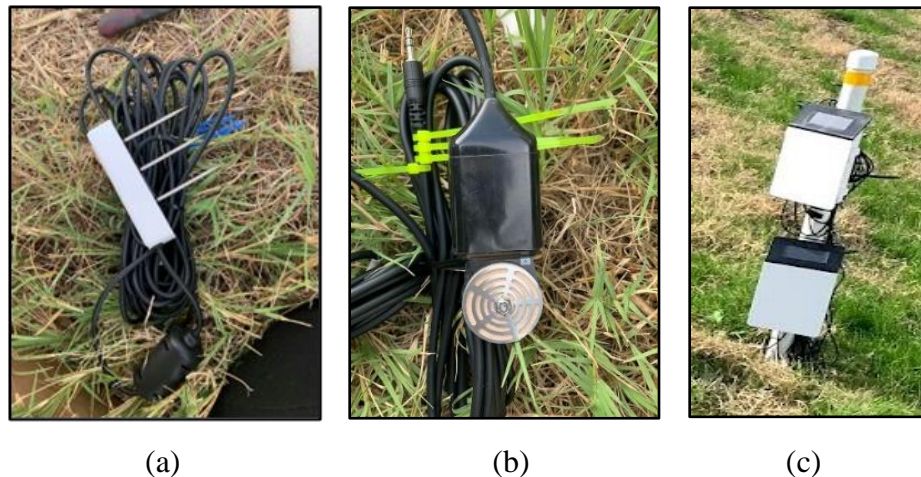


Figure 4-5 (a) Integrated Moisture-Temperature Sensor (b) Soil Water Potential Sensor (c) Datalogger.

In order to measure the lateral deformation of the slope a Digitilt Inclinometer Probe from DGSI was used as seen in Figure 4-6. The inclinometer is used to measure the tilting angle of the device from a reference vertical line. Additionally, vertical settlement of the slope is measured by conducting a topographic survey using the total station.



(a)



(b)

Figure 4-6 (a) Vertical Slope Indicator with Datamate (b) Total Station.

4.3.2 Calibration of Sensors

Integrated moisture and temperature sensors were calibrated prior to field instrumentation to ensure proper performance. In order to perform calibration of the integrated moisture temperature sensors, moisture content of several samples was manually determined and compared with sensor measurements (Cobos and Chambers, 2010). Recorded values showed good agreement with manually measured moisture content as shown in Figure 4-7.

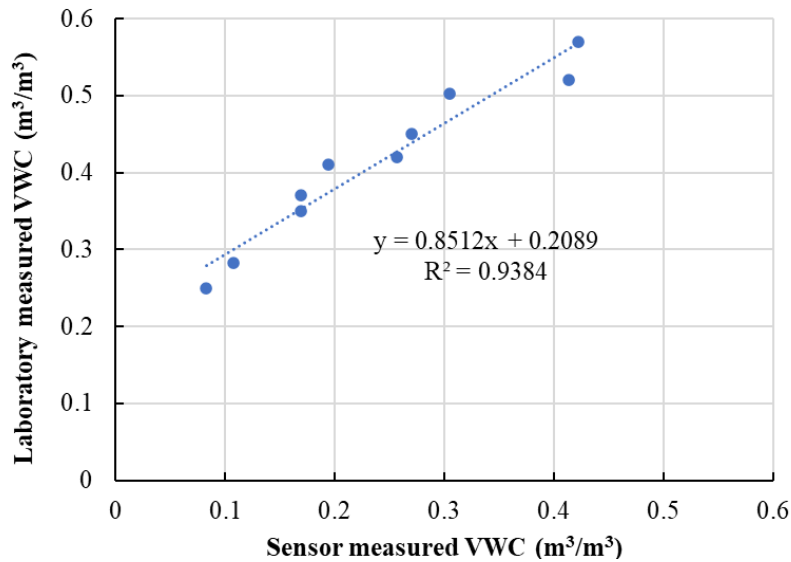


Figure 4-7 Calibration of Sensors.

4.3.3 Installation of Sensors

Sixteen integrated moisture-temperature sensors and soil water potential sensors were installed at the crest of the slope. Two 10 ft. deep boreholes were drilled at the MMB section and the control section to install the sensors at varying depths (at depths of 3 ft., 5 ft., 7 ft., and 9 ft.). The locations of the sensors at the MMB Section are shown in Figure 4-8. It should be noted that at the MMB section, the borehole was drilled, and sensors were installed after a trench was excavation and prior to the installation of the MMB. A total of 8 integrated moisture-temperature sensors and 8 soil water potential sensors were installed at the crest of the slope. After the installation of each sensor, the soil was carefully compacted to avoid damage to the sensor. The process of sensor installation is depicted in Figure 4-9. The sensors were then connected to a data logger to the ZL6 which was set to record hourly readings. Furthermore, two boreholes each of 2 feet depth were drilled using a hand auger after a period of 23 months at the middle section of the slope at the MMB section and control section. A total of four sensors, two integrated moisture and temperature sensors and two soil water potential sensors, were installed at depths of 2 feet and 1 feet below the ground surface. The sensors were then collected to a datalogger to collect hourly readings. The layout of sensor installation is shown in Figure 4-4.

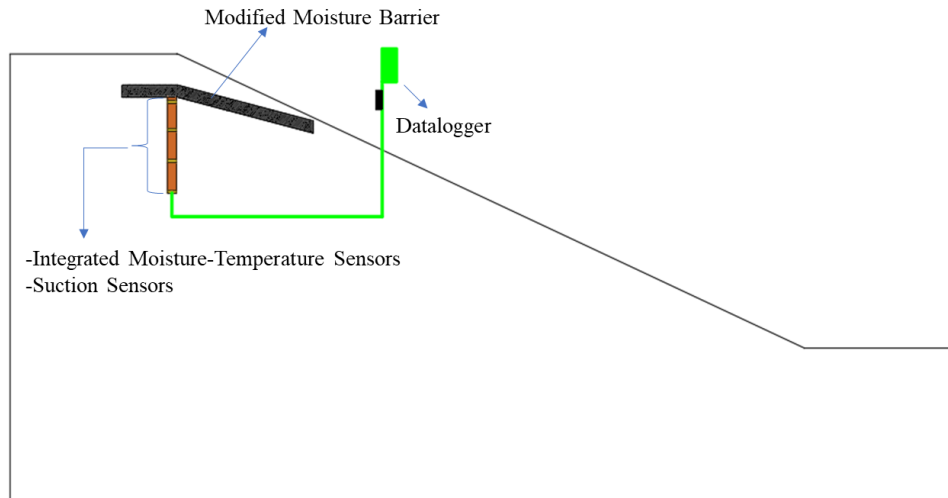


Figure 4-8 Location of sensors and data logger for MMB Section.



(a)



(b)



(c)

Figure 4-9 Installation of Sensors (a) Installation of the sensor at the desired depth (b) Moisture sensor inserted into the soil (c) Compaction of backfilled soil into the borehole.

4.3.4 Installation of Inclinometer Casings

An inclinometer is a device used to measure the incremental lateral displacement by passing a probe into a casing installed at a point of interest (Dunnicliff and Green, 1993). Three vertical inclinometer casings, each of 30 ft. depth, were installed at each of the test sections to monitor the lateral deformation. The locations of the inclinometer casings at the crest of the slope are shown in Figure 4-4.

First, a 30 ft. deep borehole was drilled with a hollow stem auger of 4 in. diameter. Commercially available inclinometer casings are 10 ft. in length, therefore three casings each 10 ft. long (total of 30 ft.), were connected and taped at the joints. The bottom of the casing was sealed using a bottom cap and the 30 ft. length casing was then placed into the previously drilled borehole. The grooves of the casing were adjusted to be parallel to the slope and the area around the casing was filled with dry bentonite chips. The process of inclinometer installation is depicted in Figure 4-10.



(a)

(b)



(c)

Figure 4-10 Installation of Inclinator Casing (a) Drilling of borehole (b) Placement of inclinometer casing into borehole (c) Complete inserted casing.

4.3.5 Data Collection and Field Monitoring

Soil moisture content, temperature and matric potential data were collected from the datalogger at site on a monthly basis. The lateral deformation profile of the slope was obtained by passing the probe through the installed vertical inclinometer casings. Monthly topographic surveys were also

conducted to measure the vertical settlement of the slope. The monitoring schedule is presented in Table 4-2.

Table 4-2 Monitoring Schedule.

Instrumentation	Monitoring Frequency
Integrated Moisture-Temperature Sensor	Continuous
Suction Sensor	Continuous
Inclinometer	Monthly
Topographic Survey	Monthly

4.4 Field Testing

4.4.1 Hydraulic Conductivity

Field testing program was undertaken to measure the field hydraulic conductivity of the soil by performing in situ permeability tests using the Guelph Permeameter. Guelph Permeameter is an in hole constant head permeameter which employs the Mariotte Principle. A constant depth (head) of water is maintained in a cylindrical well hole by controlling the position of the bottom of the air tube located at the center of the permeameter and discharged into unsaturated soil. This method involves measuring the steady state of water discharge. An example of the field setup for the Guelph permeameter is shown in Figure 4-11.

Tests were carried out in all sections at the crest and middle sections of the slope, as shown in Figure 4-12. The testing procedure for the MMB Section is shown in Figure 4-13. At first, a test borehole of 2 ft. depth was drilled using a hand auger of 2 in. diameter and the borehole was cleared of all debris. The components of the Guelph Permeameter are assembled and the permeameter was placed in the test borehole. The instrument's reservoir is filled with about 2.5 liters of water and

an airtight plug was used to seal the water inlet hole, which was then secured with a clamp tied to a nylon tube. Water was then allowed to flow from the well head scale at a head of 10 cm. Hydraulic conductivity of the soil is measured by taking readings from the inner reservoir of the permeameter and using a set of equations developed by Zhang et al. (1998).



Figure 4-11 Instrumental Setup of Guelph Permeameter.

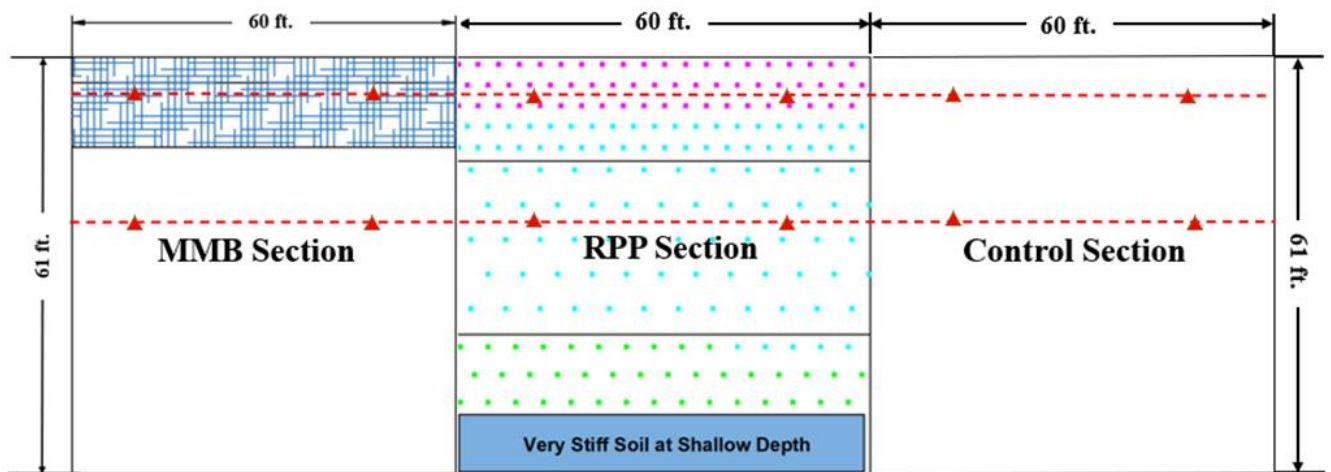


Figure 4-12 Field Testing Location.

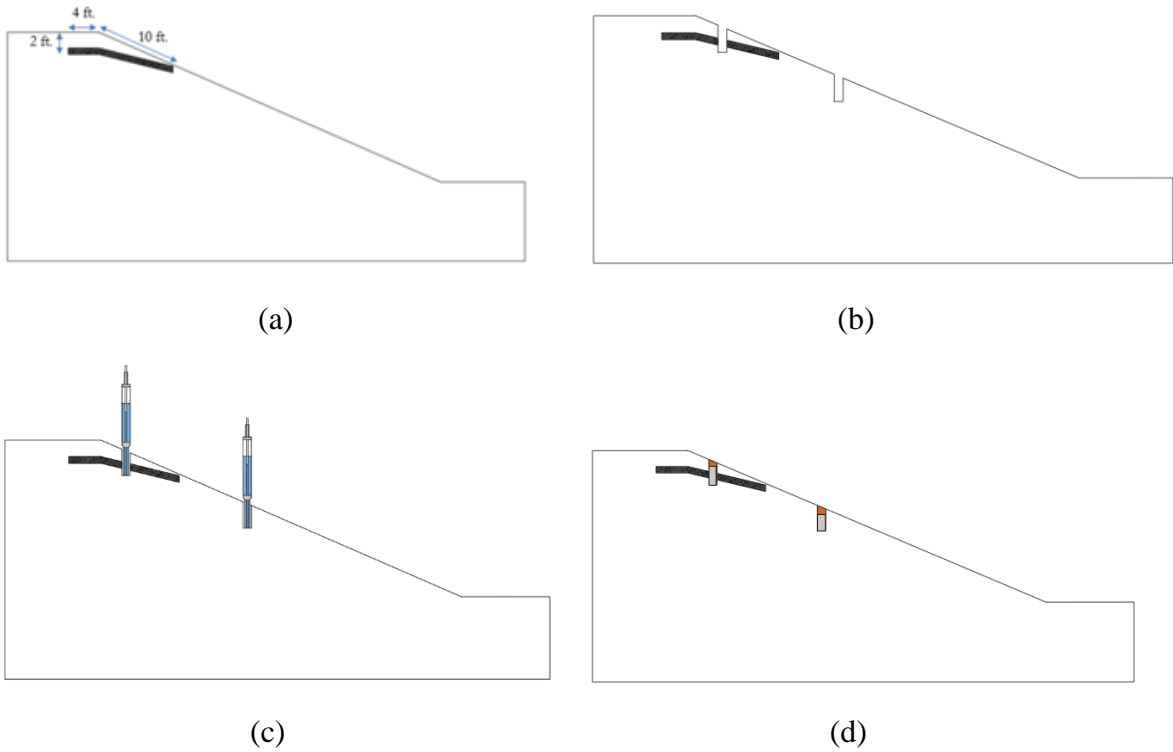


Figure 4-13 Hydraulic Conductivity Testing Procedure for (a) MMB Section (b) 2 ft. Deep Test Boreholes (c) Test Performed using Guelph Permeameter (d) Backfilling of Test Boreholes.

CHAPTER 5 FIELD RESULTS AND DISCUSSION

5.1 Introduction

This chapter presents the field performance monitoring results and evaluates the effect of the modified moisture barrier on slope stability. Performance monitoring was carried out using integrated temperature moisture sensors, soil water potential sensors, slope inclinometers, topographic surveys using total station and hydraulic conductivity testing using the Guelph permeameter. Monitoring data for a period of 3 years (September 2019 to August 2022) is presented in this chapter. The effectiveness of the proposed approach has been discussed by comparing the performance of the MMB Section with RPP and Control Sections. Furthermore, the results are compared to findings from existing literature.

5.2 Variation of Volumetric Moisture Content and Matric Suction

Hourly data recorded by integrated temperature moisture sensors (Teros 12) and soil water potential sensors (Teros 21) were averaged to obtain daily volumetric water content and matric suction.

5.2.1 Variation of Volumetric Moisture Content

A total of twelve (12) integrated temperature moisture sensors and soil water potential sensors were installed at the MMB Section and Control Section as shown in the layout in Figure 4-4. Eight (8) sensors were installed at the crest of the slope, four at each test section in September 2019 at depths of 3 ft., 5 ft., 7 ft., and 9 ft while four (4) sections were installed at the middle of the slope in March 2021 at depths of 1 ft. and 2 ft.

5.2.1.1 MMB Section

Variation of daily average soil volumetric moisture content with time and rainfall events at the MMB section for a monitoring period of 36 months (September 2019 to August 2022) is presented

in Figure 5-1. During this monitoring period a cumulative rainfall of 99.4 in was recorded by the nearest weather station. The frequency of rainfall was higher during the wet period and lower during the summer. However, insignificant variation in volumetric water content was observed in the MMB sections despite rainfall events. At all depths, moisture content showed no dependency with precipitation events. Although a rise in water content was recorded at all depths April 2020, the increase in moisture content was first recorded by the deepest sensor at 7 ft. followed by that at 5 ft. and lastly an increase was observed at depth of 3 ft. This trend implied an upward movement of water as opposed to an increase in moisture content due to rainfall infiltration. Furthermore, following this rise, volumetric moisture content in the MMB section has remained almost constant at 19 %, 24 %, and 28 % at depths of 3 ft., 5 ft., and 7 ft. respectively throughout the monitoring period. The insignificant fluctuation of moisture content in the MMB section can be attributed to the effectiveness of the modified moisture barrier in preventing rainfall infiltration into the underlying soil.

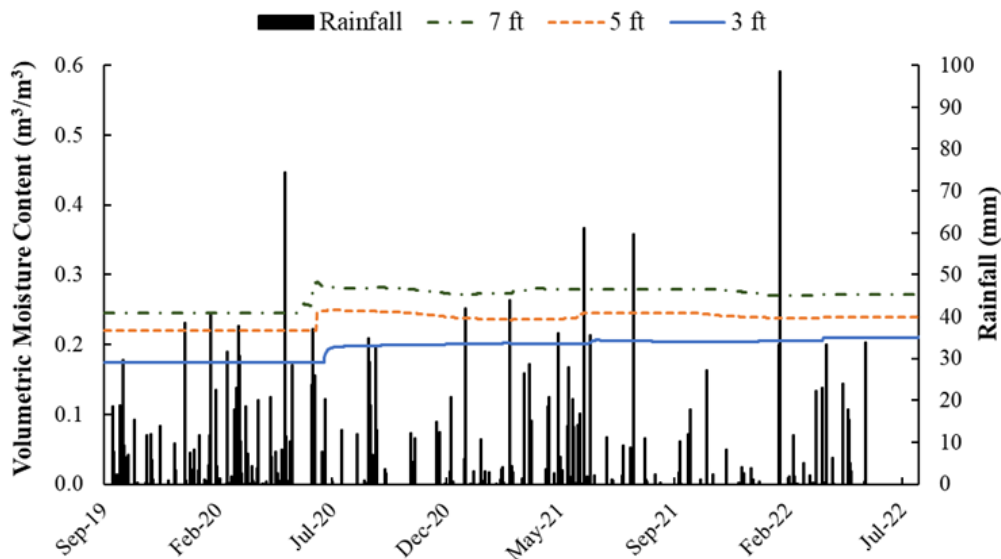
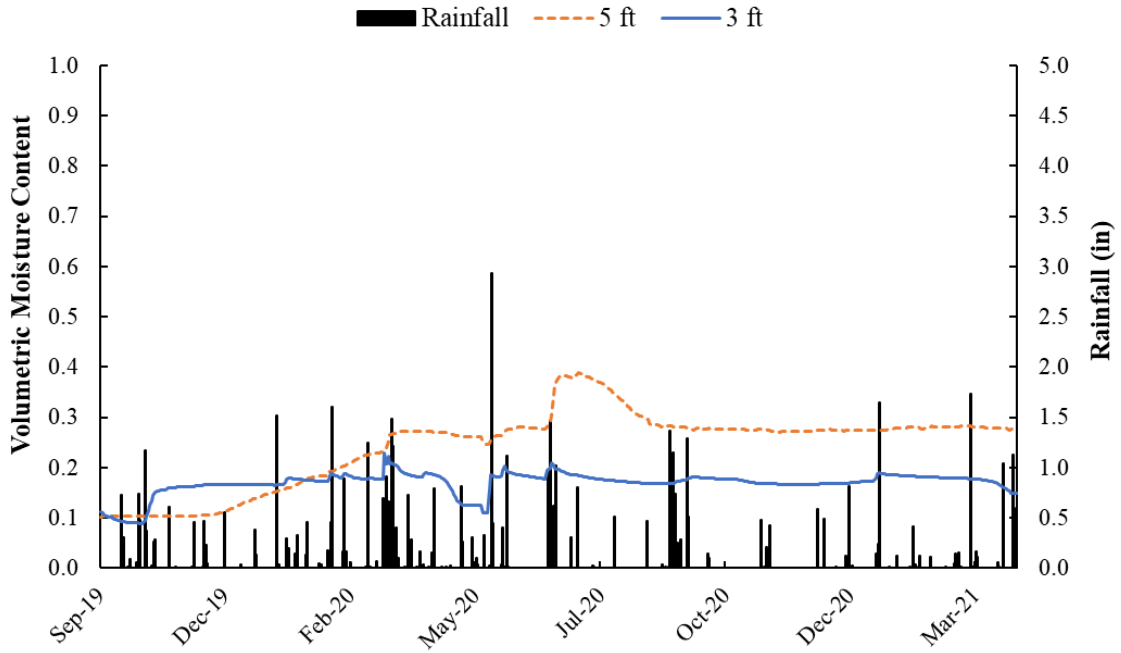


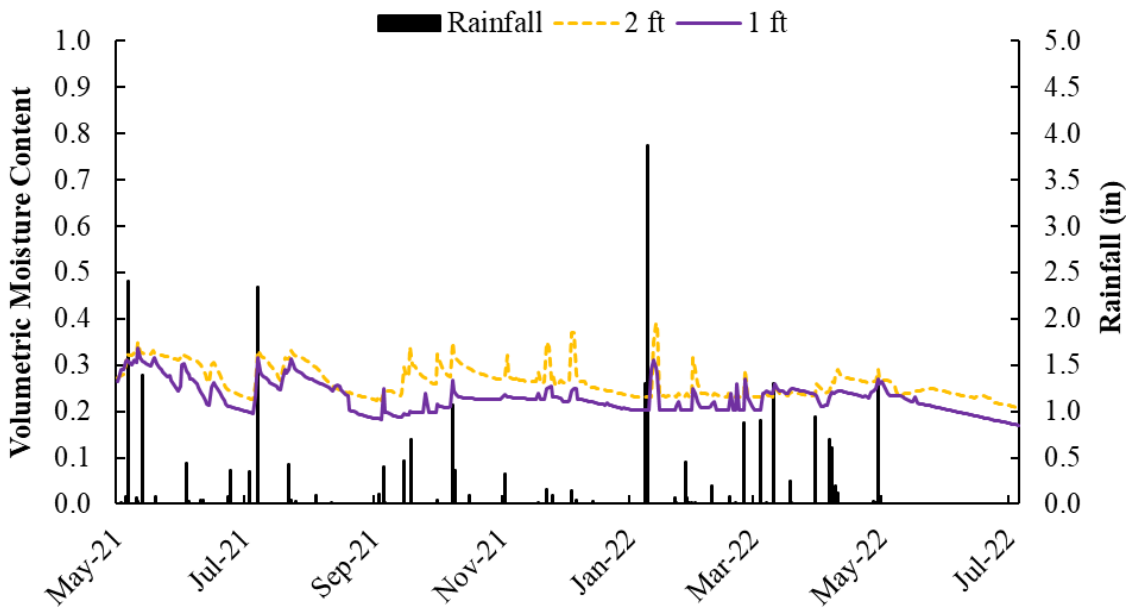
Figure 5-1 Variation of volumetric moisture content with time and rainfall events at the MMB Section.

5.2.1.2 Control Section

Variation of volumetric water content with time and rainfall events at the control section at the crest of the slope and middle section of the slope is presented in Figure 5-2 (a) and (b), respectively. The average moisture content at the crest of the slope was 16 % and 24 % at depths of 3 ft and 5 ft respectively. Sensors installed showed a direct relationship between soil moisture content and rainfall. Several peaks and drops in the value of volumetric moisture content were observed to occur due to precipitation events. For instance, on 18th May 2020, rainfall of 2.93 in was recorded and consequently water content increased from 10% to 19% and 25% to 28% at depths of 3 ft and 5 ft respectively. Contrastingly, during the period of June to August 2020 with relatively less rainfall moisture content was observed to decrease from 20 % to 16 % at depth of 3 ft. The fluctuation was more pronounced at shallower sensors where the peaks were observed right after rainfall events, as shown in Figure 5-2 (b). On the other hand, at deeper depths, the change in moisture content was more gradual and influenced by long term events with no prominent peaks and drops in the graph with respect to rainfall events. The increase in moisture content recorded by the sensors installed in the control section can be attributed to the infiltration of rainwater into the slope.



(a)



(b)

Figure 5-2 Variation of volumetric moisture content with time and rainfall events at the control section (a) Crest of the slope (b) Middle of the slope.

5.2.1.3 Comparison of Test Sections

The variation of volumetric moisture content, at a depth of 3 feet below the ground surface at the crest of the slope, with time and rainfall events was compared for the control and MMB sections and the result is presented in Figure 5-3. Several peaks and drops depicting sudden increase and decrease of moisture content were observed in the control section while the volumetric moisture content of the MMB section remained almost constant, with respect to precipitation events. The observed peaks and drops of the control section moisture content can be attributed to infiltration of rainwater into the slope soil. Additionally, the moisture content of the barrier section was lower than that of the control section. These observations indicate that the proposed approach can effectively control fluctuation of soil moisture content caused by climatic variation.

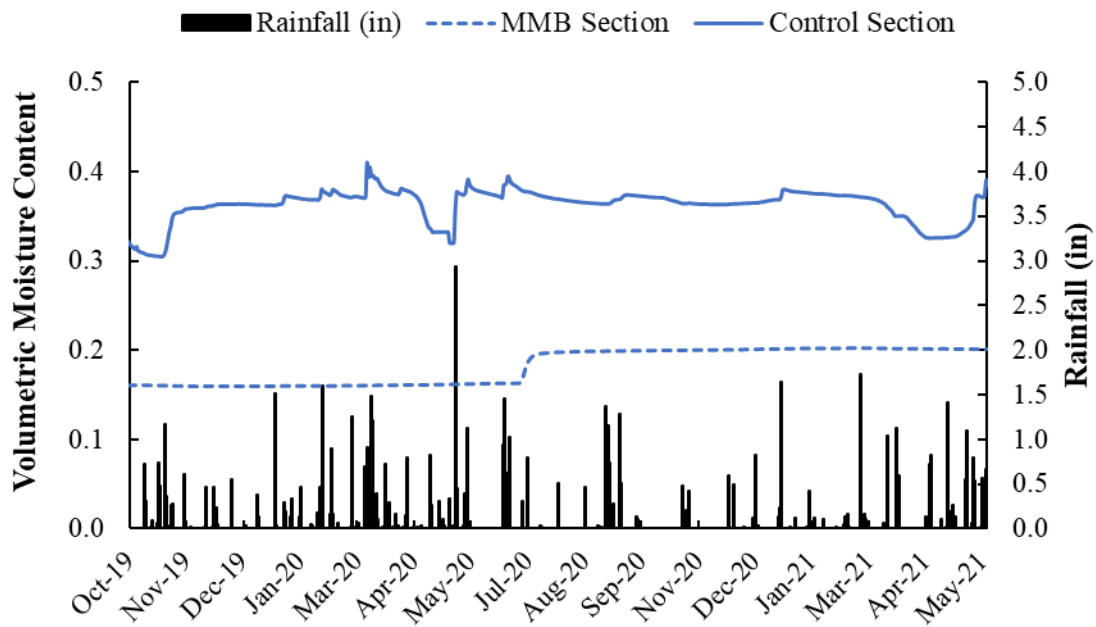


Figure 5-3 Comparison of moisture content variation at 3 ft depth at the crest of the slope.

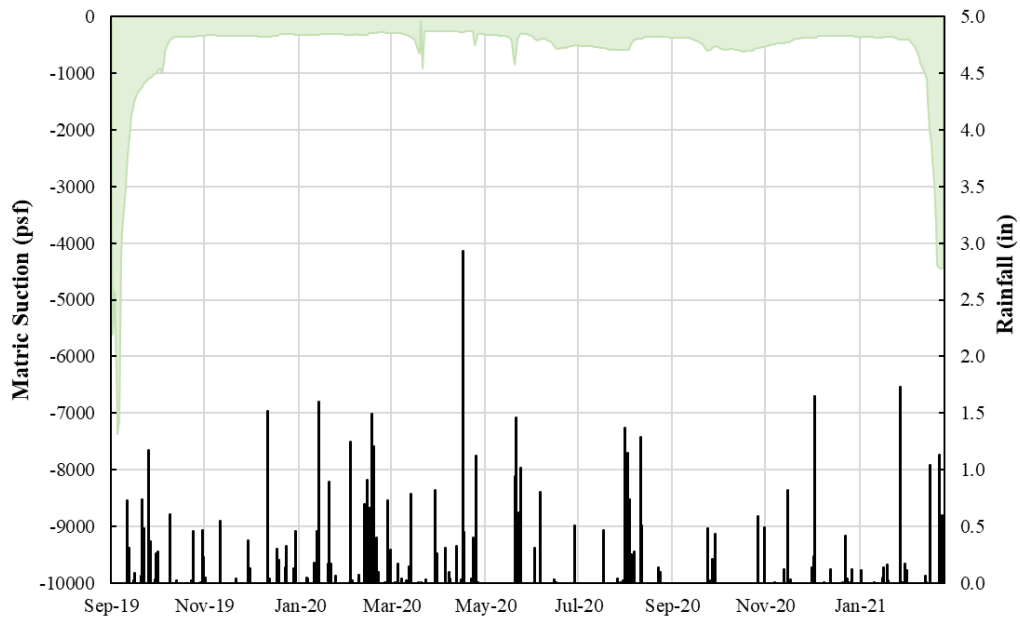
5.2.1.4 Comparison with previous literature

The study conducted by Sapkota (2019) implemented the modified moisture barrier in conjunction with recycled plastic pins to stabilize a shallow slope failure as discussed in Section 2.8.7. The variation of moisture content with time and rainfall for the pin plus barrier section and controls section as obtained in the study are presented in Figure 2-39. Sapkota (2019) reported that the fluctuation in moisture content of the control section ranged from 4 to 32.8 % while that in the pin plus barrier section remained less than 4 % during the monitoring period. Similar results were observed in the current study where the control section experienced a fluctuation of moisture content from 14.73 to 32.68 % while that of the MMB section remained almost constant.

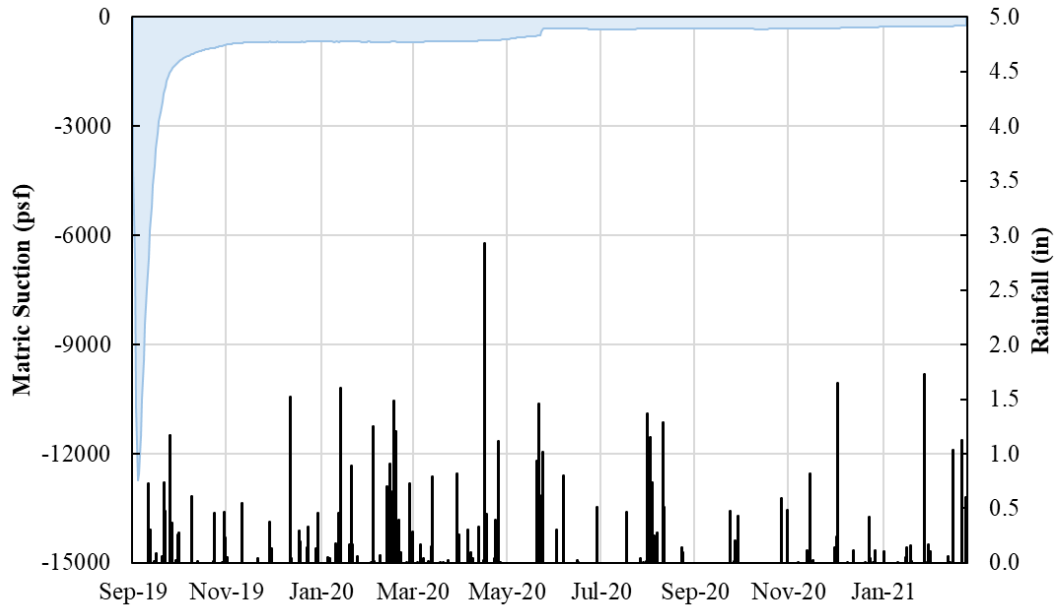
5.2.2 Variation of Matric Suction

Variation of matric suction with time and rainfall events were computed for the MMB section and control section and the results for the sensor at a depth of 3 feet is shown in Figure 5-4. The variation of matric suction of the control section of the slope with time and rainfall events can be observed in Figure 5-4 (a). Field monitoring of matric suction of the natural slope showed that soil suction exists even under long term conditions of rainfall infiltration. Initially, very high matric suction is observed which can be attributed to the dry period during which the sensor was installed and to the relative disturbance of the surrounding soil post installation of the sensor. With rainfall infiltration matric suction gradually decreased and was maintained at about -300 psf during periods the relatively wet periods and it increased to a maximum -900 psf during the relatively drier periods. The minimum value of matric suction corresponded to 18 % volumetric moisture content while maximum suction corresponds to 8 % volumetric moisture content in the field. The fluctuation of the matric suction further confirms that the natural slope is subjected to wet and dry climatic conditions.

On the contrary, as can be seen in Figure 5-4 (b), the MMB section maintains a minimum suction value of -600 psf throughout the monitoring period indicating that the soil underneath the barrier was not subjected to rainfall infiltration or evaporation. Higher suction value observed initially can be attributed to the adjustment period immediately after installation as the soil surrounding the sensor was relatively disturbed. Therefore, the modified moisture barrier can effectively maintain constant soil matric suction in the underneath soil hence preserving the soil shear strength by reducing infiltration of rainwater.



(a)



(b)

Figure 5-4 Variation of matric suction with time and rainfall events (a) Control Section (b) MMB Section.

5.2.2.1 Comparison with previous literature

Existing literature has reported variation of matric suction in the active zone of the soil mass due to seasonal wetting and drying (Rahardjo et al., 2005; Hossain, 2013). Increase in porewater pressure (reduction in matric suction) decreases soil effective stress thus reducing its shear strength. Infiltration and considerable change of porewater pressure of the near surface soils can initiate rainfall induced slope instability at the crest (Gerschovich et al., 2006; Zhang et al., 2011).

Even though moisture control systems have been widely used in pavement subgrades, very few studies have used them in stabilizing shallow slope failures. The study conducted by Rahardjo et al. (2012) and Rahardjo et al. (2013) used a capillary barrier system comprised of a layer of fine sand and granite chips/ recycled crushed concrete aggregate (RCA) to function as the fine grained

and coarse-grained layer, respectively to stabilize shallow slope failures as discussed in Sections 2.8.3 and 2.8.4, respectively. The variation of porewater pressure with rainfall for the sections with and without the CBS, are presented in Figure 2-29 and Figure 2-31. It is observed that as rainfall infiltrates the slope, the section with the CBS undergoes lower fluctuation of porewater pressure compared to the sections without the CBS. Similar results are obtained in the current study, where fluctuation in matric suction is reduced in the MMB section and is maintained almost constant at -600 psf.

5.2.3 Variation of Temperature

Variation of soil temperature is a function of incident solar radiation, rainfall, local vegetation cover, air temperature, humidity, type of soil and depth in the earth (Olness et al., 2001). Soil temperature of the test sections was monitored at depths of 3 ft., 5 ft., 7 ft., and 9 ft., as presented in Figure 5-5. The highest temperature recorded was about 84 °F in August 2020 while the lowest was about 46 °F in February 2021. Up to a depth of 7 ft., changes in temperature were more pronounced. With increase in depth, the amplitude of the annual cycle of temperature decreased and the phase of the annual cycle also shifted. These observations were found to be consistent with previous studies where temperature variation was monitored (Al-Hinti et al., 2017).

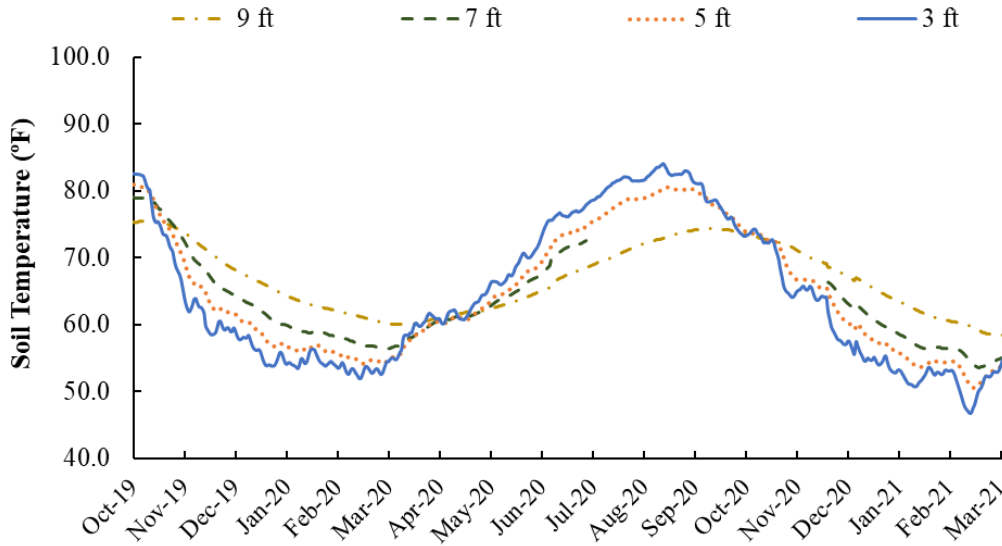


Figure 5-5 Variation of soil temperature with time.

5.3 Lateral Deformation of the Slope

The lateral deformation of the slope test sections was monitored using an inclinometer. Three inclinometer casings were installed up to a depth of 30 ft., perpendicular to the slope surface as shown in Figure 4-4. The lateral deformation of the slope was assessed by monitoring the spatial orientation of the inclinometer casings on a monthly basis. The lateral deformation observed with time for the control section, MMB section and RPP section are presented in the following section.

5.3.1 Control Section

Variation of lateral deformation of the control section with time and rainfall events is computed and the result is presented in Figure 5-6. Maximum lateral deformation of 0.48 inches occurred in August 2022 and it was observed near the ground surface. As depth from the ground surface increased, lateral deformation was observed to decrease. Furthermore, it is observed that the increase in lateral deformation was more sensitive to cycles of persistent rainfall events. For instance, following the wet period of May to June 2021, when 11.2 inches of cumulative rainfall

was recorded, lateral deformation of the control section almost doubled from 0.18 inches to approximately 0.36 inches at a depth of 2 feet below the ground surface. Furthermore, lateral deformation was lower during the relatively drier period compared to the wetter periods which depicts the cyclic swelling and shrinkage behavior of the slope induced by seasonal climatic conditions. During the rainy season, lateral movement of the slope gradually increased and decreased and eventually became stable during the comparatively drier season. For instance, reduction in the movement of the slope at a depth of 2 ft below the ground surface was observed in both November 2020 and November 2021 after the slope was subjected to a period of less rainfall events. Therefore, lateral movement of the slope is significantly influenced by rainfall events.

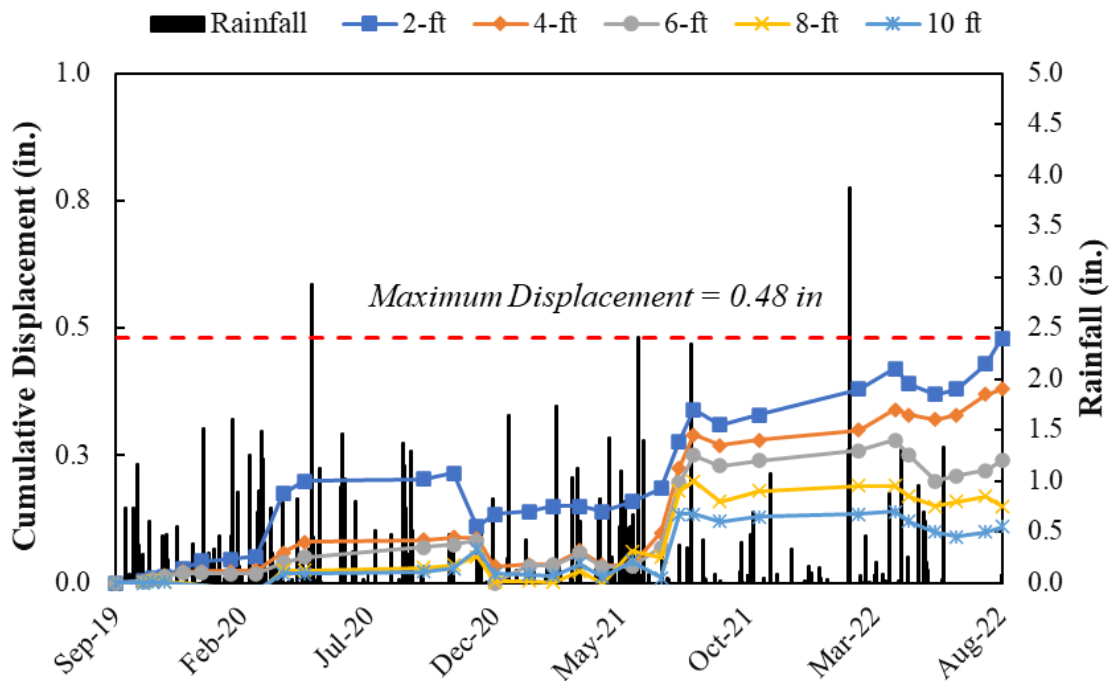


Figure 5-6 Lateral deformation with time and rainfall for control section.

5.3.2 MMB Section

Variation of lateral deformation of the MMB section with time and rainfall events is computed the result is presented in Figure 5-6. Maximum lateral deformation of 0.29 inches occurred in August 2022 and it was observed near the ground surface. As depth from the ground surface increased, lateral deformation was observed to decrease. Maximum lateral deformation experienced by the MMB section near the ground surface was approximately 66% less than that of the control section. This is due to the presence of the modified moisture barrier below the ground surface which prevented the infiltration of rainwater into the underlying soil consequently preventing the soil from undergoing swelling induced lateral displacement. However, the barrier was only placed at the crest of the slope which resulted in overall lateral deformation of the slope.

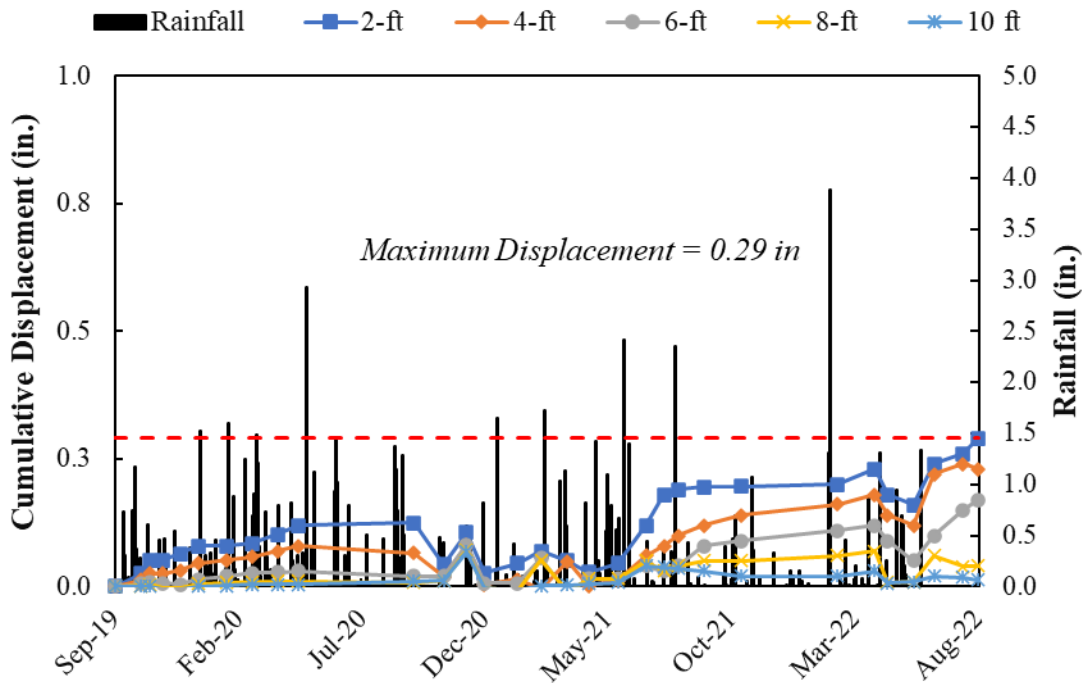


Figure 5-7 Lateral deformation with time and rainfall for MMB section.

5.3.3 RPP Section

Variation of lateral deformation of the RPP section with time and rainfall events is computed the result is presented in Figure 5-8. Maximum lateral deformation of 0.26 inches occurred in August 2022 and it was observed near the ground surface. As depth from the ground surface increased, lateral deformation was observed to decrease. The maximum lateral deformation experienced by the RPP section was the least out of the three test sections. This is because recycled plastic pins provided additional reinforcement to the slope to prevent movement from occurring.

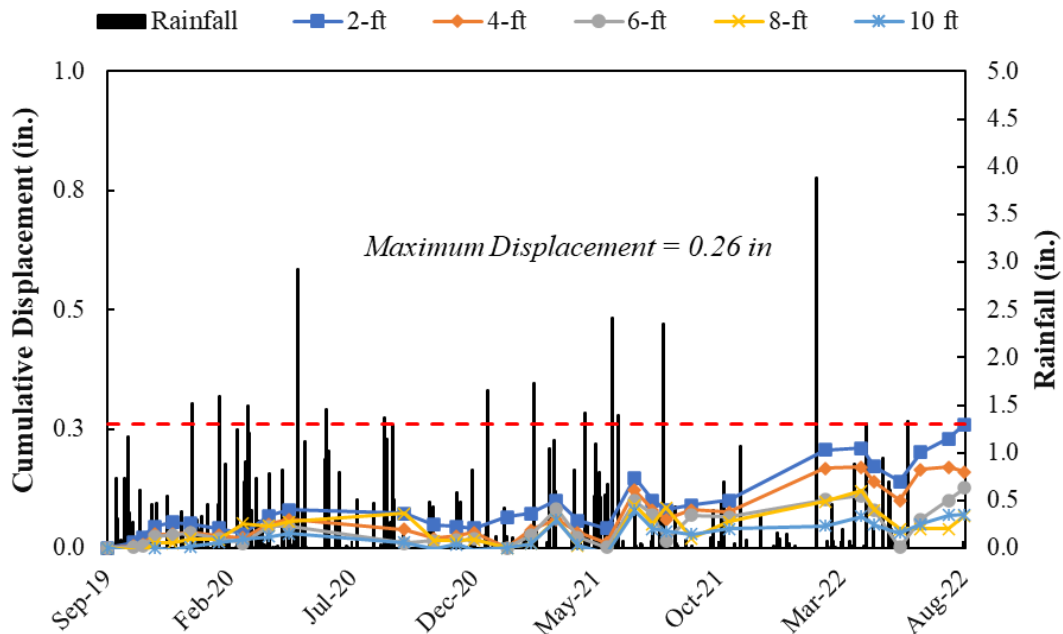
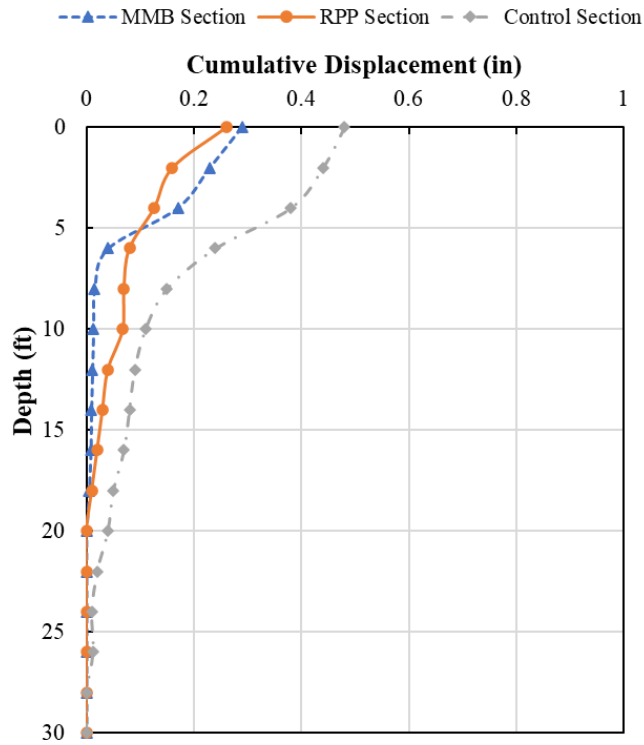


Figure 5-8 Lateral deformation with time and rainfall for RPP section.

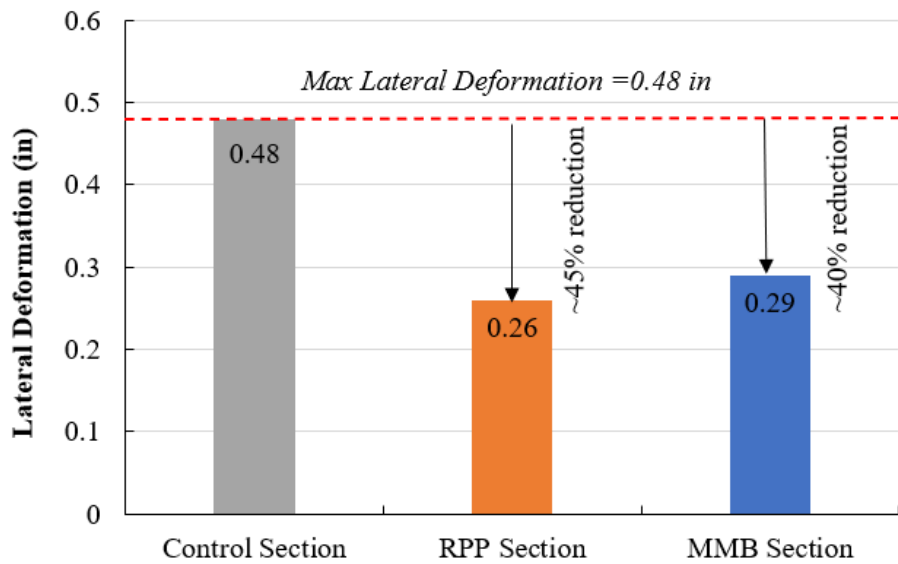
5.3.4 Comparison of Lateral Deformation of Test Sections

The maximum lateral deformation of the slope was observed in August 2022 near the ground surface. Therefore, the measurement of slope deformation from August 2022 is used for comparing movement of the three test sections. Lateral deformation of each test section has been computed along the entire depth of the inclinometer casing and the results are presented in Figure 5-9 (a).

Movement was observed in the control section up to a depth of about 20 feet while that was limited to about 10 feet for the test sections. Of the three test sections the maximum lateral deformation of 0.48 inches is observed in the control section near the ground surface while the least was approximately 0.26 inches in the RPP section. Although the movement of the slope in the MMB section is higher than the RPP section in the top 5 feet, the movement decreases rapidly and ceases to almost zero at a depth about 15 feet below the ground surface. On the other hand, the RPP section experiences slight increase in movement between depths of 5 and 10 feet below the ground surface which may be attributed to the increase in the spacing of the RPP along the middle of the slope. Overall, the MMB section and control section experienced similar trend in movement along the depth of the inclinometer however, the maximum movement of the MMB section was approximately 40 % lower than the control section near the ground surface which was due to the prevention of rainwater infiltration caused by the barrier. In comparison, the maximum lateral displacement of the RPP section was approximately 45% lower than that of the control. Therefore, the performance of the MMB section was comparable to that of mechanically reinforced RPP section, in terms of slope lateral deformation.



(a)



(b)

Figure 5-9 Comparison of test sections (a) Depth wise lateral deformation (b) Maximum lateral deformation.

5.3.5 Comparison with previous literature

Sapkota et al. (2019) used the MMB in conjunction with RPP to stabilize shallow slope failures as described in section 2.8.7. The summary of lateral deformation in all test sections is presented in Table 5-1. Sapkota (2019) reported 44.5% and 76.4% reduction in lateral movement of the pin only section and pin plus barrier section, respectively. Similar results were observed in the current study, lateral movement was reduced by 45% in the RPP section. Although the reduction of lateral movement in the current study and that conducted by Sapkota (2019) was similar, the field test sections of the two studies were not identical. Therefore, it should be noted that additional factors such as soil properties, slope geometry, climatic variation also have an effect in lateral movement of the slope. Furthermore, in the current study the reduction in lateral movement of the MMB section was 40 %. Therefore, it can be concluded that the increased reduction of the lateral movement of the pin plus barrier section in the study conducted by Sapkota (2019) was due to the additional reinforcement provided by the recycled plastic pins.

Table 5-1 Summary of test sections (Sapkota et al.,2019)

Section	Maximum lateral deformation (in)	Reduction in movement (%)
Control section	1.28	-
Pin only section	0.71	44.5%
Pin plus barrier section	0.30	76.4%

5.4 Vertical Settlement of Slope

The vertical deformation of the slope was monitored by conducting topographic surveys at the crest and middle sections of the slope using a total station on a monthly basis as shown in Figure

5-10. The survey was first conducted in September 2019 once the slope was backfilled following field installation and it was used as the base line for movement. While conducting the survey, three fixed points were utilized to align the periodically obtained survey data. Among the three permanent points, two were located on the top and bottom of a concrete retaining wall while the third was at the bottom of a pole. The result of the topographic survey is presented in the following sections.

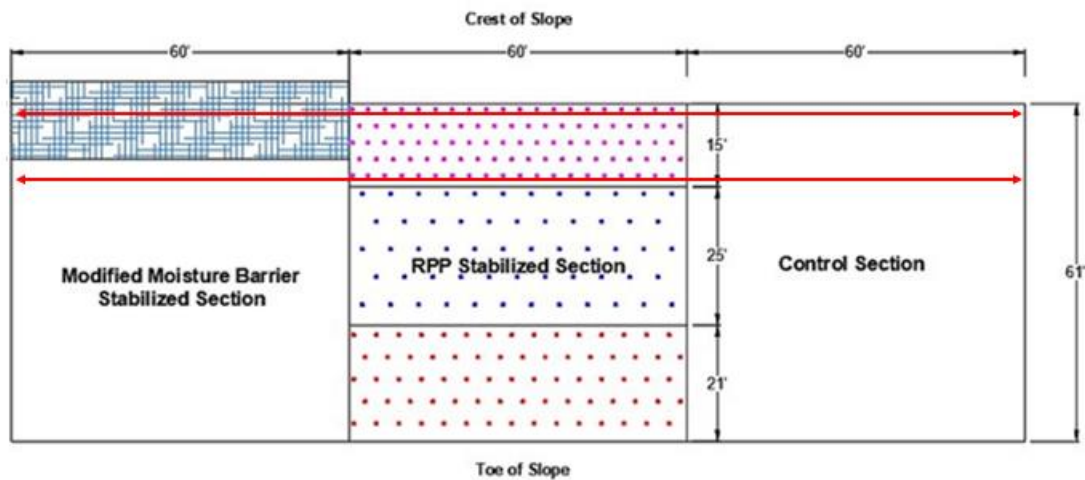


Figure 5-10 Location of survey lines.

5.4.1 Crest of the Slope

Vertical settlement of the crest of the slope is presented in Figure 5-11. Although monitoring began in September 2019, notable vertical settlement was first observed after 3 months in December 2019. Initially, the deformation lags behind the change of moisture content. Similar results were observed in a study conducted by Dai et al. (2020) where development of surface deformation took some time. During the 36 months monitoring period the average settlement of the MMB section and RPP section were 0.50 inches and 0.91 inches respectively while that of the control section was 1.44 inches. Of the three test sections, the least vertical settlement is observed in the MMB section while the maximum settlement of 1.70 inches is experienced in the control section. The

moisture barrier effectively reduces swelling and shrinkage of the slope by preventing rainwater infiltration.

Furthermore, the control section experienced a lower increase in vertical settlement during the summer months of 2020 which was also the relatively wetter period in the year. This can be attributed to the swelling behavior of expansive soil. During rainfall events as water infiltrates the slope, expansive clayey soil swells causing insignificant vertical settlement (Jones and Jefferson, 2012). On the contrary, the drier period of the year causes the soil to shrink and thus causes an increase in the vertical settlement of the slope (Jones and Jefferson, 2012).

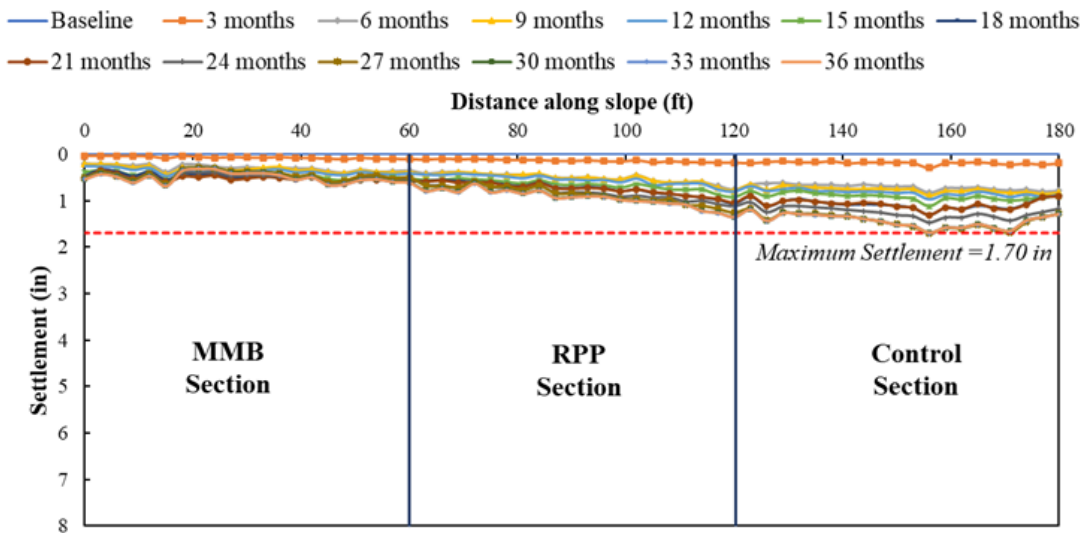


Figure 5-11 Vertical settlement at the crest of the slope.

5.4.1.1 Comparison of Test Sections

The average settlement during the 36 months monitoring period was determined and the results are presented in Figure 5-12. The control section experienced the greatest average settlement experience of 1.44 inches. The average settlement experienced by the MMB section was approximately 65% less than the control section while that of the RPP section was about 37%

lower. The MMB successfully prevents the infiltration of rainwater into the underlying soil which reduces swelling and shrinkage of the soil while this phenomenon is experienced in the RPP and control sections. As a result, the vertical deformation is lower compared to the other test sections.

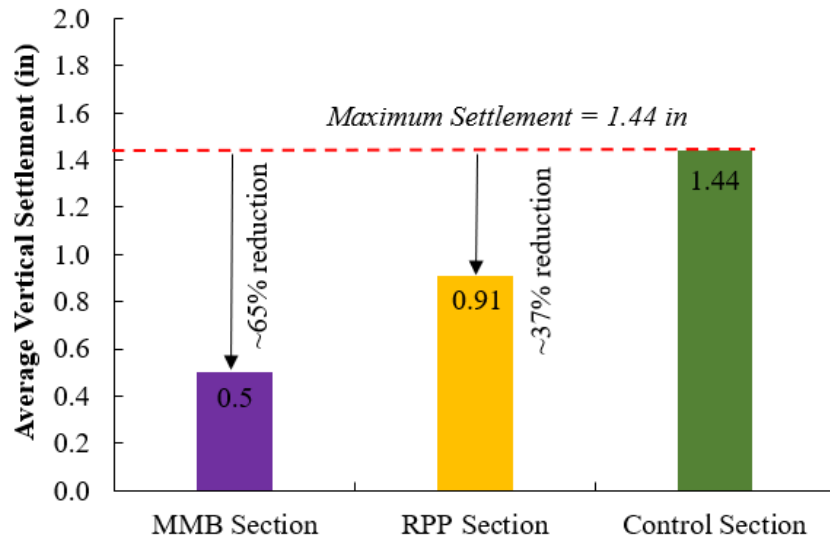


Figure 5-12 Comparison of average settlement of test sections at crest of the slope.

5.4.2 Middle of the Slope

Vertical settlement of the middle of the slope is presented in Figure 5-13. During the 36 months monitoring period the average settlement of the MMB section and RPP section were 0.63 inches and 0.58 inches respectively while that of the control section was 0.88 inches. Of the three test sections, the least vertical settlement is observed in the RPP section while maximum vertical settlement of 1.21 inches is experienced by the control section. Overall, lower settlement is observed at the middle of the slope compared to the crest. However, the MMB section experienced more settlement at the middle of the slope. This difference can be attributed to the fact that the barrier does not extend to the location of the survey line at the middle of the slope, hence the soil is subjected to climatic conditions.

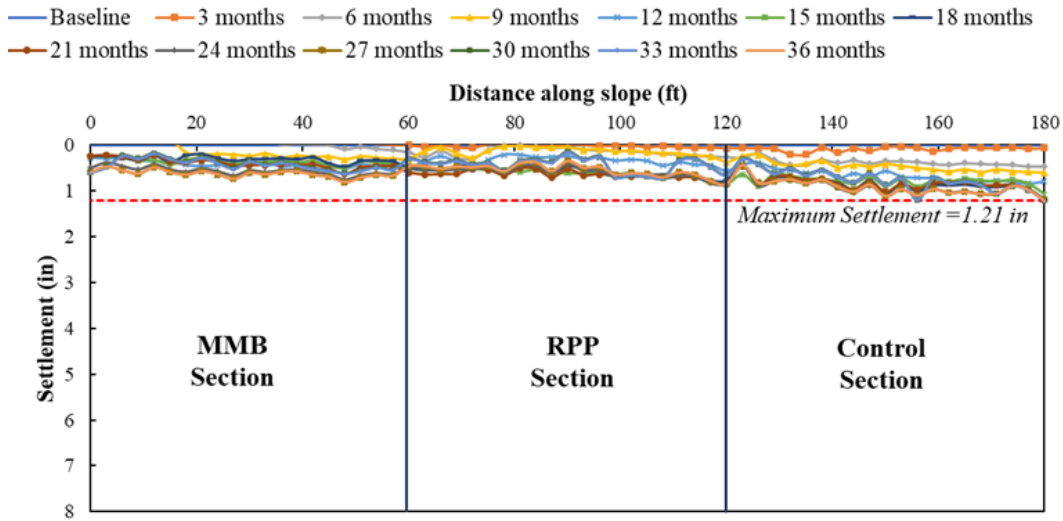


Figure 5-13 Vertical settlement at the middle of the slope.

5.4.2.1 Comparison of Test Sections

The average settlement during the 36 months monitoring period was determined and the results are presented in Figure 5-14. The control section experienced the greatest average settlement of 0.88 inches. The average settlement experienced by the MMB section was approximately 28% lower than that of the control section while that of the RPP section was about 34% lower. At the middle of the slope, the MMB does not extend to the location of the survey line in the MMB section while in the RPP section, the center to center spacing of the RPPs transitions from 3 feet to 5 feet. As a result, the reduction of the vertical deformation compared to the control section is lower at the middle of the slope compared to the crest.

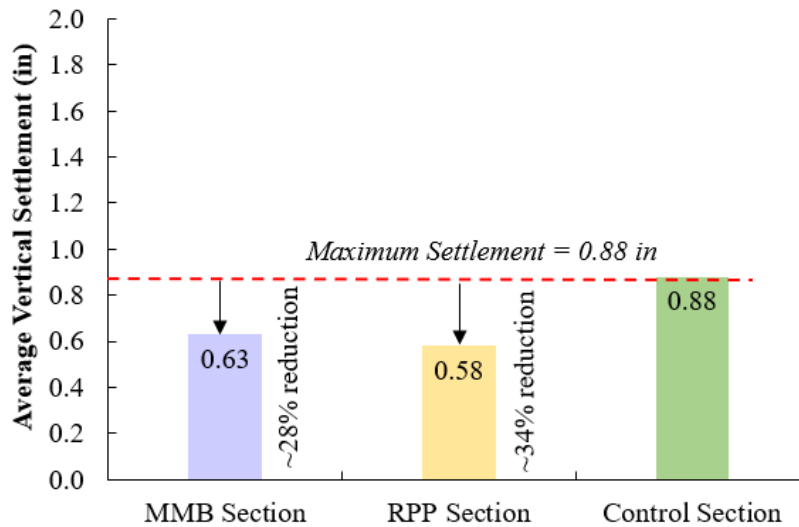


Figure 5-14 Comparison of average settlement of test sections at middle of the slope.

5.4.3 Comparison with Previous Literature

A study was conducted by Lees et al. (2013) to monitor the temporal movement of an old clay fill embankment in the UK. Cyclical shallow shrinkage and swelling movement depicted by mode ‘a’ in Figure 5-15 was observed during seasonal changes which was depicted by changes in the porewater pressure of the soil. Tony et al. (2006) monitored the performance of an unsaturated expansive soil slope when subjected to artificial rainfall. Swelling of the slope surface was observed during rainfall events, which led to an increase in positive vertical movement of the slope. On the other hand, as the rainfall event ended the porewater pressure was recovered and the vertical movement decreased due to shrinkage. Similar results were observed in the control section and RPP section of the current study. However, in the MMB section the effect was minimized as the soil was protected from climatic variation hence reducing its swelling and shrinkage.

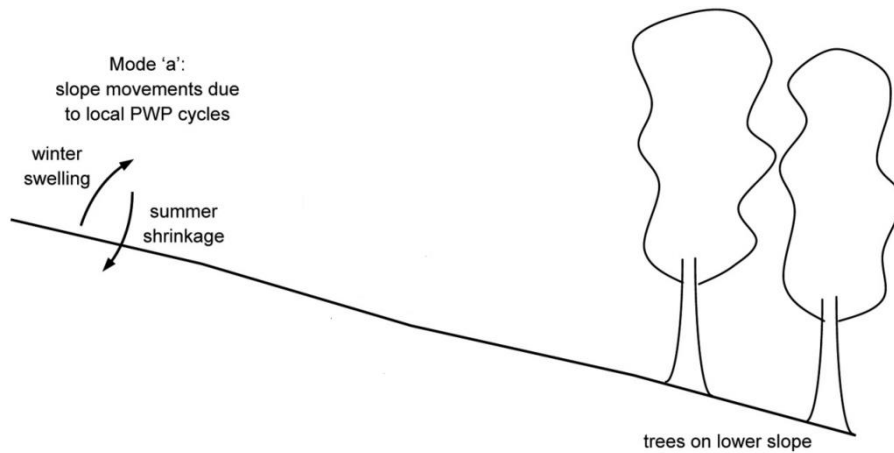


Figure 5-15 Seasonal slope movement patterns (Less et al., 2013).

5.5 Variation of Field Hydraulic Conductivity

The impact of wetting and drying cycles on soil included the destruction of bonds and alteration of soil microstructure, which leads to a loss of strength, and increase in hydraulic conductivity (Kamei et al., 2013; Cuisiner et al., 2020). The function of the modified moisture barrier is to prevent infiltration of rainwater into the underlying soil which inhibits the wetting and drying phenomenon caused by climatic variation. As rainwater is not allowed to infiltrate the soil, its shear strength will be preserved which in turn stabilizes the slope. The effectiveness of the MMB in reducing rainwater infiltration was seen in terms of variation of soil moisture content and soil water potential as discussed in sections 5.2.1 and 5.2.2, respectively. To further evaluate the performance of the MMB in reducing rainfall infiltration, the hydraulic conductivity of the soil underneath the MMB was measured and compared to that of the other test sections.

To this end, field hydraulic conductivity tests were conducted at the crest of the slope and middle section of the slope using the Guelph Permeameter on a monthly basis. Hydraulic conductivity testing began in November 2021 following the procedure outlined in section 4.4.1. Variation of

soil hydraulic conductivity with rainfall was assessed, and the results of are presented in the following sections.

5.5.1 Crest of the Slope

The hydraulic conductivity of the soil was measured at the crest of the slope at all test sections. Two tests were conducted at each section and the average field saturated hydraulic conductivity was reported. The variation of hydraulic conductivity, at the crest of the slope, with rainfall is presented in Figure 5-16. The 12-month monitoring period (November 2021 to October 2022) reflects one cycle of climatic variability based on rainfall. The first four months, November 2021 to February 2022, can be considered the dry period with cumulative rainfall of 10.17 inches while the next seven months, March 2022 to September 2022, can be considered as the relatively wet period with cumulative rainfall of 14.13 inches. It should be noted that that 7.17 inches of rainfall event that occurred on August 22, 2022, was considered an extreme event and has been excluded from the data.

At the control section, an overall increase of hydraulic conductivity is observed with decrease in the rainfall prior to the time the test was conducted. At high moisture content, fine grained soils have low hydraulic conductivity (McCartney et al., 2007). When rainfall is high, the soil becomes saturated. When the clay soil is wet and swollen, only macropores that are open for flow can conduct water, this causes a reduction in the saturated hydraulic conductivity (Messing and Jarvis, 1990). Furthermore, at high moisture content fine grained soils sometimes contain a layer of adsorbed water on their surface which is not free to move under gravity, hence reducing the soil's hydraulic conductivity (Arora, 2008). Between June and July 2022, the hydraulic conductivity is observed to increase almost by two orders of magnitude. Such an increase can be attributed to the

formation of cracks during the drought experienced in July 2022 on the surface of the soil which act as pathways for water conductivity.

Similar trend of variation of hydraulic conductivity was also expected at the RPP section, however the change in hydraulic conductivity was observed to be lower compared to the control. This can be attributed to an increase in soil compaction level due to the installation of recycled plastic pins. At higher compaction, the density of the soil is higher which causes a decrease in its hydraulic conductivity (Matthews et al., 2010). Furthermore, it is noted that the hydraulic conductivity of the RPP section was generally higher than that of the control section. This is attributed to the presence of a layer of sandy soil at the crest of the slope near the RPP section, which significantly increased the soil's hydraulic conductivity.

Contrastingly, at the MMB section the hydraulic conductivity of the soil remains nearly constant with respect to seasonal variation and rainfall events. As the MMB prevents the underlying soil from being subjected to rainfall or evaporation, there is limited fluctuation of soil moisture content. Therefore, no corresponding change in soil hydraulic conductivity is observed. Thus, the effectiveness of the MMB in preserving the soil's physical structure is proven from its ability to maintain a constant hydraulic conductivity over time. Hence it can also be inferred that the MMB can successfully conserve the shear strength of the soil resulting in greater slope stability.

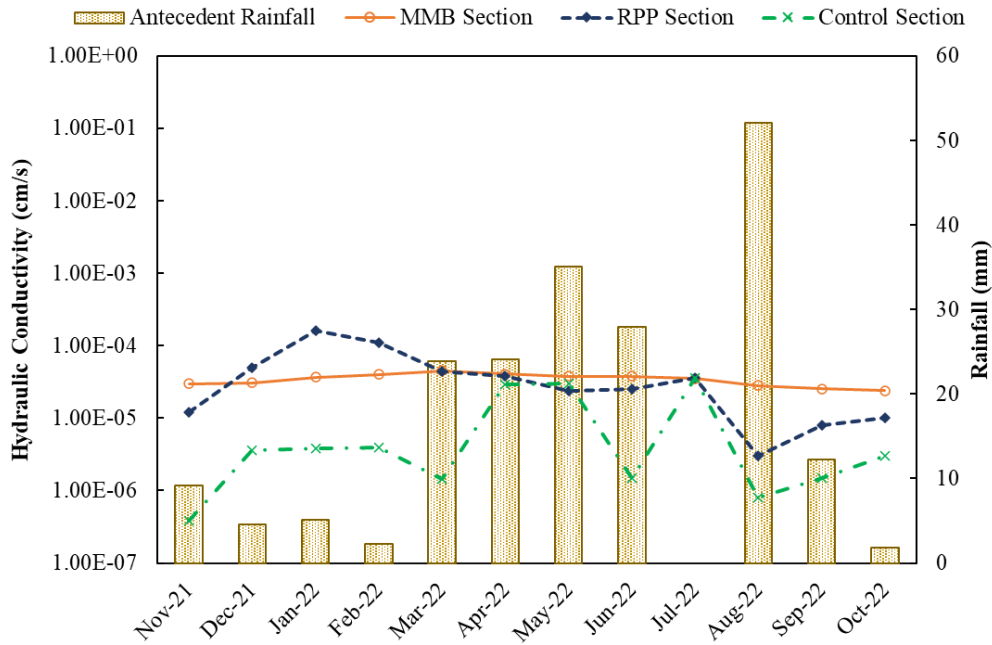


Figure 5-16 Variation of field hydraulic conductivity at the crest of the slope.

5.5.2 Middle of the Slope

The hydraulic conductivity of the soil was measured at the middle of the slope at all test sections. Two tests were conducted at each section and the average field saturated hydraulic conductivity was reported. The variation of hydraulic conductivity, at the middle of the slope, with rainfall is presented in Figure 5-17.

At the middle of the slope, similar results were obtained at all three test sections. An overall trend of increase in soil hydraulic conductivity was observed with an increase in rainfall. The variation in hydraulic conductivity was highest at the MMB section. At the crest of the slope, water was unable to infiltrate into the soil through the MMB. Any infiltrated rainwater was efficiently drained laterally along the slope. As a result, higher infiltration occurred at the MMB section resulting in a higher decrease of hydraulic conductivity. On the other hand, the least fluctuation of hydraulic

conductivity was observed in the RPP section. This can be attributed to the increased compaction of this test section due to the installation of the recycled plastic pins.

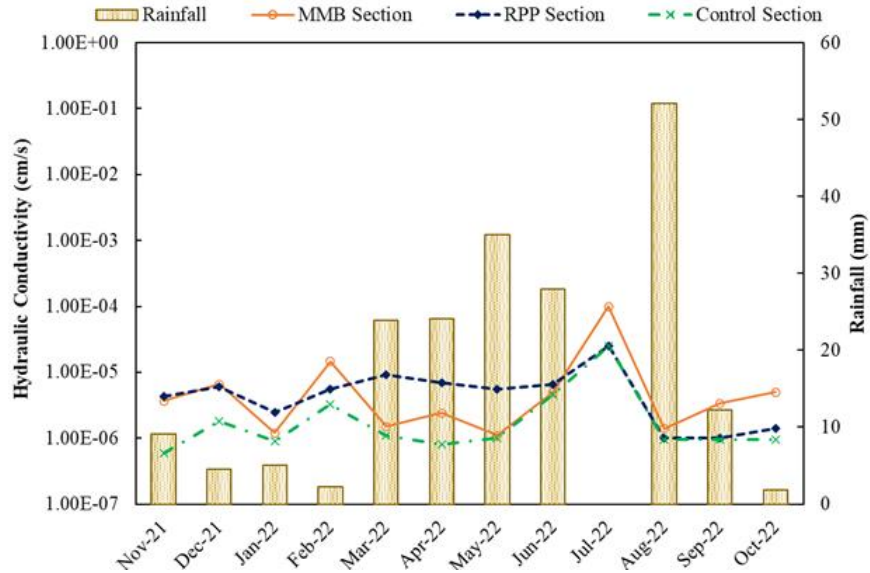


Figure 5-17 Variation of field hydraulic conductivity at the middle of the slope.

5.5.3 Effectiveness of the MMB

Variation of the hydraulic conductivity of the slope with time is an indirect measure of the slope soil undergoing changes in its physical and strength properties due to climatic variation. The effectiveness of the MMB in maintaining the hydraulic conductivity of the slope soil is assessed by comparing the permeability tests results conducted at the crest of the slope, where the soil was underneath the barrier to that at the middle of the slope where the slope soil is subjected to climatic loading due to the absence of any barrier, and the results are presented in Figure 5-18. At the crest of the slope, the hydraulic conductivity of the soil remains fairly constant. This is because the soil is protected from the impacts of climatic variation, it does not undergo continuous and cyclic fluctuation of moisture content due to rainfall and evaporation during wet and dry seasons, respectively. Therefore, the soil does not undergo swelling or shrinkage which does not alter its physical properties hence no significant change in hydraulic conductivity is observed over the

monitoring period. On the other hand, at the middle section of the slope the hydraulic conductivity of the soil changes continuously without following any specific trend. The increase in hydraulic conductivity can be attributed to lack of rainfall and the formation of desiccation cracks which acts as conduits for water infiltration during the dry periods. Contrastingly, the decrease in hydraulic conductivity can be attributed to the wet seasons when there is increased rainfall and consequent swelling of the soil due to infiltration in turn closes the cracks formed during the dry periods. Moreover, the hydraulic conductivity of the soil at the crest of the slope is observed to be generally higher, as the soil is maintained at a relatively drier condition compared to the middle section of the slope.

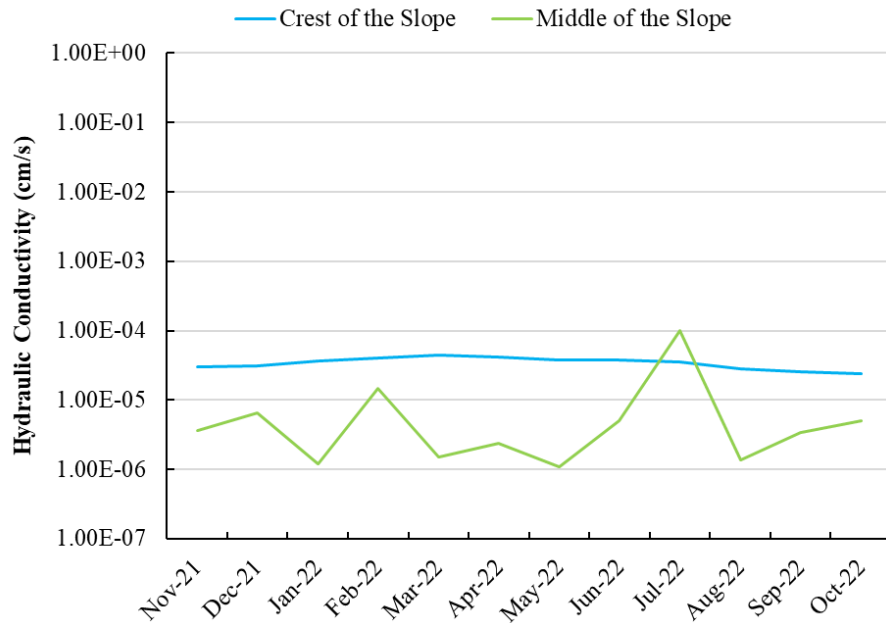


Figure 5-18 Comparison of hydraulic conductivity of the MMB section (s) crest of the slope (b) middle of the slope.

5.5.4 Comparison with Previous Literature

A study conducted by Gupta et al. (1994) assessed the spatial and seasonal variations in hydraulic conductivity of soil. The average values of hydraulic conductivity obtained using the Guelph Permeameter in each season are shown in Figure 5-19. The mean values of the hydraulic conductivity were found to differ from one season to another. Hydraulic conductivity in the fall and spring were almost 1.5 to 2 times greater than that obtained during the summer. This difference is attributed to the difference in soil physical conditions from season to season. Similar result was also observed in the current study, where lower hydraulic conductivity is observed during the summer due to lower rainfall and higher during the wetter periods. Islam (2021) conducted a study to monitor the effect of seasonal variation on hydraulic conductivity of the slope in Midlothian, Texas. The dominant pattern depicted that soil permeability increased with decrease in rainfall.

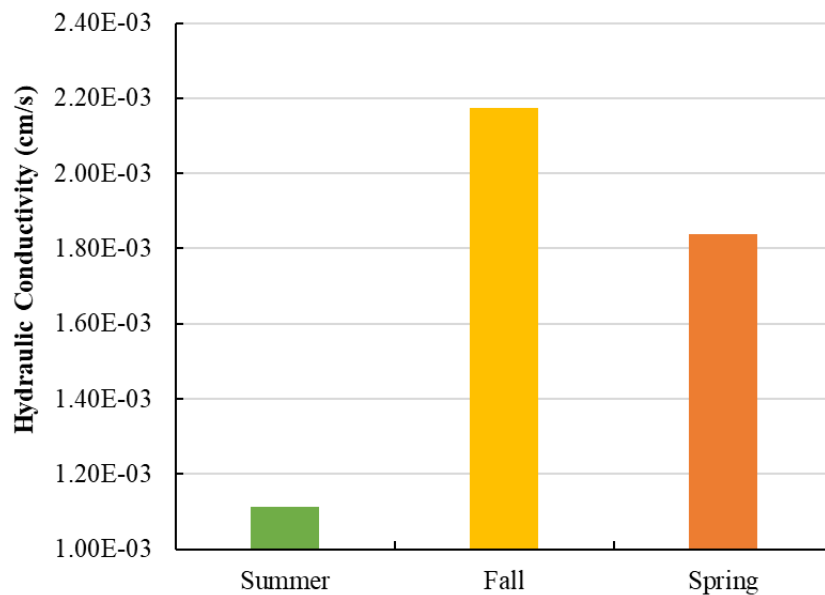


Figure 5-19 Average hydraulic conductivity in each season (Gupta et al., 1994).

CHAPTER 6 NUMERICAL STUDY

6.1 Background

The current study aims to evaluate the performance of the modified moisture barrier (MMB) in stabilizing slope failures. As part of the study, a field slope section that experienced prior shallow slope failure was installed with the MMB at its crest in Arlington, Texas. The barrier system promoted lateral drainage of infiltrated rainwater along the slope and prevented intrusion into the underlying soil increasing the overall stability of the slope. Based on field performance monitoring of the MMB and control sections, it was evident that the MMB successfully isolated the underlying soil from climatic variation hence reducing the movement of the slope improving slope stability. The impact of climatic variation on the factor of safety of the slope with and without the modified moisture barrier is further studied through numerical modeling.

In recent times, computer models are extensively utilized in engineering practice. Their ability to simulate real field conditions and solve complex soil-structure interactions through meticulous calculations make them an effective and powerful tool in research. This chapter presents the results and analysis of a numerical study conducted, using the finite element software GeoStudio. A failed highway slope section was stabilized in the current study and therefore a numerical model was established to simulate the field slope condition based on performance monitoring data. Both seepage and slope stability analyses were performed using SEEP/W and SLOPE/W, respectively, from the GeoStudio package. Once the model was calibrated, seepage and slope stability analyses were carried out with the inclusion of the modified moisture barrier (MMB) in the model and the results were compared to field performance monitoring data. The calibrated numerical model was used to conduct a parametric study with various soil shear strength parameters, soil hydraulic properties, slope geometry, rainfall intensity and duration and length of barrier along the slope.

The details of model calibration, model validation, parametric study utilizing the calibrated model and other relevant numerical modeling results are presented in this chapter.

6.2 Finite Element Based Numerical Model

GeoStudio software package provides a single platform for solving complex coupled and uncoupled physical processes in geotechnical and geosciences using combination of different platforms (GeoStudio, 2020). The software can efficiently be used to model coupled flow and slope stability analyses. The model discretizes the model domain into numerous elements and solves the governing equations for each elemental node. Configuration of the mesh and time steps play a significant role for converged solution, especially in transient seepage analysis where soil response is governed by rainwater infiltration. Since the main objective of the study is to evaluate the stability of the slope with inclusion of the MMB when subjected to climatic conditions, several trials were conducted with different mesh configurations and time steps to establish a suitable numerical scheme.

6.3 Development of Model

Numerical analysis presented in this chapter has been conducted in two steps. At first, a transient seepage analysis was conducted using the finite element-method based program SEEP/W (Geo-Slope International, 2012), and the porewater pressure profile was generated for a specific rainfall event. The generated porewater pressure profile from the seepage analysis was used as an input into SLOPE/W along with soil shear strength properties. Slope stability analysis was then carried out using the limit equilibrium method-based computer program SLOPE/W (Geo-Slope International, 2012b). The seepage analysis was conducted by solving the following differential equation which governs the two-dimensional unsteady flow of water through saturated-unsaturated soil:

$$\frac{\partial}{\partial x} \left(k_x \frac{\partial H}{\partial x} \right) + \frac{\partial}{\partial y} \left(k_y \frac{\partial H}{\partial y} \right) + Q = m_w \gamma_w \frac{\partial H}{\partial t}$$

Where k_x and k_y are the hydraulic conductivities in the x and y direction, respectively; H is the total hydraulic head; Q is the applied boundary flux; t is time; m_w is the slope of the storage curve; and γ_w is the unit weight of water.

The slope stability analysis was conducted by considering the shear strength of the soil. Fredlund et al. (1978) proposed the following equation which is an extension of the M-C theory to describe the shear strength of unsaturated soil:

$$\tau_f = c' + (\sigma_n - u_a) \tan \varphi' + (u_a - u_w) \tan \varphi^b$$

Where τ_f is the shear strength at failure; c' is the effective cohesion; σ_n is the total normal stress; u_a is the pore air pressure; u_w is the pore water pressure; φ' is the angle of internal friction associated with the change in net normal stress; φ^b is the angle representing the rate of change in shear strength relative to matric suction change. Morgenstern-Price (1965) method was adapted for the analyses. The M-P method considers both shear and normal interslice forces and satisfies both moment and force equilibrium (Lye et al., 2015).

6.3.1 Model Geometry and Boundary Conditions

The highway slope located at the intersection of interstate highway 20 (IH20) and Park Springs Blvd. in Arlington, Texas was about 15 ft. in height with an angle of 18.4°. Based on soil boring information, the slope consists of three main layers (i) silty clay layer extending to a depth of 7 ft. (ii) clay layer extending to a depth of 18 ft. (iii) sandstone extending beyond 18 ft. as shown in Figure 6-1. No structures exist at the crest of the slope while IH 20 is at the toe of the slope, hence no surcharge load was added to the model. Therefore, the geometry of the slope model was

established based on the field conditions as shown in Figure 6-1. Two different hydraulic boundary conditions were incorporated into the model: (i) the slope surface was the infiltration boundary where rainfall was applied as water flux (ii) the sides and the bottom of the geometry were considered to be no flow boundary, zero nodal flux (impervious boundary).

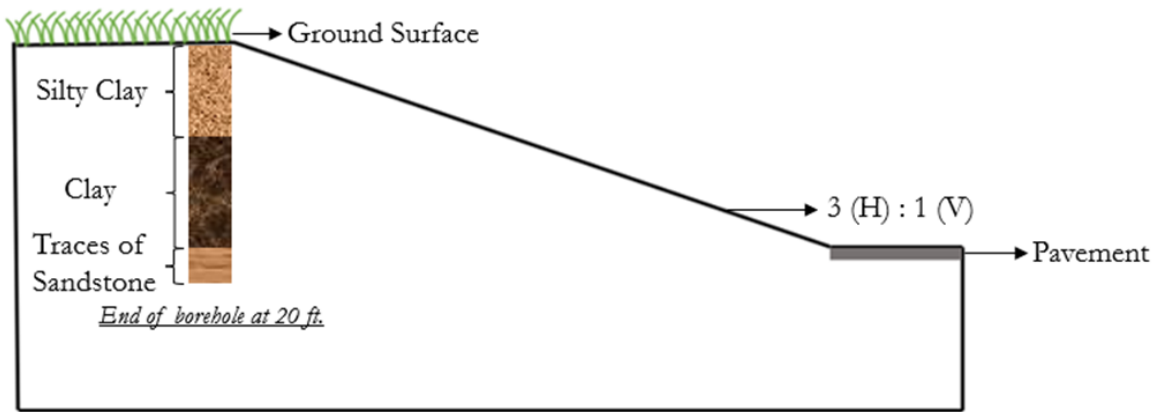


Figure 6-1 Schematic of Slope Section.

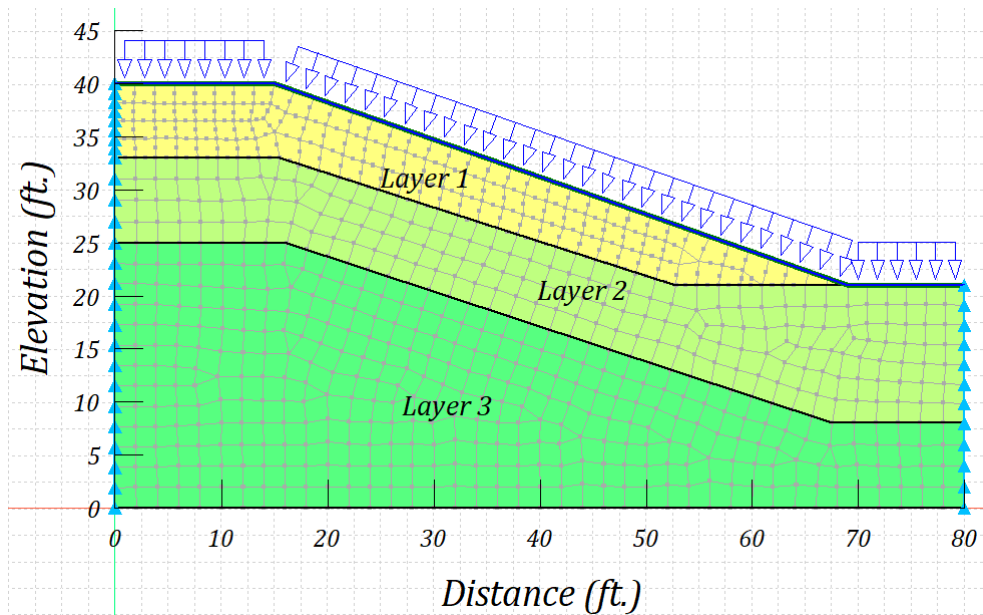


Figure 6-2 Slope geometry and boundary conditions used for analyses.

6.3.2 Material Properties

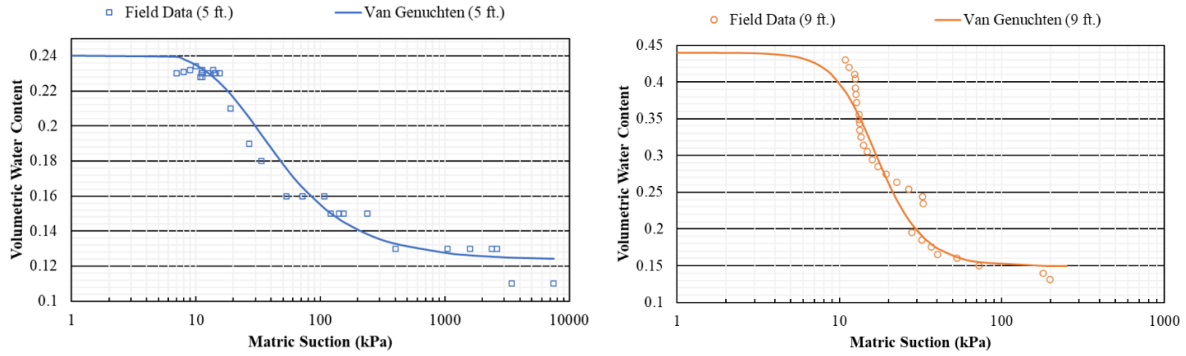
For the purpose of seepage analysis, the soil layers have been modeled using saturated/unsaturated condition. Under the saturated/unsaturated model the following were specified for each layer (i) Soil water characteristic curve (SWCC) (ii) Hydraulic conductivity function (HCF). SWCC defines the relation between matric suction and water content of the soil (Fredlund, 2006) and therefore plays an important role in controlling the flow of water into the soil.

6.3.2.1 Soil Water Characteristic Curve (SWCC)

SWCC were determined using two approaches: laboratory testing (ASTM D5298) for greater depths and using field sensor data for shallower depths. Both field and laboratory measurements of matric suction and corresponding volumetric water content were fitted with the Van Genuchten (1980) function to predict the SWCC as shown in Figure 6-3. The governing equation for prediction the SWCC is as follows:

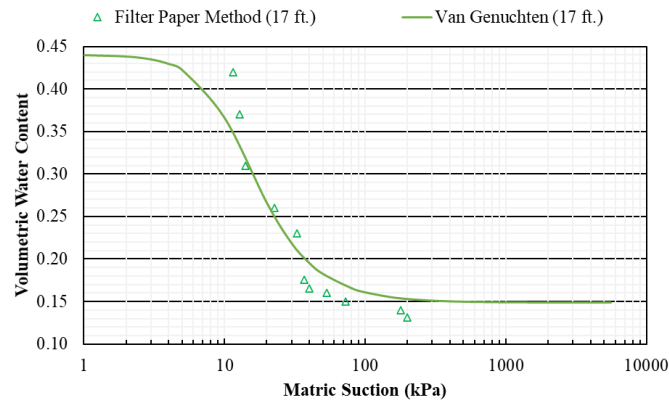
$$\theta_w = \theta_r + \frac{\theta_s - \theta_r}{\left[1 + \left(\frac{\psi}{a}\right)^n\right]^m}$$

Where θ_w is the volumetric water content; θ_s is the saturated volumetric water content; ψ is matric suction; and a, n and m are curve fitting parameters. The curve fitting parameters a, n and m are related to the inverse of the air entry value, pore size distribution of the soil and symmetry of the curve, respectively. The parameter m is frequently set equal to $(1-1/n)$ which reduces the flexibility of the equation but results in greater stability during fitting.



(a)

(b)



(c)

Figure 6-3 SWCC (a) Layer 1 (b) Layer 2 (c) Layer 3.

6.3.2.2 Hydraulic Conductivity Function (HCF)

Field permeability tests were conducted at a depth of 2 ft. using the Guelph Permeameter (GP) according to Reynolds et al. (1986), and thus the saturated hydraulic conductivity of layer 1 was determined. Hydraulic conductivity values for layer 2 and layer 3 were determined in the laboratory following the flexible wall permeameter test method (ASTM D5084), as described by Bishop and Henkel (1962). The saturated hydraulic conductivity of the soil at different depths are shown in Table 6-1. Several empirical and statistical closed form equations exist in literature to derive the hydraulic conductivity function based on the soil water characteristic curve and

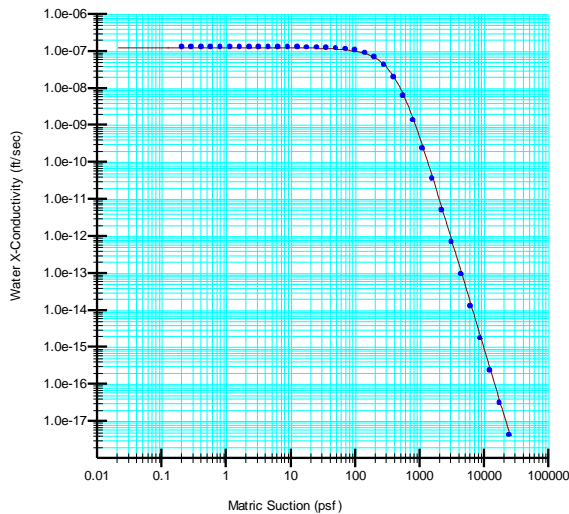
conductivity at saturation. Van Genuchten (1980) proposed the following closed form equation to describe the hydraulic conductivity of a soil as a function of matric suction:

$$k_w = k_s \frac{[1 - (\alpha\psi^{(n-1)})(1 + (\alpha\psi^n)^{-m})]^2}{((1 + \alpha\psi^n)^m)^{1/2}}$$

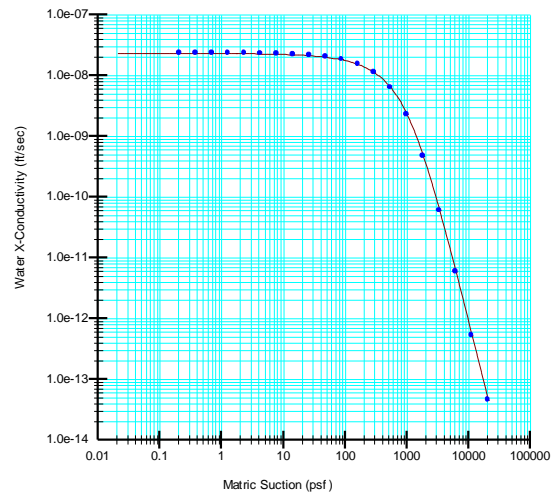
where k_s =saturated hydraulic conductivity; a, n, m =fitting parameters; $n=1/(1-m)$, and ψ =required suction range. The estimated hydraulic conductivity functions of the soil layers are shown in

Table 6-1 Saturated hydraulic conductivity determined from field and laboratory testing.

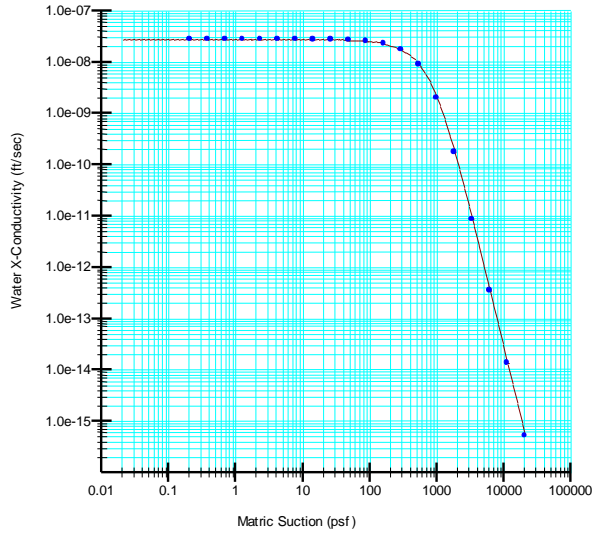
Depth (ft.)	Saturated Hydraulic Conductivity (ft/s)
2	1.25×10^{-7}
7	2.32×10^{-8}
15	2.76×10^{-8}



(a)



(b)



(c)

Figure 6-4 HCF (a) Layer 1 (b) Layer 2 (c) Layer 3.

6.3.2.3 Shear Strength Parameter

For the purpose of the slope stability analysis conducted in SLOPE/W, the soil layers are modeled using the Mohr-Coulomb material model. The inputs required were soil shear strength and density parameters determined from laboratory testing as described in Chapter 3. Input parameters for SLOPE/W are presented in Table 6-2.

Table 6-2 Soil shear strength properties used for slope stability analysis.

Soil Layer	Unit Weight (pcf)	Effective Cohesion (psf)	Effective Friction Angle (°)	Friction Angle due to Matric Suction, ϕ^b (°)
1	100	69	8	4
2	120	200	12	6
3	135	2400	31	15.5

6.3.3 Climatic Flux Boundary

Climatic flux boundary condition in terms of rainfall and evapotranspiration has been applied to the model. Real time rainfall data collected from the nearest weather station has been applied as a water flux boundary as shown in Figure 6-2. Rainfall has been characterized as a step function as data changes abruptly over time. Potential evapotranspiration for the site has been estimated theoretically by the Thornthwaite method (Palmer and Havens, 1958) and available soil moisture in the field. Using the Thornthwaite method, an estimate of the potential evaporation for each month of the year can be calculated using the monthly mean temperatures from the measurements. This method has been used widely throughout the world. The method uses the following equation to calculate maximum possible evaporation i.e., potential evapotranspiration for different times of the year and the estimated PET is shown in Figure 6-5.

$$PET = 16 * \left(\frac{10T_i}{I} \right)^{\alpha} * \frac{N}{30} * \frac{L}{12}$$

$$I = \sum_{i=1}^{12} \left(\frac{T_i}{5} \right)^{1.514}$$

$$\alpha = (492390 + 17920I - 771I^2 + 0.675I^3) * 10^{-6}$$

where, PET is potential evapotranspiration (in/month); L is the monthly mean daytime duration (hours); N is the number of days in a month; T_i is the mean monthly temperature; and I is the heat index.

However, it should be noted that soil is rarely at its full capacity and the real time rate of evaporation may vary spatially and temporally based on available soil moisture. Therefore, actual evapotranspiration from the soil may be significantly different than the potential evapotranspiration which can be computed by modifying the potential evapotranspiration based

on soil properties including available soil moisture content, field capacity, and wilting point. The equation that can be used to determine actual evapotranspiration is shown below. Figure 6-5 (b) shows the curve of AET/PET ratio as a function of field matric suction which was provided as a modifier function in the numerical model for modifying potential evapotranspiration. As the figure suggests, AET becomes equal to PET when suction is zero which is when the soil is at its full saturation, however with the increase in suction actual evapotranspiration becomes less than potential evapotranspiration.

$$AET = \frac{\theta - \theta_{WP}}{\theta_{FC} - \theta_{WP}} * PET$$

where AET is actual evapotranspiration; θ is the soil moisture content from sensors; θ_{WP} is the moisture content at the wilting point of the soil corresponding to 1500 kPa; and θ_{FC} is the moisture content at field capacity of soil corresponding to 10-30 kPa.

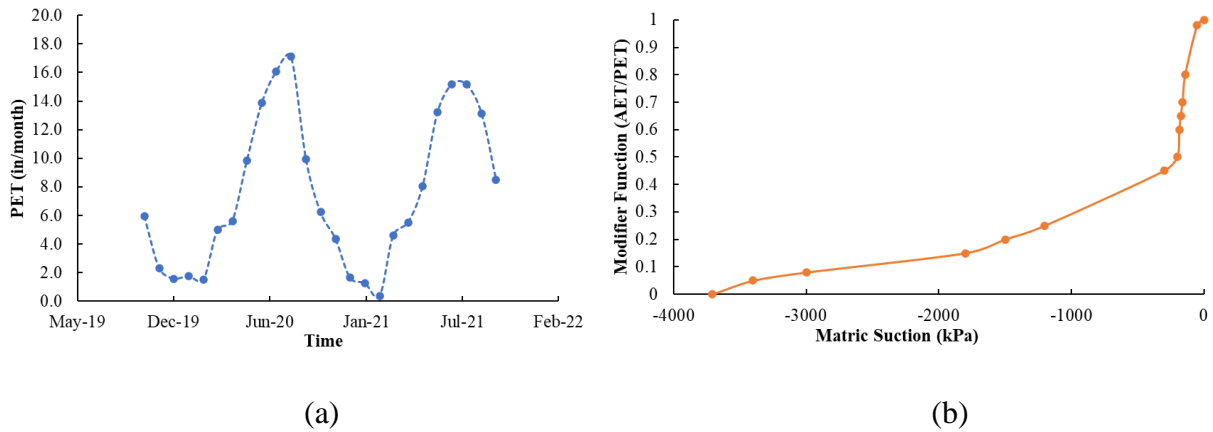


Figure 6-5 (a) Estimated PET (b) AET/PET as a function of suction.

6.2 Model Calibration

Model calibration is considered an important step for performing finite element modeling since the developed model should be able to simulate real field response with acceptable agreement. A steady state seepage analysis of the slope is conducted by assigning the hydraulic properties of the

soil layers and no ground water table (based on site investigation), to determine the initial porewater pressure distribution. At the initial stage the porewater pressure of the slope is negative which represents matric suction of the soil. The highest matric suction exists near the crest of the slope, about 2600 psf (125 kPa) and it decreases linearly with depth.

After the establishment of the initial condition, 3 months of real rainfall data (October 2019 to December 2019) was applied to the model and a transient seepage analysis was conducted for seepage calibration. Several iterations were performed by varying the saturated hydraulic conductivity and SWCC to calibrate the model to actual field conditions. Figure 6-7 shows the comparison of volumetric water content fluctuation due to real rainfall, obtained from the field sensor data and the numerical analysis. The results show very close agreement between the field and numerical data, in terms of both magnitude and pattern. The volumetric water content of the soil increased after rainfall events and decreased during periods of no rainfall. The slight difference in magnitude can be attributed to the evapotranspiration that occurs in the field being different from the theoretical estimation. Variation of porewater pressure with time and depth obtained from the field sensor data and the numerical analysis is shown in Figure 6-8. The porewater pressure as obtained from the numerical analysis and field measurements are also in close agreement. Initially, the porewater pressure is highly negative at all depths, the highest matric suction being at the slope surface. As rainfall is applied to the slope, loss of matric suction is observed from the ground surface to a depth of approximately 3 feet, after which it remains highly negative. It can be inferred from this trend that as rainwater infiltrates the slope, the matric suction is lost in the upper 3 feet of the soil due to the propagation of the wetting front. At depths beyond 3 feet, the loss of matric suction is almost negligible. The result is as expected, since during initial field reconnaissance of the failure of the slope the depth of failure was estimated to be around 2 to 3 feet.

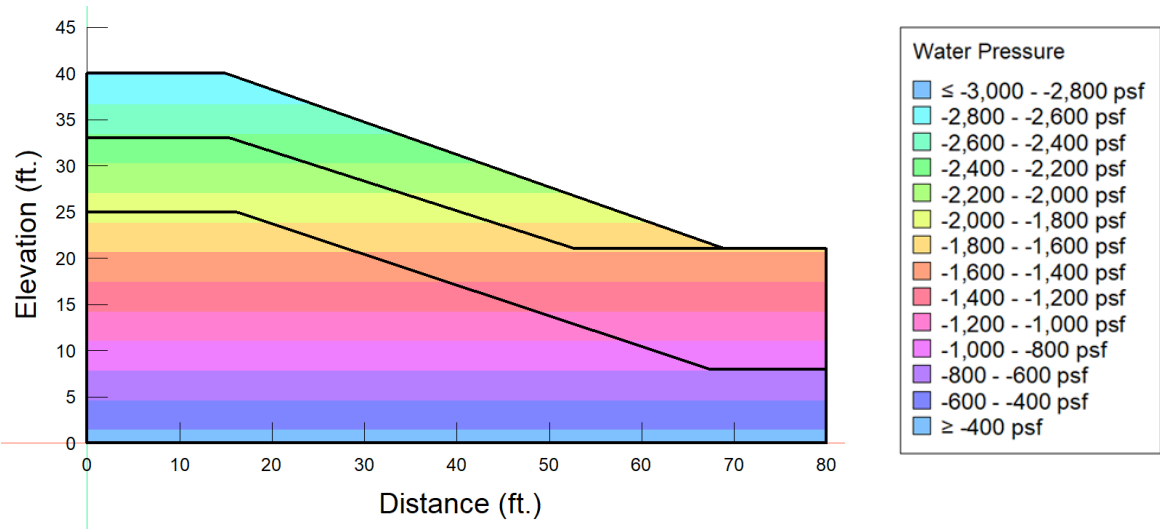


Figure 6-6 Initial porewater pressure distribution profile.

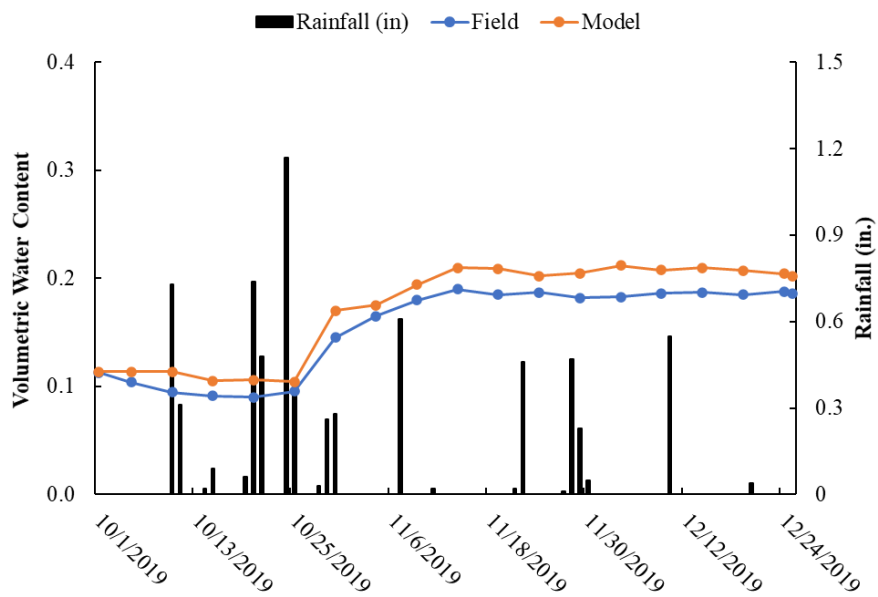


Figure 6-7 Measured and Modeled Volumetric Water Content.

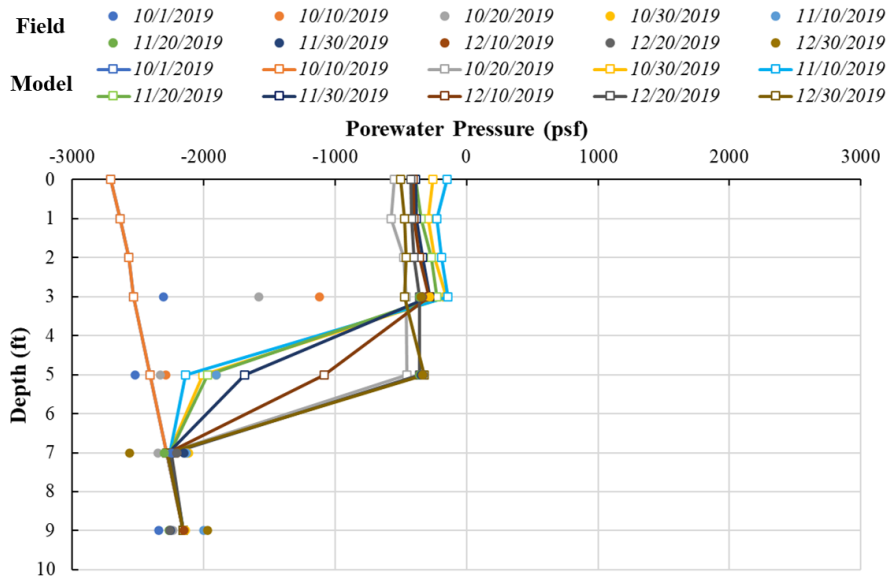


Figure 6-8 Variation of Porewater Pressure with Time.

Slope stability analysis was conducted using the Morgenstern Price method in SLOPE/W. Addition to the soil parameters listed in Table 6-2, the porewater pressure distribution throughout the slope (generated from the seepage analysis) is also used as an input for the slope stability analysis in terms of a model of porewater pressure heads. Possible slip surface locations were defined by specifying a grid of possible centers of rotation and a series of slip circle radii. The most critical slip surface is shown in Figure 6-9. Several iterations were performed by changing the shear strength parameters of soil layer 1 within a certain range as obtained from laboratory testing to calibrate the model to replicate field conditions. The factor of safety was found to be 1.000. Since the initial factor of safety is below the limit value of 1.5 it simulates the initial field condition.

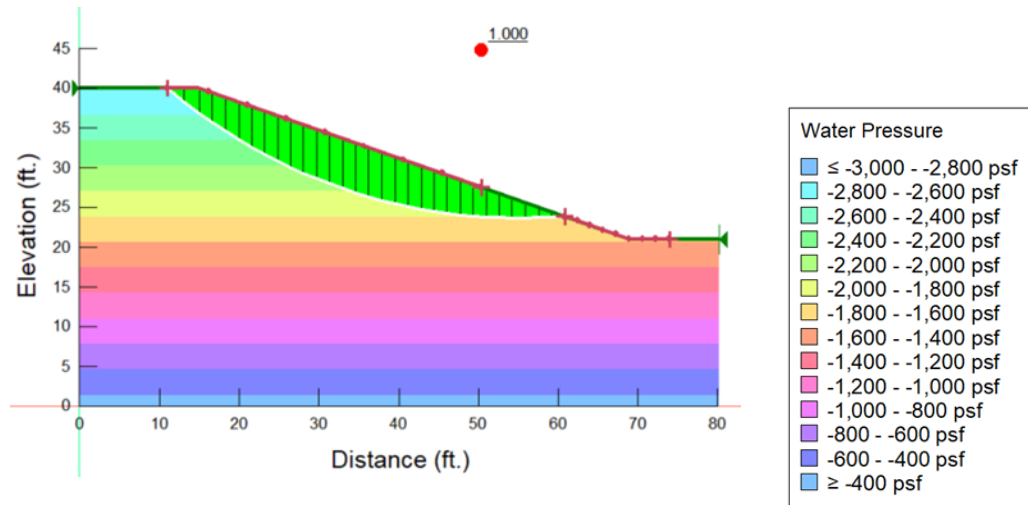


Figure 6-9 Result of slope stability analysis (initial).

6.4 Addition of Modified Moisture Barrier

Once the model was validated, an impermeable moisture barrier system (MMB) is introduced to the model to evaluate the performance of the slope in presence of the moisture control system. The modified moisture barrier comprises of a layer of geocomposite (geotextile-geonet-geotextile) over a layer of geomembrane. Several studies can be found in literature with the focus of numerically modeling geosynthetic materials as soil layers with appropriate hydraulic properties (Iryo and Rowe, 2005; Bahador et al., 2013; Nadukuru et al., 2017; Yang et al., 2018; Ahmed and Islam, 2020). In the current study the geocomposite has been modeled as soil layers of negligible thickness while an impervious boundary condition has been assigned at the bottom of the geocomposite layer to simulate the effect of the impermeable geomembrane layer. The hydraulic properties of the geotextile and geocomposite have been estimated from the manufacturer's datasheet, Stormont and Ramos (2004) and Ramos (2001).

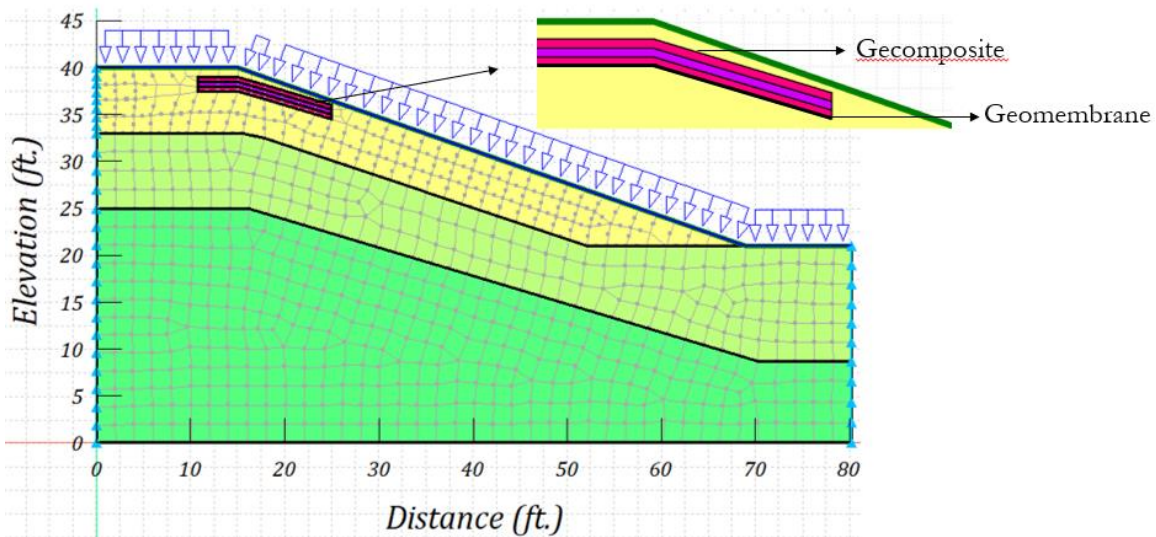


Figure 6-10 Model geometry with MMB.

Table 6-3 Hydraulic Properties for MMB.

Material	θ_s	θ_r	α	n	k_{sat} (ft/s)
Geotextile	0.754	0	2.577	1.680	1.13×10^{-4}
Geonet	0.85	5×10^{-3}	50.251	2.19	0.328

Transient seepage analysis was carried out using real rainfall data covering both wet and dry periods. Fluctuation of volumetric water content with time and rainfall, measured from the field MMB section and that obtained from the model, are presented in Figure 6-11. It can be seen that volumetric water content under the modified moisture barrier remains almost constant with precipitation events and the results from field and numerical model are in close agreement. Figure 6-12 shows the variation in porewater pressure under the MMB. The modeled porewater pressure remains constantly negative depicting matric suction in the soil as there is no infiltration of rainwater into the soil underneath the MMB. On the other hand, the measurements from the field suction sensors show scatter to an extent.

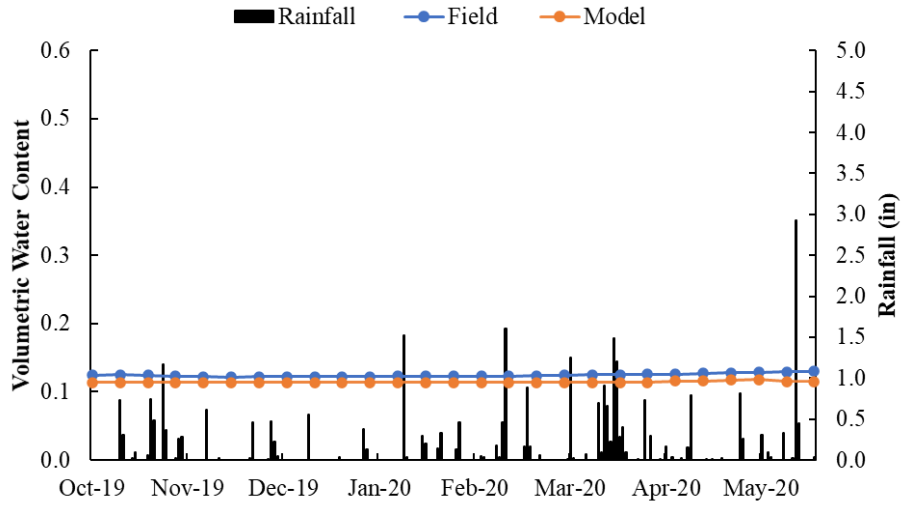


Figure 6-11 Measured and Modeled Volumetric Moisture Content for Slope with MMB.

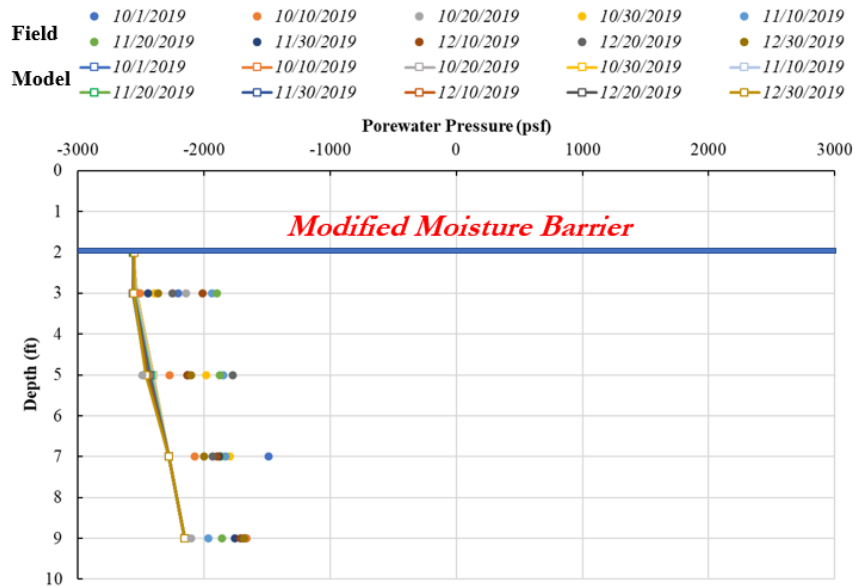


Figure 6-12 Measured and Modeled Porewater Pressure for Slope with MMB.

6.2.1 Slope Stability Analysis

Slope stability analysis for the section with the modified moisture barrier was conducted by utilizing the shear strength parameters of the soil as listed in Table 6-2 and the porewater pressure generated as a result of the seepage analysis. Based on field performance results, the soil

underneath the modified moisture barrier undergoes insignificant fluctuation in volumetric moisture content when subjected to rainfall which prevents soil shear strength reduction due to the cyclic swelling and shrinkage phenomenon. Results of slope stability analysis obtained by applying real time rainfall for a period of 90 days for the slope with and without a modified moisture barrier is shown in Figure 6-13. Inclusion of the modified moisture barrier preserves the strength of the soil underlying it thereby increasing its factor of safety. The factor of safety of the slope is observed to increase to 1.354 with the inclusion of the MMB, and the critical slip surface is observed to have shifted downwards along the slope.

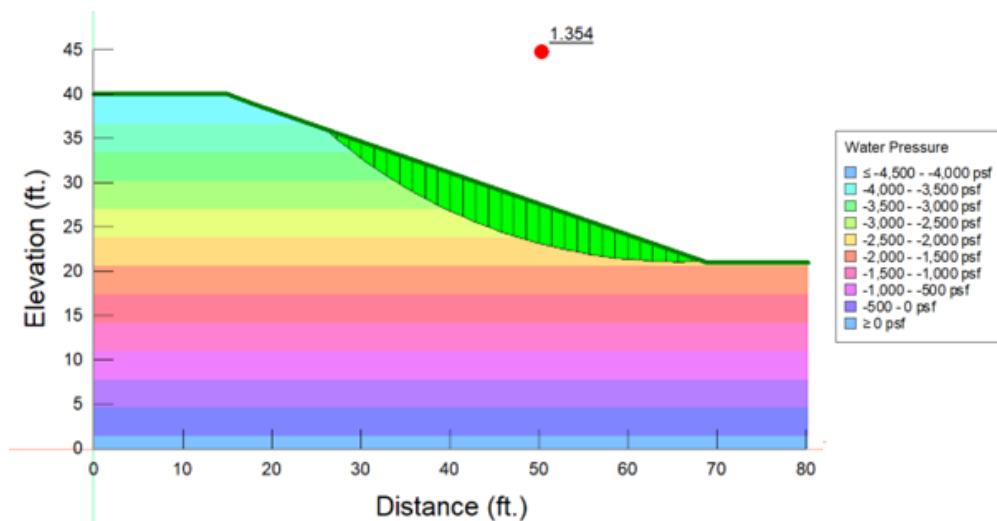


Figure 6-13 Results of Slope Stability Analysis after 90 days of Natural Rainfall for the slope with MMB.

6.5 Flow Analysis of Modified Moisture Barrier System

Ten locations within the geocomposite have been chosen to investigate the flow along the geocomposite by assessing fluctuations of porewater pressure and volumetric water content, with rainfall. Five points (1-5) are along the interface of the upper geotextile (Geotextile 1) and the

geonet, while the other five points are along the interface of the geonet and the lower geotextile (Geotextile 2), as shown in Figure 6-14.

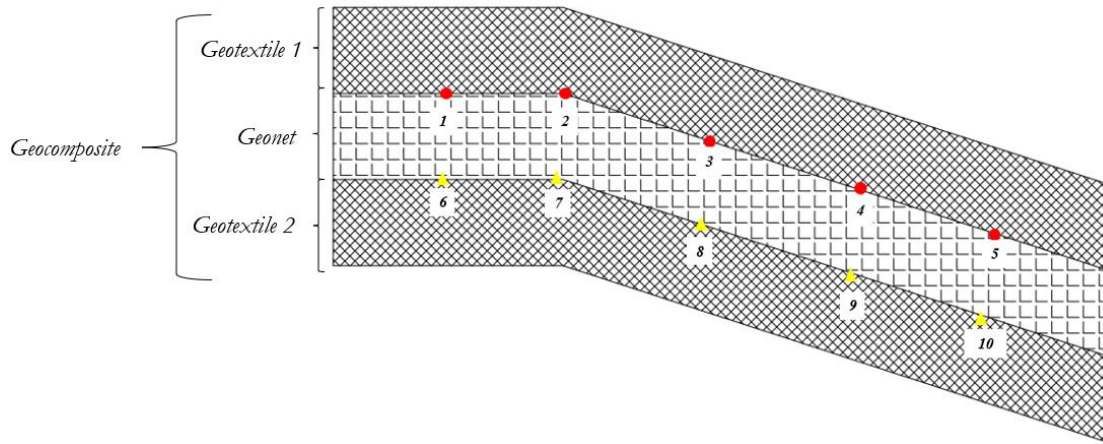


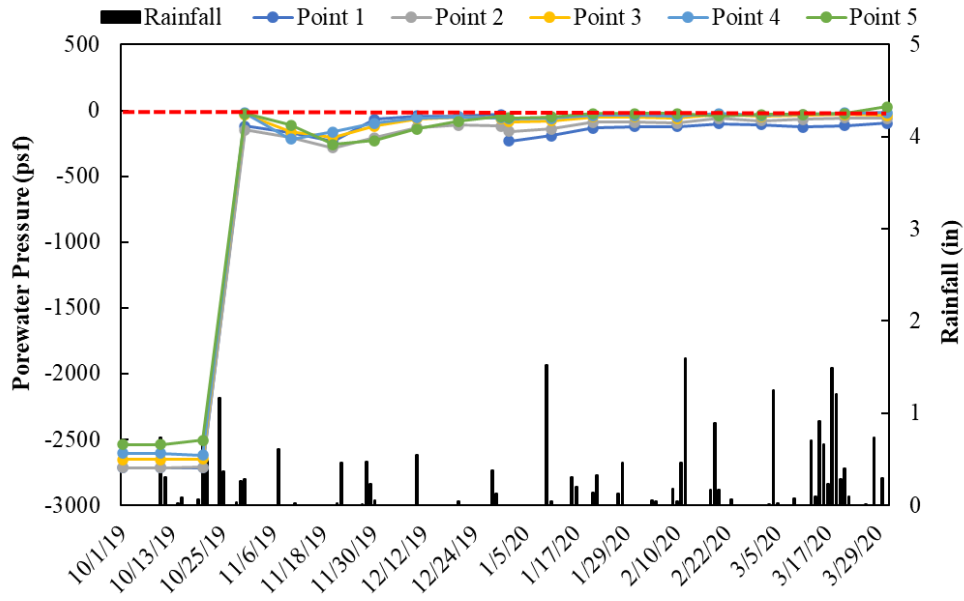
Figure 6-14 Points along the geocomposite.

6.5.1 Variation of Porewater Pressure within MMB

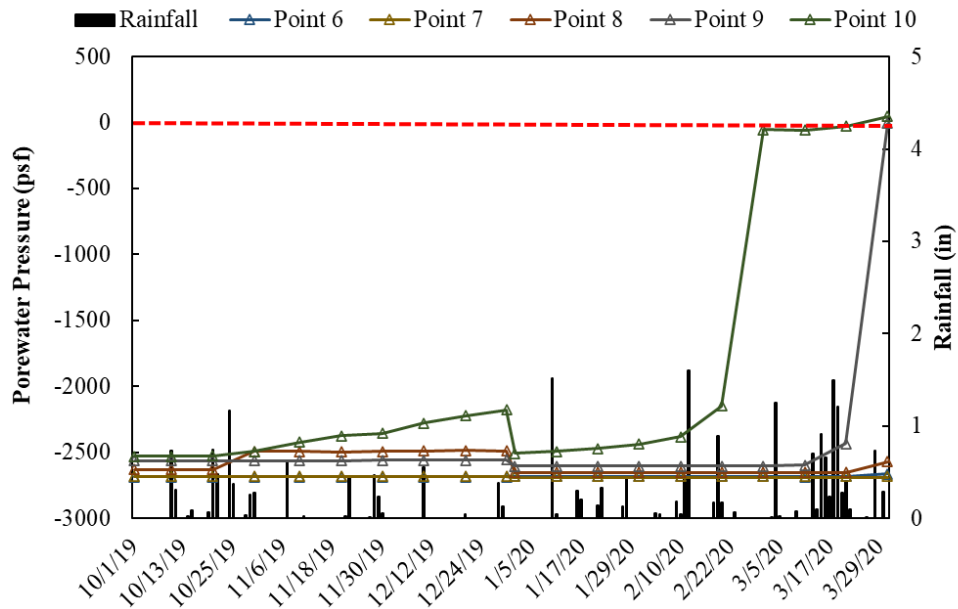
The fluctuation of porewater pressure with time and rainfall, within the geocomposite is shown in Figure 6-15. Initially, the average porewater pressure is about -2550 psf which represents the dry stage post construction of the slope. With successive rainfall events, the porewater pressure increases and remains at an average of -150 psf, which indicates that water accumulates above the interface and does not infiltrate the geonet layer. After a period of five months, in March 2020, the porewater pressure at point 5 is observed to be positive representing water flow into the geonet layer. Positive porewater pressure is observed to increase in the downdip locations of the modified moisture barrier which indicates that breakthrough of water into the geonet first takes place at a downdip location. Similarly, the initial average porewater pressure at the interface of the geonet and the underlying geotextile 2 is about -2550 psf. At this interface, the porewater pressure remains negative for longer while positive porewater pressure is observed at the upper interface. This shows that although water flow takes place into the geonet layer, the wetting front takes some time to

reach the second geotextile later. With successive rainfall events, the porewater pressure is observed to increase. However, this increase first occurs at point 10 at the downdip location and gradually progresses towards the crest of the slope. Positive porewater pressures are observed at point(s) 10 and 9, depicting the infiltration of water from the geonet to the geotextile 2 in the downdip locations. This observation is in agreement with the theory proposed by Ross (1990) which states that near the up-dip boundary of the capillary barrier system, nearly all infiltrating water will be laterally diverted. As one proceeds downdip, at the maximum diversion length of the barrier the water will no longer be laterally diverted, and it will infiltrate into the underlying coarse layer.

Therefore, when rainfall infiltration into the slope begins, the upper geotextile layer serves as the transport layer while the geonet layer functions as a capillary barrier layer. With this configuration, infiltrated rainwater is laterally diverted towards the downward direction of the slope. After a period of 5 months, the upper geotextile layer is wet enough that the capillary forces can no longer exclude water entirely from the geonet layer and thus breakthrough occurs into the underlying layer. The breakthrough is portrayed by the increase in porewater pressure at point (s) 4, 5 and consequently at point (s) 9 and 10.



(a)

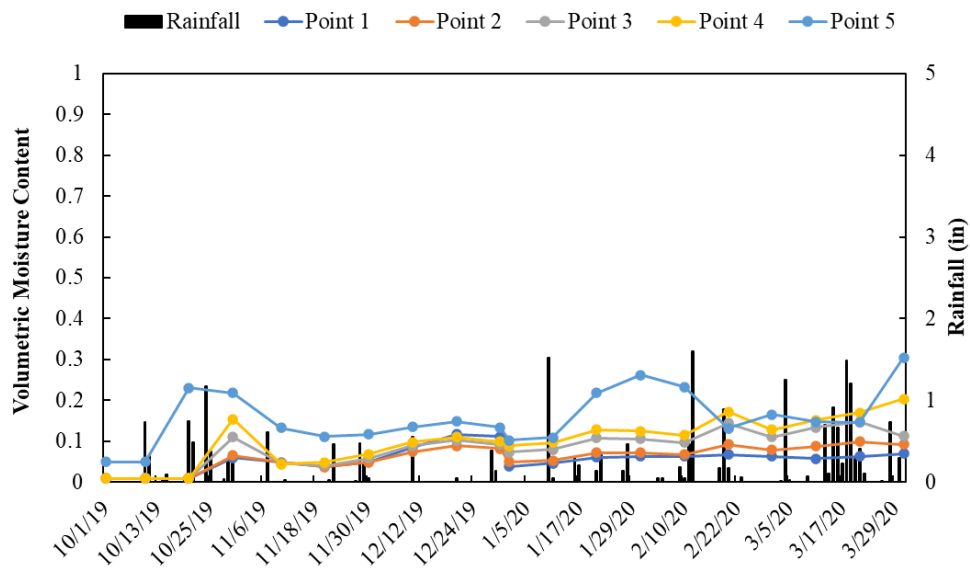


(b)

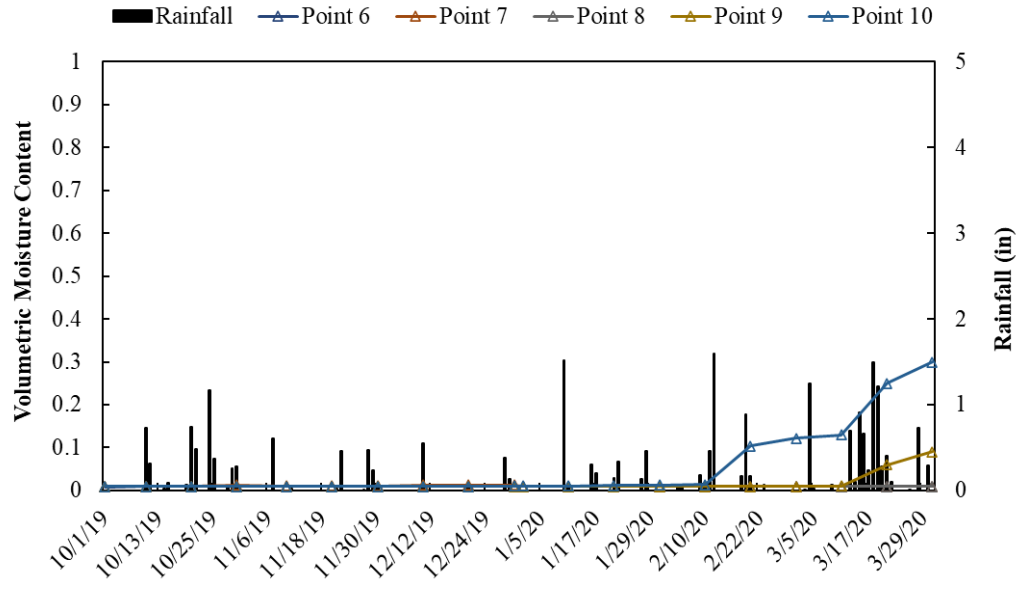
Figure 6-15 Change in Porewater Pressure within the MMB (a) at the interface of Geotextile 1 and the Geonet (b) at the interface of the Geonet and Geotextile 2.

6.5.2 Variation of Volumetric Water Content within MMB

The fluctuation of volumetric water content within in the geocomposite with time and rainfall is shown in Figure 6-16. Increase in volumetric water content of the upper geotextile layer, due to rainwater infiltration, is shown by the peaks in Figure 6-16 (a). The peaks are followed by periods of rainfall events while drier periods are represented by sharp drops. Higher water content is observed in the downdip direction with the highest water content at point 5 followed by point 4. On the other hand, the interface between the geonet and the geotextile 2 initially has low volumetric water content as water travels laterally downwards without entering the geonet. However, an increase in volumetric water content is observed as capillary break takes place and water flows into the underlying geonet and geotextile 2 layers. This trend further asserts the lateral diversion mechanism of the modified moisture barrier.



(a)



(b)

Figure 6-16 Change in Volumetric Water Content within the MMB (a) at the interface of Geotextile 1 and the Geonet (b) at the interface of the Geonet and Geotextile 2.

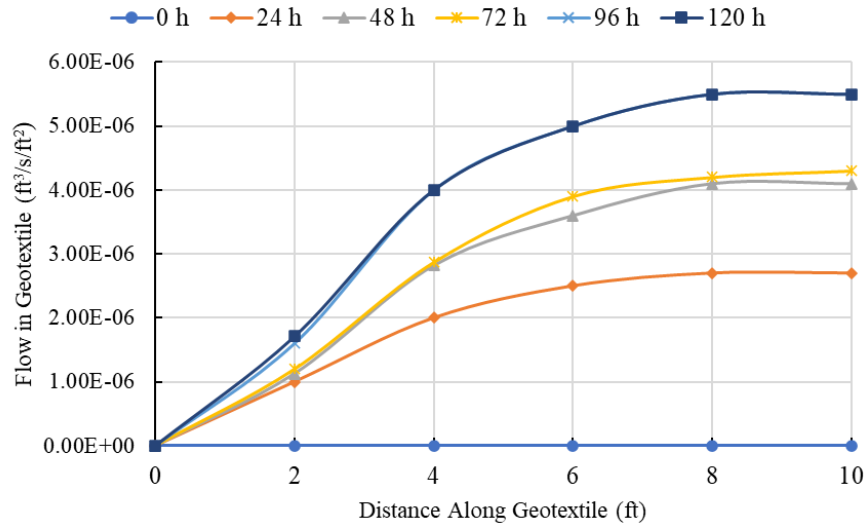
6.5.3 Flow Diversion Capacity of the MMB

The flow diversion capacity of the modified moisture barrier was evaluated by observing the flow within the geotextile and geonet with respect to the distance along the sloping portion of the MMB, as presented in Figure 6-17 (a) and (b), respectively. For this purpose, a rainfall intensity of 0.15 in/h was adapted, and it was applied uniformly for a period of 5 days.

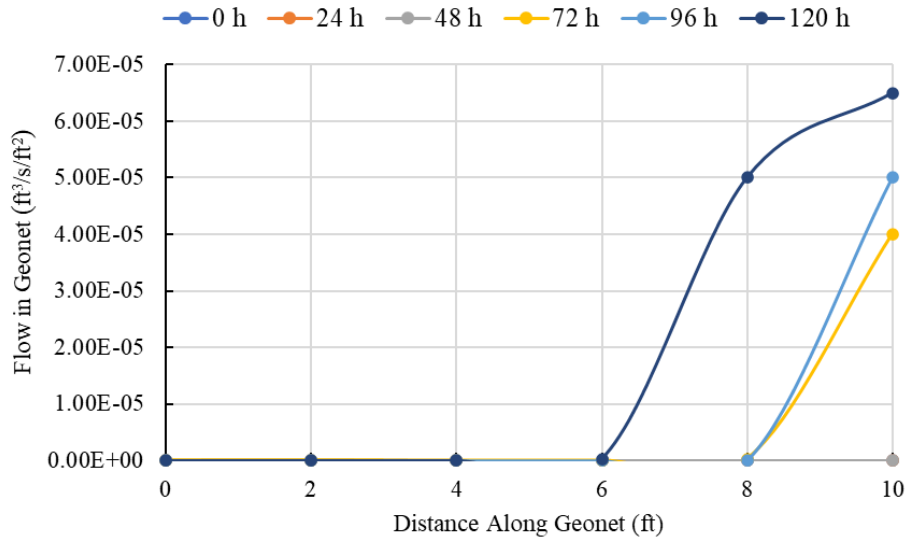
As seen in Figure 6-17 (a), flow within the geotextile does not occur as soon infiltration takes place. Once the wetting front reaches the soil-geotextile interface, further advancement is halted owing to the different water characteristics of soil and geotextile (Iryo and Rowe, 2005). Flow into the geotextile begins when the porewater pressure of the soil immediately above the geotextile exceeded the water entry value of the geotextile. Flow into the geotextile is observed to begin after 24 hours of rainfall infiltration. Once the flow within the geotextile began, it increased until it

reached the maximum lateral flow capacity of the geotextile and then became constant towards the downdip end of the slope.

Once the flow withing the geotextile reached its maximum capacity and the pore pressure at the bottom of the geotextile became equivalent to atmospheric pressure, flow into the geonet occurs towards the lower end of the slope. With time, the zone where there is flow into the geonet extended towards the upper part of the slope. For instance, flow into the geonet begins at a distance of 6 feet at $t = 120$ h, while that was at 8 feet at $t = 96$ h. All the flow entering the geonet continues to flow within the geonet layer to the presence of the impermeable geomembrane underneath.



(a)



(b)

Figure 6-17 Development of infiltration into MMB (a) Flow in geotextile (b) Flow in geonet.

6.5.4 Diversion Length of the MMB

In a slope installed with a modified moisture barrier, water diverts twice during infiltration: first at the soil-geotextile interface and second at the interface of the geotextile and the geonet within the geocomposite. This is due to the difference in the hydraulic characteristic of the soil, the geotextile and the geonet. The distance from the upper end of the slope to the point where the flow into the geonet begins, is defined as the diversion length in this study as shown in Figure 6-18. Variation of flow in the geonet is assessed by varying the rate of rainfall infiltration and slope angles and the results are presented in Figure 6-19 and Figure 6-20, respectively. As rainfall intensity (infiltration rate) decreases, flow in the geonet occurs towards the lower part of the slope. On the other hand, with increasing slope angle, the zone over which there was no flow in the geonet, decreases. In other words, steeper slopes provide a more extensive capillary barrier. Therefore, maximum lateral flow capacity increases with higher slope angles. In conclusion, the diversion length of the modified moisture barrier is a function of the permeability of the geotextile,

infiltration rate and slope angle. Analytical solutions exist in literature for different capillary barriers, and they have been discussed in the following sections.

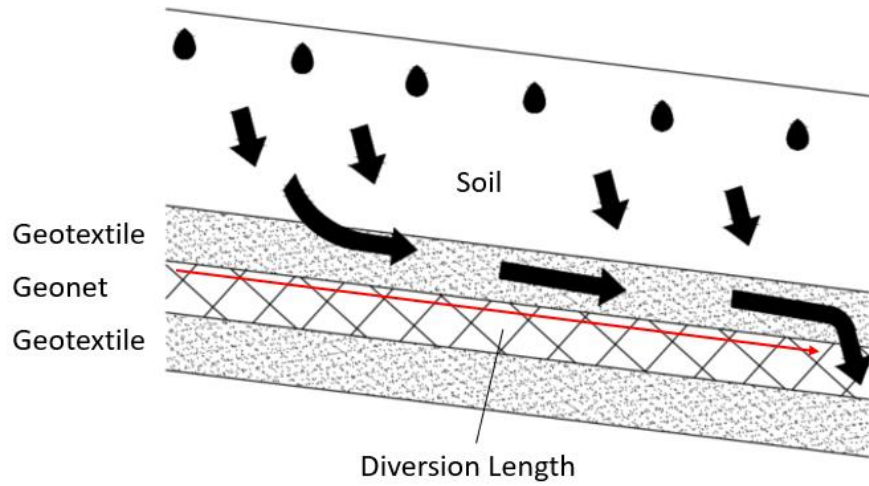


Figure 6-18 Schematic of flow diversion for MMB in slope.

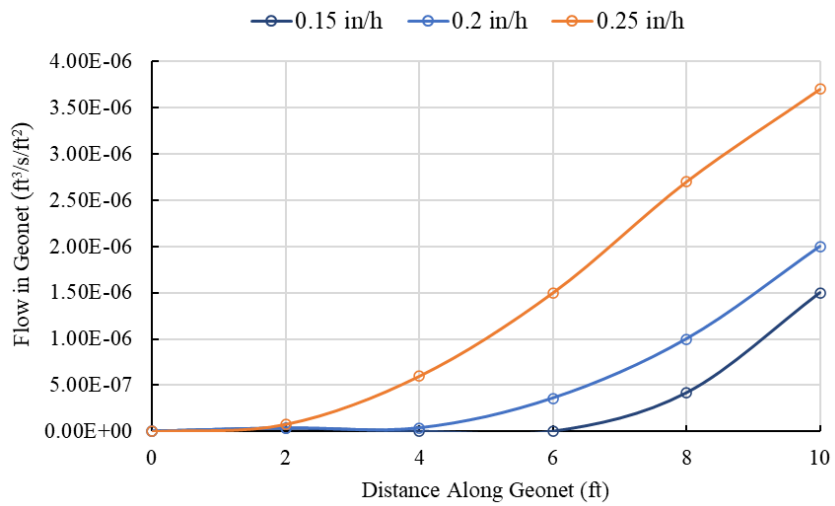


Figure 6-19 Flow in geonet with various rainfall intensity.

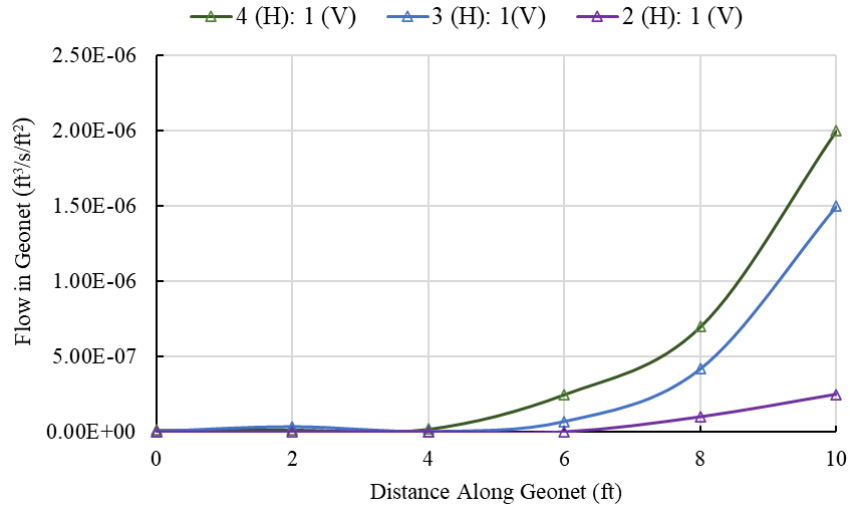


Figure 6-20 Flow in geonet with various slope angles.

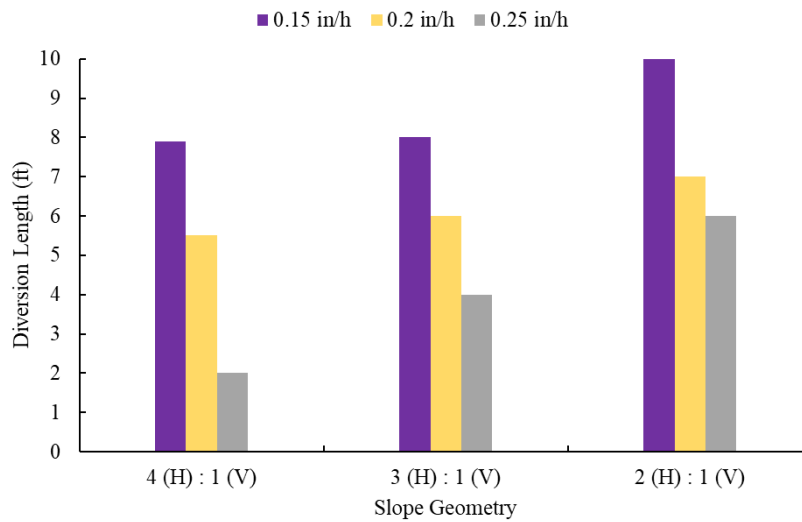


Figure 6-21 Diversion length against slope inclination.

6.5.4.1 Comparison with Analytical Solutions

Ross (1990)

In a capillary barrier system, infiltrated water is diverted laterally towards the downdip direction.

As infiltration increases, the volume of water moving laterally increases and it reaches a point

where the capillary barrier effect is no longer able to drain infiltration and water enters the underlying coarse layer. The diversion length has been defined as the length in the down-dip direction to a point where the barrier does not divert any additional water and a downward flux is experienced in both the fine and coarse layers. Ross (1990) proposed an analytical solution for the length of fully effective capillary barrier system as follows:

$$L < \frac{k_s \tan \phi}{q\alpha}$$

Where K_s is the saturated hydraulic conductivity of the fine layer, ϕ is the slope angle, q is the infiltration rate and α is the sorptive number of the fine-grained soil.

Stormont (1996)

Stormont (1996) studied the effectiveness of two sloping capillary barriers and proposed that the diversion length can be estimated as follows:

$$L = \frac{K \sin \phi b}{q}$$

Where b is the thickness of the transport layer, ϕ is the slope inclination and q is the infiltration rate.

Stormont and Stockton (2000)

Stormont and Stockton (2000) suggested that drainage capacity of the geocomposite capillary barrier is limited by the transmissivity of the transport layer. The maximum diversion length of a geocomposite capillary barrier system is given by the following equation:

$$L = \frac{\theta}{q} i$$

where L is the diversion length, θ is the saturated transmissivity, q is the infiltration flux rate and i is the gradient.

Comparison

In the current study the diversion length of the MMB has been obtained using the proposed analytical solutions in literature and compared to that obtained from the numerical model as shown in Figure 6-22. The diversion length obtained from the numerical analysis of the current study most closely agrees with the analytical solution proposed by Stormont (1996). The difference in diversion obtained from the analytical solution proposed by Stormont and Stockton (2000) and the numerical analysis is about 8 %. This difference can be attributed to the transmissivity of the geocomposite. While it was suggested to use the saturated transmissivity of the geotextile, for the purpose of calculation the manufacture provided transmissivity value has been utilized. Lastly, the result of the numerical analysis had the highest difference, of approximately 23%, with the solution proposed by Ross (1990). This difference can be attributed to the inaccurate estimate of the sorptive number.

Furthermore, although breakthrough into the geonet does occur, it should be noted that the underlying layer of impermeable geomembrane does not let water to infiltrate into the underlying soil. As a result, the MMB remains effective as a moisture barrier.

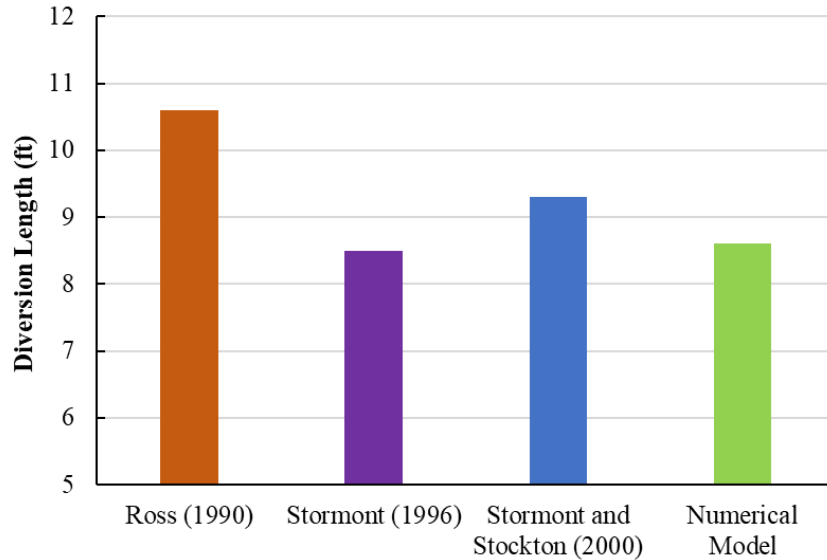


Figure 6-22 Comparison of flow diversion length obtained from numerical study and analytical solutions.

Therefore, the diversion length of the MMB can be obtained by using adapting the analytical solution proposed by Stormont (1996) as follows:

$$L_B = \frac{k \sin \beta b}{q_i}$$

where L_B is the length of MMB along the slope, k is the in-plane permeability of the geotextile, β is the slope angle, b is the thickness of the geotextile layer and q_i is the design infiltration rate. In some cases where flow is diverted laterally above the geotextile, the flow entering the geonet is lower than the amount of infiltrated water. In such cases, L_B derived using the above equation is conservative. It should be noted that the in-plane flow capacity of the geotextile may be affected by several factors over time resulting in reduced performance of the material.

6.6 Effect of Length of MMB on Slope Stability

When a slope section is constructed with MMB, the initial factor of safety of the slope is presumed to increase. As observed from the field performance monitoring results in section 5.2, the MMB can effectively reduce fluctuation of volumetric water content and soil matric suction, compared to a natural slope. Since matric suction is preserved in the soil underneath the MMB, it has higher shear strength which results in an overall increase in the factor of safety of the slope. The length of MMB along the slope has been increased from 10 feet to 35 feet with 5 feet increments each time and the corresponding porewater pressure profile generated as a result of the transient seepage analysis is presented in Figure 6-23. It is observed that as the length of MMB along the slope increases, the portion of the slope that loses its matric suction due to rainfall infiltration decreases. The soil underneath the MMB is able to maintain negative porewater pressure hence resulting in higher shear strength.

Consequently, the effect of increase in length of MMB along the slope, on its factor of safety is assessed through a coupled slope stability analysis. The change in FOS with respect to length of MMB along slope is presented in in Figure 6-24. For the current study, the factor of safety for 10 ft. of MMB along the slope was approximately 1.4. According to the TxDOT Geotechnical Manual, a minimum factor of 1.3 is required for both long term drained condition and short-term undrained condition. It is further recommended to ensure a factor of safety of 1.5 or greater slopes that support buildings, critical utilities or other installations that have a low tolerance of failure. Therefore, the current 10 feet of MMB is sufficient to meet TxDOT FOS requirement. As the length of the MMB is increased along the slope, the factor of safety increases to approximately 2.2. It should be noted that this variation of FS of the slope due to the length of MMB is only applicable for the current study condition. A comprehensive parametric study is presented in

Section 6.8 to study the influence of length of MMB along with variation of other important slope stability factors.

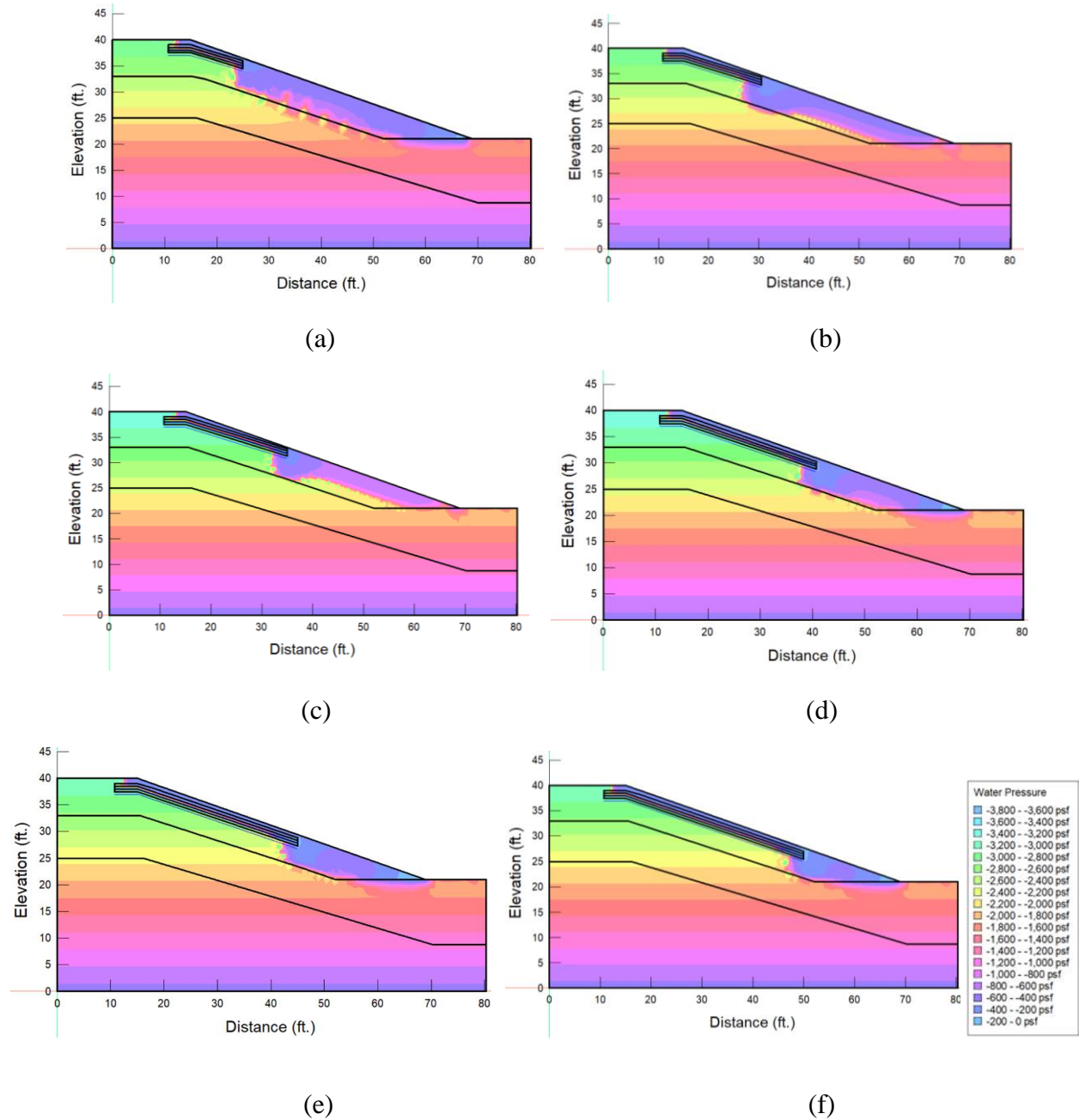


Figure 6-23 Porewater pressure profiles for different lengths of MMB along slope (a) 10 ft. (b) 15 ft. (c) 20 ft. (d) 25 ft. (e) 30 ft. (f) 35 ft.

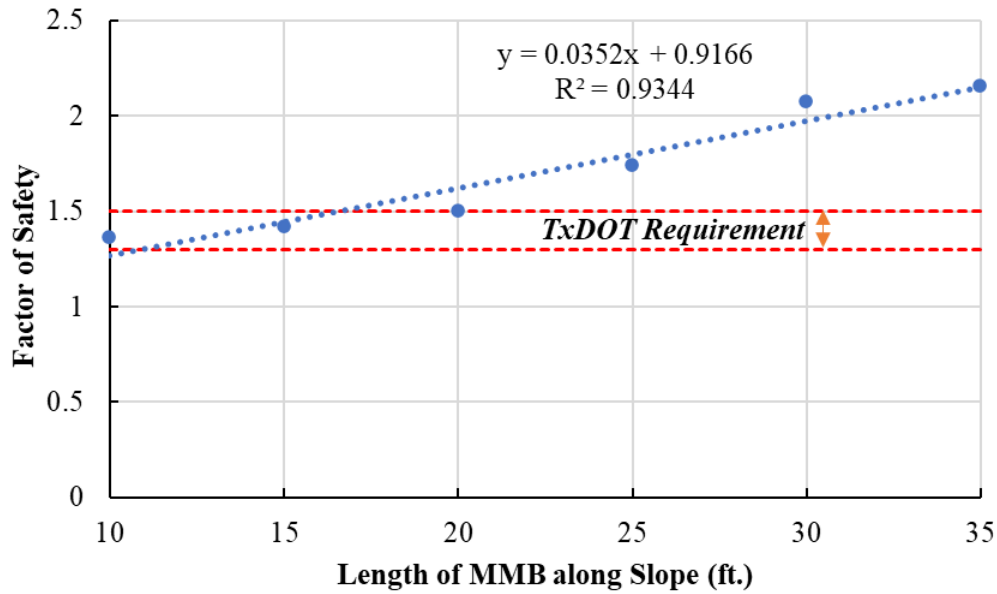


Figure 6-24 Effect of length of MMB on slope stability.

6.7 Effect of Rainfall on Slope Stability

The primary objective of using a modified moisture barrier in slope stabilization is to reduce infiltration of rainwater into the slope soil. If the intrusion of rainwater can be controlled, the fluctuation of volumetric water content of the soil will be reduced and as a result the matric suction of the soil will be preserved. The existence of matric suction increases the shear strength of the soil. Hence the overall stability of the slope will be higher. A slope of with a factor of safety of 1, representing unstable conditions is shown in Figure 6-25. In order to evaluate the performance of a MMB stabilized slope when subjected to rainfall, compared to other methods, three slope stabilization methods are considered in this section: (a) Recompacted slope (b) Slope stabilized with recycled plastic pins and (c) Slope stabilized with the modified moisture barrier.

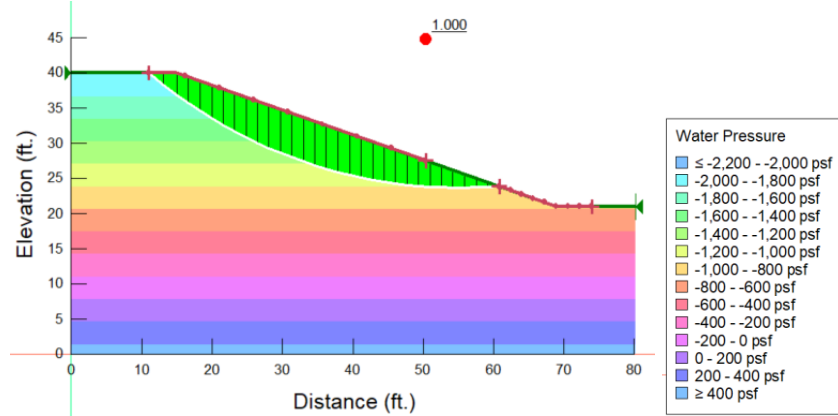


Figure 6-25 Slope at failure

Recompacted slope

Slope re-compaction is the most common method of repair. The failed soil mass is pushed back and recompacted to attain the required density. The shear strength of the soil increases which increases the factor of safety as shown in Figure 6-26 (a). When subjected to rainfall infiltration, the topsoil layer gets saturated and experiences an increase in porewater pressure. As the soil loses matric suction, the FS of the slope reduces as shown in Figure 6-26 (b).

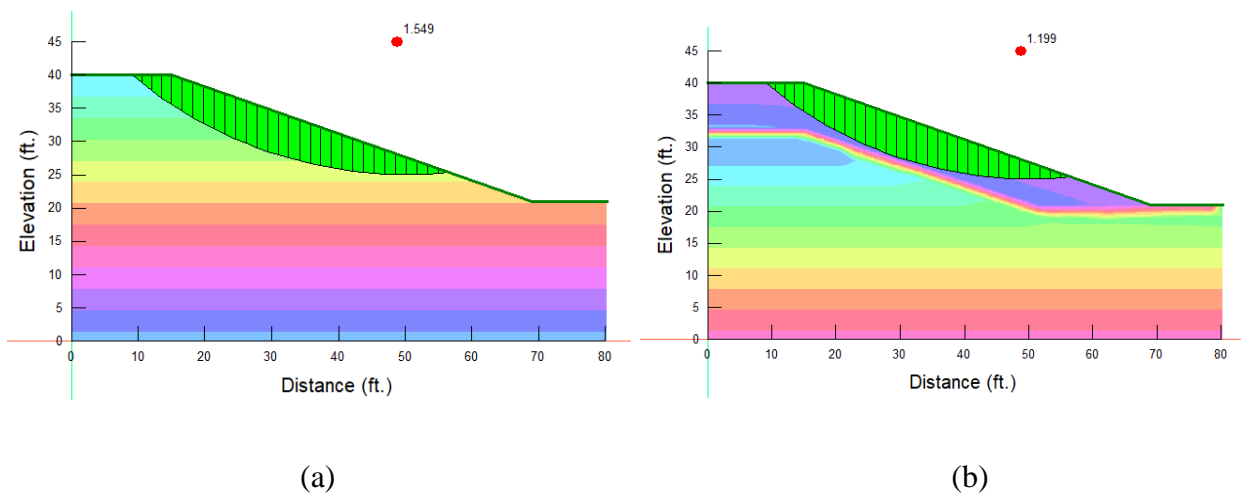


Figure 6-26 Factor of safety of recompacted slope (a) Initial (b) After Rainfall.

Slope stabilized with RPP

Recycled plastic pins stabilize a slope by providing additional resistance against the mobilized shear stress of the soil. The design of the RPP stabilized slope was done in the numerical model according to the field test section. Commercially available 10 feet long RPPs were used with a 3 ft. c/c spacing at the crest, 5 ft. c/c spacing at the middle and 4 ft. c/c spacing at toe. Additionally, the RPPs were 8 feet and 7 feet in length at the middle portion and toe of the slope respectively. Reinforcement of the slope with RPPs yielded a FS of 1.7 as shown in Figure 6-27 (a). Once the slope was subject to rainfall infiltration, the top layer of soil to a depth of approximately 6 feet developed positive porewater pressure. Hence the FS of the slope dropped to 1.452 due to rainfall infiltration.

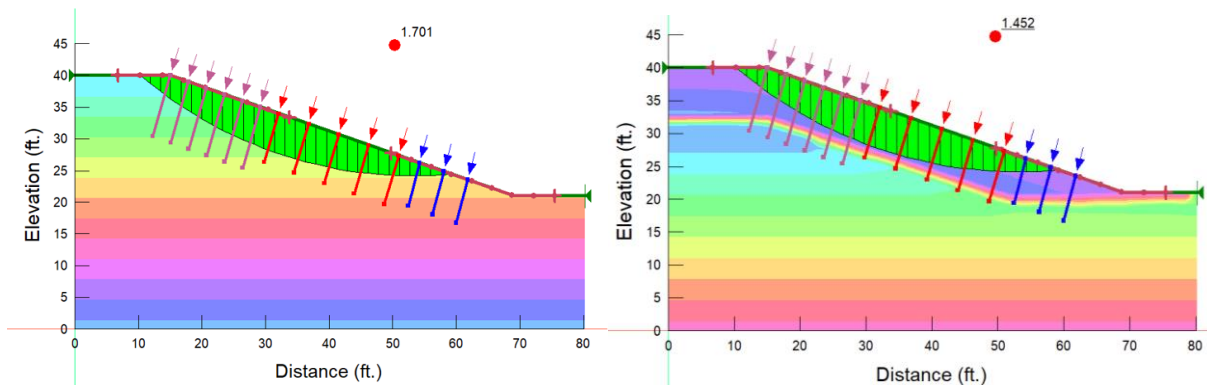


Figure 6-27 Factor of safety of slope stabilized with RPP (a) Initial (b) After Rainfall.

Slope stabilized with MMB

A modified moisture barrier stabilizes a slope by enhancing drainage of infiltrated rainwater and preventing further intrusion into the underlying soil. MMB was added to the numerical model with 10 feet length along the slope and 4 feet towards the crest. The initial FS of the slope was observed to be 1.354 as shown in Figure 6-28 (a). When subjected to rainfall infiltration, the soil underneath

the MMB is able to preserve matric suction. Therefore, a lesser portion of the slope area develops positive porewater pressure. The FS of the slope decreased to 1.253.

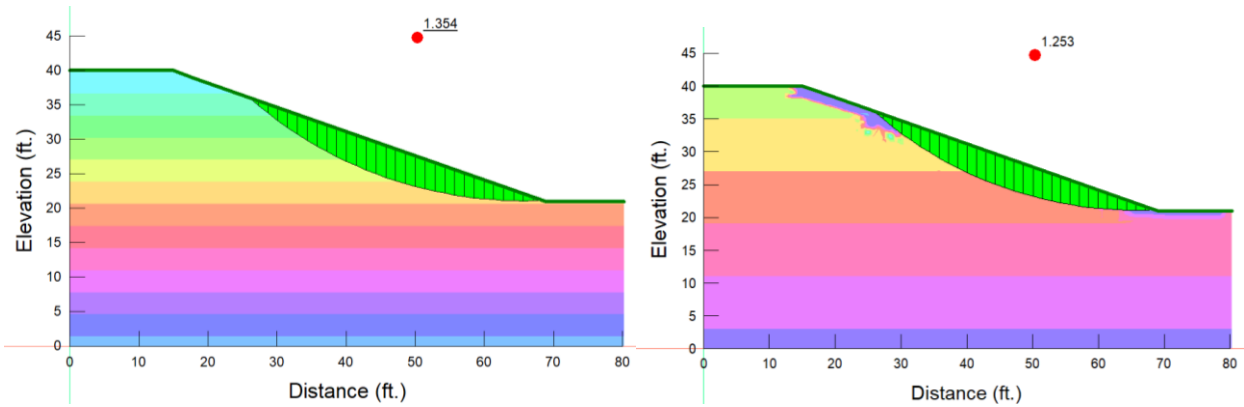


Figure 6-28 Factor of safety of slope stabilized with MMB (a) Initial (b) After Rainfall.

Comparison

The three stabilization methods discussed above have been compared in terms of the percentage reduction of FS due to rainfall infiltration, as shown in Figure 6-29. A recompacted slope experiences 23 % with respect to its initial FS after construction while that of the RPP stabilized slope is 15 %. In comparison, the MMB stabilized slope experiences the least FS reduction of 7 %. Although the FS of a MMB stabilized slope is not as high as that of a mechanically stabilized

slope (for example RPP), it will experience lower reduction of factor of safety over time when subjected to climatic variation.

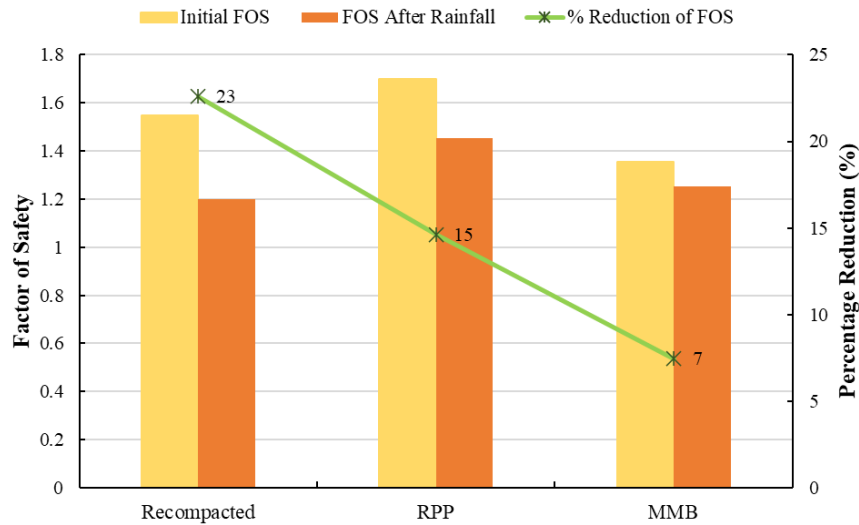


Figure 6-29 FS reduction due to rainfall for different stabilization methods.

6.8 Parametric Study

After the calibration of the numerical model, a parametric study was conducted to investigate the effect of varying soil shear strength properties, soil hydraulic properties, rainfall intensity, slope geometry, and moisture barrier parameters on slope stability. The stability of slope is determined by the factor of safety, where the strength required to maintain state of limiting equilibrium, is compared to the shear strength of the soil along an assumed failure surface. The primary objective of the parametric study was to develop a comprehensive dataset to understand the behavior of a slope stabilized with a modified moisture barrier. A parametric study matrix was formulated as shown in Table 6-4, considering the probable controlling parameters. The range of each controlling parameter to determine the factor of safety of the slope were selected based on previous studies with similar conditions.

For the purpose of parametric study, soil properties of only layer 1 were varied. According to field performance monitoring data, fluctuations of moisture content due to climatic conditions were observed up to a depth of 5 feet. Furthermore, maximum lateral deformation of the slope was also observed near the ground surface. Therefore, it is hypothesized that the factor of safety of the slope will be mostly affected by the properties of soil layer 1.

The properties of the modified moisture barrier were kept constant and only the length of the barrier along the slope varied from 10 ft (as used in the current study) up to a length of 35 feet along the slope.

The parametric study was conducted in three steps: (a) SEEP/W: steady state analysis (b) SEEP/W: transient analysis (c) SLOPE/W: slope stability analysis. A transient seepage analysis was conducted by applying a uniform intensity rainfall over a period of 5 days or 120 hours. A period of 5 days has been chosen as the maximum duration in order to simulate the effect of antecedent rainfall. Antecedent rainfall is the rain that falls in the days immediately preceding a slope failure event (Au, 1998; Rahardjo et al., 2001; Cal and Ugai, 2004). It is important to take the effect of antecedent rainfall into account because in soils with low permeability (like clayey soil) there is lower possibility for drainage of water and hence a gradual build up in porewater pressure is likely (Rahardjo et al., 2001) which makes it critical in slope stability analysis. Results of the transient seepage analysis were then incorporated into SLOPE/W along with soil shear strength parameters to conduct the slope stability analysis.

Results of variation of the aforementioned parameters in slope stability are presented in the following sections of this chapter.

Table 6-4 Parametric Study Matrix.

Case	Slope Geometry		Shear Strength Properties		Hydraulic Properties	Rainfall Intensity, I (in/h)	Length of Barrier (ft)
	Slope Angle	Slope Height (ft)	Cohesion, c (psf)	Angle of Friction, ϕ (°)	Saturated Hydraulic Conductivity, k_s (ft/s)		
Base Case	3 (H): 1 (V)	15	70	8	1.00E-07	0.15	10
							15
							20
							25
							30
							35
1 (a)	2 (H): 1 (V) 2.5(H): 1 (V) 3.5 (H): 1 (V) 4 (H): 1 (V)	15	70	8	1.00E-07	0.15	10
							15
							20
							25
							30
							35
1 (b)	3 (H): 1 (V)	10	70	8	1.00E-07	0.15	10
		20					15
		25					20
		30					25
							30
							35
2 (a)	3 (H): 1 (V)	15	70	5	1.00E-07	0.15	10
				10			15
				15			20
				20			25
				25			30
							35
3	3 (H): 1 (V)	15	70	8	1.50E-07	0.15	10
					3.00E-07		15
					1.50E-06		20
					3.00E-06		25
					1.50E-05		30
							35

4	3 (H): 1 (V)	15	70	8	1.50E-07		10
						0.15	15
						0.2	20
						0.25	25
							30
	35						

6.8.1 Effect of Slope Geometry

In order to study the effect of slope geometry on factor of safety, two parameters were varied: slope angle and slope height. Based on the slope failure inventory developed by Islam (2021), slope failure events begin to occur as slope angles exceed 13°. Four different slope angles were considered, as shown in Figure 6-30, from 4 (H): 1 (V) [14°] to 2 (H): 1 (V) [26°] with the current study having a slope angle of 3.5 (H): 1 (V) [18°]. At first, a seepage analysis was conducted by applying a uniform rainfall of 0.15 in/h for a period of 5 days, while keeping all other factors constant. The generated seepage profile along with soil shear strength properties of the base model were used to carry out a slope stability analysis.

The effect of variation of slope angle on factor of safety of the slope (with 10 feet of MMB along the slope), is presented in Figure 6-31. As slope angle increases from 4 (H): 1 (V) to 2 (H): 1 (V), the initial FS of the slope is observed to decrease. This trend agrees with results obtained in previous numerical studies where the slope FS was observed to increase with decreasing slope inclination (Islam, 2021; Taher et al., 2022). With the application of constant rainfall, the factor of safety of the slopes are observed to decrease and the time taken for the slope to reach an unstable condition is dependent on the slope angle. Slopes with the greatest inclination 2H:1V required the least amount of time to reach a factor of safety of 1 while the slope with an inclination of 4H:1V requires the longest time.

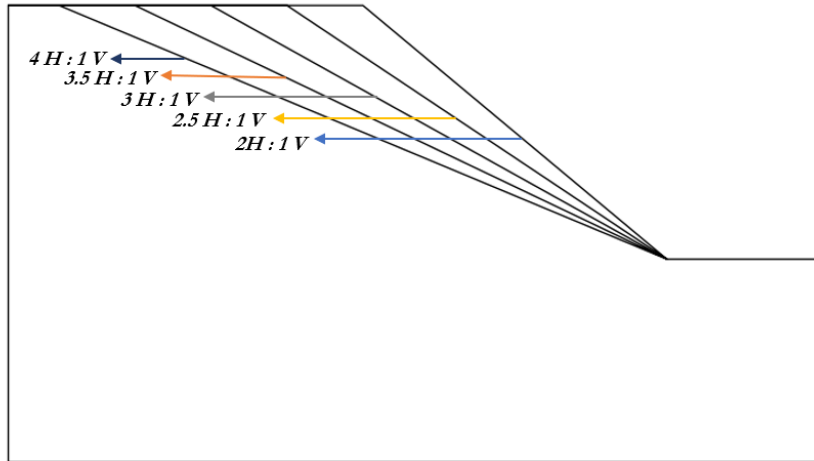


Figure 6-30 Schematic of slope angles used for parametric study.

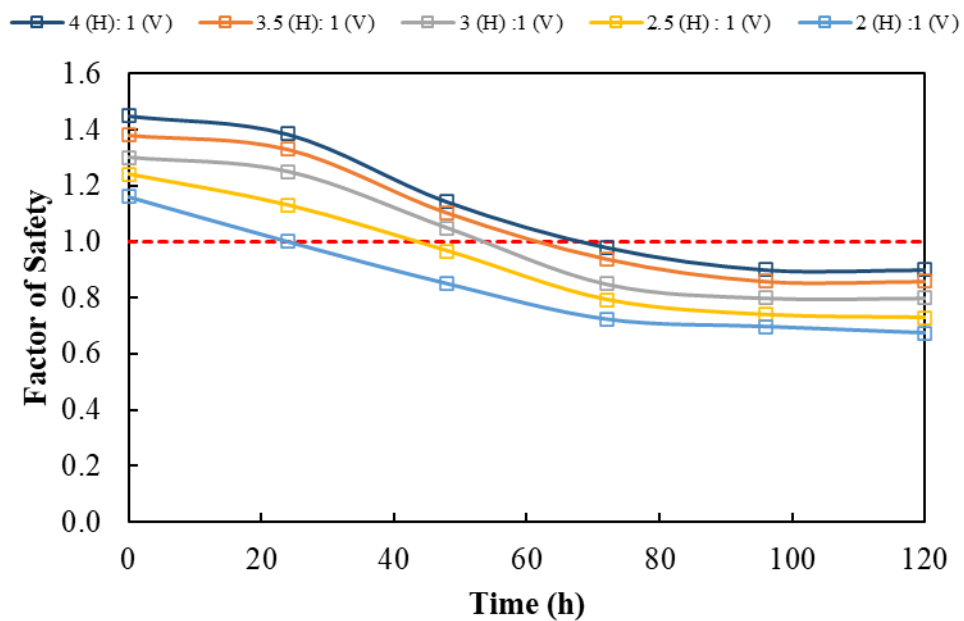


Figure 6-31 Effect of slope angle on factor of safety.

The combined effect of the slope angle and length of MMB along the slope was studied by varying the length of MMB along the slope from 10 feet to 35 feet for each slope inclination and the results are presented in Figure 6-33. A strong positive linear relationship was observed between length of MMB and slope factor of safety, at all slope inclinations. For example, in the current analysis a

slope with the least inclination 4 (H): 1(V) yielded the greatest FS with 35 feet of MMB along the slope. Although it is important to determine the initial factor of safety of a slope, the effect of rainfall on slope stability over time should also be considered. A constant rainfall intensity of 0.15 in/h was applied on slopes of all inclinations and the length of MMB was also varied for each slope angle and the results are presented in Figure 6-33. It is observed that as the length of MMB along the slope increases, the reduction of FS decreases when subjected to rainfall. When 20 feet of MMB is laid along the slope, the FS does not reduce to 1 for all slope inclinations. Moreover, for slope angles of 2.5H:1V and 2H:1V, once the length of MMB along the slope is 25 feet, no reduction of FS is observed. With higher slope angle, the maximum lateral flow capacity of the MMB increases. High slope inclination and increased length of MMB along the slope facilitates drainage of infiltrated rainwater preserving the overall FS of the slope.

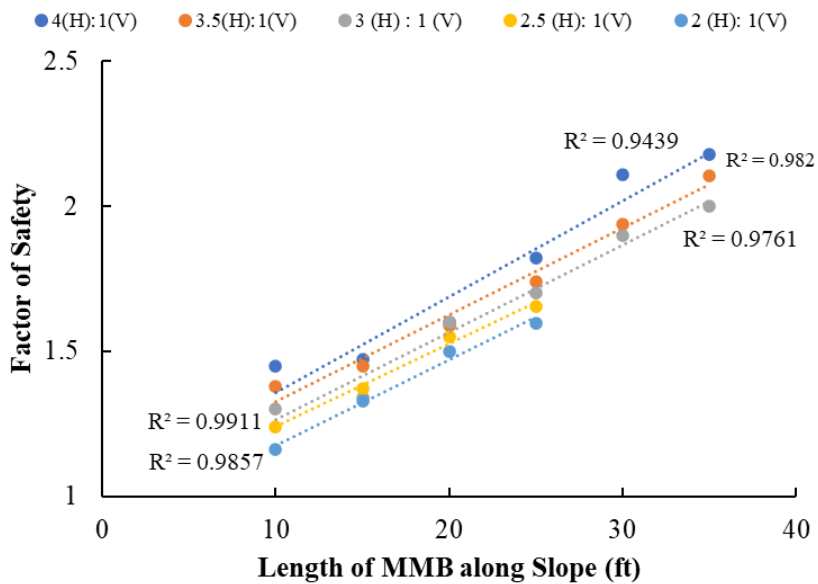


Figure 6-32 Variation of FS with respect to increase in MMB length for different slope inclination.

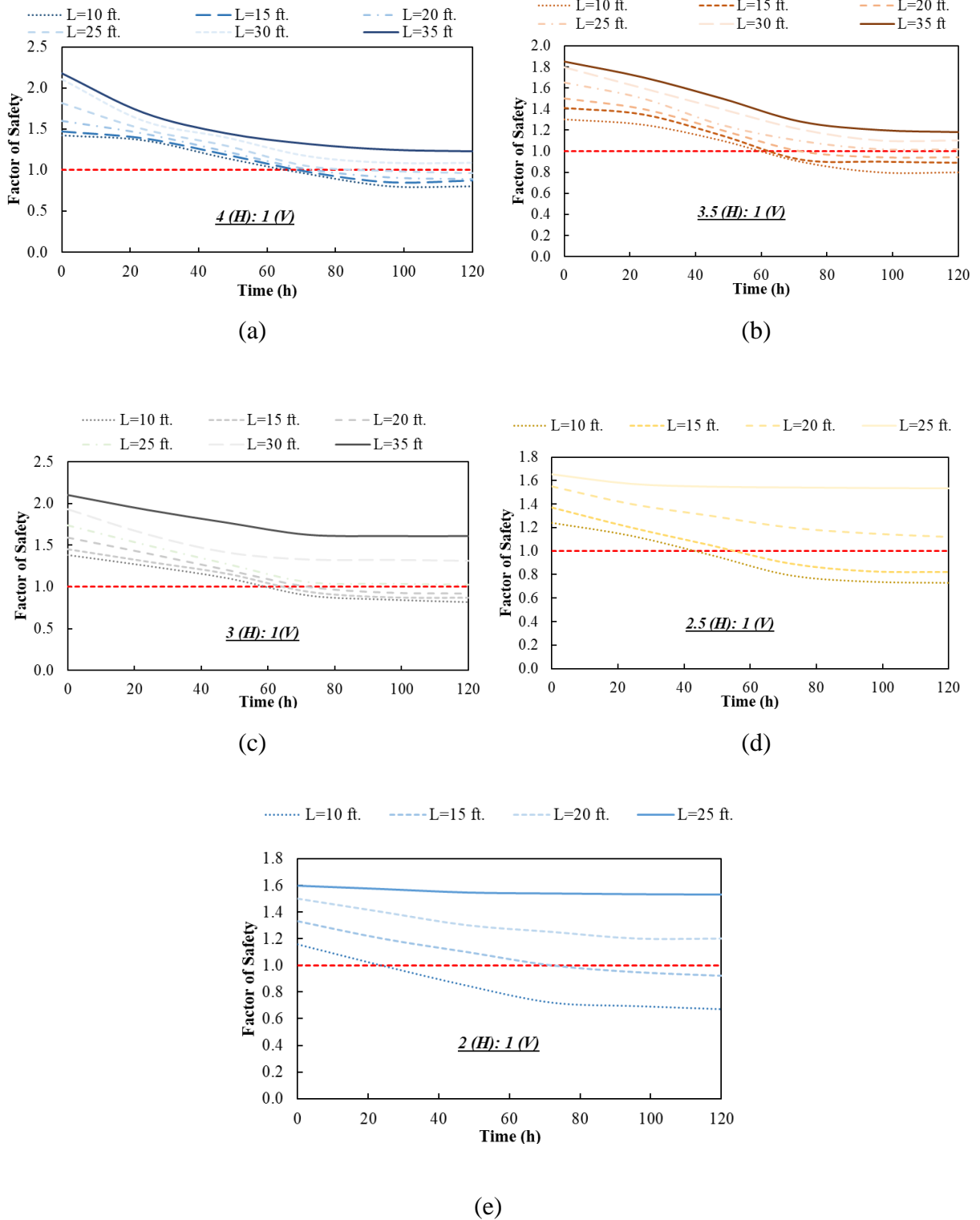


Figure 6-33 Combined effect of MMB and slope angle on FS of the slope (a) 4 (H): 1 (V) (b) 3.5 (H): 1 (V) (c) 3 (H): 1 (V) (d) 2.5 (H): 1 (V) (e) 2 (H): 1 (V).

The height of the slope has been varied from 10 feet to 30 feet as shown in Figure 6-34, with the current study having a slope height of 15 feet, keeping all other factors constant. Results of the transient seepage analysis with constant rainfall of 0.15 in./h is incorporated into the slope stability analysis and the results are presented in Figure 6-35. In general, for a constant length of MMB along the slope, as the slope height increased, the factor of safety of the slope is observed to decrease due to the increase in slope area with increase in height. Therefore, larger areas are subjected to rainwater infiltration and subsequent reduction of soil shear strength. When subjected to rainfall, factor of safety of slopes with greater heights reduce to 1 while that of slope with a height of 10 feet does not reach unstable condition.

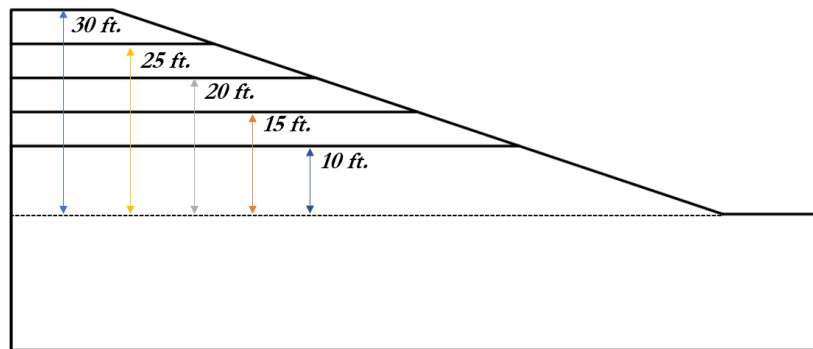


Figure 6-34 Schematic of slope height range used in parametric study.

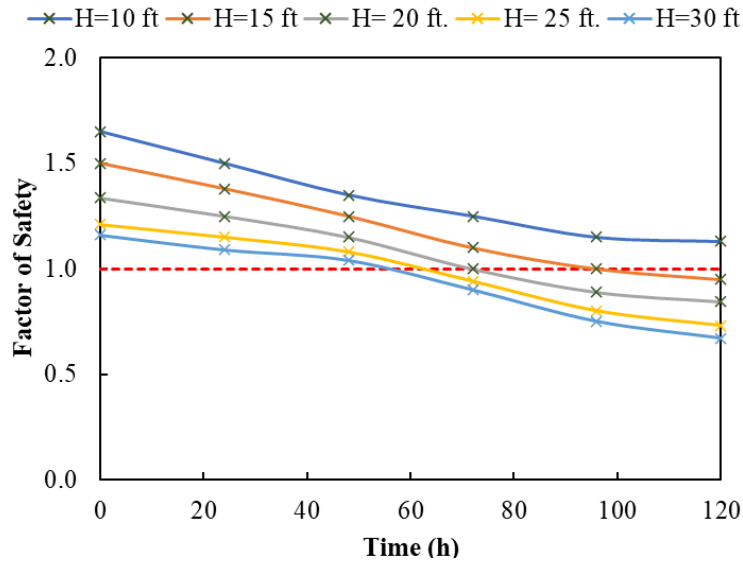


Figure 6-35 Effect of slope height on factor of safety.

The effect of length of MMB along the slope was studied by varying the length of MMB from 10 feet to 35 feet for each slope height and the results are presented in Figure 6-36. In general, as the length of the MMB is increased along the length of the slope, the FS is observed to increase for all slope heights. Additionally, slopes of lower heights yielded higher factor of safety. For instance, slope with height of 10 feet and 35 feet of MMB yielded the greatest FS. Furthermore, the effect of rainfall on slope stability was also studied with changing slope height and length of MMB and the results are shown in Figure 6-37. It is observed that with increase in MMB length, the time taken for the slope to reach a FS of 1 (unstable condition) increases. However, for slope heights greater than 20 feet, even the maximum studied length of 35 feet of MMB is not sufficient to maintain the stability of the slope, as the FS drops to 1 when subjected to rainfall infiltration. On the other hand, when the slope height is 10 feet, inclusion of 20 feet of MMB along the length of the slope maintains the factor of safety of the slope.

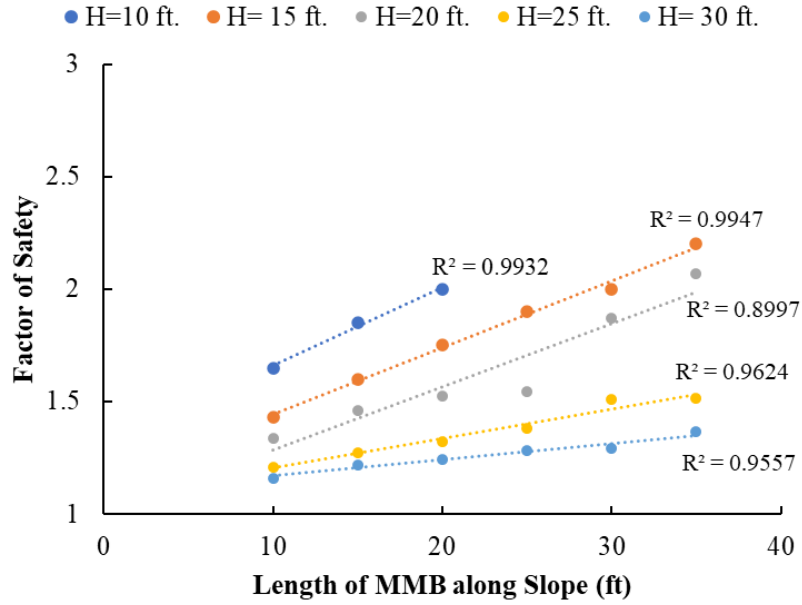
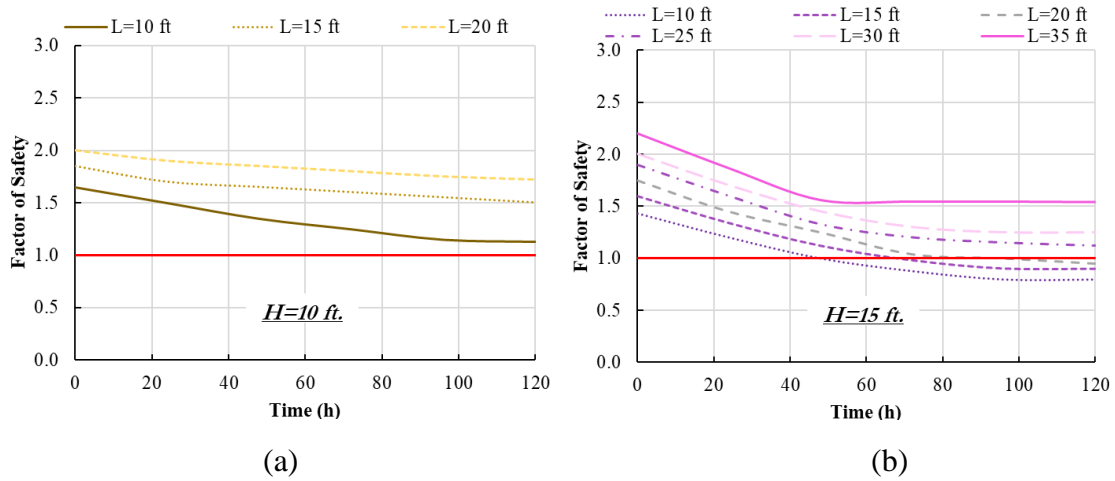


Figure 6-36 Effect of MMB on FOS for different slope heights.



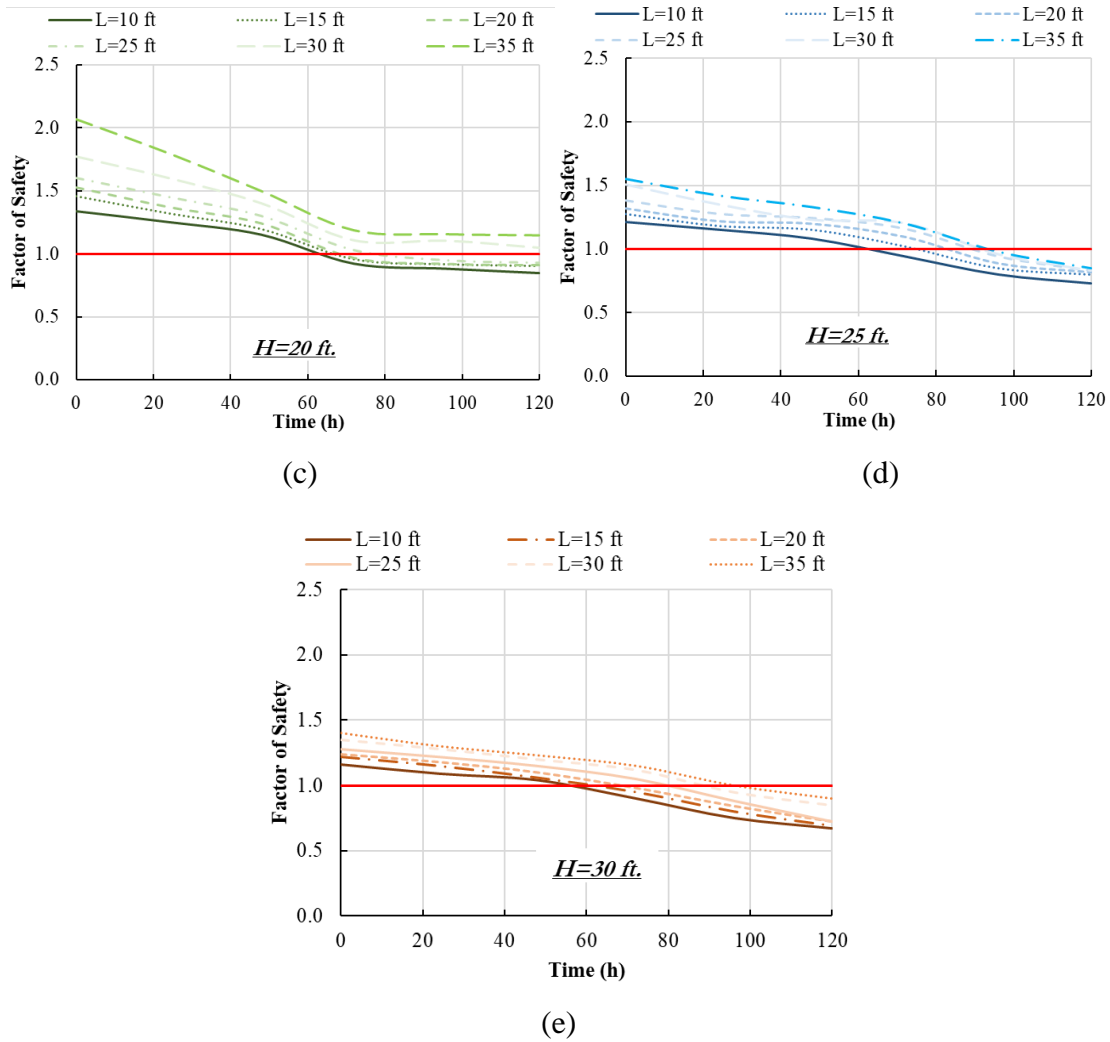


Figure 6-37 Combined effect of MMB and slope height on FS of slope (a) $H=10$ ft. (b) $H=15$ ft. (c) $H=20$ ft. (d) $H=25$ ft. (e) $H=30$ ft.

6.8.2 Effect of Soil Shear Strength Properties

In order to study the effect of soil shear strength properties on slope stability, cohesion, and angle of friction of soil layer 1 are varied, while keeping all other factors constant. Based on field performance monitoring of moisture fluctuation due to climatic conditions occurred within the top 5 feet which was determined to be the active zone. Shear strength properties of soil layer 1 are subjected to softening mechanism due to wet and dry cycles caused by seasonal variation. As a result, the change in factor of safety was assessed by varying properties of soil layer 1. Coupled

seepage and slope stability analyses were conducted by applying rainfall of 0.15 in/h for a period of 120 hours and varying the cohesion of the soil from 100 to 300 psf with the current study having a cohesion of 70 psf while keeping all other factors constant. Results of slope stability analysis are presented in Figure 6-38. The initial factor of safety of the slope is observed to increase with increasing cohesion of the soil. As rainfall is applied, the factor of safety of the slope is observed to decrease. This decrease becomes less evident with an increase in cohesion. At a cohesion of 300 psf, the factor of safety of the slope is maintained at an almost constant value. Furthermore, 10 feet of MMB along the slope is sufficient to maintain the stability of the slope since the FS does not reach the limiting value of 1.

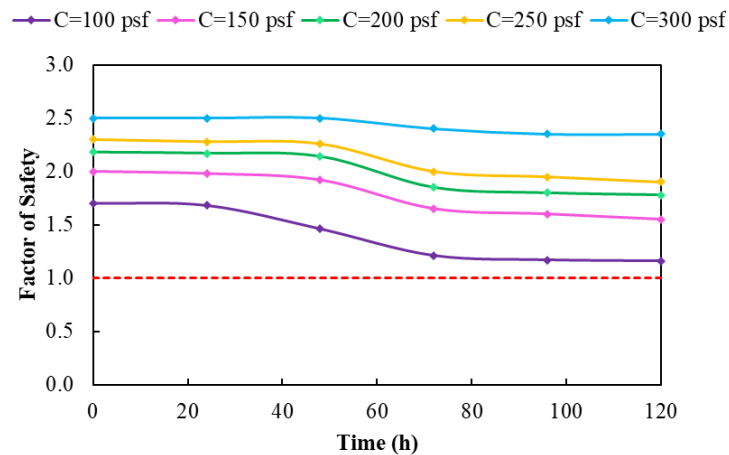


Figure 6-38 Effect of cohesion of factor of safety.

The effect of length of MMB along the slope for different cohesion of soil layer 1 has been assessed and the results are presented in Figure 6-39. As the length of MMB along the slope increases, the FS of the slope also increases which is represented by positive linear trendlines. For instance, the highest factor of safety is observed for 35 length of MMB along the slope when the cohesion of soil layer 1 was taken to be 300 psf. Furthermore, the effect of rainfall on the slope for various length of MMB and cohesion has been evaluated and the results are presented in Figure 6-40. As

rainfall is applied on the slope, the FS is observed to reduce over time, however slopes with higher length of MMB experience lower reduction of FS. At MMB length of 10 feet along the slope, the FS is sharply reduced when subjected to rainfall while that at a MMB length of 35 feet, is maintained at an almost constant value. This is because with higher length of MMB along the slope, greater area of the slope is protected from infiltration of rainwater and subsequent reduction of shear strength.

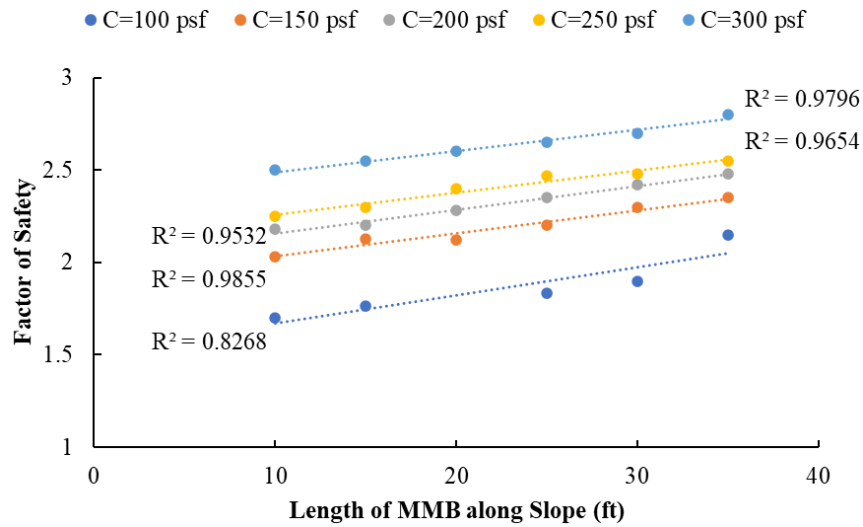
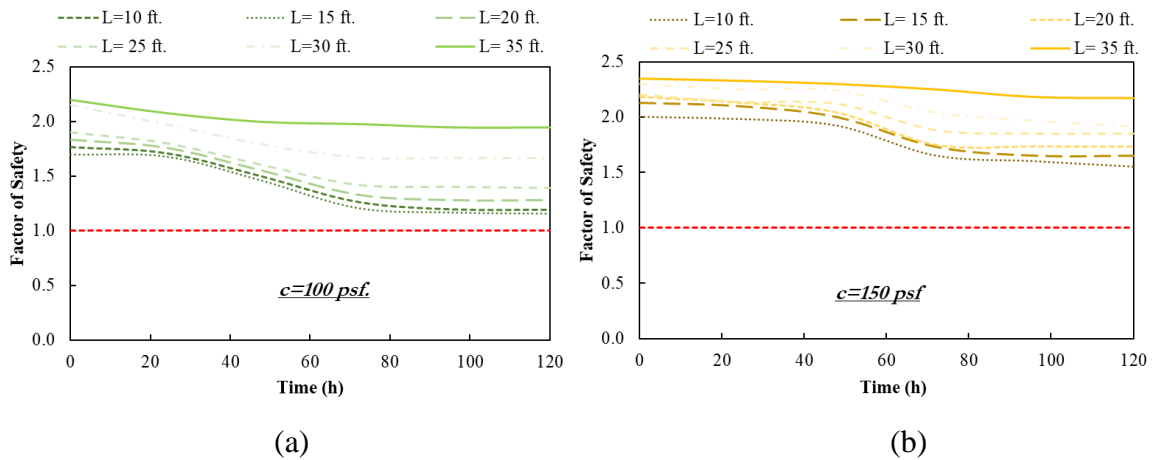


Figure 6-39 Effect of MMB on FOS for various cohesion.



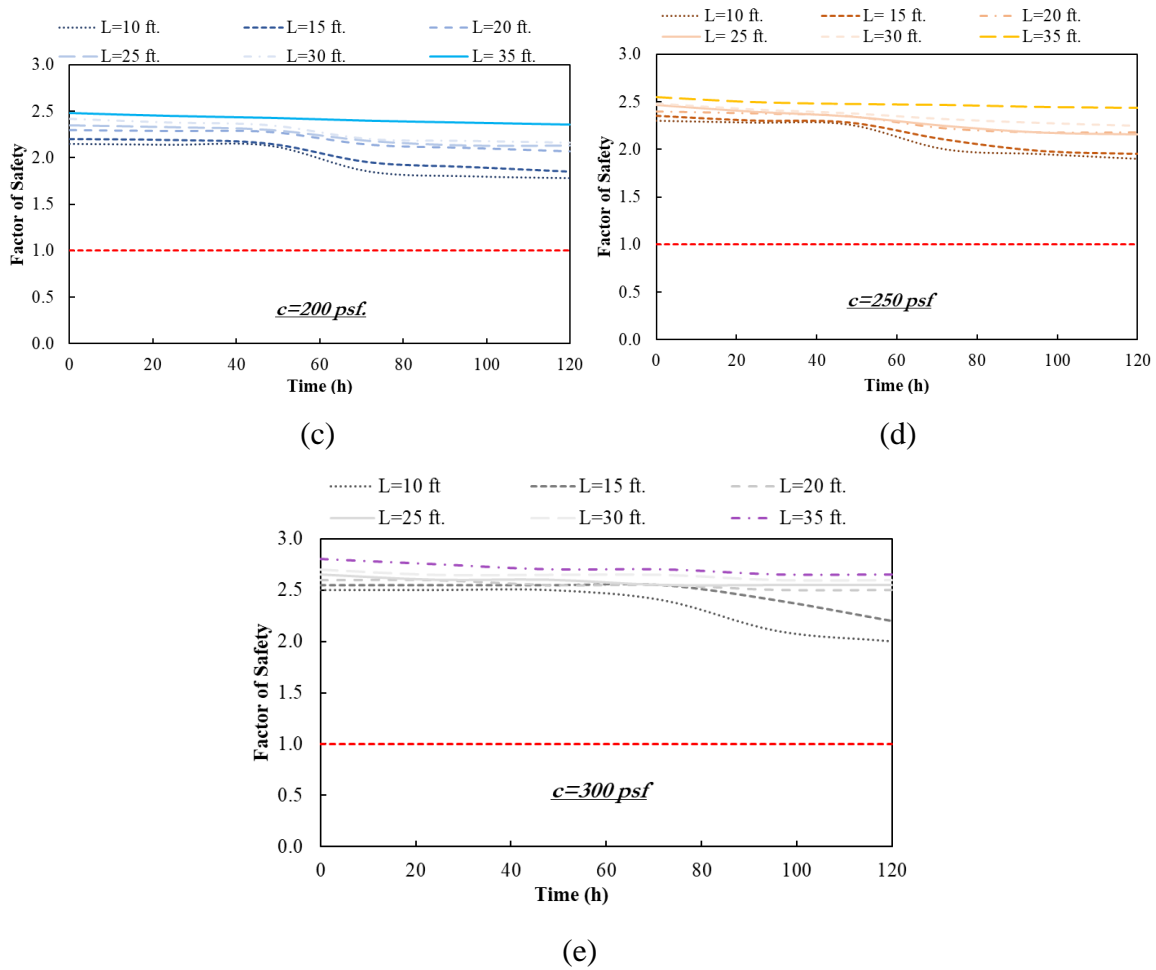


Figure 6-40 Combined effect of variation of MMB length and cohesion on FS of slope (a) $c=100$ psf (b) $c=150$ psf (c) $c=200$ psf (d) $c=250$ psf (e) $c=300$ psf.

Angle of friction of soil layer 1 has been varied from 5° to 25° with the current study having an angle of friction of 8° while keeping all factors constant to see its effect on FS of the slope. At first a transient seepage analysis was conducted by applying constant rainfall of 0.15 in/h over a period of 120 h. Porewater pressure generated from the seepage analysis was then used as input into the slope stability analysis along with soil shear strength parameters to observe the change of FS with time. As can be seen in Figure 6-41, with increase in soil friction angle, the initial FS of the slope increases. Similar trends have also been reported by Harabinova and Panulinova (2020). As the slope is subjected to rainfall, the FS is observed to decrease over time. At an angle of friction of

5°, the time taken for the slope to reach a factor of safety of 1 (unstable conditions) is around 40 hours while at an angle of friction of 25°, the FS of the slope does not decrease to 1 even after 120 hours. When the angle of friction reaches 15°, although the FS of the slope reduces, it does not reach the limiting value of 1.

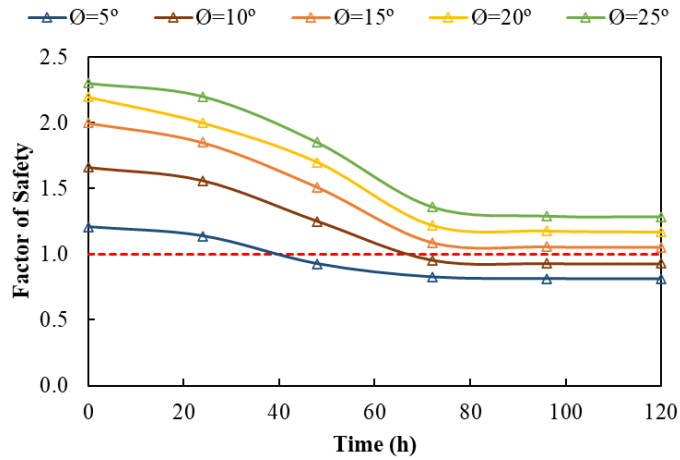


Figure 6-41 Effect of soil friction angle on slope stability at constant MMB length.

The effect of MMB on FS is also assessed for various values of angle of friction as shown in Figure 6-42. As the length of MMB along the slope increases, the FS of the slope increases. The effect of rainfall on slope stability is evaluated by varying of length of MMB along the slope and soil friction angle of soil layer 1 and the results are presented in Figure 6-43. When the slope is subjected to rainfall, the FS is observed to decrease. However, higher length of MMB along slope causes less reduction of FS due to rainfall infiltration over time. The time taken for the slope to reach a FS of 1 (unstable condition) increase with increase in MMB length. When the soil friction angle is increased to 20°, FS of the slope does not reach the limiting value of 1 for any length of MMB.

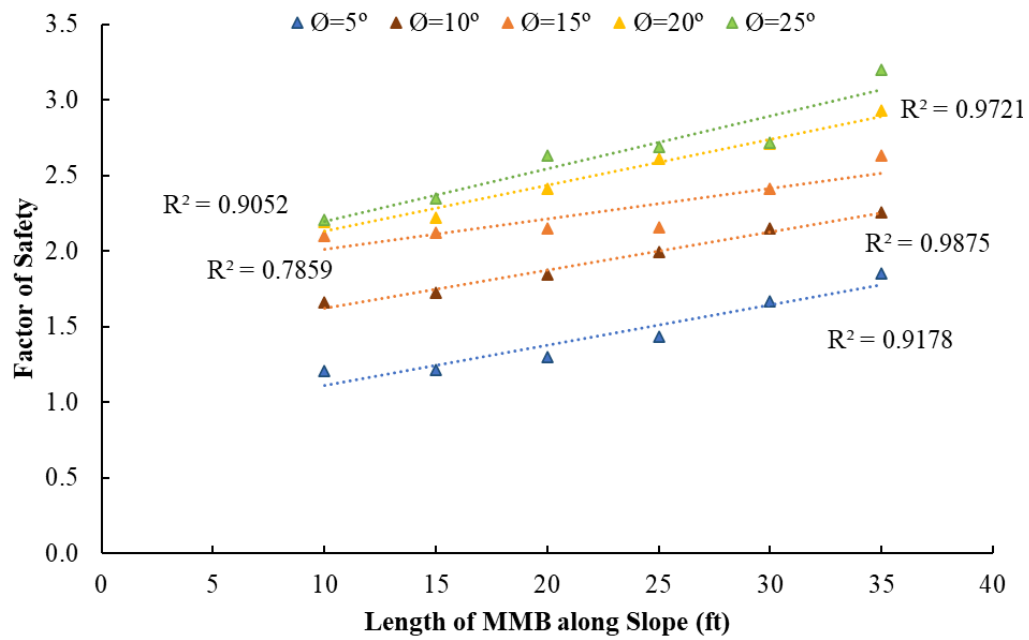
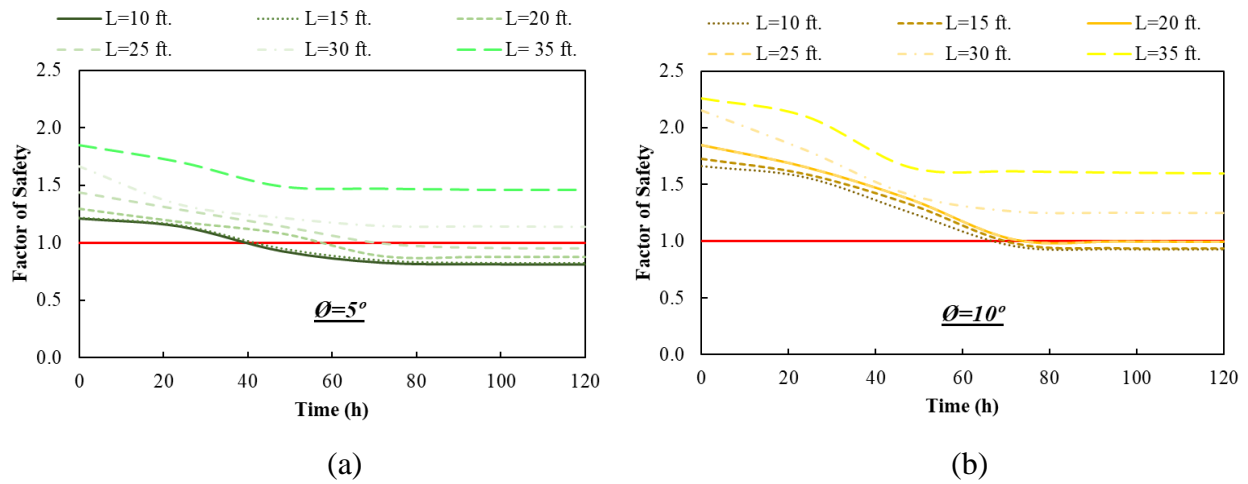


Figure 6-42 Effect of MMB on FOS for various angle of friction.



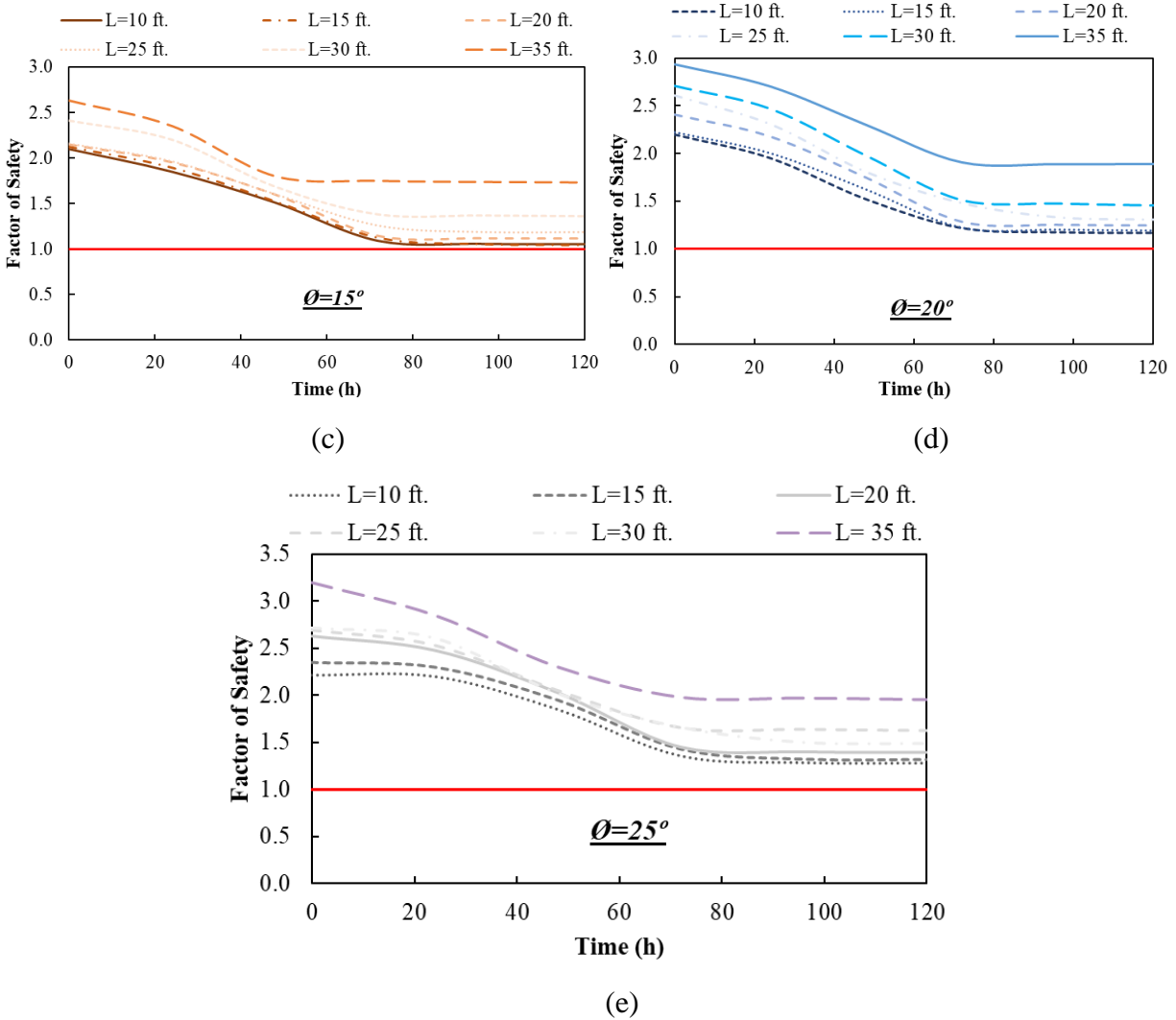


Figure 6-43 Combined effect of variation of MMB length and soil friction angle on FS of slope

(a) $\phi=5^\circ$ (b) $\phi=10^\circ$ (c) $\phi=15^\circ$ (d) $\phi=20^\circ$ (e) $\phi=25^\circ$.

6.8.3 Effect of Soil Hydraulic Properties

Soil hydraulic conductivity influences infiltration, seepage, pore water pressure buildup and hence slope stability. In order to see the effect of variation of hydraulic conductivity of the soil on slope stability, saturated permeability of soil layer 1 has been varied from 1.5×10^{-5} ft/s to 1.5×10^{-7} ft/s with the current study having a saturated permeability of 1×10^{-7} ft/s. At first, a transient seepage analysis was carried out while applying a rainfall of 0.15 in/h over a period of 120 h. Results of

the seepage analysis is used to run a slope stability analysis. The effect of variation of the hydraulic conductivity of soil layer 1 on slope stability is studied while keeping all other factors constant and the results are presented in Figure 6-44. Initial FS of the slope is not affected by change in soil hydraulic conductivity as the shear strength properties of the slope remain the same with changes in hydraulic conductivity. When subjected to rainfall infiltration, the FS of the slope is observed to decrease with time. Initially as rainfall is applied on the slope, the FS has a sharp reduction and then a constant value is maintained. This is because with rainfall infiltration the soil becomes saturated, and it impedes further infiltration, hence preserving the FS. As the hydraulic conductivity of the soil increases, it facilitates infiltration of water which results in the wetting front reaching greater depths. The porewater pressure increases to a greater extent and the FS of the slope is reduced. At low hydraulic conductivity, the FS of the slope experiences less reduction and does not reach the limiting value of 1.

The combined effect of variation of length of MMB along slope and hydraulic conductivity of soil layer 1 has been assessed and the results are presented in Figure 6-45. As the length of MMB along the slope increases, the initial factor of safety of the slope is considered to increase due to the new construction of the slope stabilized with MMB. With decrease in soil hydraulic conductivity, the length of MMB required along the slope also decreases. This is because, at lower soil hydraulic conductivity rainwater cannot infiltrate the slope and runoff takes place. As a result, there is a lower buildup of porewater pressure which in turn helps to maintain the stability of the slope. For instance, when the soil hydraulic conductivity is 1.5×10^{-7} ft/s even 10 feet of MMB along the slope is able to maintain the FS above the limiting value of 1 (unstable condition).

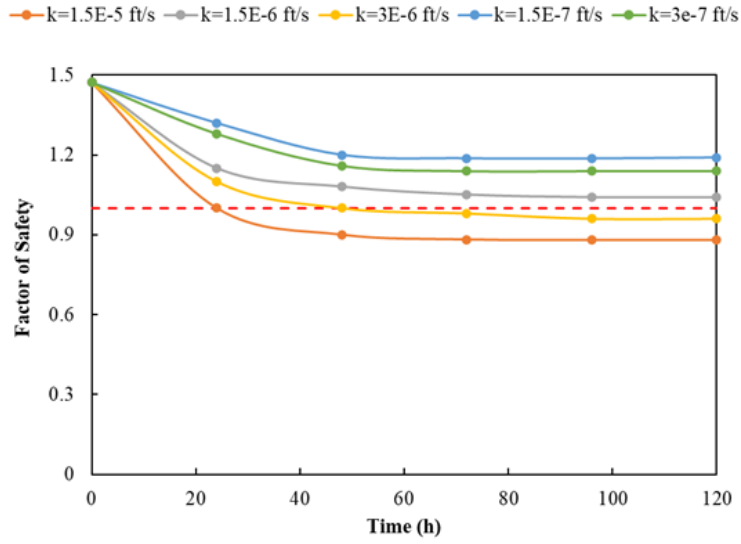
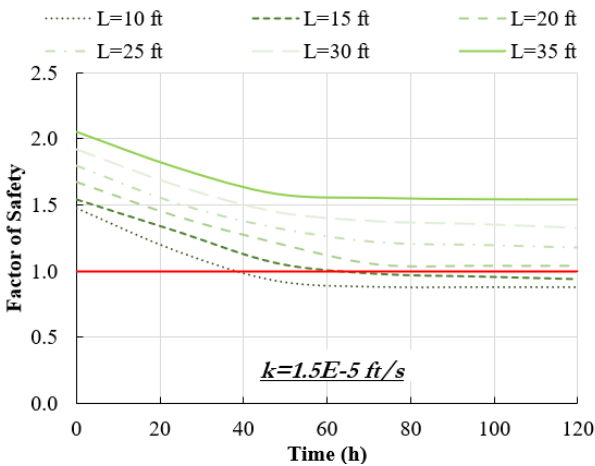
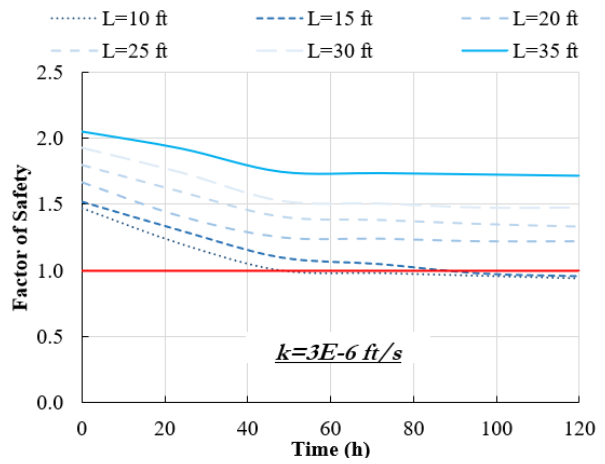


Figure 6-44 Effect of soil hydraulic conductivity on slope stability.



(a)



(b)

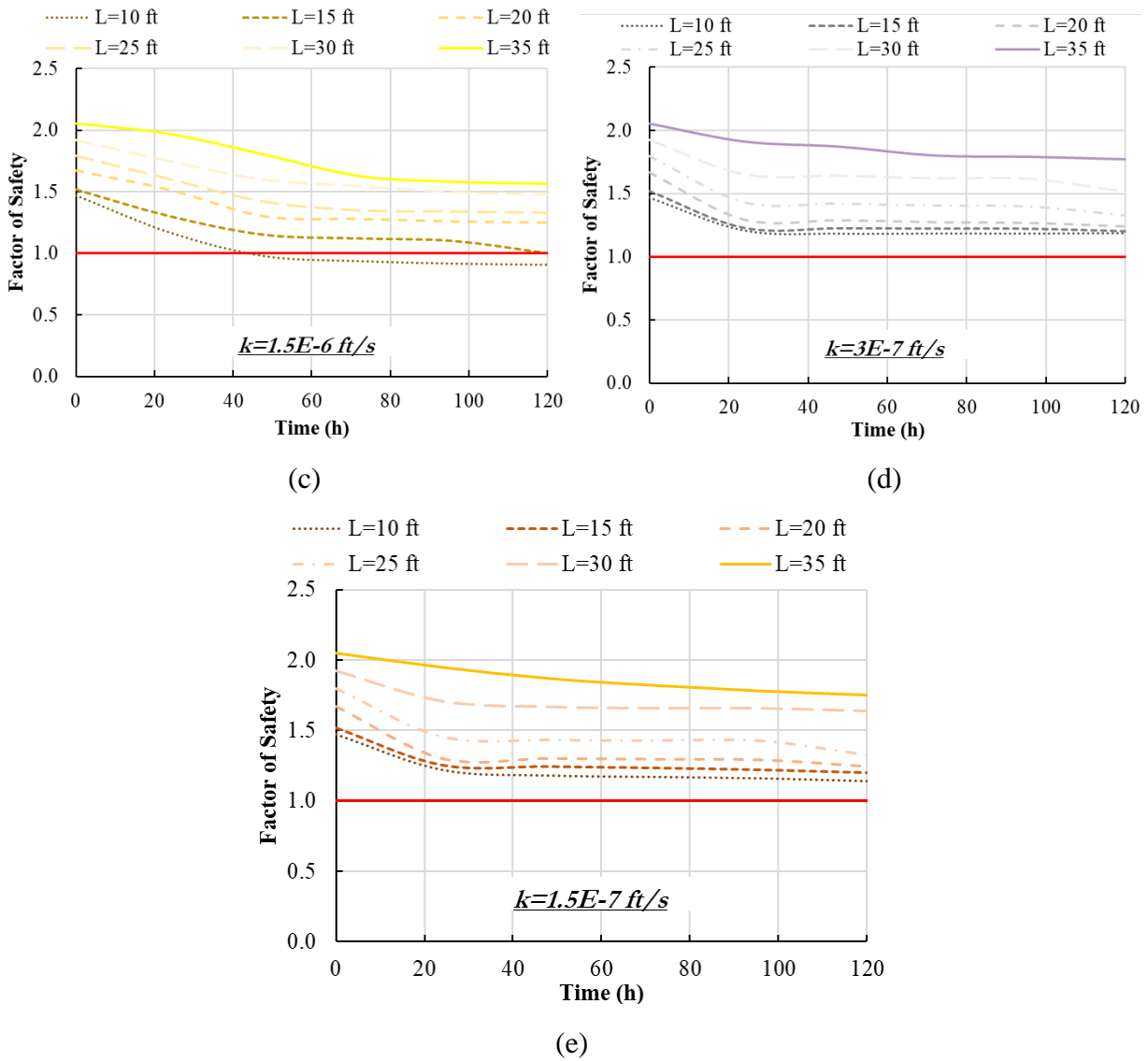


Figure 6-45 Combined effect of variation of MMB length and soil hydraulic conductivity on slope FS (a) $k=1.5 \times 10^{-5} \text{ ft/s}$ (b) $k=1.5 \times 10^{-6} \text{ ft/s}$ (c) $k=3 \times 10^{-6} \text{ ft/s}$ (d) $k=1.5 \times 10^{-7} \text{ ft/s}$ (e) $k=3 \times 10^{-7} \text{ ft/s}$.

6.8.4 Effect of Rainfall Intensity

The effect of rainfall intensity on slope stability is assessed by varying the uniform rainfall intensity over a period of 120 hours or 5 days. Antecedent rainfall is the rain that falls in the days immediately preceding a slope failure event (Au, 1998; Rahardjo et al., 2001; Cal and Ugai, 2004). A period of 5 days has been chosen as the maximum duration in order to simulate the effect of antecedent rainfall. It is important to take the effect of antecedent rainfall into account because in

soils with low permeability (like clayey soil) there is lower possibility for drainage of water and hence a gradual build up in porewater pressure is likely (Rahardjo et al., 2001). Rainfall of past 10 years (2012 to 2022) was analyzed, and rainfall intensities were selected to be varied from 0.15 in/h and 0.25 in/h. It should also be noted that a rainfall intensity of 0.25 in/h applied over a period of 120 h results in a total rainfall of 30 inches, which is an average annual rainfall estimate for the Dallas Fort Worth region, where the test slope section is located. A transient seepage analysis is carried out for a period of 120 hours while keeping all other factors constant. The porewater pressure profile generated as a result of seepage analysis is then used to run a slope stability analysis. The results of varying rainfall intensity on slope stability for a constant length of MMB along the slope is shown in Figure 6-46. Initially the slope has an FS of approximately 1.5. When rainfall is applied to the slope, it experiences a reduction of factor of safety due to the buildup of porewater pressure. The FS decreases with the start of rainfall infiltration and then remains constant. This is because once the slope gets saturated up to a level, no further advancement of wetting front can take place and therefore FS does not reduce any further. With increasing rainfall intensity, the time taken for the FS of the slope to reach the limiting value of 1 (unstable condition) decreases. For instance, at rainfall intensity of 0.25 in/h the slope reaches FS of 1 after 20 h while that at rainfall intensity of 0.15 in/h occurs after 40 h.

The combined effect of change in length of MMB along the slope and variation of rainfall intensity has been assessed and the results are shown in Figure 6-47. As the length of MMB along the slope increases, less area of the slope is subjected to rainfall infiltration. Thus, there is a lower decrease in FS of the slope. For instance, when the length of MMB along the slope is at least 30 feet, the factor of safety does not reach the limiting value of 1 (unstable condition) despite increasing rainfall intensity.

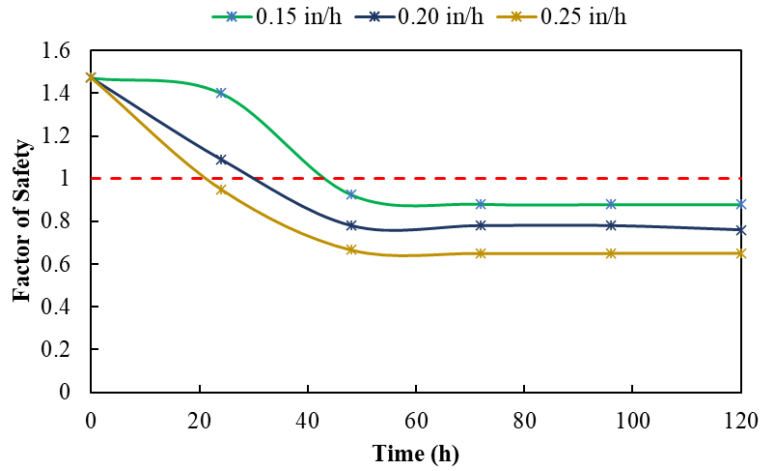
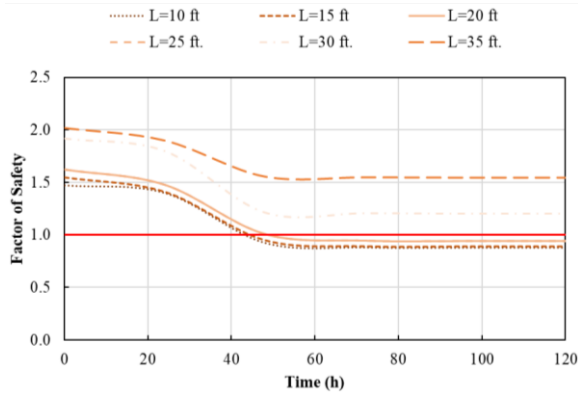
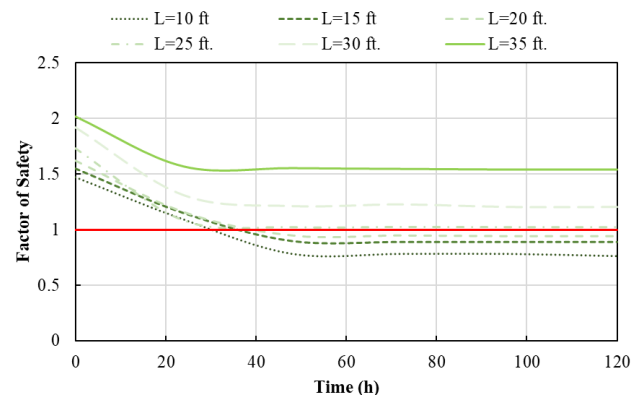


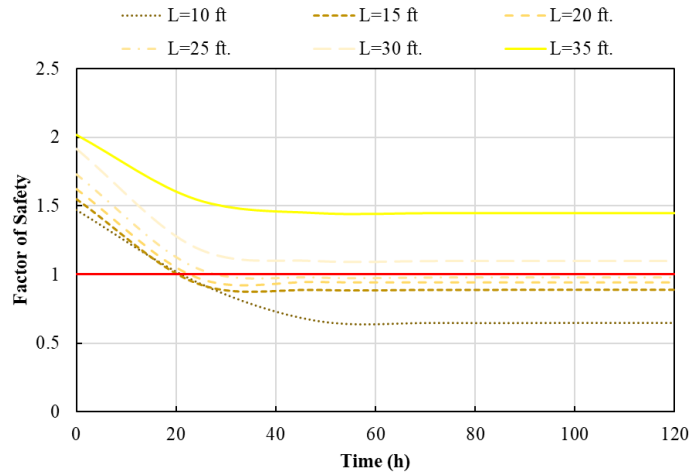
Figure 6-46 Effect of rainfall intensity on slope stability.



(a)



(b)



(c)

Figure 6-47 Combined effect of length of MMB and rainfall intensity on slope stability (a) $q=0.15$ in/h (b) $q=0.20$ in/h (c) $q=0.25$ in/h.

6.8.5 Sensitivity Assessment

The effect of each parameter on the factor of safety of the slope was quantitatively compared in a sensitivity assessment. Figure 6-48 presents the results of the sensitivity assessment in terms of the percentage change in slope FS with respect to the percentage change in input parameters. Rainfall and soil hydraulic conductivity were not included in the sensitivity assessment since they govern the way in which the FS of the slope reduces over time rather than affecting the slope's initial factor of safety. The influence of soil shear strength parameters (cohesion and angle of internal friction), slope geometry (height of slope and slope inclination) and the length of modified moisture barrier along the slope on stability were evaluated. Increase in slope geometry parameters yields a decrease in the FS, depicted by the downward sloping graphs of slope height and angle. On the other hand, increase in soil shear strength parameters positively change the FS of the slope. Very similar trend is also observed by the increase in length of MMB along the slope. Therefore, it can be concluded that the increase of MMB length along the slope generates similar effect on

slope FS as increase in the soil's shear strength parameter. Hence it is further confirmed the use of MMB in a slope increases its FS and it can be used as a method of slope stabilization.

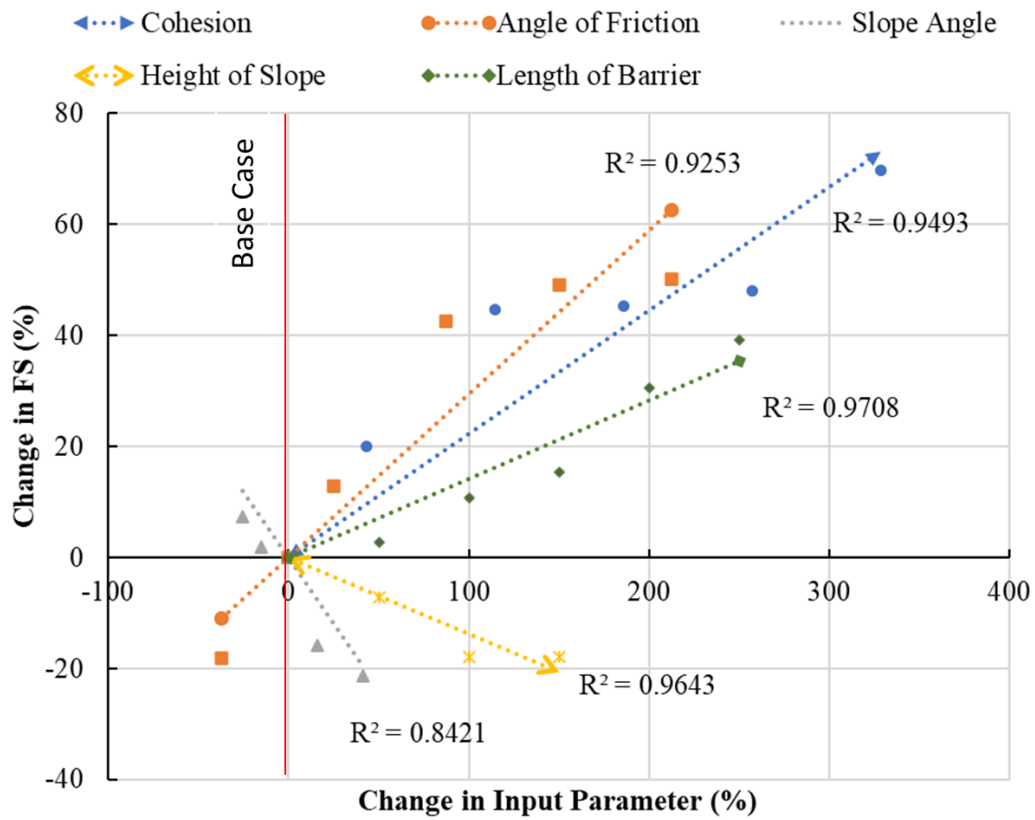


Figure 6-48 Sensitivity assessment: percentage change in factor of safety versus percent of change in input parameters.

CHAPTER 7 PREDICTION MODEL

7.1 Background

The objective of the current study was to evaluate the performance of the modified moisture barrier (MMB) as a slope stabilization method. A slope that had experienced prior shallow slope failure was stabilized with a MMB at the crest and portion of the original slope with similar dimensions was established as the control section for this study. The slope was instrumented with integrated temperature-moisture sensors, soil water potential sensors, and vertical inclinometer casings to monitor its performance. Field performance monitoring results showed that the MMB was able to reduce fluctuations of soil volumetric moisture content, preserve matric suction and subsequently reduce lateral deformation of a slope relative to a natural slope. A numerical model of the field test slope was developed in order to study the stability of the slope. The effect of variation in soil hydraulic properties, soil shear strength properties, slope geometry and rainfall were assessed by conducting a parametric study of the numerical model. Additionally, the length of MMB was also varied to observe its effect on the stability of the slope.

The factor of safety is one of the major aspects to be considered when designing structures like embankment and artificial slopes (Gordan et al., 2016). Therefore, the next phase of the study was to develop a predictive model for the factor of safety of a slope stabilized with a modified moisture barrier. A statistical approach was adopted for this purpose. Results of the parametric study conducted in Section 6.8 was utilized for development of a prediction model. A comprehensive dataset obtained from numerical modeling involving slope geometry, soil shear strength parameters, soil hydraulic conductivity and rainfall, were statistically analyzed to generate a prediction model. Once the prediction model was developed, a new set of data was used to validate

the proposed equation. Lastly, the generated prediction model was used to develop simple design charts.

7.2 Statistical Analysis

Field implementation studies or laboratory scale experimental studies are not always feasible due to constraints in time and budget. Researchers have adopted various statistical methods such as artificial neural networks (ANN), fuzzy logic systems, evolutionary polynomial regression (EPR), and multiple linear regression (MLR) to evaluate relationships between parameters and develop prediction models for slope stability (Ahangar-Asr et al., 2010; Erzin and Cetin, 2012; Mohamed et al., 2012; Sakellariou and Ferentinou, 2005). The objective of the current study is to utilize the results from the parametric study and develop a slope stability prediction model using Multiple Linear Regression (MLR). Regression analysis is a statistical tool used for predicting the nature of relationship between multiple variables (Chakraborty and Goswami, 2017). The main purpose of MLR is to evaluate the relationship between several independent (predictor) variables and one dependent or criterion variable (Yilmak and Yuksen, 2008). In the current study, several important parameters such as slope height, slope angle, soil cohesion, soil friction angle, soil hydraulic conductivity and rainfall were used as input parameters while factor of safety of the slope (FOS) was the output parameter. The Minitab Student Version was used to perform the statistical analysis. The flow of analysis is presented in Figure 7-1.

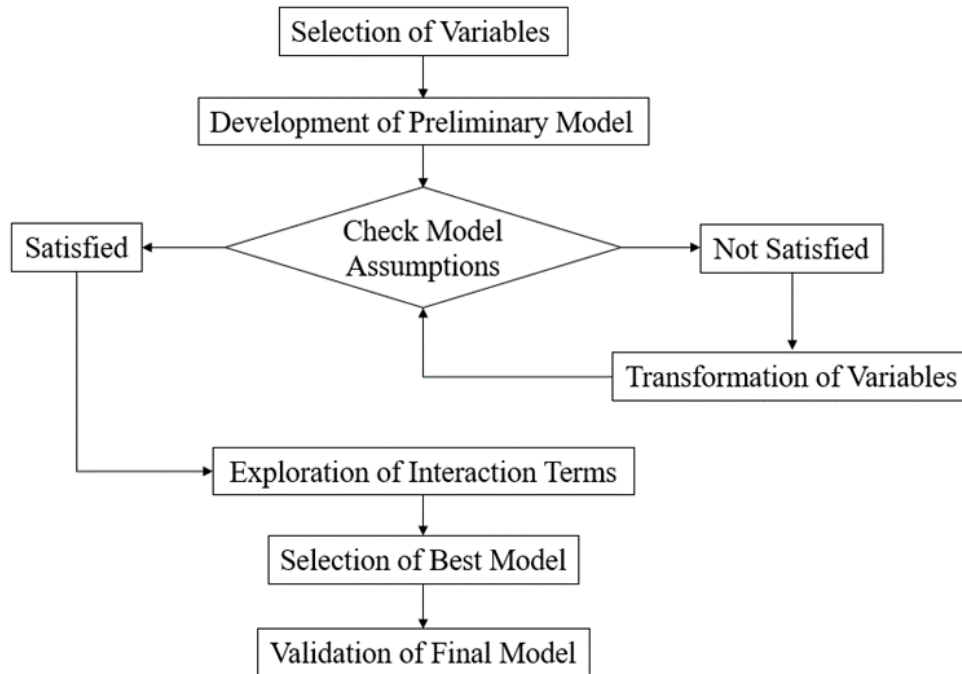


Figure 7-1 Flow of statistical analysis for model development.

7.2 Selection of Parameters

According to Neter et al. (1996), while developing a statistical model, there should be no correlation among the predictor variables. Correlation measures the observed covariation between two variables, i.e., how one varies by due to the other. High collinearity among predictor variables can lead to smaller coefficient of regression, higher variance, and difficulties in explaining the effect of unit change of predictors on the response (Stevens, 2012). Factor of safety of the slope was modeled to be the response while soil hydraulic conductivity, soil shear strength properties (cohesion and angle of internal friction), slope geometry (slope height and slope angle), rainfall, and length of MMB along the slope were modeled as predictors. Based on the numerical study, all independent parameters observed to have an effect on the FS of the slope were included in the preliminary statistical model. The parameters are denoted as follows:

FS = Factor of Safety

C= Cohesion of soil (psf)

ϕ =Friction angle of soil ($^{\circ}$)

H= Height of slope (ft.)

β = Slope inclination ($^{\circ}$)

q=cumulative rainfall obtained from a uniform rainfall intensity (in)

L_B = Length of MMB along slope (ft.)

K_s = saturated permeability of soil (ft/s)

7.3 Correlation Analysis

In order to evaluate the relationship between the response variable and each of the predictor variables, correlation analysis was performed. Similar analysis was also performed among the predictor variables to assess multicollinearity. The existence of multicollinearity implies that two or more predictor variables can explain similar variation of the response.

7.3.1 Predictor vs Predictor

Results of correlation analysis conducted between predictors to determine collinearity are presented in Figure 7-2. Based on the plot, no significant relationship is observed among the predictors. Pearson's r, known as the coefficient of linear correlation, is the most commonly used measure of correlation. The Pearson correlation coefficients between the predictors is tabulated in Table 7-1. The strongest correlation was found between slope height and slope angle (0.635). However, Kutner et al., (2015) stated that any correlation lower than 0.7 can be stated as weak. Thus, it can be concluded that no significant collinearity existed between the predictors.

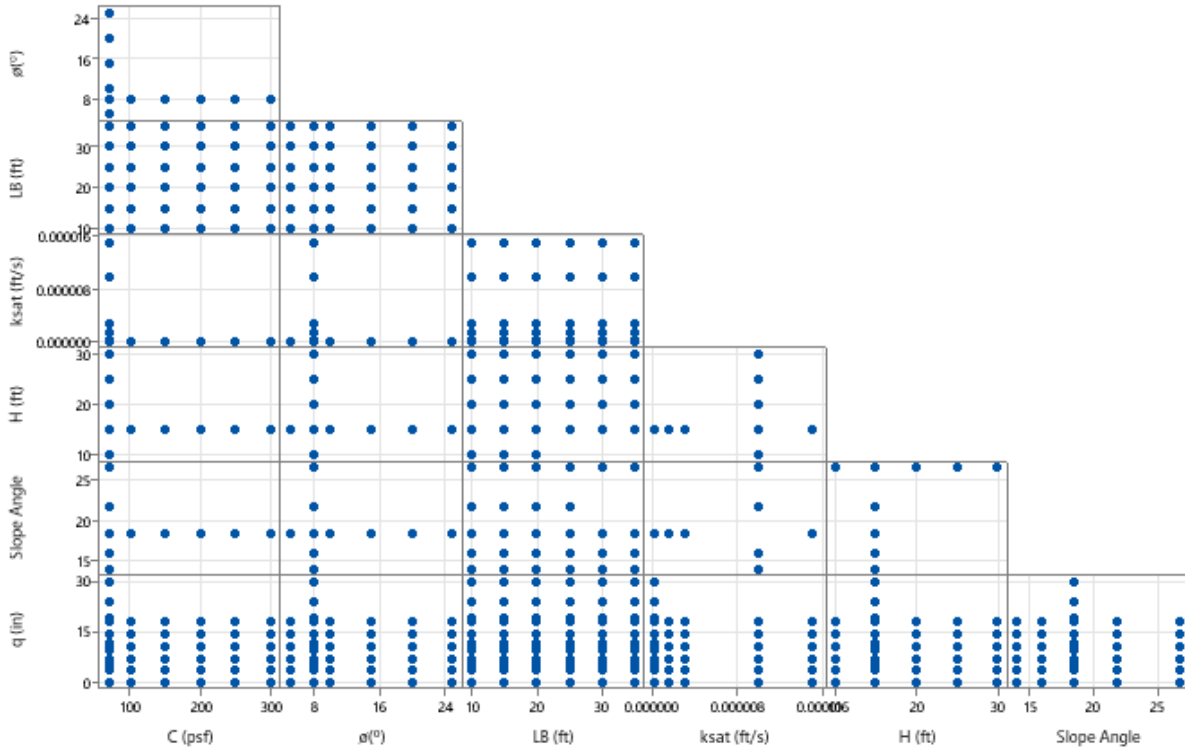


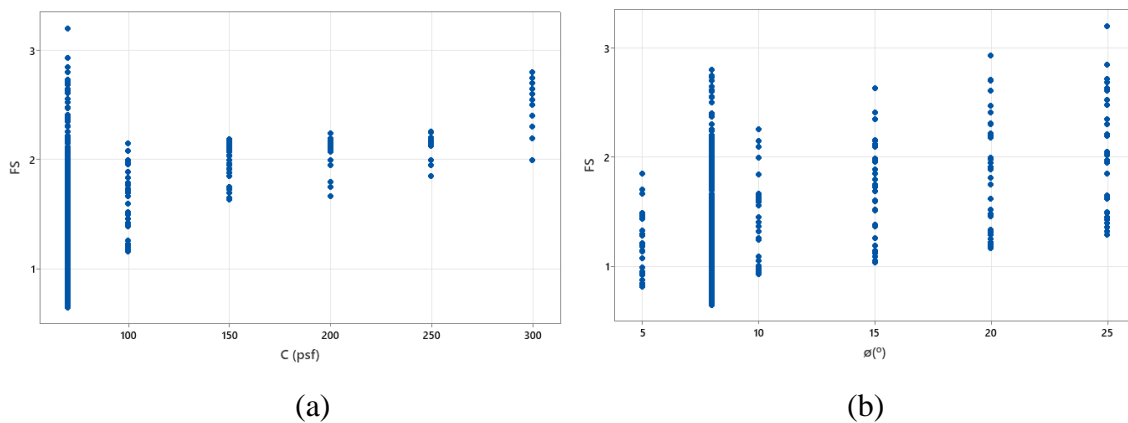
Figure 7-2 Correlation among predictor variables.

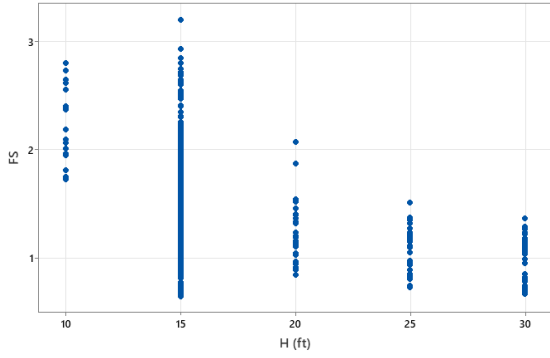
Table 7-1 Correlation between predictor variables.

Variable	C (psf)	$\phi(^{\circ})$	LB (ft)	H (ft)	$\beta(^{\circ})$	q (in)	k_{sat} (ft/s)
C (psf)	1	-0.139	0.027	-0.127	-0.15	-0.013	-0.303
$\phi(^{\circ})$	-0.139	1	0.023	-0.099	-0.117	-0.019	-0.236
LB (ft)	0.027	0.023	1	0.039	-0.0185	0.003	-0.065
H (ft)	-0.127	-0.099	0.039	1	0.630	-0.014	0.391
$\beta(^{\circ})$	-0.150	-0.117	-0.085	0.630	1	-0.016	0.464
q (in)	-0.013	-0.019	0.003	-0.014	-0.016	1	-0.050
k_{sat} (ft/s)	-0.303	-0.236	-0.065	0.391	0.464	-0.05	1

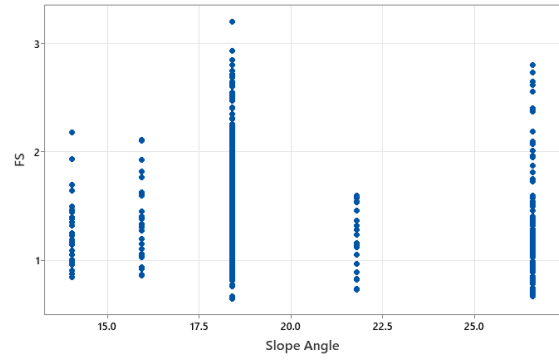
7.3.2 Response vs Predictor Plots

The response variable (factor of safety) was plotted against each of the predictor variable and the results are presented in Figure 7-3. No specific trend is followed by the relationship between the response and the predictor variables. Correlation analysis was conducted to assess the linear strength between the response and predictor variables and the coefficients are tabulated in Table 7-2. Based on the statistical analysis, soil shear strength parameters (cohesion and angle of friction) and the length of MMB along the slope have positive correlation with factor of safety. Any increase in the aforementioned factors will cause an increase in the factor of safety of the slope. On the other hand, slope geometry (slope height and angle), soil hydraulic conductivity and rainfall have negative correlation with factor of safety. Therefore, any increases in these factors will cause a decrease in the factor of safety of the slope. Soil cohesion was found to have the strongest correlation (0.612) with factor of safety which suggests that soil cohesion can could explain most of the variability in factor of safety variation. Similarly, rainfall (-0.417) and length of MMB along slope also showed strong correlation. Among all parameters, slope angle showed the least correlation (-0.172) with factor of safety of the slope.

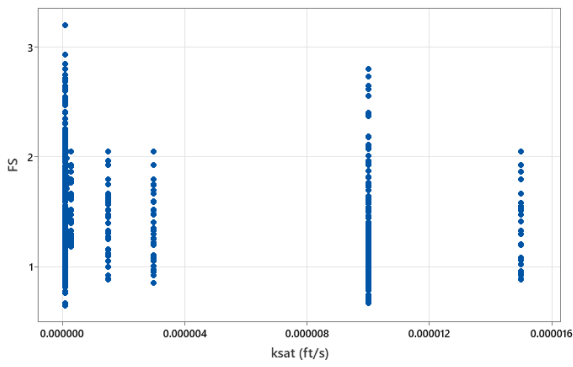




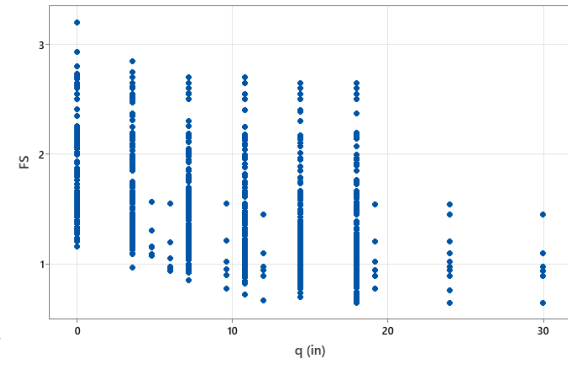
(c)



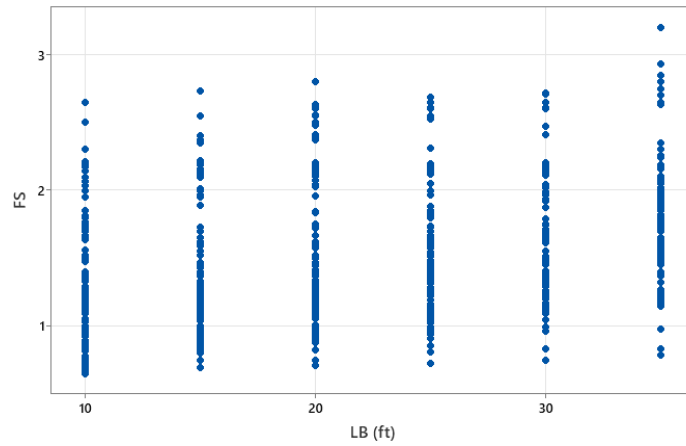
(d)



(e)



(f)



(g)

Figure 7-3 Correlation of FS with predictor variables (a) cohesion (b) angle of friction (c) height of slope (d) slope angle (e) hydraulic conductivity (f) rainfall (g) length of MMB.

Table 7-2 Correlation between factor of safety and predictor variables.

C (psf)	ø(°)	H (ft)	β(°)	k_{sat} (ft/s)	q (in)	L_B (ft)
0.612	0.241	-0.319	-0.172	-0.323	-0.417	0.333

7.4 Preliminary Model Development

Once it was concluded that no multilinearity existed between the predictor variables, a preliminary multiple linear regression (MLR) model was developed including all the predictors as follows:

$$FS = \beta_0 + \beta_1 C + \beta_2 \phi + \beta_3 H + \beta_4 \theta + \beta_5 k + \beta_6 q + \beta_7 L_B + \varepsilon_i$$

Where β_0 is a constant, $\beta_1, \beta_2, \beta_3, \beta_4, \beta_5, \beta_6, \beta_7$ are correlation coefficients determined through regression analysis by minimizing the sum of squared errors for the model data, and ε_i is the random error. In this equation, the regression coefficients represent the independent contributions of each independent variable in the prediction of the dependent variable. Multiple linear regression analysis was performed on the model dataset. The parameter estimates and ANOVA (Analysis of Variance) are presented in Table 7-3 and Table 7-4, respectively. The sign conventions of the coefficients are as expected. The t-statistics (in absolute value) for all the variables were greater than 2, indicating significance except for variable k. This indicates that parameter k should not be included as an explanatory variable. The standardized effect of each parameter is visually presented in Figure 7-4. It can be observed that all the parameters cross the reference line of 1.96 at $\alpha=0.05$, except permeability (k). This means that all the parameters except permeability (k) are statistically significant. Based on the ANOVA summary, the adjusted R^2 was found to be satisfactory and acceptable. The p-value of the residuals is also very low. The preliminary fitted MLR equation can be presented as follows:

$$FS = 0.7060 + 0.005109C + 0.03538\varnothing - 0.04914H - 0.03216\beta - 2428k - 0.03112q \\ + 0.02012 L_B$$

The next step is to verify whether the MLR model assumptions are met. The model should satisfy the MLR checks such as constant error variance, normality of residuals, outliers, and multicollinearity among the predictor variables (Stevens, 1996; Neter et al., 1996; Faysal, 2017). Graphical plots and different statistical tests will be used to verify the following model assumptions:

- Linear relationship between the response and predictor variables.
- Constant variance of residuals.
- Normal distribution of residuals.
- The residuals should not be auto correlated.

Table 7-3 Parameter estimates of the preliminary model.

	Coefficient	Std. Error	t value	p value	VIF
(constant)	0.70598	0.059461	11.87	<2e-16	
C	0.00511	0.000130	39.31	<2e-16	1.16
∅	0.03538	0.001842	19.21	<2e-16	1.12
L_B	0.02021	0.000873	23.16	<2e-16	1.02
K	-2427.79	1831.425	-1.33	0.185	1.51
H	-0.04914	0.002639	-18.62	<2e-16	1.72
β	-0.03216	0.002980	10.79	<2e-16	1.85
q	-0.03112	0.001118	-27.85	<2e-16	1.01

Table 7-4 ANOVA Summary of preliminary model.

Residual Standard Error	R ²	Adjusted R ²	F-statistic	p-value
0.2152	0.8179	0.8161	549.66	<2.2e-16

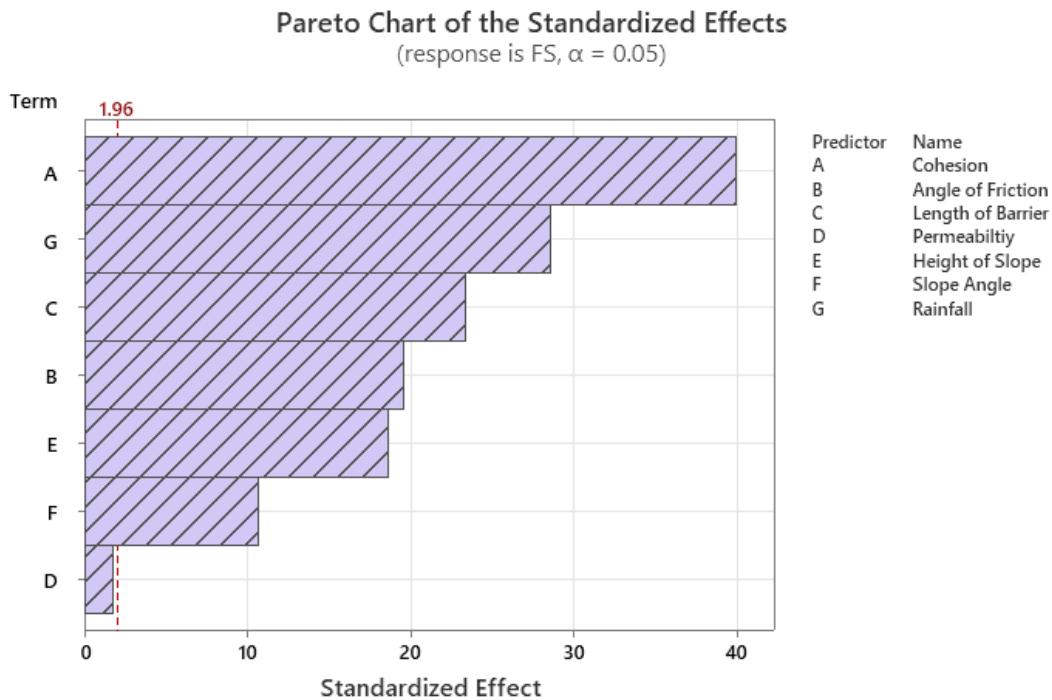


Figure 7-4 Pareto chart showing standardized effects for the preliminary model.

7.5 Verification of Preliminary Model

7.5.1 Constant Error Variance

One of the main assumptions of linear regression is that the residuals should be distributed with equal variance at each level of the predictor. Graphical plots depicting residuals vs predictor variables and residuals vs fitted values assist to check for constant error variance or homoscedasticity. Residuals should not show any specific trend when plotted against fitted values. The presence of a funnel shape or any curvilinear trend indicates presence of heteroscedasticity in

the model, in which case the regression might not be valid. Transformation of variables can be performed to mitigate this condition. As seen in Figure 7-5, the loess smoothing line (shown by the red line) does not show significant curvature indicate the presence of constant variance. A plot of square root of the absolute value of the standardized residuals versus the fitted values, as shown in Figure 7-6, is an additional graphic that can help to flag heteroscedasticity. Furthermore, the Breusch Pagan test was carried out to determine the constant error variance mode. The p value from the test was found to be 0.021 which is greater than $\alpha=0.01$. So, the null hypothesis was not rejected indicating that the residual are not homoscedastic at $\alpha=0.01$.

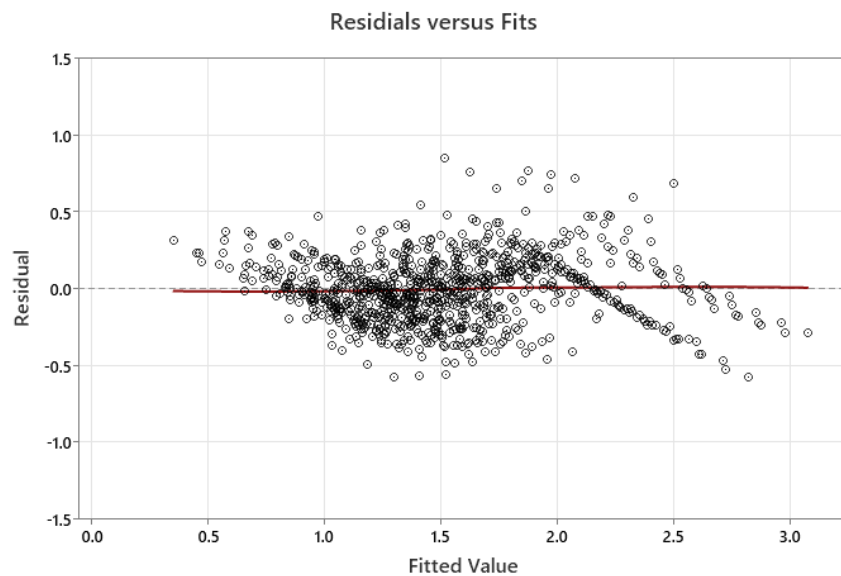


Figure 7-5 Plot of residual vs. fitted value for the preliminary model.

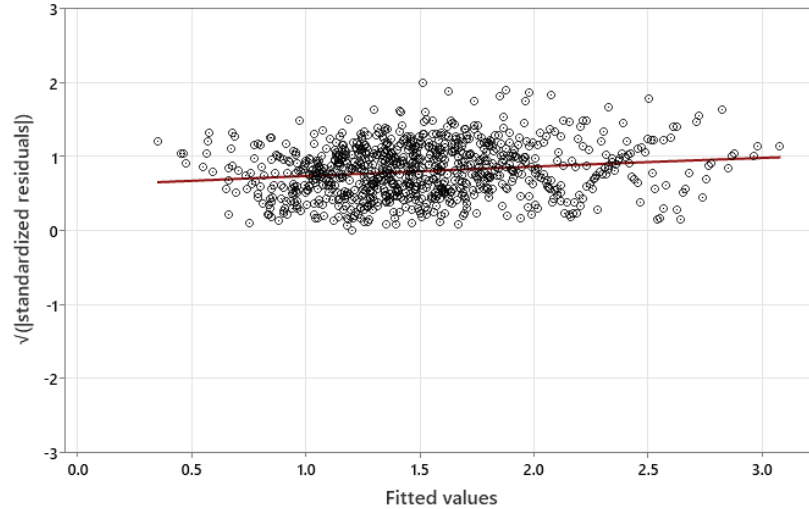


Figure 7-6 Plot of standardized residuals versus fitted values for preliminary model.

7.5.2 Normality

In addition to being homoscedastic, the residuals of an MLR should have normal distribution. A normal probability plot or formal hypothesis tests can be utilized to determine normality. A moderately linear plot means that the residuals are normally distributed. The normal probability plot for the preliminary MLR model is shown in Figure 7-7. The red line indicates where the residuals would fall if they were normally distributed. Short tails at both sides can be seen from the plot indicating that the residuals may not be normally distributed. To determine the normal distribution of the residuals, Anderson-Darling Normality Test was carried out. The test estimated a p-value of 0.097 which is greater than $\alpha=0.01$. So, the null hypothesis failed to be rejected indicated that the residuals are normally distributed at $\alpha=0.01$. The normal distribution of the residuals can also be observed from the bell-shaped histogram as shown in Figure 7-8.

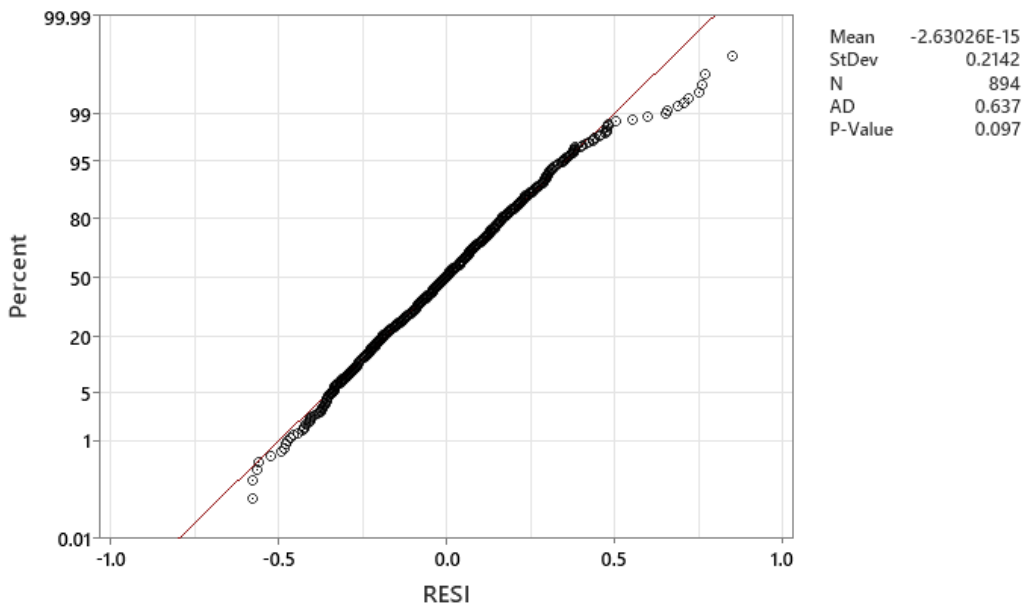


Figure 7-7 Normal probability plot for the preliminary model.

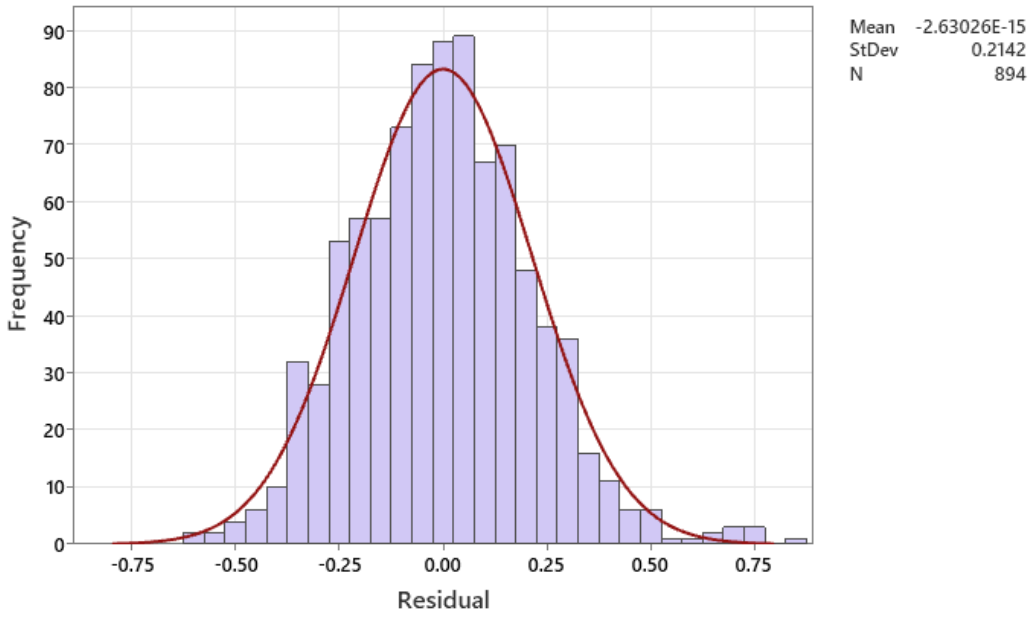


Figure 7-8 Histogram of residuals for preliminary model.

7.5.3 Outlier

Outliers are extreme observations in a given dataset which can mislead the regression by pulling the fitted line disproportionately towards the extreme observation (Kutner et al., 2005). Leverage and influence statistics are means to detect predictor and response variable that lie outside the bulk of the data and therefore have the capability to generate an unstable regression model. Leverage is the measure of an outlier in the x direction. Observations that exhibit high leverage may not necessarily affect the regression. However, observations with high influence are those with high leverage and when the observation is removed, substantially affect the estimated regression line. Standard tests such as DFFITS and Cook's Distance were used to check the influence of outliers in the preliminary model. The most widely used measure of influence is Cook's D (Belsley et al., 1980). Similarly, observations with Cook's D (D_i) > F (p, n-p) should also be flagged for further check. The F-statistic to compare the Cook's Distance for this test set was 1.638 for $\alpha=0.05$. For an MLR model, the critical value of Cook's D should be in the range of 1.6 to 2.0. The obtained result was satisfactory. Another influence diagnostic is DFFITS (Difference in Fits) measure estimates the influence of an observation on the predicted value. An observation is considered to have high influence if $|DFFITS_i| \geq 2\sqrt{\frac{p}{n}}$ (Belsley et al., 1980) where p is the number of estimated parameters in the model and n is the number of observations. It is suggested that an absolute value of DFFITs greater than 1 should be flagged for further check. It is also suggested that observations with D_i greater than 0.5 should be investigated as they can be influential.

7.5.4 Multicollinearity

An important assumption of MLR is that the predictors should not have a strong correlation among themselves. Variance inflation factor (VIF) presented by Marquardt (1970) is a widely used diagnostic for evaluating multicollinearity. For a variable j , the VIF is calculated as follows:

$$VIF_j = \frac{1}{1 - R_j^2}$$

where R_j^2 is the R^2 from a regression of the j th explanatory variable on all of the other explanatory variables. VIF quantifies how much the variation is inflated in a model and can be used to check for multicollinearity. The ideal is $VIF \approx 1$ which means there is no correlation among the predictors. There is no universal definition of a large VIF but a $VIF = 10$ is commonly considered large while some researchers have used VIF as low as 4 (Kutner et al., 2004; O' Brien, 2007 and Vatcheva et al., 2016). Furthermore, a $VIF > 10$ suggests high multicollinearity indicating poor estimate of the response. Based on the results in Table 7-3, all the values of VIF are within the suggested range. Therefore, multicollinearity does not exist among the predictor variables.

7.6 Transformation of Variables and MLR Assumptions Check

The preliminary MLR model passed the constant variance and normality tests. Therefore, transformation of the model was not required. As outlier data was detected in the model, the outliers were removed, and multiple linear regression was carried out. The parameter estimates and summary of the analysis of variance (ANOVA) are presented in Table 7-5 and Table 7-6, respectively. The ANOVA summary shows that R^2 has a value of 0.8683 which is satisfactory and acceptable. The sign conventions of the coefficient are also as expected. The p-value of the residuals is also very small. The final fitted MLR equation can be represented as follows:

$$FS = 0.8279 + 0.005316C + 0.0338\emptyset - 0.03023H - 0.0083\beta - 3477k - 0.029406q \\ + 0.19913 L_B$$

Table 7-5 Parameter estimates of the final model.

Coefficient	Std. Error	t value	p value	VIF
-------------	------------	---------	---------	-----

(constant)	0.8279	0.0523	16.4840	0.00	
C	0.0053	0.0001	52.3651	0.00	1.07
ø	0.3380	0.0017	19.5347	0.00	1.05
L_B	0.0199	0.0007	27.5559	0.00	1.01
K	-3476.9	2022.1	-1.7195	0.08591	1.04
H	-0.0302	0.0029	-10.499	0.00	2.68
β	-0.0083	0.0031	2.6425	0.00839	2.64
q	-0.02941	0.0009	-31.4989	0.00	1.00

Table 7-6 ANOVA summary of final model.

Residual Standard Error	R²	Adjusted R²	F-statistic	p-value
0.1721	0.8683	0.8671	747.84	0.000

The next step is to check whether MLR model assumptions are verified.

7.7 Verification of Final Model

7.7.1 Constant Error Variance

The plot of residuals vs fitted values is shown in Figure 7-9. No curvilinear or funnel shape is detected from the plot. Residuals are observed to be randomly scattered. The square root of the absolute values standardized residuals was also plotted as shown in Figure 7-10. Further analysis was conducted using the studentized Breusch Pagan test. The p value from the test was 0.08n which is greater than $\alpha=0.01$. So, the null hypothesis failed to be rejected indicating that the residuals are homoscedastic at $\alpha=0.01$. There, the constant error variance assumption was met for the final model.

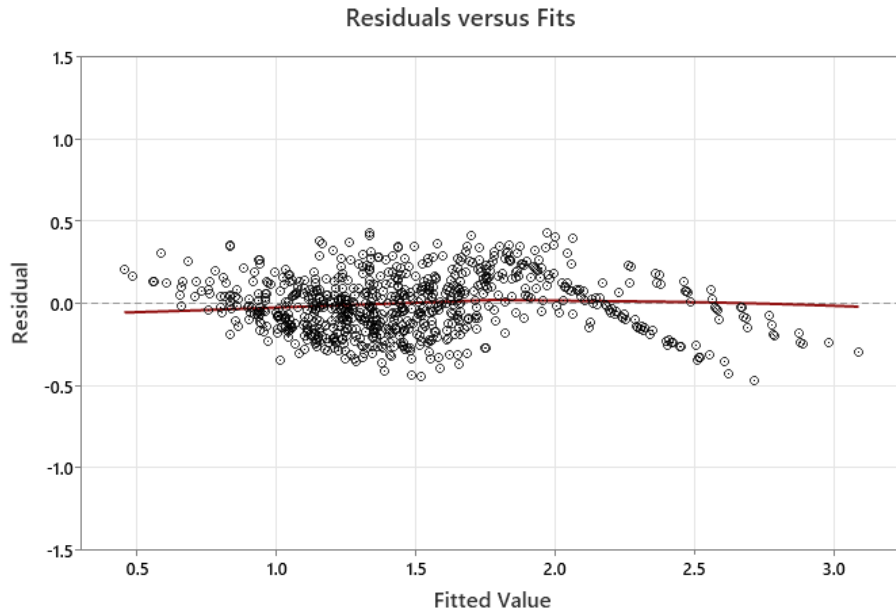


Figure 7-9 Plot of residual vs. fitted value for the final model.

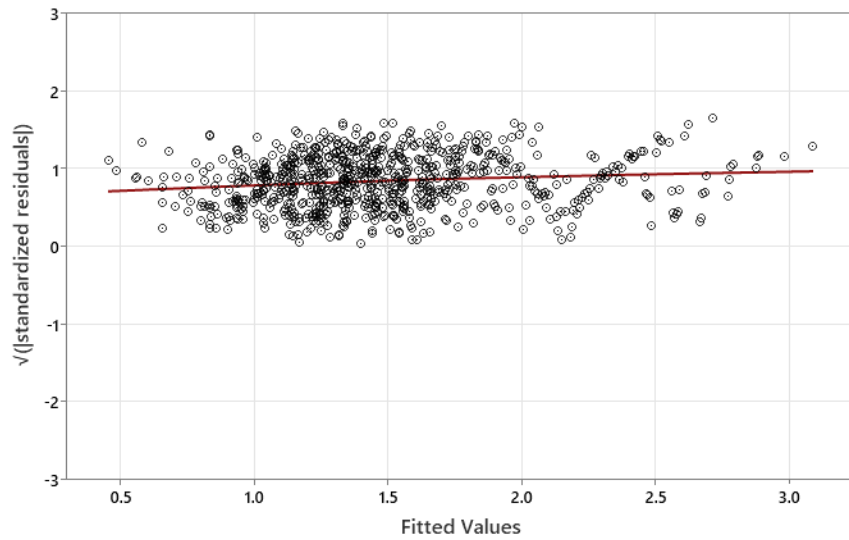


Figure 7-10 Plot of standardized residuals versus fitted values for the final model.

7.7.2 Normality Test

The normal probability plot for the final model is shown in Figure 7-11. To verify the normal probability assumption, Anderson Darling normality test is carried out. A p value 0.07 was

obtained which is greater than $\alpha=0.01$. Therefore, the null hypothesis was failed to be rejected indicating that the residuals are normally distributed at $\alpha=0.01$. The normal distribution of the residuals is further confirmed by the frequency distribution plot, as shown in Figure 7-12.

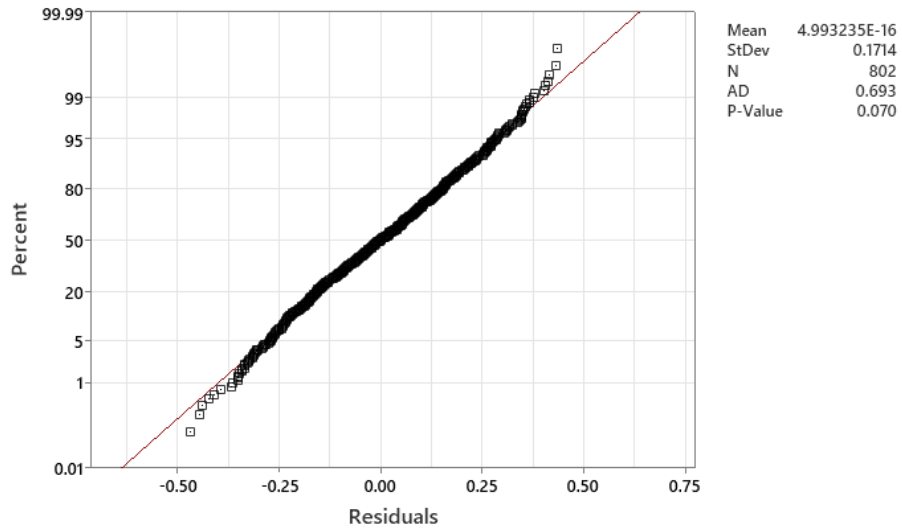


Figure 7-11 Normal probability plot for the final model.

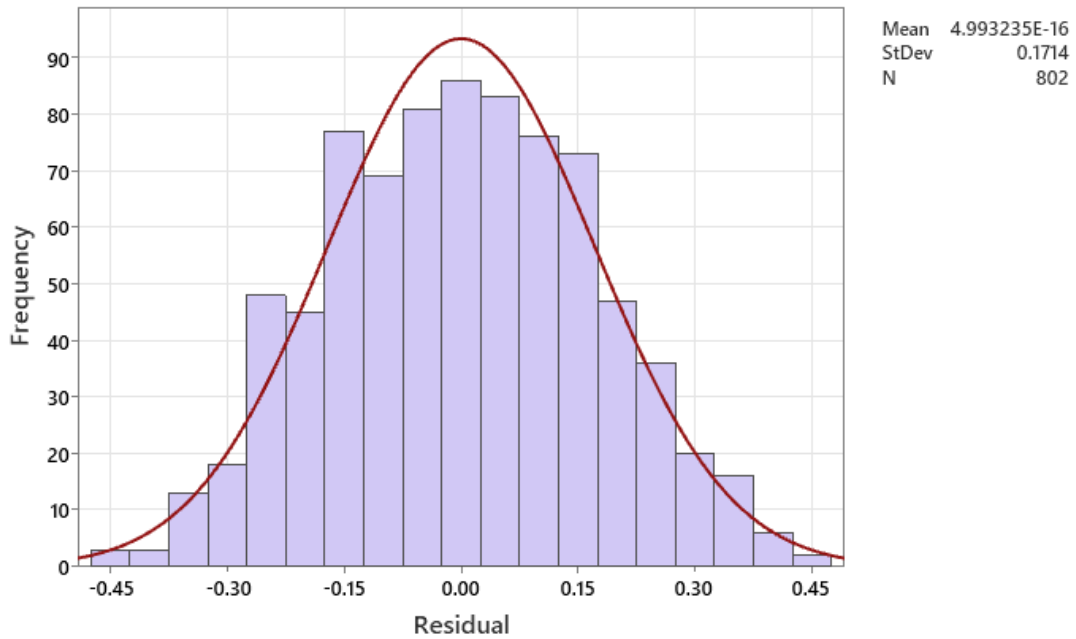


Figure 7-12 Frequency distribution of residuals for final model.

7.7.3 Outlier Test

Standard tests such as DFFITS and Cook's Distance were used to assess the effect of outliers on the preliminary model. DFFITS (Difference in Fits) estimates the influence of an observation on the predicted value. It is suggested that an absolute value of DFFITS greater than 1 should be flagged for further check. Similarly, observations with Cook's D (D_i) $>$ $F(p, n-p)$ should also be flagged for further check. The F statistic to compare the Cook's Distance for this set was 1.892 for $\alpha=0.05$. All the observations satisfied the assumptions based on DFFITS and Cook's D.

7.7.4 Multicollinearity

Based on the results presented in Table 7-5, all the VIFs are within suggested range. Therefore, no serious multicollinearity existed among the predictor variables.

7.8 Final Model Selection

One of the major issues in MLR is determination of the appropriate approach in selection of variable. Inclusion of additional variables to an MLR model helps to explain more of the variance in the response variable. However, the cost of adding additional variables is the loss of degree of freedom. A good model explains as much of the variance of the response variable as possible with a small number of predictor variables. Simply minimizing the SSE (error sum of squares) or maximizing R^2 are not sufficient criteria. Therefore, in order to finalize the model, best subset method, stepwise regression and backward elimination were performed.

7.8.1 Best Subset Selection

The best subset selection method performs analyses for different combinations of predictor variables to determine the best model. The parameters considered for the selection of the best model are R^2 , adj. R^2 , Mallows's C_p , and Bayesian Information Criteria (BIC). This method selects the model with the highest R^2 , adj. R^2 and the lowest Mallows's C_p and BIC. Based on this method,

the combination of six predictors (c, ϕ , L_B, H, β , and Q) with the exclusion of predictor K was selected as the best model. The parameter values for each criterion under consideration are presented in Table 7-7.

Table 7-7 Summary of best subset selection method.

Predictor Variables							Selection Parameters			
C	ϕ	L _B	K	H	β	Q	R ²	Adj R ²	C _P	BIC
√	-	-	-	-	-	-	49.2	49.1	2264.8	548.2
-	-	-	-	-	-	√	15.9	15.7	4275.0	952.9
√	-	-	-	-	-	√	64.3	64.3	1353.6	271.0
√	-	√	-	-	-	-	60.5	60.4	1583.1	352.3
√	-	√	-	-	-	√	76	75.9	651.3	-40.7
√	√	-	-	-	-	√	71.7	71.6	909.5	91.2
√	√	√	-	-	-	√	83.7	83.6	189.4	-344.4
√	-	√	-	√	-	√	80.2	80.1	404.2	-185.7
√	√	√	-	√	-	√	86.7	86.6	14.1	-497.5
√	√	√	-	-	√	√	85.0	84.9	115.3	-402.4
√	√	√	√	√	-	√	86.7	86.6	9	-493.9
√	√	√	-	√	√	√	86.8	86.7	8	-498.0
√	√	√	√	√	√	√	86.8	86.7	13	-494.3

7.8.2 Backward Elimination

The backward elimination method begins with including all the predictors in the model. Then, it incrementally removes the statistically insignificant variables. When no insignificant variable

remains in the model, the analysis is concluded. The backward elimination algorithm ensures that the final model has only significant variables. However, it does not ensure the best model because it does not consider the combined significance of a group of variables. Based on this method all predictor variables, k_{sat} had a p-value of 0.086 which shows it was not significant at $\alpha=0.01$ significance level and therefore the variable was removed.

7.8.3 Stepwise Regression

Stepwise regression method utilizes both backward selection and forward selection algorithms. The model begins with the most significant predictor variable, regression is carried out and the parameters under consideration are calculated. Then, other variables are incrementally added based on their significance. The procedure is repeated until the model with the best criteria parameters is obtained. Variables that are significant when entering the model will be eliminated if later, they test as insignificant. The F-statistic test is used to conduct the statistical significance test (Kutner et al., 2005). Based on the results of stepwise regression, the inclusion of six predictor variables (H , θ , L_B , c , ϕ , and q) formed the best model.

Finally, it was decided to use six predictor variables in the model to explain the variation of FS. The parameter estimates and analysis of variance (ANOVA) of the final model are shown in Table 7-8. The final equation, after the removal of k_{sat} as a predictor variable is as follows:

$$FS = 0.8115 + 0.005343C + 0.03413\phi - 0.02991H - 0.00842\beta - 0.029355q + 0.019898 L_B$$

Table 7-8 Parameter estimates of the final model with 6 predictors.

	Coefficient	Std. Error	t value	p value	VIF
(constant)	0.8115	0.0494	16.44	0.000	

C	0.005343	0.0001	53.19	0.000	1.05
ø	0.03413	0.00172	19.83	0.000	1.03
L_B	0.019898	0.00723	27.50	0.000	1.01
H	-0.02991	0.0288	-10.40	0.000	2.66
θ	0.00842	0.00315	2.68	0.008	2.64
q	-0.029355	0.000934	-31.42	0.000	1.00

Table 7-9 ANOVA summary of final model with 6 predictors.

Residual Standard Error	R²	Adjusted R²	F-statistic	p-value
0.1723	0.8678	0.8668	869.84	0.000

Lastly the final model was once against checked against the three assumptions of linear regression analysis.

7.9 Final Model Validation

The final prediction model was validated using a new and separate set of data. Numerical analysis was conducted using the calibrated numerical model, utilizing randomly selected variables to obtain values for factors of safety of the slope. The same parameters were used in the equation to predict values for the factor of safety. The comparison of factor of safety values obtained from the predictive equation and numerical model is presented in Figure 7-13. Based on the results, the developed prediction model can explain 92.91 % of slope factor of safety at different combination of parameters. The bias values were calculated by taking a ratio of numerical model values to predicted values. The mean of the bias values was 1.01. The coefficient of variation (COV) of the

bias values was 9.31%. This demonstrates a good agreement between the numerical and statistical methods.

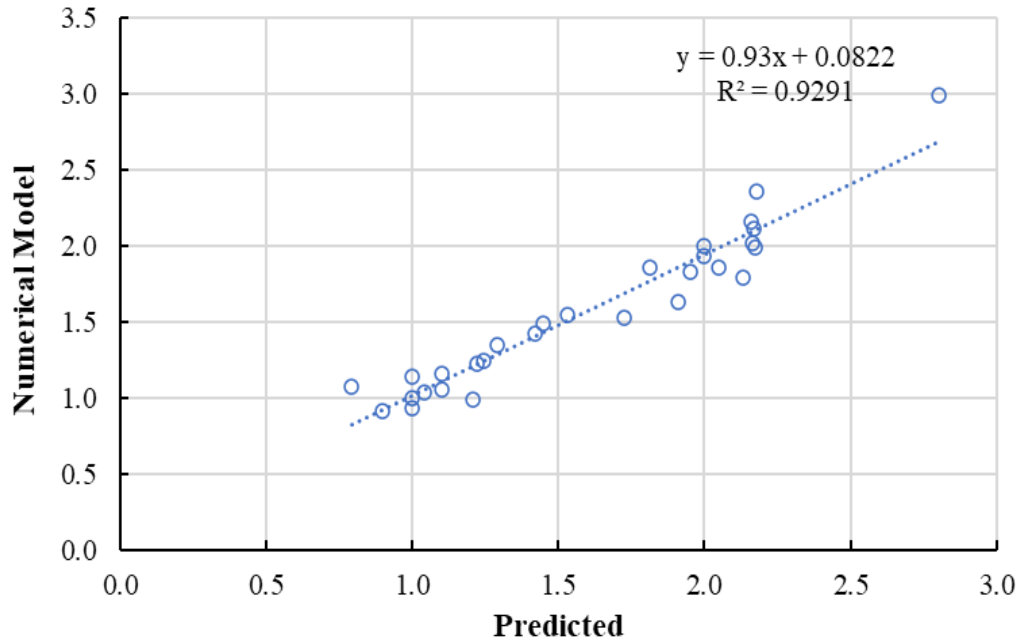


Figure 7-13 Validation of final prediction model.

7.10 Design Methodology

A slope stabilized with a modified moisture barrier (MMB) can be used to successfully stabilize a shallow slope failure and prevent a rainfall induced failure from occurring. In order to design a slope with MMB, some necessary steps should be taken, as presented below. The flow of the design methodology is shown in Figure 7-14.

- Step 1: Calculate the factor of safety of the natural slope utilizing conventional hand calculation methods (ordinary method of slices, infinite slope method) or by utilizing the statistical equation developed in section 7.8 considering the length of MMB along slope (L_B) and the rainfall (q) are equal to 0.

- Step 2: If the FS is determined to be less than or equal to 1, the natural slope is unstable, and stabilization is required.
- Step 3: Select a length of modified moisture barrier to be provided along the length of the slope (L_B). The L_B can be selected considering drainage property of the geocomposite as discussed in Section 6.5.4. Determination of L_B based on drainage is shown below:

$$L_B = \frac{K \sin \beta b}{q_i}$$

Where K is the in-plane permeability of the geotextile, b is the thickness of the transport layer, β is the slope inclination and q_i are the infiltration rate.

- Step 4: Determine the FS of the slope using the following statistical equation using the chosen value of L_B and q as 0:

$$FS = 0.8115 + 0.005343C + 0.03413\phi - 0.02991H - 0.00842\beta - 0.029355q \\ + 0.19898 L_B$$

The above calculated value of FS provides the initial post construction factor of safety of a slope stabilized with MMB.

- Step 5: The FS of the slope stabilized with MMB should also be assessed by considering the effect rainfall. This can be done by inputting an appropriate value of q into the statistical equation.
- Step 6: Determine the value of q to input into the equation. First a uniform rainfall intensity ($I_{uniform}$) should be determined. Rainfall intensity can be determined considering the geographical location of the slope or on other important design criteria. Next the cumulative rainfall, in inches, should be determined as follows:

$$q = I_{uniform} * t$$

Where q is cumulative the rainfall in inches, I_{uniform} is the rainfall intensity in in/day while t is the number of days.

- Step 7: Determine the FS of the slope by inputting the L_B selected in step 3 and q determined in step 6.
- Step 8: If the FS determined in step is greater than required, the slope can be designed using chosen length and commercially available geocomposite and geomembrane. However, if the FS does not meet the requirement, a different length of MMB should be selected and the process should be repeated until a desired FS is obtained.

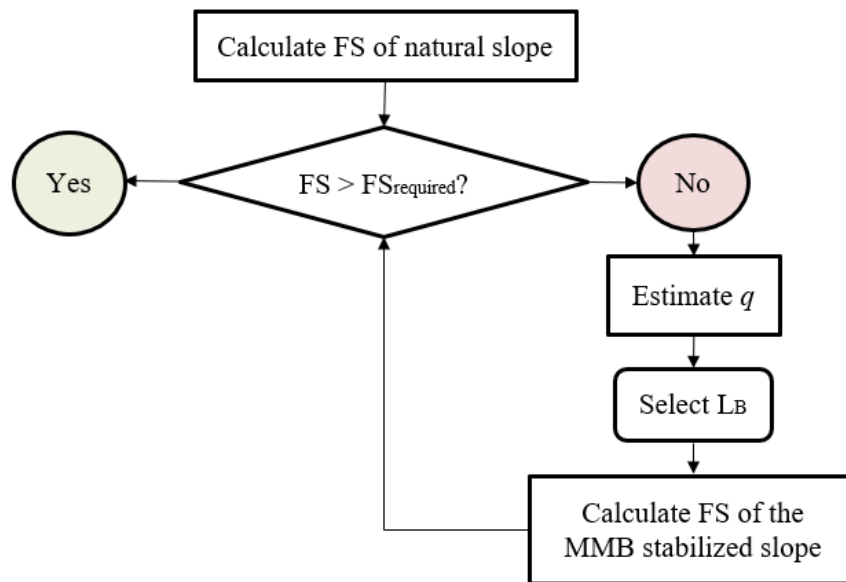
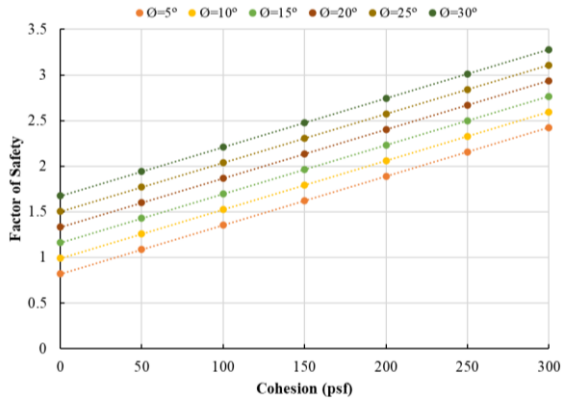


Figure 7-14 Flowchart for designing MMB stabilized slope.

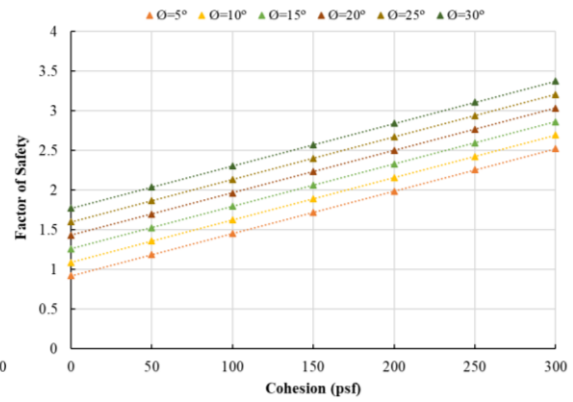
7.10.1 Design Charts

The statistical prediction model developed can be used to develop design charts for ease of use when designing a slope stabilized with MMB. Design charts for different lengths of MMB along slope with variation in cohesion and angle of friction for a slope height of 15 feet and geometry of

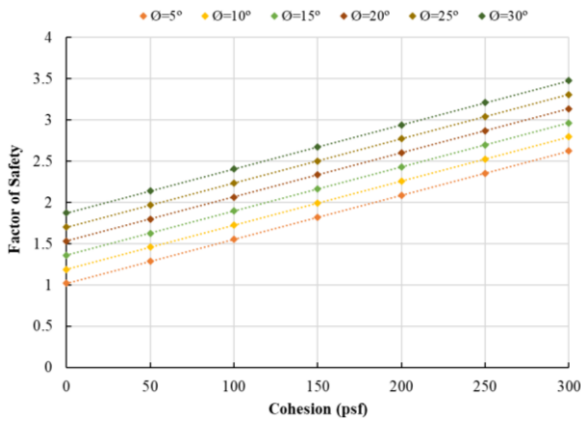
3 (H): 1 (V) were developed, as shown in Figure 7-15. The design charts in Figure 7-15 are for the DFW region where the 30-year average rainfall was 36.14 inches with 80 wet days.



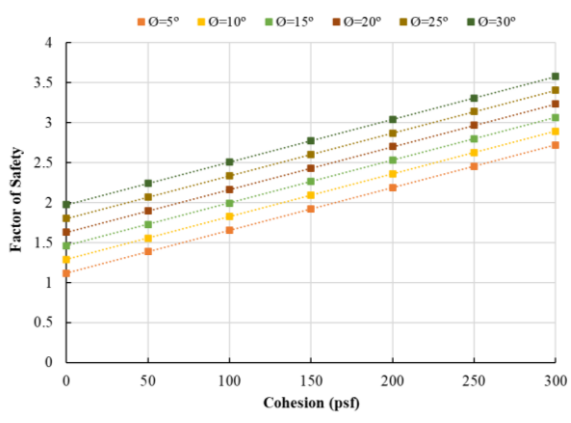
(a)



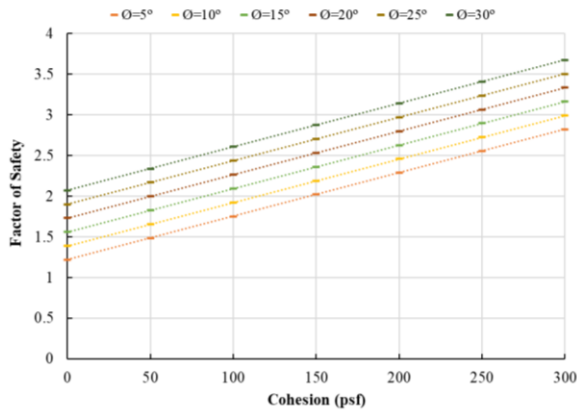
(b)



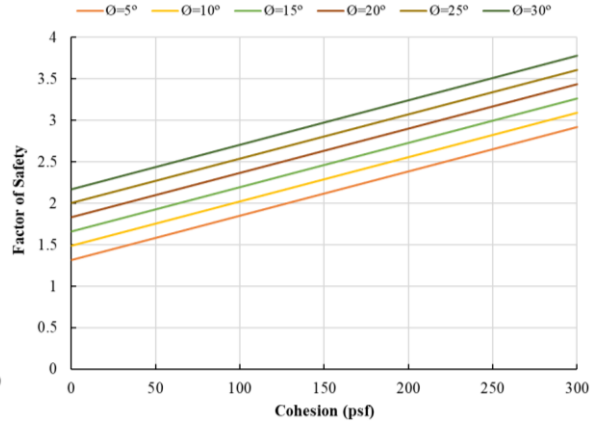
(c)



(d)



(e)



(f)

Figure 7-15 Design charts for slope height of 15 feet and 3 (H): 1 (V) geometry (a) $L_B=10$ ft. (b) $L_B=15$ ft. (c) $L_B=20$ ft. (d) $L_B=25$ ft. (e) $L_B=30$ ft. (f) $L_B=35$ ft.

7.10.2 Design Example

An example calculation is presented in this section to show the steps involved in designing a slope with an MMB. The geometry and stratification of the slope is as shown in Figure 7-16 and the soil properties are as follows:

$$\gamma_1 = 100 \text{ pcf}, c_1 = 70 \text{ psf}, \phi_1 = 8^\circ$$

$$\gamma_2 = 120 \text{ pcf}, c_2 = 145 \text{ psf}, \phi_2 = 18^\circ$$

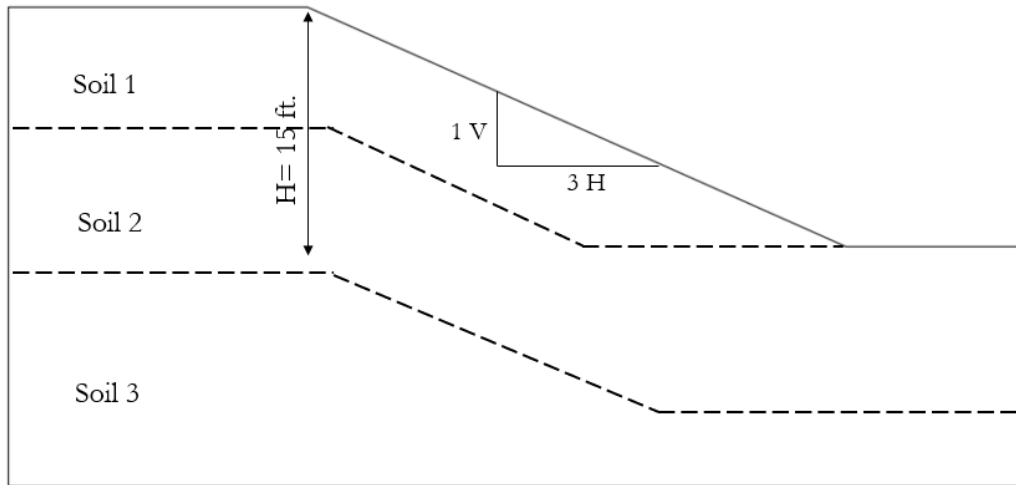


Figure 7-16 Schematic of slope for example calculation.

The first step is to calculate the factor of safety of the original slope. This can be achieved by utilizing the conventional method of slices.

7.10.2.1 Ordinary Method of Slices

The ABC arc shown in Figure 7-17 is a trial slip surface with center O and radius r . The soil mass above the slip surface is divided into a number of vertical slices. The active forces that act on a typical slice are also shown in Figure 7-17, where W is the weight of the n th slice. The forces N and T are normal and tangential components of reaction R . F_n and F_{n+1} are the normal forces that act on the side of the slice while T_n and T_{n+1} are the shearing/tangential components of interslice forces acting on the sides of the slice. During analysis, the normal and tangential components of the interslice forces acting on the two sides of the slice are assumed to be equal, and opposite in direction, and are considered to be acting along the same line of action. The porewater pressure is assumed to be zero.

Here,

Normal component of reaction, $N=W * \cos \alpha$

Tangential component of reaction/Driving Force= $W * \sin \alpha$

$$T_d = \tau_d \Delta L = \frac{\tau_f}{FS} \Delta L = \frac{1}{FS} * (c' + \sigma' \tan \phi') * \Delta L$$

Where, W = weight of slice; α = angle between normal component of reaction and vertical axis; τ_d = allowable/design shear stress; τ_f = shear stress at failure; ΔL = base width of slice; FS = factor of safety; σ' = effective stress; c' = effective cohesion and ϕ' = effective angle of friction.

$$\text{The normal stress, } \sigma' = \frac{N}{\Delta L} = \frac{W \cos \alpha}{\Delta L}$$

Now, considering the equilibrium of the trial slip surface ABC at the center of the slip circle the resisting moment equals the driving moment.

$$\text{Driving moment at the center of the slip circle, } M_d = \sum_{n=1}^{n=p} W * r * \sin \alpha$$

$$\text{Resisting moment at the center of the slip circle, } M_r = \sum_{n=1}^{n=p} \frac{1}{FS} * (c' + \frac{W \cos \alpha}{\Delta L} * \tan \phi') * \Delta L * r$$

Therefore, the factor of the safety of the slope can be determined as follows:

$$FS = \frac{\sum_{n=1}^{n=p} (c' * \Delta L + W \cos \alpha * \tan \phi')}{\sum_{n=1}^{n=p} W * \sin \alpha}$$

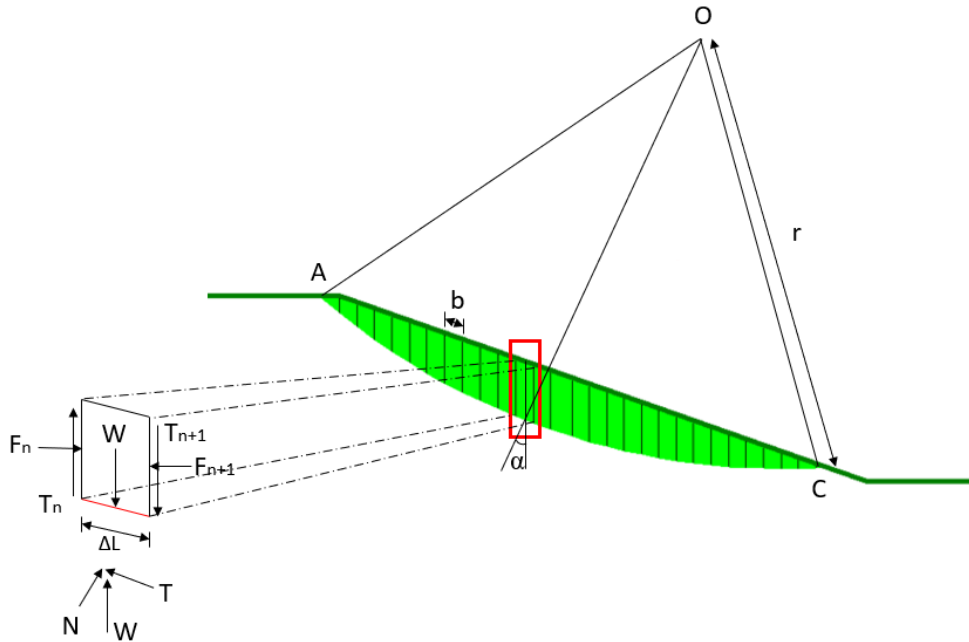


Figure 7-17 Schematic for Ordinary Method of Slices.

The details for each vertical slice are presented in Table 7-10. It is assumed that slip surface will pass through soil layer 1 and therefore only properties of soil layer 1 have been used in calculation.

Table 7-10 Summary table for calculating factor of safety using ordinary method of slices.

Slice Information							Driving Force	Resisting Force
Slice No	Base Width b (ft.)	Mid Height d (ft.)	Base Length ΔL (ft.)	Base angle α	Area A = b*d	W = A * γ (ft ²)	W * sin α (lb/ft)	c' * ΔL + W cos α * tan φ'
1	2.5	1.04	3.25	39.65	2.6	260.0	165.9	252.4
2	1.81	2.45	2.28	37.50	4.4	443.5	270.0	206.8
3	1.81	3.15	2.22	35.70	5.7	570.2	332.7	218.3
4	1.81	3.78	2.18	34.02	6.8	684.2	382.8	230.1
5	1.81	4.32	2.14	32.30	7.8	781.9	417.8	240.5
6	1.81	4.79	2.10	30.69	8.7	867.0	442.5	249.6
7	1.81	5.20	2.07	29.07	9.4	941.0	457.2	258.1
8	1.81	5.54	2.03	27.50	10.0	1002.7	463.0	265.1
9	1.81	5.81	2.01	25.90	10.5	1051.6	459.3	271.4
10	1.81	6.02	1.98	24.30	10.9	1089.6	448.4	276.2
11	1.81	6.17	1.96	22.80	11.2	1116.8	432.8	279.9
12	1.81	6.27	1.94	21.30	11.3	1134.9	412.2	282.5

13	1.81	6.31	1.92	19.79	11.4	1142.1	386.7	283.5
14	2.16	6.29	2.28	18.16	13.6	1358.6	423.3	338.8
15	1.78	6.22	1.86	16.50	11.1	1107.2	314.5	277.5
16	1.78	6.09	1.85	15.10	10.8	1084.0	282.4	274.7
17	1.78	5.92	1.84	13.70	10.5	1053.8	249.6	270.8
18	1.78	5.71	1.83	12.20	10.2	1016.4	214.8	265.5
19	1.78	5.44	1.82	10.80	9.7	968.3	181.4	259.3
20	1.78	5.13	1.81	9.40	9.1	913.1	149.1	251.5
21	1.78	4.78	1.80	7.99	8.5	850.8	118.3	242.6
22	1.78	4.38	1.80	6.60	7.8	779.6	89.6	232.7
23	1.78	3.94	1.79	5.20	7.0	701.3	63.6	221.7
24	1.78	3.45	1.79	3.80	6.1	614.1	40.7	209.5
25	1.78	2.92	1.79	2.41	5.2	519.8	21.9	196.4
26	1.78	2.35	1.78	1.02	4.2	418.3	7.4	181.6
27	1.78	1.73	1.78	-0.37	3.1	307.6	-2.0	166.0
28	1.78	1.07	1.78	-1.76	1.9	190.5	-5.8	149.6
29	1.78	0.36	1.78	-3.15	0.6	64.1	-3.5	131.8
Sum							7216.5	6984.6

Therefore, the factor of safety of the slope, $FS = \frac{6984.6}{7216.5} = \mathbf{0.97}$

7.10.2.2 Infinite Slope

The factor of safety can also be determined utilizing the infinite slope approach. The schematic of the infinite slope approach with seepage parallel to the slope is shown in Figure 7-18. Considering seepage level coincides with the ground surface, the shear strength of the soil is given by:

$$\tau = c' + \sigma' \tan \phi'$$

Considering the slope element ABCD, the forces that act on the vertical faces AB and CD are equal and opposite. The total weight of the slope element of unit length is given by:

$$W = \gamma_{sat} * L * h$$

Where γ_{sat} is the saturated unit weight of the soil. The components of W in the direction of normal and parallel to plane B are:

$$N_a = N_r = W * \cos\beta = \gamma_{sat} * L * h * \cos\beta \text{ and } T_a = T_r = W * \sin\beta = \gamma_{sat} * L * h * \sin\beta$$

The total stress and shear stress at the base of the element are:

$$\sigma = \frac{N_r}{L \cos\beta} = \gamma_{sat} * h * \cos^2\beta \text{ and } \tau = \frac{T_r}{L \cos\beta} = \gamma_{sat} * h * \cos\beta * \sin\beta$$

The resistive shear stress developed at the base of element is given by:

$$\tau_d = c'_d + \gamma' * h * \cos^2\beta * \tan\phi'_d$$

Considering $c'_d = \frac{c'}{FS}$ and $\tan\phi'_d = \frac{\tan\phi}{FS}$, the factor of safety is given by:

$$FS = \frac{c' + h\gamma' \cos^2\beta * \tan\phi'}{\gamma_{sat} * h * \sin\beta * \cos\beta}$$

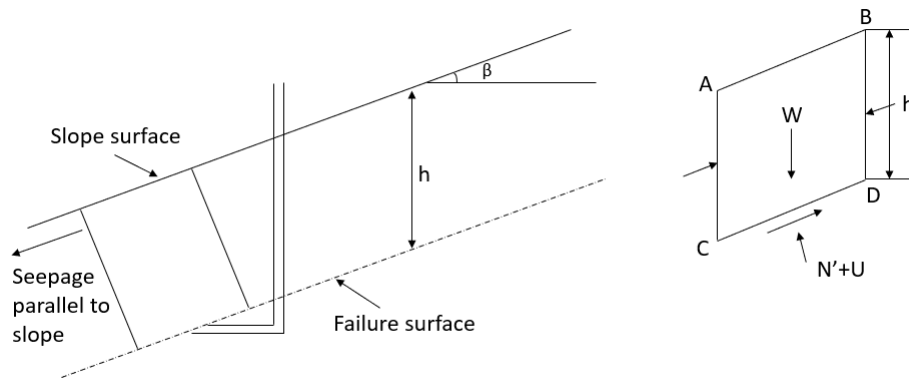


Figure 7-18 Schematic of infinite slope approach.

For the given example, the saturated unit weight of water is considered to be 115 pcf and h is assumed to be 5 feet assuming a shallow slope failure. Therefore, for the given example, the FS is calculated as follows:

$$FS = \frac{70 + 7 * (115 - 62.4) * \cos^2 18.4 * \tan 8}{115 * 7 * \sin 18.4 * \cos 18.4} = \mathbf{0.78}$$

7.10.2.3 Prediction Equation

The factor of safety of the slope is then determined by using the equation developed in Section 7.8. The factor of safety is determined by as follows:

$$FS = 0.8115 + 0.005343C + 0.03413\phi - 0.02991H - 0.00842\beta - 0.029355q \\ + 0.19898 L_B$$

For the current example, L_B will be considered 0 since the slope does not have any MMB. Additionally, q will also be considered 0.

$$FS = 0.8115 + 0.005343 * 70 + 0.03413 * 8 - 0.02991 * 15 - 0.00842 * 18.4 = \mathbf{0.87}$$

The factor of safety obtained from the developed equation is comparable and lower than that obtained from the conventional method. Therefore, the statistical equation provides a reasonable conservative prediction of the factor of safety of the slope.

Addition of MMB

The factor safety of the original slope is found to be less than 1 utilizing various methods (ordinary method of slices, infinite slope approach and statistical prediction equation) depicting unstable conditions. Now, in order to add a MMB into the model, the length of MMB along the slope should be determined. Considering $L_B = 10$ ft, the factor of safety of the slope is found to be 1.45 as shown below. In the initial condition q is considered to be 0.

$$FS = 0.8115 + 0.005343 * 70 + 0.03413 * 8 - 0.02991 * 15 - 0.00842 * 18.4 \\ + 0.019898 * 10 = \mathbf{1.45}$$

Furthermore, the slope stabilized with MMB should be designed considering the amount of rainfall the slope will be subjected to. Considering the slope is located in the DFW region, the average annual rainfall for 30 years is 36.14 inches with 80 wet days. The uniform rainfall intensity is given by:

$$I_{uniform} = \frac{P}{N} = \frac{36.14}{80} = 0.45 \text{ in/day}$$

Where P is annual rainfall (in) and N is the number of wet days in a year. Cumulative rainfall is then calculated as:

$$q = I_{uniform} * 5 = 0.45 * 5 = 2.25 \text{ in}$$

Therefore, the FS of the MMB stabilized slope with 10 feet MMB along the slope in the DFW region is determined to be 1.32, as shown below.

$$FS = 0.8115 + 0.005343 * 70 + 0.03413 * 8 - 0.029911 * 15 - 0.00842 * 18.4 \\ - 0.029355 * 2.25 + 0.019898 * 10 = \mathbf{1.32}$$

Alternatively, the FS can be obtained the design chart for $L_B=10$ ft. as shown in Figure 7-19.

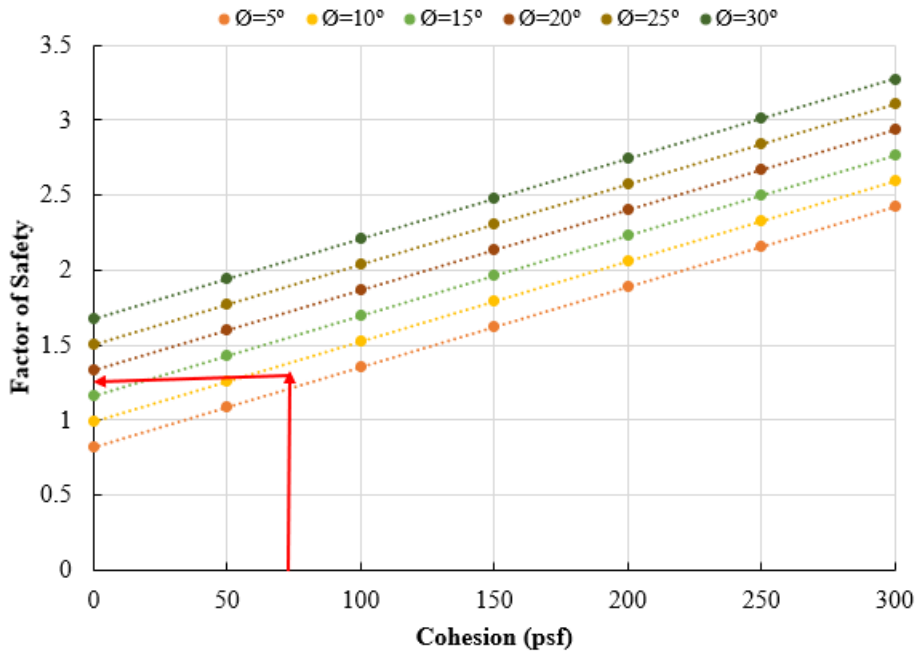


Figure 7-19 Obtaining FS using design chart.

7.11 Limitations of the Prediction Model

The statistical prediction model has been developed considering some assumptions and thus, limitations of the model are inevitable. They are outlined below:

1. Soil shear strength properties, slope geometry and rainfall were varied within a certain range to conduct a parametric study as shown in Table 6-4. Predictability of the statistical model developed using the parametric study results is strong within the range only. Input values beyond the range may not produce reliable output.
2. The prediction model was developed utilizing cumulative precipitation resulting from a uniform rainfall intensity applied over a period of 5 days, as five-day antecedent rainfall was found to be critical for slope stability (Rahardjo et al., 2001). Therefore, the inputs of rainfall (q) into the prediction model should be derived from constant rainfall intensity applied for a maximum period of 5 days.

3. The study was conducted using a numerical model which was calibrated with the field test section. As groundwater table was not encountered in the field, it was not incorporated in the numerical model.
4. The prediction model did not incorporate the effect of soil unit weight. However, a parametric study can be conducted to take the effect of unit weight into account.

CHAPTER 8 SUMMARY AND CONCLUSIONS

8.1 Background

The current study emphasized the stabilization of highway slopes constructed on expansive clayey soil, prone to rainfall induced failures. During the cyclic wet and dry periods of climatic variation, clayey soils undergo swelling and shrinkage phenomenon. Such volumetric changes of the soil lead to the formation of desiccation cracks during the dry periods which act as pathways for rainwater intrusion during the wet periods. The infiltration of water into the soil generates positive porewater pressure, causing the soil to lose its matric suction. Consequently, loss of matric suction in the soil reduces its shear strength ultimately leading to slope failures. Shallow slope failures are commonplace in North Texas due to large surface deposits of clayey soil. Therefore, an approach using a moisture barrier known as the modified moisture barrier (MMB) was proposed to inhibit infiltration of rainfall into the slope and hence increase the lateral stability of the slope.

The main objective of the study was to evaluate the performance of the modified moisture barrier as a method of slope stabilization. Moreover, the performance of a MMB stabilized slope would be compared to that of a mechanically reinforced slope, stabilized with recycled plastic pins (RPP). To this end, a slope that had experienced prior shallow slope failure was selected for this study. The failed section of the slope was divided into two test sections: MMB section and RPP section. A portion of the natural slope identical to the test sections in dimension, was established as the control section for this study. The MMB section was stabilized with the modified moisture barrier at the crest of the slope while the RPP section was stabilized using recycled plastic pins. All three test sections (including the control section) were instrumented with temperature moisture sensors, soil water potential sensors and vertical inclinometer casings to routinely monitor the variation of soil temperature, volumetric water content and matric suction and lateral deformation of the slope.

Additionally topographic survey of the slope was done monthly using the total station to monitor the vertical settlement of the slope and field hydraulic conductivity testing was carried out using the Guelph permeameter to monitor changes in hydraulic conductivity of the slope with time. Routine performance monitoring of the slope was conducted for a period of three years to evaluate the effectiveness of the modified moisture barrier as a slope stabilization method. Results from the current study are summarized below:

8.1.1 Site Investigation

- Prior to slope stabilization, site investigation was carried out utilizing geotechnical drilling and geophysical testing. Both disturbed and undisturbed soil samples were collected. Laboratory testing was carried out to classify the soil and determine its shear strength parameters.
- TCP blow counts indicated that soil ranged from stiff to very stiff consistency.
- Based on Atterberg limits and grain size distribution tests, the soil was classified as clays with low plasticity or lean clay (CL) according to USCS classification. At a depth of 5 feet, the soil had cohesion of 115 psf, friction angle of 11° and unit weight of 110 pcf.
- Results of electrical resistivity imaging showed the soil was loose with high void ratio near the surface while a zone of high moisture existed approximately at 5 feet depth.

8.1.2 Variation of Moisture Content and Matric Suction

- Volumetric moisture content measured in the control section showed spontaneous response to rainfall events, while that of the MMB section remained almost constant with respect to rainfall.

- In the control section, average soil moisture was found to be higher during the wet periods and lower in the dry periods with fluctuations of moisture content ranging from 14.7 to 32.6 %.
- Matric suction was preserved in the MMB section while the soil in the control section was observed to experience loss of matric suction due to rainfall infiltration.
- Variation of moisture content and matric suction in the MMB section does not depict rainfall dependent behavior. Therefore, it can be concluded that the MMB effectively controls moisture infiltration into the slope.

8.1.3 Lateral Deformation

- Among all three test sections, maximum lateral deformation of about 0.48 inches was observed in the control section. Lateral deformation was found to be the least in the RPP section, approximately 0.26 inches near the ground surface. On the other hand, lateral deformation of the MMB section was about 0.29 inches.
- Recycled plastic pins reduced the lateral deformation of the slope by 45 % while that in the MMB section was about 40%. This is because RPPs were installed throughout the entire slope length which controlled the slope's movement while the MMB only extended a length of 10 feet along the slope.
- Lateral deformation was greatest near the ground surface and was observed to decrease with increase in depth.
- Based on lateral deformation readings, RPPs were most effective in reducing a slope's lateral movement while the performance of the MMB was comparable to that of RPPs.

8.1.4 Vertical Settlement

- Average vertical settlements of 1.44 inches and 0.91 inches were observed in the control section and RPP section, respectively while that in the MMB section was approximately 0.50 inches, at the crest of the slope.
- MMB reduced the vertical settlement of the slope by 65 % compared to the control section. This is because the moisture barrier prevents the soil from undergoing cyclic swelling and shrinkage caused by changes in soil moisture content.
- Based on vertical settlement results, it can be concluded that the MMB can effectively reduce vertical movement of the slope.

8.1.5 Hydraulic Conductivity

- Variation of field hydraulic conductivity of the soil was observed with time. During the wet period when there was increased rainfall, the hydraulic conductivity of the slope decreased. On the other hand, during the dry periods, decreased rainfall events increased the hydraulic conductivity of the slope.
- Contrastingly, the soil underneath MMB experience insignificant change hydraulic conductivity with respect to seasonal changes.
- Based on the results of hydraulic conductivity, it can be concluded that the MMB effectively prevents moisture intrusion of the slope which prevents soil properties like hydraulic conductivity from change. Changes in hydraulic conductivity of the slope with time are detrimental to its stability.

8.1.6 Numerical Study

- Coupled transient seepage and slope stability analysis of a slope with and without MMB were carried out to observe the change in porewater pressure profile and subsequent variation in the slope's factor of safety.
- Inclusion of the MMB increased the factor of safety of the slope by preserving the matric suction of the soil.
- Flow analysis of the MMB was carried out and it was observed that two capillary barriers form in a slope with the MMB system: at the soil geotextile interface and at the geotextile-geonet interface. Flow into the geonet layer represented by increase in water content and porewater pressure indicated that the capillary barrier was broken. However, flow of water remained along the geonet layer due to the underlying impermeable geomembrane.
- The diversion length of the MMB was found to be a function of the permeability and thickness of the geotextile layer, slope angle and the rate of infiltration.
- A parametric study was conducted utilizing the calibrated numerical model to observe the effect of variation of soil shear strength properties, soil hydraulic properties, slope geometry, rainfall, and the length of MMB along the slope, on slope factor of safety.
- Increase in soil shear strength properties increase the initial factor of safety of the slope while increasing the length of MMB, decreased the rate of reduction of slope FS.
- Increase in both slope height and angle, decreased the initial FS of the slope. With greater length of MMB along the slope, the FS reduced at a slower rate when subjected to rainfall. However, at higher angle with increase in length of MMB, lateral drainage was enhanced, and the FS of the slope was preserved.

- When subjected to rainfall infiltration, increase in the soil hydraulic conductivity decreased the FS of the slope.

8.1.7 Prediction Model and Design Methodology

- The comprehensive dataset obtained from the parametric study was used to develop a prediction model for the factor of safety of the slope. Statistical analysis was carried out and the developed multiple linear regression model is as follows:

$$FS = 0.8115 + 0.005343C + 0.03413\phi - 0.02991H - 0.00842\beta - 0.029355q + 0.19898 L_B$$

where FS= factor of safety, c=cohesion (psf), ϕ = angle of friction (degrees), H=slope height (ft.), β =slope inclination (degrees), q=cumulative rainfall obtained from a uniform intensity (in) and L_B is the length of MMB along the slope (ft).

- The model was validated with an independent set of data and R^2 value of 0.9291 was obtained.
- Design steps for calculating the FS of a MMB stabilized slope were outlined using a calculation example.

Based on the field performance monitoring and numerical study results, it can be concluded that the MMB can effectively stabilize shallow failures as well as prevent rainfall induced slope failures.

8.2 Recommendation for Future Studies

Based on the findings of the current study, the following recommendations are proposed for future research:

- The field study was conducted on one slope section of certain geometry and soil type. More field scale studies with the application of the modified moisture barrier can corroborate the results of the current study.
- Geocomposites and geomembranes of different types and properties can be considered investigated to perform as the modified moisture barrier.
- Rainfall analysis can be conducted to develop a threshold for critical rainfall when designing a slope using a modified moisture barrier.
- A broader range of predictor variables should be incorporated in the prediction model.
- Machine learning can be utilized to develop a prediction model for the factor of safety of a slope installed with a modified moisture barrier.

REFERENCES

1. Abd, I. A., Fattah, M. Y., & Mekkiyah, H. (2020). Relationship between the matric suction and the shear strength in unsaturated soil. *Case Studies in Construction Materials*, 13, e00441.
2. Ahangar-Asr, A., Faramarzi, A., & Javadi, A. A. (2010). A new approach for prediction of the stability of soil and rock slopes. *Engineering Computations*.
3. Ahmed, A. (2017). *Effects of Climatic Loading in Flexible Pavement Subgrades in Texas* (Doctoral dissertation).
4. Ahmed, A., Hossain, S., Khan, M. S., & Shishani, A. (2018). "Data-Based Real-Time Moisture Modeling in Unsaturated Expansive Subgrade in Texas". *Transportation Research Record*, 2672(52), 86-95.
5. Akhtar, M. A., Mahjabin, S., Hossain, M. S., Mina, Z., & Hossain, M. I. Characterization of Eagle Ford Shale by Using Laboratory Electrical Resistivity Imaging. In *Geo-Congress 2022* (pp. 159-168).
6. Amakye, S. Y., Abbey, S. J., Booth, C. A., & Mahamadu, A. M. (2021). Enhancing the engineering properties of subgrade materials using processed waste: A review. *Geotechnics*, 1(2), 307-329.
7. Au, S. W. C. (1998). Rain-induced slope instability in Hong Kong. *Engineering Geology*, 51(1), 1-36.
8. Barrett, R. K. (1980). *Use of Horizontal Drains: Case Histories from the Colorado Division of Highways* (No. 783).
9. Bouazza, A., Zornberg, J., McCartney, J. S., & Singh, R. M. (2013). Unsaturated geotechnics applied to geoenvironmental engineering problems involving geosynthetics. *Engineering geology*, 165, 143-153
10. Bowders, J. J., Loehr, J. E., Salim, H., & Chen, C. W. (2003). Engineering properties of recycled plastic pins for slope stabilization. *Transportation Research Record: Journal of the Transportation Research Board*, 1849(1), 39-46.
11. Bruce, D. A., & Juran, I. (1997). *Drilled and Grouted Micropiles: State-of-Practice Review, Volume I: Background, Classifications, Cost*.

12. Cai, F., & Ugai, K. (2004). Numerical analysis of rainfall effects on slope stability. *International Journal of Geomechanics*, 4(2), 69.
13. Carpenter, G. W., & Stephenson, R. W. (1986). Permeability testing in the triaxial cell. *Geotechnical Testing Journal*, 9(1), 3-9
14. Chakraborty, A., & Goswami, D. (2017). Prediction of slope stability using multiple linear regression (MLR) and artificial neural network (ANN). *Arabian Journal of Geosciences*, 10(17), 1-11.
15. Chen, C. W., Salim, H., Bowders, J., Loehr, E., and Owen, J. (2007). "Creep Behavior of Recycled Plastic Lumber in Slope Stabilization Applications." *J. Mater. Civ. Eng.*, 19(2), 130-138
16. Chen, F. H. (2012). *Foundations on expansive soils* (Vol. 12). Elsevier.
17. Chowdhury, R. N., & Zhang, S. (1991). Tension cracks and slope failure. In *Slope stability engineering developments and applications: Proceedings of the international conference on slope stability organized by the Institution of Civil Engineers and held on the Isle of Wight on 15–18 April 1991* (pp. 27-32). Thomas Telford Publishing.
18. Christopher, B., Hayden, S., and Zhao, A. (2000). "Roadway Base and Subgrade Geocomposite Drainage Layers." *Testing and Performance of Geosynthetics in Subsurface Drainage*, ASTM International, 100 Barr Harbor Drive, PO Box C700, West Conshohocken, PA 19428-2959, 35-35–17.
19. Cobos, D. R., & Chambers, C. (2010). Calibrating ECH2O soil moisture sensors. *Application note*, 1-5.
20. Collins, B. D., & Short, R. (2006). *Testing and Evaluation of Driven Plate Piles in Full-Size Test Slope: New Method for Stabilizing Shallow Landslides* (No. 06-0299).
21. Cuisinier, O., Masroui, F., & Mehenni, A. (2020). Alteration of the hydro-mechanical performances of a stabilised compacted soil exposed to successive wetting-drying cycles. *Journal of Materials in Civil Engineering*, 32(11), 04020349.
22. Dai, Z., Chen, S., & Li, J. (2020). Physical model test of seepage and deformation characteristics of shallow expansive soil slope. *Bulletin of Engineering Geology and the Environment*, 1-16.
23. Das, B. M. (Ed.). (2010). *Geotechnical engineering handbook*. J. Ross publishing.

24. Day, R. W. (1996). Design and Repair for Surficial Slope Failures. *Practice Periodical on Structural Design and Construction*, 1(3), 83-87.
25. Divya, P. V., Viswanadham, B. V. S., & Gourc, J. P. (2012). Influence of geomembrane on the deformation behaviour of clay-based landfill covers. *Geotextiles and Geomembranes*, 34, 158-171.
26. Dunne, T., Zhang, W., & Aubry, B. F. (1991). Effects of rainfall, vegetation, and microtopography on infiltration and runoff. *Water Resources Research*, 27(9), 2271-2285.
27. Dunncliff, J. (1993). *Geotechnical instrumentation for monitoring field performance*. John Wiley & Sons.
28. Elseifi, M., Al-Qadi, I., Loulizi, A., and Wilkes, J. (2001a). "Performance of Geocomposite Membrane as Pavement Moisture Barrier." *Transportation Research Record: Journal of the Transportation Research Board*, 1772, 168–173.
29. Faysal, M. (2017). *Structural Competency and Environmental Soundness of the Recycled Base Materials in North Texas* (Doctoral dissertation).
30. Foley, J. L., & Silburn, D. M. (2002). Hydraulic properties of rain impact surface seals on three clay soils—influence of raindrop impact frequency and rainfall intensity during steady state. *Soil Research*, 40(7), 1069-1083.
31. Fredlund, D. G., Xing, A., Fredlund, M. D., & Barbour, S. L. (1996). The relationship of the unsaturated soil shear strength to the soil-water characteristic curve. *Canadian geotechnical journal*, 33(3), 440-448
32. Gerscovich, D. M. S., Vargas Jr, E. A., & De Campos, T. M. P. (2006). On the evaluation of unsaturated flow in a natural slope in Rio de Janeiro, Brazil. *Engineering Geology*, 88(1-2), 23-40.
33. Gordan, B., Armaghani, D. J., Adnan, A. B., & Rashid, A. S. A. (2016). A new model for determining slope stability based on seismic motion performance. *Soil Mechanics and Foundation Engineering*, 53(5), 344-351.
34. Gupta, R. K., Rudra, R. P., Dickinson, W. T., & Wall, G. J. (1994). Spatial and seasonal variations in hydraulic conductivity in relation to four determination techniques. *Canadian Water Resources Journal*, 19(2), 103-113.
35. Harabinová, S., & Panulinová, E. (2020). Impact of shear strength parameters on slope stability. In *MATEC Web of Conferences* (Vol. 310, p. 00040). EDP Sciences.

36. Henry, K. S., Stormont, J. C., Barna, L. A., and RAMOS, R. D. (2002). "Geocomposite Capillary Barrier Drain for Unsaturated Drainage of Pavement." *Geosynthetics: State of the Art-Recent Developments. Proceedings of the Seventh International Conference on Geosynthetics, 7-ICG*, AA Balkema, Nice, France, 877–80
37. Hossain, J. (2013). Geohazard potential of rainfall induced slope failure on expansive clay.
38. Hossain, S., Khan, S., & Kibria, G. (2017). *Sustainable slope stabilisation using recycled plastic pins*. CRC Press.
39. Huat, B. B., Ali, F. H., & Low, T. H. (2006). Water infiltration characteristics of unsaturated soil slope and its effect on suction and stability. *Geotechnical & Geological Engineering*, 24(5), 1293-1306.
40. Islam, M. A. (2021). *Rainfall-Induced Slope Failure—An Early Warning System* (Doctoral dissertation, The University of Texas at Arlington).
41. Mohamed, T., Anuar, K. A. S. A., & Mukhlisin, M. (2012). Prediction of slope stability using statistical method and fuzzy logic. *TOJSAT*, 2(4), 68-73.
42. Jones, L. D., & Jefferson, I. (2012). Expansive soils.
43. Lees, A. S., MacDonald, G. J., Sheerman-Chase, A., & Schmidt, F. (2013). Seasonal slope movements in an old clay fill embankment dam. *Canadian Geotechnical Journal*, 50(5), 503-520.
44. Neter, J., Kutner, M. H., Nachtsheim, C. J., & Wasserman, W. (1996). Applied linear statistical models.
45. O'brien, R. M. (2007). A caution regarding rules of thumb for variance inflation factors. *Quality & quantity*, 41(5), 673-690.
46. Kamei, T., Ahmed, A., & Ugai, K. (2013). Durability of soft clay soil stabilized with recycled Bassanite and furnace cement mixtures. *Soils and foundations*, 53(1), 155-165.
47. Khan, M. S. (2014). Sustainable slope stabilization using recycled plastic pin in Texas.
48. Khan, M. S., Hossain, S., & Kibria, G. (2016). Slope stabilization using recycled plastic pins. *Journal of Performance of Constructed Facilities*, 30(3), 04015054.
49. Khan, M. S., Hossain, S., Ahmed, A., & Faysal, M. (2017). Investigation of a shallow slope failure on expansive clay in Texas. *Engineering geology*, 219, 118-129.

50. Kim, Y. K., & Lee, S. R. (2010). Field infiltration characteristics of natural rainfall in compacted roadside slopes. *Journal of geotechnical and geoenvironmental engineering*, 136(1), 248-252.
51. Kodikara, J. K. (2018). Desiccation. *Encyclopedia of engineering geology. Encyclopedia of earth sciences series*. Springer. https://doi.org/10.1007/978-3-319-73568-9_87.
52. Koerner, R. M. (2012). *Designing with geosynthetics-Vol. 1* (Vol. 1). Xlibris Corporation.
53. Lim, T. T., Rahardjo, H., Chang, M. F., & Fredlund, D. G. (1996). Effect of rainfall on matric suctions in a residual soil slope. *Canadian Geotechnical Journal*, 33(4), 618-628.
54. Loehr, J. E., & Bowders, J. J. (2007). Slope Stabilization Using Recycled Plastic Pins, Phase III.
55. Lye, L. M., Hussein, A., & Dey, R. IMPROVED SENSITIVITY ANALYSIS IN CIVIL ENGINEERING DESIGN USING STATISTICAL DESIGN OF EXPERIMENTS (DOE).
56. Matthews, G. P., Laudone, G. M., Gregory, A. S., Bird, N. R. A., de G Matthews, A. G., & Whalley, W. R. (2010). Measurement and simulation of the effect of compaction on the pore structure and saturated hydraulic conductivity of grassland and arable soil. *Water Resources Research*, 46(5).
57. McCartney, J. S., Villar, L., & Zornberg, J. G. (2007, November). Estimation of the hydraulic conductivity function of unsaturated clays using an infiltration column test. In *Proc., 6th Brazilian Conference on Unsaturated Soils (NSAT)*.
58. McLaren, M. G. (1995, April). Recycled plastic lumber & shapes design and specifications. In *Restructuring: America and Beyond* (pp. 819-833). ASCE.
59. Messing, I., & Jarvis, N. J. (1990). Seasonal variation in field-saturated hydraulic conductivity in two swelling clay soils in Sweden. *Journal of soil science*, 41(2), 229-237.
60. Nelson, J. D., Overton, D. D., & Durkee, D. B. (2001). Depth of wetting and the active zone. In *Expansive clay soils and vegetative influence on shallow foundations* (pp. 95-109).
61. Nicholson, R. V., Gillham, R. W., Cherry, J. A., & Reardon, E. J. (1989). Reduction of acid generation in mine tailings through the use of moisture-retaining cover layers as oxygen barriers. *Canadian geotechnical journal*, 26(1), 1-8.

62. Omid, G. H., Thomas, J. C., & Brown, K. W. (1996). Effect of desiccation cracking on the hydraulic conductivity of a compacted clay liner. *Water, Air, and Soil Pollution*, 89(1), 91-103.
63. Pandey, P., Manjur Dola, M., & Hossain, M. S. Controlling Pavement Distresses Using Modified Moisture Barrier. In *Geo-Congress 2022* (pp. 442-452).
64. Park, K. D., & Fleming, I. R. (2006). Evaluation of a geosynthetic capillary barrier. *Geotextiles and Geomembranes*, 24(1), 64-71.
65. Parra, J. R., Loehr, J. E., Hagemeyer, D. J., & Bowders, J. J. (2003). Field performance of embankments stabilized with recycled plastic reinforcement. *Transportation research record*, 1849(1), 31-38.
66. Rahardjo, H., Li, X. W., Toll, D. G., & Leong, E. C. (2001). The effect of antecedent rainfall on slope stability. In *Unsaturated soil concepts and their application in geotechnical practice* (pp. 371-399). Springer, Dordrecht.
67. Rahardjo, H., Lee, T. T., Leong, E. C., & Rezaur, R. B. (2005). Response of a residual soil slope to rainfall. *Canadian Geotechnical Journal*, 42(2), 340-351.
68. Rahardjo, H., Santoso, V. A., Leong, E. C., Ng, Y. S., & Hua, C. J. (2012). Performance of an instrumented slope covered by a capillary barrier system. *Journal of geotechnical and geoenvironmental engineering*, 138(4), 481-490.
69. Rahardjo, H., Satyanaga, A., & Leong, E. C. (2012). Unsaturated soil mechanics for slope stabilization. *Southeast Asian Geotechnical Journal*, 43(1), 48-58.
70. Rahardjo, H., Santoso, V. A., Leong, E. C., Ng, Y. S., Tam, C. P. H., & Satyanaga, A. (2013). Use of recycled crushed concrete and Secudrain in capillary barriers for slope stabilization. *Canadian Geotechnical Journal*, 50(6), 662-673.
71. Rauss, C. (2019). *Long Term Performance Monitoring of Shallow Slope Stabilization Utilizing Recycled Plastic Pins* (Doctoral dissertation, The University of Texas at Arlington).
72. Rogers, L. E. and Wright, S. G. (1986). The effect of wetting and drying on the long-term shear strength parameters for compacted Beaumont clay. Final Report. Research.
73. Ross, B. (1990). The diversion capacity of capillary barriers. *Water Resources Research*, 26(10), 2625-2629.

74. Royster, D. L. (1980). Horizontal drains and horizontal drilling: an overview. *Transportation Research Record*, 783, 16-20.
75. Sakellariou, M. G., & Ferentinou, M. D. (2005). A study of slope stability prediction using neural networks. *Geotechnical & Geological Engineering*, 23(4), 419-445.
76. Saleh, A. A., & Wright, S. G. (1997). *Shear strength correlations and remedial measure guidelines for long-term stability of slopes constructed of highly plastic clay soils* (No. FHWA/TX-98/1435-2F).
77. Sapkota, A., Ahmed, A., Pandey, P., Hossain, M. S., & Lozano, N. (2019, March). Stabilization of rainfall-induced slope failure and pavement distresses using recycled plastic pins and modified moisture barrier. In *Geo-Congress 2019: Embankments, Dams, and Slopes* (pp. 237-246). Reston, VA: American Society of Civil Engineers.
78. Senior, R. B. (1981). Tensile strength, tension cracks, and stability of slopes. *Soils and foundations*, 21(2), 1-17.
79. Shahandashti, M., Hossain, S., Khankarli, G., Zahedzahedani, S. E., Abediniangerabi, B., & Nabaei, M. (2019). *Synthesis on rapid repair methods for embankment slope failure* (No. FHWA/TX-18/0-6957-1).
80. Singh, Shruti. (2022). Design of Crack Attenuating Mix using Waste Plastic.
81. Skempton, A.W. (1977). "Slope Stability of Cuttings in Brown London Clay". In *Proceedings of Ninth International Conference on Soil Mechanics and Foundation Engineering*, Tokyo, Vol. 3, 261-270.
82. Spencer, E. (1967). A method of analysis of the stability of embankments assuming parallel inter-slice forces. *Geotechnique*, 17(1), 11-26.
83. Stark, T. D., Boerman, T. R., & Connor, C. J. (2008). Puncture resistance of PVC geomembranes using the truncated cone test. *Geosynthetics International*, 15(6), 480-486.
84. Steenhuis, T. S., Parlange, J. Y., & Kung, K. J. S. (1991). Comment on "The diversion capacity of capillary barriers" by Benjamin Ross. *Water Resources Research*, 27(8), 2155-2156.
85. Steinberg, M. L. (1989). "Further Monitoring of Twelve Geomembrane Sites in Texas DHT-18". Austin, TX.
86. Stevens, J. P. (2012). *Applied multivariate statistics for the social sciences*. Routledge.

87. Stormont, J. C. (1996). The effectiveness of two capillary barriers on a 10% slope. *Geotechnical & Geological Engineering*, 14(4), 243-267.
88. Stormont, J. C., & Stockton, T. B. (2000). Preventing positive pore water pressures with a geocomposite capillary barrier drain. In *Testing and Performance of Geosynthetics in Subsurface Drainage*. ASTM International.
89. Sun, S. W., Zhu, B. Z., & Wang, J. C. (2013). Design method for stabilization of earth slopes with micropiles. *Soils and Foundations*, 53(4), 487-497. Titi, H. H., & Helwany, S. (2007). *Investigation of vertical members to resist surficial slope instabilities* (No. WHRP 07-03). Wisconsin. Dept. of Transportation. Bureau of Technical Services.
90. TAHER, N. R., Mesut, G. Ö. R., AKSOY, H. S., & AHMED, H. Numerical investigation of the effect of slope angle and height on the stability of a slope composed of sandy soil. *Gümüşhane Üniversitesi Fen Bilimleri Dergisi*, 12(2), 664-675.
91. Tamrakar, S. (2015). *Slope stabilization and performance monitoring of I-35 and sh-183 slopes using Recycled plastic pins* (Doctoral dissertation).
92. TxDOT. (2000). *Geotechnical Manual*. Austin, Texas.
93. Vatcheva, K. P., Lee, M., McCormick, J. B., & Rahbar, M. H. (2016). Multicollinearity in regression analyses conducted in epidemiologic studies. *Epidemiology* (Sunnyvale, Calif.), 6(2).
94. Yilmaz, I., & Yuksek, A. G. (2008). An example of artificial neural network (ANN) application for indirect estimation of rock parameters. *Rock Mechanics and Rock Engineering*, 41(5), 781.
95. Zhan, T. L., Ng, C. W., & Fredlund, D. G. (2007). Instrumentation of an unsaturated expansive soil slope. *Geotechnical Testing Journal*, 30(2), 1641.
96. Zhang, Z. F., Groenevelt, P. H., & Parkin, G. W. (1998). The well-shape factor for the measurement of soil hydraulic properties using the Guelph Permeameter. *Soil and Tillage Research*, 49(3), 219-221.
97. Zhang, L. L., Zhang, J., Zhang, L. M., & Tang, W. H. (2011). Stability analysis of rainfall-induced slope failure: a review. *Proceedings of the Institution of Civil Engineers-Geotechnical Engineering*, 164(5), 299-316.

98. Zornberg, J. G., & Gupta, R. (2009). Reinforcement of pavements over expansive clay subgrades. In *Proceedings of the 17th International Conference on Soil Mechanics and Geotechnical Engineering (Volumes 1, 2, 3 and 4)* (pp. 765-768). IOS Press.

Appendix A

Soil Boring Logs

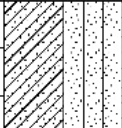
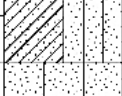
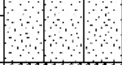

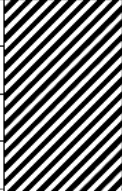

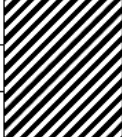
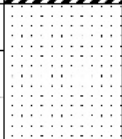
GEO TECH BH COLUMNS - GINT STD US.GDT - 6/21/19 13:28 - C:\USERS\PIXB3319\ONE DRIVE - UNIVERSITY OF TEXAS AT ARLINGTON\FORTWORTH INSTALLATION\DRILLING\BORELOG14. I20 AND PARK SPRINGS BLVD\F1 AND PARK SPRINGS BLVD\F2 AND PARK SPRINGS BLVD\F3

Logo uta

BORING NUMBER BH-1

PAGE 1 OF 1

CLIENT <u>TxDOT - Fort Worth</u>	PROJECT NAME <u>Fort Worth Slope Stabilization</u>
PROJECT NUMBER <u>4</u>	PROJECT LOCATION <u>I20 and Park Springs Blvd.</u>
DATE STARTED <u>6/21/19</u> COMPLETED <u>6/21/19</u>	GROUND ELEVATION _____ HOLE SIZE _____
DRILLING CONTRACTOR _____	GROUND WATER LEVELS:
DRILLING METHOD <u>Hollow Stem Auger</u>	AT TIME OF DRILLING <u>--</u>
LOGGED BY <u>UTA</u> CHECKED BY <u>UTA</u>	AT END OF DRILLING <u>--</u>
NOTES _____	AFTER DRILLING <u>--</u>

DEPTH (ft)	GRAPHIC LOG	MATERIAL DESCRIPTION	SAMPLE TYPE NUMBER	BLOW COUNTS (N VALUE)	MOISTURE CONTENT (%)
0					
		Brown Fill clayey sand	AU		
		Reddish brown Clayey sand	AU		
5		Whiteish gray Silty sand	TCP	14-9 (23)	
		Dark brown Silty clay	AU		
10		Gray Clay with traces of silt	SH TCP	24-35 (59)	
		Brown Clay	AU		
15		Reddish brown Clay with traces of water and silt	SH TCP	17-50 (3')	
		Dark reddish brown Sandstone	AU TCP	50 (0'')-50 (0'')	
20		Bottom of borehole at 20.0 feet.			

GEO TECH BH COLUMNS - GINT STD US.GDT - 82'16" 0'28" - C:\USERS\PIXB331\BONE\DRIVE - UNIVERSITY OF TEXAS AT ARLINGTON\FORTH\MORTH INSTALLATION\DRILLING\BORELOGS4_I20 AND PARK SPRINGS BLDV.D20 AND PARK SPRINGS BLDV.D20 AND PARK SPRINGS BLDV.D20



uta

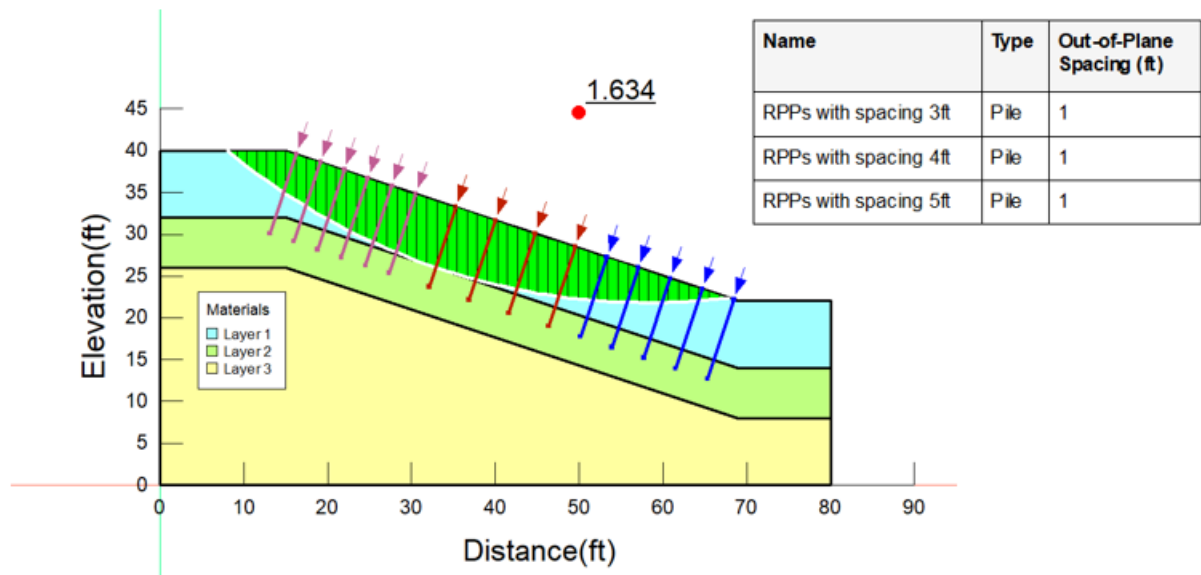
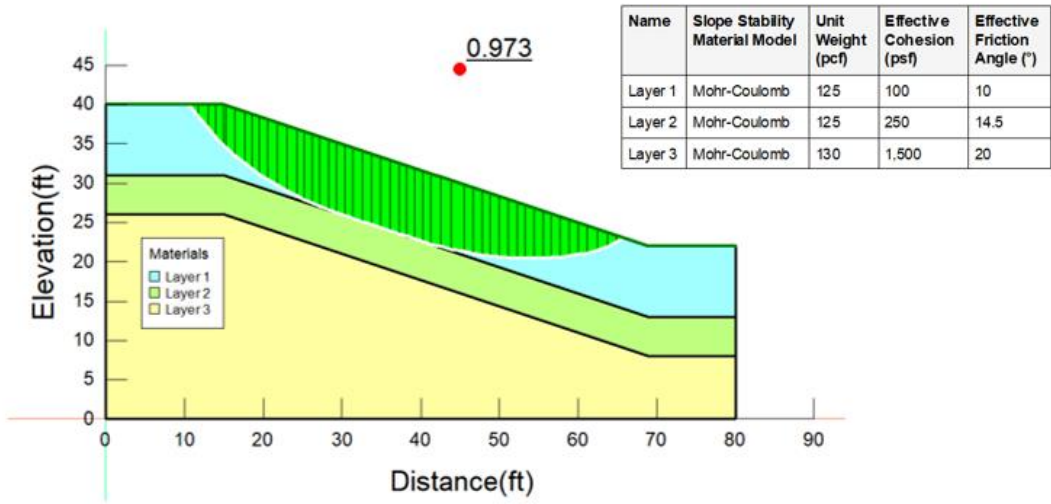
BORING NUMBER BH-2

PAGE 1 OF 1

CLIENT TxDOT - Fort Worth	PROJECT NAME Fort Worth Slope Stabilization
PROJECT NUMBER 4	PROJECT LOCATION I20 and Park Springs Blvd.
DATE STARTED 6/21/19	COMPLETED 6/21/19
DRILLING CONTRACTOR	GROUND ELEVATION
DRILLING METHOD Hollow Stem Auger	GROUND WATER LEVELS:
LOGGED BY UTA	CHECKED BY UTA
NOTES	AT TIME OF DRILLING ---
	AT END OF DRILLING ---
	AFTER DRILLING ---

DEPTH (ft)	GRAPHIC LOG	MATERIAL DESCRIPTION	SAMPLE TYPE NUMBER	BLOW COUNTS (N VALUE)	MOISTURE CONTENT (%)
0					
0 - 5		Reddish brown Sandy clay	AU TCP	25-27 (52)	
5 - 8		Reddish brown Silty clay	AU		
8 - 10		Reddish brown Clay	SH	29-35 (64)	
10 - 13		Gray Shally clay	TCP		
13 - 15		Light gray Silty sand			
15 - 19		Brown Clay with traces of sandstone	AU SH TCP	50 (0.5")- 50 (0.5")	
19 - 20		Dark brown Sandstone	AU TCP	50 (0.75")- 50 (0.5")	
Bottom of borehole at 20.0 feet.					

Appendix B



BIOGRAPHY

Muhasina Manjur Dola was born in Dhaka, Bangladesh. She completed her Bachelor of Science in Civil Engineering from the University of Texas at Arlington in May 2019. She then joined the BS to PhD program in Geotechnical Engineering at the University of Texas at Arlington in June 2019 and worked as a graduate research assistant under the supervision of Dr. Sahadat Hossain. Currently, she works as a senior staff engineer at Converse Consultants in Monrovia, California. The author's research experience and interests include the areas of expansive soil, slope stability, application of geosynthetic materials, geophysical testing, laboratory testing, numerical study, statistical modeling, and sustainable waste management among others.